A Vapour-Dominated High-Sulphidation System: Geology, Alteration and Mineralization of the Hypogene Au (Ag-Cu) Bowone and Binebase Deposits, Sangihe Island, Indonesia

by

Julia Jenner King

A thesis submitted to the Faculty of Graduate Studies and Research in partial fulfillment of the requirements for the degree of Master of Science

Department of Earth and Planetary Sciences

McGill University, Montreal, QC, Canada

November 2012

Abstract

The Bowone and Binebase Au (Ag-Cu) deposits are related prospects, located 1 km apart on the volcanic island of Sangihe, Northeastern Indonesia. The deposits occur at the southern and oldest end of the island, and are hosted in Quaternary volcanic and volcaniclastic formations. Each deposit has a supergene and hypogene mineralized zone, although only the supergene zone of the Binebase deposit is of significant thickness. This thesis focuses on the hypogene zones of the deposits, and was undertaken with the goal of understanding the formation of high-sulphidation epithermal precious metal (Au, Ag) deposits.

The hypogene mineralized zones at both Bowone and Binebase are spatially related to intense advanced (quartz, pyrite, pyrophyllite, natroalunite, alunite, kaolinite and dickite) and intermediate (quartz, pyrite, kaolinite, dickite and illite) argillic alteration that resulted in enhanced secondary porosity and silica-rich zones. However, vuggy or residual silica, which is characteristic of high-sulphidation epithermal deposits, is not well developed. The mineralization occurred in three main stages: 1) early gold-bearing pyrite (Pyrite I) in textural equilibrium with advanced and intermediate argillic alteration; 2) replacement and veining of massive gold-bearing Pyrite II and; 3) barite-enargite (Au and Ag bearing) veins. In each stage, gold and silver are hosted in pyrite and locally enargite, either in solid solution or as nanoparticles. The occurrence of gold-bearing pyrite in textural equilibrium with hydrothermal alteration minerals that are widely considered to have formed from condensed acidic vapours shows that the same fluids were also mineralizing, and transported gold (and other metals).

The metals likely originated from an oxidizing felsic magma that was emplaced at high crustal levels and exsolved a low-density supercritical fluid into which the metals partitioned preferentially. The metals were transported by this fluid (which evolved to vapour on cooling) as hydrated species that ascended through the volcanic pile via fractures and zones of enhanced permeability. The fluid condensed at depths between 920 and 1260 m to form an acidic liquid with a pH between 0.5 and 4. The temperature ranged between 250 and 340°C and $\Delta \log fO_2$ (HM) was between -1 and +4. At high fluid/rock ratios, advanced argillic assemblages formed, whereas at low fluid/rock ratios, an intermediate argillic I alteration and a distal intermediate argillic II alteration assemblage formed. The alteration also created porosity through the dissolution of minerals. The metals accumulated in zones of high fluid/rock ratios controlled by sub-vertical conduits and the porosity of the sub-horizontal host rocks, where they were concentrated by adsorption onto the faces of pyrite crystals and incorporated in the pyrite through substitution for Fe or deposition as nanoparticles.

Pyrite contains Ag, As, Au, Bi, Co, Cu, Fe, Ni, Pb, S, Sb, Se, Te and Zn. Pyrite I is host to an average of 1.1 ppm Au and 33.0 ppm Ag, pyrite II contains an average of 3.0 ppm Au and 80.6 ppm Ag, and enargite 0.53 ppm Au and 101.6 ppm Ag. Although there is a correlation between Au and As concentration, the absolute arsenic content is much lower than in other deposits containing auriferous pyrite; it averages 329.7 ppm in Pyrite II. Pyrite II has the highest concentration of minor and trace elements overall, and contains up to 6.0 wt% Cu. Imaging by EMPA shows that growth and sector zones are common in Pyrite II. They are made evident by differences in the distribution of Cu and other elements. The anomalously high concentration of Cu and presence of both growth and sector zoning in Pyrite II enabled development of a tool for

assessing relative changes in physicochemical conditions. Partition coefficients determined for Cu between paired sector zones in Pyrite II, showed that Cu, Au (and other metals) were preferentially incorporated in pyrite during periods when physicochemical conditions were stable.

Résumé

Les gîtes d'or (cuivre-argent) Bowone et Binebase de l'île volcanique Sangihe, au nord-est de l'Indonésie, sont distants d'un kilomètre et géologiquement associés. Les gisements se trouvent à l'extrémité sud de l'île et sont associés aux formations volcaniques et volcano-sédimentaires quaternaires les plus anciennes de l'île. Chaque gîte possède des minéralisations supergènes et hypogènes, mais seule la zone supergène du gîte Binebase est d'une épaisseur considérable. Cette thèse porte principalement sur les zones hypogènes de chacun des gisements et a été réalisée dans le but de comprendre la formation des gîtes d'Au-Ag sulfato-acides.

Les zones hypogènes minéralisées de Bowone et Binebase sont spatialement liées à une forte altération de style argileuse avancée (quartz, pyrite, pyrophyllite, natroalunite, alunite, kaolinite et dickite) et une altération argileuse intermédiaire (quartz, pyrite, kaolinite, dickite et illite) qui ont produit des zones de porosité secondaire et des zones riches en silice. Toutefois, la silice vacuolaire ou résiduelle, qui est caractéristique des gisements sulfato-acides épithermaux, est peu développée. La minéralisation s'est effectuée en trois principales étapes : 1) formation de pyrite aurifère précoce (Pyrite I), en équilibre textural avec les altérations argileuses avancée et intermédiaire, puis 2) remplacement par la pyrite aurifère massive (Pyrite II), associé à la mise en place de veines, et enfin, 3) formation de veines de barite et d'énargite aurifères et argentifères. A chaque étape, l'or et l'argent sont associés à la pyrite et localement à l'énargite, soit en solution solide, soit sous forme de nanoparticules. La présence de la pyrite aurifère en équilibre textural avec des minéraux d'altération hydrothermale, qui sont principalement considérés comme s'étant formés à partir de vapeurs acides condensées, montre que ces mêmes fluides ont également été minéralisant et ont transporté l'or et les autres métaux.

Les métaux sont vraisemblablement issus d'un magma felsique oxydant, mis en place à des niveaux élevés au sein de la croûte continentale. Ce magma aurait produit par exsolution un fluide supercritique de faible densité au sein duquel les métaux auraient été préférentiellement concentrés. Les métaux on par la suite été transportés par ce fluide (qui s'est transformé en vapeur lors de son refroidissement), sous forme hydratée, à travers la séquence de roches volcaniques via les fractures et les zones de perméabilité accrue. Le fluide s'est condensé à des profondeurs comprises entre 920 et 1260 m pour former un liquide acide avec un pH entre 0,5 et 4. La température a varié entre 250 et 340 °C pour un $\Delta \log fO_2$ (HM) compris entre -1 et +4. Pour des rapports fluide/roche élevés, les assemblages argileux avancés se sont formés, alors que pour des rapports fluide/roche faibles, l'altération a conduit à la formation d'assemblages d'altération argileuse intermédiaire et intermédiaire distale (I et II). L'altération a également créé de la porosité par dissolution. Les métaux accumulés dans les zones de rapports fluide/roche élevés ont été contrôlés par la présence de conduits sub-verticaux et par la porosité sub-horizontale des roches encaissantes, où ils se sont concentrés, par adsorption sur les faces cristallines de la pyrite, et incorporés dans la pyrite par substitution du fer ou encore par dépôt sous forme de nanoparticules.

La pyrite analyser contient les éléments suivants : Ag, As, Au, Bi, Co, Cu, Fe, Ni, Pb, S, Sb, Se, Te et Zn. La pyrite I se caractérise par un contenu moyen de 1,1 ppm Au et 33,0 ppm Ag, alors que la pyrite II contient en moyenne 3,0 ppm Au et 80,6 ppm Ag, et l'énargite 0,53ppm Au et 101,6 ppm Ag. Bien qu'il existe une corrélation entre les concentrations d'or et d'arsenic, la concentration absolue d'arsenic est beaucoup plus faible que dans les autres dépôts contenant da la pyrite aurifère puisqu'elle est, en moyenne, de 329,7 ppm pour la pyrite II.

La pyrite II montre la plus forte concentration d'éléments mineurs et traces et contient, en plus de l'or et de l'argent, jusqu'à 6,0 % en poids de cuivre. L'imagerie par microsonde électronique montre que les zones de croissance et les zonations de secteur sont fréquentes dans la pyrite II. Elles sont mises en évidence par la distribution différentielle du cuivre et des autres éléments. La concentration anormalement élevée de cuivre et la présence des zones de croissance et des zonations de secteur au sein de la pyrite II ont permis le développement d'un outil pour évaluer des changements relatifs de conditions physico-chimiques. Les coefficients de partage déterminés pour le cuivre entre les différentes zones et secteurs de la pyrite II montrent que le cuivre et l'or (et les autres métaux) ont été préférentiellement incorporés dans la pyrite pendant les périodes où les conditions physico-chimiques étaient stables.

Contributions of Authors

This thesis contains an introductory chapter that includes a literature review and a description of the research objectives, two chapters that contain the main findings of the research, which have been written in the form of manuscripts for publication in international refereed journals, a concluding chapter that lists the principal conclusions of the study and its contributions to knowledge, and a set of appendices with the data and a detailed description of the research techniques. The first of the manuscripts (Chapter II) is entitled, "High-Sulphidation Epithermal Au (Ag-Cu) Ore Formation by Condensed Magmatic Vapours on Sangihe Island, Indonesia" and will be co-authored by Julia J. King, Dr. A. E. Williams-Jones, Dr. Vincent van Hinsberg, Dr. Tom Mulja and Dr. Glyn Williams-Jones. The second manuscript (Chapter III) is entitled "Applications of Growth and Sector Zoned Pyrite from the Bowone and Binebase Au (Ag-Cu) High-Sulphidation Deposits, Indonesia" and will be co-authored by Julia J. King, Dr. Vincent van Hinsberg and Dr. A. E. Williams-Jones.

The chapters have been written in accordance with the regulations of the Faculty of Graduate Studies and Research at McGill University. The project was initially identified and proposed to Dr. Williams-Jones by Dr. Tom Mulja. The samples and data were collected by Julia King in the summers of 2008 and 2009 with the guidance and advice of Dr. A. E. and Dr. Glyn Williams-Jones, Dr. Mulja and Mr. Arodji Wisannggono. Drillhole and assay datasets and general geology reports were made by East Asia Minerals over the course of their exploration project and supplied to the authors. The concept and method of sectoral zoning analysis in pyrite was proposed and developed with the assistance of Dr. van Hinsberg. Sample preparation, analysis and interpretation was done by Julia King under the guidance and collaboration of Dr. A.E.

Williams-Jones and Dr. van Hinsberg. Initial manuscript preparation was by Julia King with supervision and revisions provided by Dr. A.E. Williams-Jones.

Acknowledgements

This project would not have been possible without the support of NSERC and East Asia Minerals, particularly Tom Mulja, Aroji, Tom, Grace and her family, Eddie, Mike, the team at the Jakarta office, and the helpers and cooks from the village of Binebase. I am so grateful to my supervisor and mentor, Willy for putting together this project, for your enthusiasm, kindness/fierceness as needed, for guiding this great project, and for the freedom to take it in all sorts of directions – as suggested by Vincent van Hinsberg whose enthusiasm, curiosity and faith in science are infectious and who is a remarkable mentor. Thank you Jeanne Paquette for your support and interest in these amazing pyrite crystals. Thanks to Glyn Williams-Jones and the volcanology crew of Kawah Ijen for a whirlwind introduction to Indonesia's volcanoes. This project was analytically intensive, thank you to all those who took time to train me and shared their labs and expertise: Lang Shi, Jeanne Percival, Michel Preda, Simon Jackson, Grant, Kristyn and Boz. Special thanks to the Willy group for feedback and support, particularly Artash Migdisov, Jim Clark and Ariel Harlap for their input and instruction and Sam and Ana, my partners in the mysteries of invisible gold. Thanks to EPS staff, professors and graduate students for creating an environment that fosters both science and friendship and the Earth Sciences department at St. Francis Xavier University, particularly Alan Anderson and Brendan Murphy, who prepared me for this challenge.

Thanks also to Goldfields, the SEG and Geotop for taking an interest in my career and research by supporting me financially and also scientifically by hosting events and conferences that remind me why I am excited about the science of exploration geology.

Finally, thanks to Dejan for your patience and everything else, and my friends (many of whom are listed above) for their support, patience and love during this project. Dejan, Libby, Denis, Ryan, Grant, Sarah, Keith, Carolyn, Stephanie, John & John, thank you all for your skill at transitioning from beer tasting to insightful scientific discussion and back again, and for inspiring me with your own scientific endeavours.

Thank you to my wonderful family for your encouragement, for taking such delight in my adventures, for supporting me wherever I am, and for being there when I get home.

List of Figures

Figure I-1 Sangihe Island showing the location of the active volcano, Awu, the dormant/extinct volcanic centers (Tahuna, Kakiraeng, Malisang) and the Bowone and Binebase deposits. Bathymetry contours are at 50m intervals. Compiled in ArcGIS from SRTM data (USGS, 2004) and the General Bathymetric Chart of the Oceans (GEBCO_08 Grid, version 20091120, http://gebco.net) 11

Figure I-2 Distribution of gold deposits and volcanism in northern Sulawesi, Indonesia and the southern Philippines. Compiled in ArcGIS from: 1) ore deposits datasets (Kirkham and Dunne, 2000; Gosselin and Dubé, 2005; Franklin et al., 2006); 2) the Smithsonian Institution Global Volcanism Program (Siebert and Simkin, 2002-2011); and 3) the General Bathymetric Chart of the Oceans (GEBCO_08 Grid, version 20091120, http://gebco.net)........ 15

Figure II-1 Distribution of gold deposits and volcanism in northern Sulawesi, Indonesia and the southern Philippines. Compiled in ArcGIS from: 1) ore deposits datasets (Kirkham and Dunne, 2000; Gosselin and Dubé, 2005; Franklin et al., 2006); 2) the Smithsonian Institution Global Volcanism Program (Siebert and Simkin, 2002-2011); and 3) the General Bathymetric Chart of the Oceans (GEBCO_08 Grid, version 20091120, http://gebco.net)........ 28

Figure II-2 Sangihe Island showing the location of the active volcano, Awu, the dormant/extinct volcanic centers (Tahuna, Kakiraeng, Malisang) and the Bowone and Binebase deposits. Bathymetry contours are at 50m intervals. Compiled in ArcGIS from SRTM data (USGS, 2004) and the General Bathymetric Chart of the Oceans (GEBCO_08 Grid, version 20091120, http://gebco.net) 29

Figure II-3 The geology of south Sangihe Island and the location of the Bowone and Binebase deposits, modified from Garwin (1990)........ 30

Figure II-4 Representative lithological cross-section A. through the Bowone deposit and B. through the Binebase deposit......... 32

Figure II-5 Photographs of the host rocks at Bowone and Binebase. A. Plagioclase phyric andesite. B. Plagioclase-biotite-hornblende-magnetite andesitic porphyry. C. Andesite crystal tuff, the host rock to the ore at Bowone, with broken plagioclase crystals and rare lithic fragments D. Flow-banded rhyolite, the basal unit of the Binebase Gp. at Bowone. The scale is 1 cm........ 33

Figure II-6 A TAS (Total Alkali vs. Silica) diagram of unaltered (or least altered) samples from each of the main rock types at Bowone and Binebase. Diagram after Le Bas et al. (1986)......... 35

Figure II-7 AFM Diagram of unaltered (or least altered) samples from each of the main rock types at Bowone and Binebase showing their calc-alkaline affinity. Diagram after Irvine and Baragar, 1971......... 36

Figure II-8 Photographs of intensely altered core. A. Advanced argillic (quartz, pyrite, alunite) alteration of fragments (light grey) in a matrix of fine-grained quartz and pyrite (dark grey). B

Massive pyrite breccias, showing complete replacement of the host rock by PyI, with PyII infilling vugs, and relic fragments of altered host rock with kaolinite replacing phenocrysts. C. Photograph of an advanced argillically altered sample showing a PyI-kaolinite-quartz core rimmed by quartz-alunite-PyI. D. Argillically altered rhyolite showing leached cavities of crystals and replacement of its matrix by kaolinite and quartz. The scale is 1 cm. 39

Figure II-9 Photomicrographs showing the textures of the altered rocks as observed in transmitted and reflected light (the scale is 10 µm). A. A relict phenocryst replaced by pyrite, quartz and kaolinite in a fine-grained argilically altered matrix (transmitted light). B. Amphibole phenocrysts replaced by PyI in a groundmass replaced by fine-grained quartz, kaolinite ± dickite (reflected light). C. Fine grained intergrowth of quartz, alunite and pyrite I in contact with massive pyrite II (transmitted light, crossed-polars). D. Fine-grained intergrowth of quartz, alunite and pyrite, typical of argillic alteration (reflected light). 40

Figure II-10 Representative alteration cross-section A. through the Bowone deposit and B. through the Binebase deposit. Hypogene alteration facies established using X-Ray diffraction analysis and core logging. 42

Figure II-11 Photomicrographs in reflected light showing textural features of the four stages of Au mineralization (the scale is 10 µm). A. Massive PyII with a vug containing rare chalcocite (Cc) and barite (Brt) crystals. B. Zoned drusy crystals of PyII infilling a vug in andesite altered to fine-grained PyI and quartz (blue-grey is epoxy). C. Fractured and zoned crystals of massive PyII cut by a barite-enargite (En) vein. D. Sphalerite (Sp), arsenopyrite (Apy), chalcopyrite (Ccp) and electrum (El) crystals in a barite vein. 46

Figure II-12 BSE images of PyI and PyII (the scale is 100 µm). The brightness of each mineral correlates to relatively higher atomic weight than the surrounding material. A. Zoned drusy PyII overgrowing porous, massive PyII. B. Disseminated PyI (white) in a matrix of quartz and alunite, and a vug infilled by blades of an aluminosilicate phase. C. Zoned PyII (grey) in a vein with barite crystals (white). D. Disseminated porous PyI grains (grey) in a matrix of quartz and accessory phases. 47

Figure II-13 BSE images of later generations of mineralization. Brighter areas correspond to relatively higher atomic weight than the surrounding material. A. and B. Barite-enargite veins with µm scale, homogeneous subhedral-euhedral enargite crystals intergrown with mm-scale subhedral barite (white crystals surrounding PyII fragments) (the scale is 100µm). C. Electrum (El) grain surrounded by subhedral chalcopyrite (Ccp), barite (Brt) and sphalerite (Sp) (the scale is 10 µm). D. Electrum grains in chalcopyrite, surrounded by barite and spalerite (the scale is 100 µm). 48

Figure II-14 The distribution of Au, Ag, Cu, As and Sb from a section of drillhole BOD1 (Pb, Zn levels were too low to be detected and Mo and Ba were not analysed). 52

Figure II-15 A Binary plot showing the distribution of TiO_2 and Zr in variably altered rocks of the Bowone and Binebase deposits. See the text for an interpretation of the significance of these data. 53

Figure II-16 Relative gains and losses of elements for advanced argillically altered rocks from Bowone (red), intermediate argillically altered I samples from selected porphyry and crystal tuffs from Bowone and Binebase (yellow) and intermediate argillically II altered (purple) rock samples from Binebase (crystal tuffs), calculated using the method of Grant (1986). A value of 1 indicates relative immobility, less than 1 indicates a relative loss and more than 1 indicates a gain. 55

Figure II-17 Binary plots of trace element concentration in pyrite analysed by LA-ICPMS. The term afu refers to atomic force units. 61

Figure II-18 BSE images (right) and corresponding copper maps (left) showing strong sector and growth zones in PyII (the scale is 50 µm). In the Cu maps, light blue-green represents higher Cu concentration and the darker the blue, the lower is the Cu concentration. A. and B. Complex, micron scale, strongly growth zoned drusy pyrite overgrown on massive, porous pyrite, also zoned. The growth zoning is perpendicular to the crystal growth direction and records the primary growth history. C. and D. Two morphological varieties of pyrite II showing growth zonation (banding), decreasing Cu concentration to the right, and sector zoning, crystallographically controlled zones delineated by variable copper content, perpendicular to the growth zones. 63

Figure II-19 Composite Cu (green), Fe (blue) and As or Se (red) maps (right) of PyII and the corresponding BSE images (right). Brighter colours correspond to higher concentrations of an element. A. and B. Drusy, PyII with growth and sector zones and very high Cu concentrations (green) and variably As-rich (red) bands transitioning into massive, porous PyII with lower Cu concentration and isolated zones of As enrichment (the scale is 50 µm). C. and D. Cross-section through a euhedral PyII crystal displaying growth zoning with alternating As (red) and Cu (green) enriched bands. Sector zoning presents most strongly as a Cu enrichment on three equivalent faces, about a three-fold axis (the scale is 500µm). E. and F. Drusy PyII crystals displaying complex growth zoning in either Cu (green) or Se (red) bands. Sector zoning in Cu is also present in the form of a cross at the center of a cubic pyrite grain, top-centre (the scale is 500 µm). F. and G. Broken PyII aggregate of subhedral crystals with growth zones surrounded by barite (white in BSEI) and enargite (light grey in BSEI, and yellow in map composite), taken from a late barite-enargite vein. Growth zoning is visible in enriched Cu growth zones (green), whereas enargite crystals with both high As (red) and Cu (green) appear yellow and are homogeneous and unzoned (the scale is 50 µm). 65

Figure II-20 An example of a processed depth profile through three growth zones of a Py II crystal produced by LA-ICPMS, showing counts vs. time for major and trace elements. Arsenic, Te, and Au covary through the three growth zones and are independent of Co, Cu, Ni, Zn, Se and Bi, whereas Ag, Pb and to some extent Sb covary independently of the other two trends.... 67

Figure II-21 A plot of counts vs. time (s) in a depth profile through an enargite crystal analysed by LA-ICPMS. Silver and Te covary and are roughly antithetic to Fe and Sb. Copper, As, S Se remain relatively constant and Au values are near the detection limit, although from 32 to 37s they may correspond to the increased Ag and Te signal. 70

Figure II-22 Stability relationships among minerals in the systems K-Na-Al-Si-O-H and Fe-S-O as a function of temperature and pH. Also shown on the diagram are the fields of stability of the five main alteration facies, advanced argillic I (AA I), advanced argillic II (AA II), advanced argillic III (AA III), intermediate argillic I (IA I) and intermediate argillic II (IA II). Calculations were made for 200 bar (SVP), logfO_2 = -30 (suggested by the $\delta^{34}S$ of pyrite, assuming a magmatic source, at a temperature between 250°C and 300°C), quartz and pyrite saturation, Na^+/K^+=10 (see text for details), $a\Sigma S$=0.01 (see text for details) and aAl^{3+}= 0.1. Silicate and sulphate species are blue, sulphur species are purple, and sulphides are green........................... 76

Figure II-23 Log fO_2-pH diagrams showing stability relationships for minerals in the K-Na-Al-Si-O-H and Fe-S-O systems A) at 250°C, and B) at 300°C, the mid- to high-temperature case. The diagrams were created assuming a pressure of 200 bar (SVP), logfO_2 = -30, quartz and pyrite saturation, Na^+/K^+=10, $a\Sigma S$=0.01 and aAl^{3+}= 0.1 (see text for details). Silicates and sulphate species are blue, sulphur species are purple, and sulphides are green. The black lines are $\delta^{34}S$ contours for pyrite at -1, -5 (the measured $\delta^{34}S_{H2S}$ value for Sangihe pyrite) and -10, and constrain the logfO_2 values to between -35 and -27. 77

Figure II-24 Log-log plots of the composition of pyrite from Kawah Ijen, an actively-forming high sulphidation epithermal system (Scher et al. (in press)) and this study............................... 83

Figure II-25 Plot of Kd vs. % distance from core to rim for a single pyrite crystal (BID34-84). In black is the variation in Kd: an increase in inferred to reflect an decrease in temperature and a decrease an increase in temperature; see Chapter III for additional explanation. The yellow squares represent analysis by LA-ICPMS of the gold concentration with the width of the square showing the diameter of the pit in relation to the growth zones; the Au concentration is indicated by the vertical scale on the right hand side of the diagram. The highest gold concentrations correspond to regions where the Kd is stable, whereas lower gold concentrations correspond to intervals over which there is a rapid change in Kd values; Cu concentrations (Chapter III) show the same behaviour. 86

Figure II-26 Schematic diagram showing the transition from vapour to condensed liquid in the alteration and Au-Ag-Cu depositional environment at Bowone and Binebase with the gas species (H_2O, SO_2, CO_2 and H_2S) and addition of metals (in red) and loss of major elements and LREEs (blue)... 91

Figure III-1. Example of a pyritohedron cut parallel to the 001 face showing a) growth zoning and b) sector zoning between the octahedral and cubic faces. 98

Figure III-2. The relationship between crystallography and element fractionation. A) Schematic crystal showing sector and growth zoning – different shades of green represent different compositions. Within each growth zone, there are compostional differences between non-equivalent faces; a strong difference in the shade of green represents strong fractionation and a small differences little or no frationation. The shade differences between sector zones decrease away from the core, coresponding to decreaseing fractionation and, by inference, increased temperature. B) The corresponding Kd vs. distance from the core. Open and filled circles show analysis locations. 100

Figure III-3. Photographs of core showing A) a barite-enargite (Brt-En) vein crosscutting massive PyII, B) veinlets of brassy Py II, and C) massive Py II and Py I (dark grey). The scale is 1cm. Photomicrographs showing D) fractured Py II crystals in a matrix of barite, E) euhedral Py II infilling a vug, F) multiple generations of Py II. The scale is 1mm...................................... 102

Figure III-4. Example of paired EMPA transects in BID34-84 showing analysis locations in orange taken through each sector zone with the "light" transect on the right and the "dark" on the left. The white dashed line represents the sector zone boundary. Individual pairs were matched by hand (red circles) and lines were normalized as described.. 104

Figure III-5 Images of three pyrite samples (BOD3-97, BID32-16 and BID34-84) displaying growth and sector zoning. Row 1 (A, E and I) shows BSE images of each sample; evidence of zoning is weak. Row 2 (B, F and J) illustrates the distribution of Cu for the same field of view as A, E and I. These maps show that Cu in the pyrite crystals is distributed in strongly contrasting complex growth and sector zones (the lighter shades of grey correspond to higher Cu concentrations). Row 3 (C, G, and K) shows high-resolution Cu element maps of the specific crystals in images B, F and J that were subject to quantitative EMP analysis (see text for further detail). Row 4 (D, H, and L) provides BSE images of the fields of view of images C, G, and K showing the location of the analytical spots used to calculate Kd values. The spots in each image are distributed along two transects at right angles to the growth zones in adjacent sectors. Values of Kd were obtained by dividing concentrations in the "light" sectors by the corresponding concentrations in the adjacent "dark" sectors. Sample BOD3-97 shows strongly zoned aggregates of pyrite (Py) surrounded by euhedral enargite (En) crystals. The sector zoning in the analysed crystal (C) is visible about a 3-fold axis in growth zones near its centre. Sample BID32-16 comprises drusy pyrite crystals infilling a vug. Image F reveals a complex history of growth zoning, sector zoning and intersectoral zoning. Sector zoning is evident as a cross at the centre of the analysed crystal (G). Sample BID34-84 displays colloform growth zonation in pyrite overgrown by massive, porous and unzoned pyrite (I and J). In the former, sector zoning is evident as wedge shapes of contrasting shades of grey that cross growth bands (J and K). 107

Figure III-6 Top: Concentration of Cu along transects in adjacent "light" and "dark" sectors crossing growth zones in pyrite from sample BOD3-97 (Fig. 5C and D). The distance has been normalized to a scale of 100 units with 0 representing the beginning of a transect in the core of the crystal and 100 its end at the rim. Bottom: Kd values for the transects represented in the upper figure. Error bars were calculated from the analytical error... 113

Figure III-7 Top: Concentration of Cu along transects in adjacent "light" and "dark" sectors crossing growth zones in pyrite from sample BID32-16 (Fig. 5G and H). The distance has been normalized to a scale of 100 units with 0 representing the beginning of a transect in the core of the crystal and 100 its end at the rim. Bottom: Kd values for the transects represented in the upper figure. Error bars were calculated from the analytical error... 114

Figure III-8 Top: Concentration of Cu along transects in adjacent "light" and "dark" sectors crossing growth zones in pyrite from sample BID34-84 (Fig. 5K and L). The distance has been normalized to a scale of 100 units with 0 representing the beginning of a transect in the core of the crystal and 100 its end at the rim. Bottom: Kd values for the transects represented in the upper figure. Error bars were calculated from the analytical error. 116

Figure III-9 Schematic diagram showing how error associated with matching peaks from two paried transects was calculated. 119

Figure III-10 Schematic diagram comparing the error on individual points with the error on the mean (grey boxes), for two growth zones. 121

Figure III-11 A plot of Kd vs. Cu concentration for all samples, demonstrating convergence at higher concentration or a relationship between Kd and Cu concentration. 122

Figure III-12 A schematic diagram showing how multiple transects can be made through multiple sector zones. 123

List of Tables

Table II-1 Major element compositions of selected Bowone (BOD) and Binebase (BID) (the complete analyses can be found in Appendix A). Rock- and alteration-type are indicated based on petrographic observations, bulk rock geochemistry and/or X-ray diffraction analyses (IA= Intermediate Argillic, BaEn=barite-enargite veins, AA =Advanced Argillic, see text for description). Samples of the porphyritic dykes and associated igneous breccia were not classified by alteration type as they were emplaced post-alteration/mineralization. 34

Table II-2 Inferred resources for the Bowone and Binebase deposits (Stone, 2010). Some oxide ore is present at Bowone but the quantity is negligible compared to the sulphide body and has yet to be measured. 38

Table II-3 Summary concentration data for PyI and PyII based on LA-ICPMS analyses. 59

Table II-4 Enargite composition, analysed by LAICP-MS 68

Table II-5 Sulphur isotope compositions of PyI and PyII from Bowone and Binebase. 72

Table II-6 Table showing physicochemical conditions for each alteration facies as determined by mineral stability and $\delta^{34}S$ values for Py I and Py II. 80

Table III-1 Concentrations of trace elements in adjacent dark and light sectors of pyrite. 109

List of Appendices

Appendix A Bulk rock compositions of selected Bowone (BOD) and Binebase (BID) samples. Rock- and alteration-type are indicated based on petrographic observations, bulk rock geochemistry and/or X-ray diffraction analyses (IA= Intermediate Argillic, BaEn=barite-enargite veins, AA =Advanced Argillic, see text for description). Samples of the porphyritic dykes and associated igneous breccia were not classified by alteration type as they were emplaced post-alteration/mineralization. 149

Appendix B Interpreted X-Ray Spectra showing possible mineral matches made using JADE software. 157

Appendix C Composition of pyrite (A) and enargite (B) from Bowone (BOD) and Binebase (BID) based on EMPA analysis, reported in weight % 186

Appendix D Composition of pyrite (A) and enargite (B) from Bowone (BOD) and Binebase (BID) based on LA-ICPMS analyses, reported in ppm. 193

Appendix E Translated and normalized Electron Microprobe values for 3 pairs of transects from samples BOD3-97, BID32-16, BID34-84. Each raw value from the 6 transects of sector zoned crystals has been translated and normalized to % of the total distance. Corresponding trace element concentrations are interpolated from the bracketing values enabling accurate matching of trace element concentrations between sectors (see van Hinsberg and Schumacher, 2007). Zeros indicate values were below the dection limit, blanks occur when there is no corresponding point in a transect. 196

Table of Contents

Abstract ... i

Résumé ... iv

Contributions of Authors ... vii

Acknowledgements ... ix

List of Figures ... xi

List of Tables ... xvii

List of Appendices ... xviii

Table of Contents ... xix

Chapter I Thesis Introduction ... 1

The Mineral Deposits of Sangihe Island ... 9

Tectonic and Geological Setting ... 12

Objectives ... 16

Methods ... 16

Sampling ... 16

Analysis ... 17

Thesis Organization ... 19

Chapter II High-Sulphidation Epithermal Au (Ag-Cu) Ore Formation by Condensed Magmatic Vapours on Sangihe Island, Indonesia ... 21

Introduction ... 23

Regional Geological Setting ... 25

Local Geological Setting ... 31

Hydrothermal Alteration ... 37

Hypogene Mineralization ... 44

Distribution of gold-silver mineralization ... 50

Mass Changes During Alteration ... 51

Ore Mineral Chemistry 56
Pyrite 57
Enargite 66
Sulphur Isotopes 69
Method 69
Results 71
Discussion 71
Geological Setting 71
Pressure 73
Temperature and pH 74
fO_2 78
Metal Transport 79
Ore Deposition 82
Incorporation of Trace Elements in Pyrite 87
Genetic Model 89
Conclusions 90
Chapter III Physicochemical Inferences from Growth and Sector Zoning in Pyrite of the Bowone and Binebase Au (Ag-Cu) High-Sulphidation Epithermal Deposits, Indonesia 93
Abstract 94
Introduction 95
Geologic Setting 101
Methods 103
Samples and Analysis 105
Petrography 105
Chemistry 108
Error Analysis 118
Discussion 124

Conclusions 126

Chapter IV General Conclusions 127

Contributions to Knowledge 129

Suggestions for Future Study 131

References 133

Appendix A Bulk Rock Geochemistry 149

Appendix B Interpreted X-Ray Diffraction Patterns 157

Appendix C Electron Microprobe Analyses 186

Appendix D Laser-Ablation Inductively Coupled Mass Spectrometry Tables of pyrite and enargite 193

Appendix E Translated transect values for paired-transects of sector zoned pyrite crystals...... 196

Chapter I

Thesis Introduction

The complex tectonics of South East Asia, particularly Indonesia and the Philippines, make these ideal locations in which to explore for epithermal precious metal deposits, demonstrated by discoveries of the past two decades (including Kelian, Kalimantan (Davies et al., 2008), Lebong Tandai, Sumatra (Jobson et al., 1994), Pongkor, West Java (Marcoux and Milesi, 1994), Mesel, Sulawesi (Turner et al., 1994), Mt Muro, Borneo (Simmons and Browne, 1990), Gosowong, Maluku (Carlile et al., 1998; Gemmell, 2007), Masupa Ria, Kalimantan (Thompson et al., 1994), Nalesbitan, Luzon (Sillitoe et al., 1990), and Lepanto, Luzon, Phillipines (Hedenquist et al., 1998). Some of the largest deposits belong to the high-sulphidation subclass of epithermal deposits, which are the focus of this thesis. Although the general characteristics of these deposits are well known and exploration vectors based on these characteristics have been successfully applied, there is still disagreement over the timing and processes of precious-metal concentration. For example, some authors have concluded that the precious metal mineralization post-dates the alteration and the agent of metal transport is an aqueous liquid (Stoffregen, 1987; Hedenquist et al., 1994, 1998, 2000; Arribas, 1995), whereas others have proposed that, at least in some cases, the mineralization is pene-contemporaneous with alteration and the ore fluid is a hydrothermal vapour (Cooke and McPhail, 2001; Chouinard et al., 2005; Deyell, 2005; Deyell et al., 2005; Williams-Jones and Heinrich, 2005; Davies et al., 2008; Mavrogenes et al., 2010; Voudouris, 2010; Berger and Henley, 2011; Henley and Berger, 2011). There is also the issue of whether the ore metals invariably deposit as a result of saturation of the ore fluid with a mineral like electrum, or whether deposition can occur when the metals are undersaturated in the fluid, such as if they were incorporated by adsorption in a mineral like pyrite (Chouinard et al., 2005; Barker et al., 2009; Voudouris, 2010). This thesis addresses these issues via a focused study of two recently discovered high-sulphidation epithermal Au (Ag-Cu) prospects on the volcanic island of Sanighe. Conventional geological tools, (e.g., core logging, petrography and whole-rock geochemistry) have been used to study the deposits on a macro scale, and micro-analytical tools such as EPMA, LA-ICPMS and SIMS have been used to determine the micro-scale distribution of the ore metals. The combination of macro- and micro- investigative tools has helped produce a body of work that has allowed us to establish some of the key factors controlling formation of the Sangihe deposits and contribute to our understanding of the genesis of high-sulphidation deposits globally.

Epithermal deposits form in environments where metal-rich fluids from a nearby magma chamber interact with the overlying host rocks. The subsequent alteration of the rocks by these fluids is pervasive but localized along fluid-pathways, and the interactions between the fluids, rocks and existing physicochemical barriers (e.g., depth of water table) are considered to lead to economic concentration of Au, Cu, Ag (+/- Bi, Te, As, Sb, Se, Hg). Epithermal deposits are classified as "low, intermediate, or high" based on the oxidation state of the sulphur-bearing minerals present. Each produces a characteristic alteration assemblage, mineralization and mineral textures. High-sulphidation deposits form a subclass of epithermal deposits that are an increasingly important source of gold, silver and copper. These deposits were first described by Ransome (1907), who named them "Goldfield type" deposits, but subsequently they have been referred to as "Au-alunite", "enargite Au", "acid sulfate", "high-sulphur", "alunite-kaolinite" deposits (Ransome, 1907; Emmons, 1918; Lindgren, 1933; Bonham, 1984; Heald et al., 1987; Stoffregen, 1987). The term "high-sulphidation" was coined by Hedenquist (1987) to recognize the important role in the alteration of fluids containing sulphur species in their highest oxidation state (S^{+6}) and the manifestation of this oxidation state by minerals like alunite. The alteration is interpreted to be the result of interaction of the rocks with highly acidic and oxidizing vapours from a proximal, HCl^-, H_2S^- and SO_2^- rich magma source. According to this interpretation, the gases dissociate to create the acidic species responsible for the alteration of the host rocks (Hedenquist et al., 2000). Vapours coming off the magma chambers rise through the host rocks, which are commonly of volcanic origin, and can be focused along structures, where they leach and alter the host rocks. They continue their ascent until they encounter a physical barrier (e.g., water table, impermeable layer) where physicochemical changes cause condensation to liquid, and may lead to instability of the dissolved metallic species and precipitation of the ores. Estimates of fluid temperature for high-sulphidation deposits range from 100°C to 320°C, with an average value of 230°C based on stable isotopes, fluid inclusion and phase stability data (Einaudi, 1977; White and Hedenquist, 1990; Hedenquist et al., 1994, 1998; Deyell, 2005; Voudouris, 2010). The deposits are thought to form from 500 to 200 m below the surface, although these depths are not well constrained (White and Hedenquist, 1990).

As mentioned above, there is no consensus on the nature of the phase(s) that produce(s) the mineralization. Based on the observation that the mineralization commonly occurs in pores created during alteration of the rocks, and the assumption that vapours cannot dissolve metals in concentrations sufficient to form ore deposits, most authors have concluded that the metals are deposited by later pulses of mineralizing aqueous liquid (Hedenquist et al., 1994). However there is a growing body of evidence that metals can be transported in vapours in concentrations sufficient to form ore deposits and that in some cases mineralization was contemporaneous with alteration (Chouinard et al., 2005b; Deyell et al., 2005a,b; Williams-Jones and Heinrich, 2005; Voudouris, 2010). This evidence supports a view that the vapour phase can be responsible for both alteration and precious metal mineralization in high sulphidation epithermal systems.

High sulphidation epithermal deposits are located proximal to volcanic centres, and the mineralization and host rocks are usually similar in age (Taylor, 2007).The close relationship to a volcanic edifice that is often unstable makes for poor preservation, which explains the concentration of this type of deposit in the Mesozoic and (Kerrich et al., 2005; Simmons et al., 2005). The alteration is commonly zoned with vuggy silica textured rock at the centre (this is where the host rocks have been completely leached) surrounded by a shell of advanced argillic alteration (quartz, alunite, pyrite, pyrophyllite, kaolinite and dickite). The alteration becomes less intense outwards as the acidic fluids are progressively buffered by the host rocks, and grades into argillic alteration (kaolinite, alunite, illite). Further out, argillic alteration is dominated by the assemblage, illite–smectite, and beyond this grades into propylitic alteration (chlorite, albite, carbonate, epidote, titanite). The alteration associated with high sulphidation deposits may occur on scales ranging from a few metres to tens or even hundreds of metres. The mineralization consists of native gold, electrum, and/or precious metal-bearing tellurides, sulphides and/or sulphosalts (Chouinard et al., 2005b; Taylor, 2007). The Au (Ag-Cu) mineralization is dominantly disseminated but also occurs in veins, veinlets, lenses or massive bodies, commonly controlled structurally, (e.g., Chelopech (Chambefort and Moritz, 2006) and Lepanto (Hedenquist et al., 1998)). Depending on the mineralization style, size of the system and later enrichment events (e.g., supergene processes), these deposits may be either very high grade or lower grade but comprising a large resource.

The modern analogues to this type of epithermal deposit are the feeders of fumarolic fields such as those found at Kawah Ijen volcano, Java Indonesia (e.g., Scher et al., in press) or Vulcano, Italy (Boyce et al., 2007).

Low sulphidation deposits form away from the volcanic edifice where meteoric and magmatic fluids interact near the surface to produce high-grade Au-Ag vein deposits with distinctive adularia-sericite alteration. The dominant form of sulphur is S^{2-} (reduced). The modern analogues would be solfataras and the hot springs and wells of geothermal fields (e.g., Broadlands (Hedenquist, 1990) and Cerro Prieto (Williams-Jones and Clark, 1990). The term “Intermediate sulphidation” is relatively new and refers to deposits with mineralogical and textural characteristics that are intermediate between those of the two other subclasses of epithermal deposits (Hedenquist et al., 2000).

One obstacle to our understanding of high-sulphidation epithermal deposits is that the gold in these deposits is commonly “invisible” in pyrite and the nature of this gold and the manner of its incorporation in pyrite are poorly understood. Advances in analytical techniques permitting higher resolution imaging and lower detection limits of elements now make it possible to investigate the nature and distribution of gold and other trace elements in pyrite, and determine the conditions under which they deposit. Pyrite is the dominant secondary phase and the host to the gold (“invisible”) and other trace elements at Sangihe and, based on textural observations, was deposited in multiple mineralizing pulses.

Pyrite is commonly a host for gold in epithermal deposits (e.g., Chouinard et al., 2005a; Reich et al., 2005; Kesler and Deditius, 2007; Deditius et al., 2011) as well as in several other types of deposits (e.g., Carlin-type deposits (Barker et al., 2009), orogenic deposits (Large et al., 2009), and VMS deposits (Huston et al., 1995)). It is also ubiquitous in many ore-forming and non-ore-forming geological environments. As a result, there has been extensive geochemical characterization of pyrite from many environments.

Pyrite is a cubic mineral, FeS_2, and is stable over a wide range of temperature and pressure. The face-centered cubic structure can accommodate a wide variety of minor and trace (<1 wt%) elements including: Ag, As, Au, Bi, Cd, Co, Cu, Hg, Mo, Ni, O, Pb, Pd, Ru, Sb, Se, Sb, Sn, Te, Tl and Zn (Abraitis et al., 2004). It has been established that many of these elements are present in solid solution (both stoichiometric and non-stoichiometric; Simon et al., 1999; Su et al., 2011) but they can also occur in separate phases as micro-inclusions (Simon et al., 1999; Deditius et al., 2011). Much research has focussed on how gold is incorporated in the pyrite structure as economic concentrations of "invisible gold" have been found in many deposits (e.g., Cook and Chryssoulis, 1990; Maddox et al., 1998; Hanlie et al., 1999; Chouinard et al., 2005a; Barker et al., 2009)

Numerous studies have shown that there is a strong positive correlation between the concentrations of arsenic and gold in pyrite (Cook and Chryssoulis, 1990; Arehart et al., 1993; Fleet et al., 1993; Pals et al., 2003; Reich et al., 2005; Cepedal et al., 2008; Large et al., 2009). Indeed, arsenopyrite is the most favoured host for gold, followed by arsenic-rich pyrite and finally pyrite with appreciable concentrations of arsenic (Cook and Chryssoulis, 1990; Cabri et al., 2000; Hinchey et al., 2003; Benzaazoua et al., 2007; Deditius et al., 2011). The reason given for this correlation is that arsenic (As^{2-}) substitutes for sulphur (S^{-}) in pyrite allowing for the incorporation of gold in the pyrite structure as Au^{+1}, or as Au^0 species that are not structurally bound in the mineral lattice (Cook and Chryssoulis, 1990). Advances in imaging and quantitative analysis of gold-bearing pyrite since the late 1980s (e.g., Chryssoulis et al., 1989; Fleet et al., 1989) have made it possible to discern substitution mechanisms and means of incorporation. More recently, imaging has been used to look at the spatial relationships of trace elements in pyrite (Steele et al., 2000; Deditius et al., 2008, 2011; Large et al., 2009). Although "invisible gold" occurs most commonly in arsenian pyrite, the presence of "invisible gold" in arsenic-free pyrite has also been documented (Cook et al., 2009). As pointed out by Chouinard et al. (2005a), the majority of these studies have investigated pyrite formed under near-neutral pH conditions and not at the extremely low pH and high fO_2 of high-sulphidation ore deposits. Consequently, there is still a limited understanding of the uptake and incorporation of trace elements in pyrite in this latter environment.

In high-sulphidation epithermal deposits, the common trace elements in pyrite are Ag, As, Au, Cu, Se, Te (Einaudi, 1968; Chouinard et al., 2005a; Pacevski et al., 2008). Although pyrite in many deposits is reported to have high As concentrations, in high-sulphidation epithermal deposits, Cu appears to be the most abundant minor element, up to 4.5 wt% in the Chelopech high-sulphidation deposit, Bulgaria (Pacevski et al., 2008). The highest reported concentration of Cu in pyrite thought to be in solid solution, is 10% from the Nukundamu epithermal deposit, Fiji (Frenzel and Ottemann, 1967), followed by 8 wt% Cu in pyrite from the Coka Marin polymetallic deposit, Serbia (Pacevski et al., 2008). Chouinard et al. (2005a) postulated that gold is incorporated into the pyrite of the high sulphidation deposits at Pascua by a coupled substitution of $Cu^{1+} + Au^{3+}$ for 2 Fe^{2+}. The work presented here builds on these studies, using trace element geochemistry and strong sector and growth zoning in pyrite to draw conclusions about crystallographic controls on trace element incorporation in pyrite.

A striking feature of the pyrite at Sangihe is the strong sector and growth zonation observed in many gold-bearing pyrite crystals. These crystallographic features, in principle, can be used to determine the physicochemical conditions of formation for single crystals and to make inferences about the conditions favourable for uptake of gold and other trace elements. Growth zoning is a type of compositional zoning in which changes in temperature, pressure, chemistry, fO_2, and pH of the fluid are recorded in the crystal composition and preserved as a series of zones perpendicular to the growth direction (Reeder and Paquette, 1989). This style of zonation has been observed for many minerals, and has been used to extrapolate the growth history of crystals to entire magma chambers, as in the case of plagioclase (e.g., Anderson, 1984). Importantly, this type of zoning provides a growth history, which can be used to assess the extent of recrystallization or dissolution. Sector zoning is less commonly observed, and occurs when the composition of one face is different from a coeval, adjacent non-equivalent face (e.g., cubic vs. octahedral faces). Sector zone boundaries are parallel to the growth direction and have been observed in calcite, tourmaline, arsenopyrite and recently pyrite (Reeder, 1991; Vesselinov and Kerestedjian, 1995; van Hinsberg et al., 2006). Sector zonation is controlled by each non-equivalent growth surface that samples the same fluid, and so an effective partition coefficient can be calculated between the two faces (Rakovan et al., 1997; van Hinsberg and Schumacher, 2007; Shtukenberg et al., 2009). There is a strong possibility that once sector zoning is recognized, changes in the effective partition coefficient can be used to make inferences about growth rates, substitution mechanisms, and even temperature as shown by van Hinsberg and Schumacher (2007) for tourmaline.

The Mineral Deposits of Sangihe Island

Bowone and Binebase are related high-sulphidation epithermal Au(Ag-Cu) prospects on Sangihe Island, north-eastern Sulawesi, Indonesia, which is 40km long, and is centered on Latitude 3°26’12” N and Longitude 125°34’48” (Datum WGS84) (Fig. 1). Sangihe is a former spice island with a long colonial history beginning with the Dutch in 1677, and the steep volcanic terrain is now covered by palm, nutmeg, clove, and coconut plantations. The population of 100, Tahuna, located in the middle of the island. The island is of volcanic origin, with two dormant or extinct strato-volcanoes to the south and the 1320 m high active stratovolcano, Awu, at the northern tip; Awu last underwent a significant eruption on June 12, 2004. The climate is warm and humid with an average daily temperature of 27°C and over 3.8 m of annual rainfall (Garwin, 1990; Arodji and Johnedy, 2008). The island is accessed by air, or more commonly by ferry from Manado, Sulawesi to the main harbour town of Tahuna. Access to the site takes one hour by vehicle from Tahuna. The exploration camp is located at the edge of Binebase village within sight of the Bowone prospect.

Exploration on Sangihe Island began in 1986 when PT Meares Soputan Mining and Muswellbrook Energy and Minerals Ltd began stream sediment sampling and discovered alluvial gold. After the discovery of mineralized boulders on the beach, Cu-Au exploration targets were established on the island (Carlile et al., 1990). Using geophysical surveys and diamond-drilling programs, the above exploration companies discovered the Taware porphyry, a weakly mineralized, sub-economic Cu-Au deposit to the west of the present Bowone and Binebase prospects. The portion of the tenement held by Muswellbrook Energy and Minerals Ltd was then acquired by Aurora Gold, which subsequently became Ashton Mining. It was under Ashton Mining that the first high sulphidation epithermal mineralization was discovered by geophysical surveys and subsequent diamond drilling (East Asia Minerals Annual Report, 2009). The tenement then passed to Bre-X Minerals Ltd. and PT Sungai Belayan Sejati in 1997, but as a result of the events that transpired later that year (the infamous Bre-X gold-salting scandal), the "Contract of Work" was revoked. In addition to the Bowone, Binebase and Taware prospects,

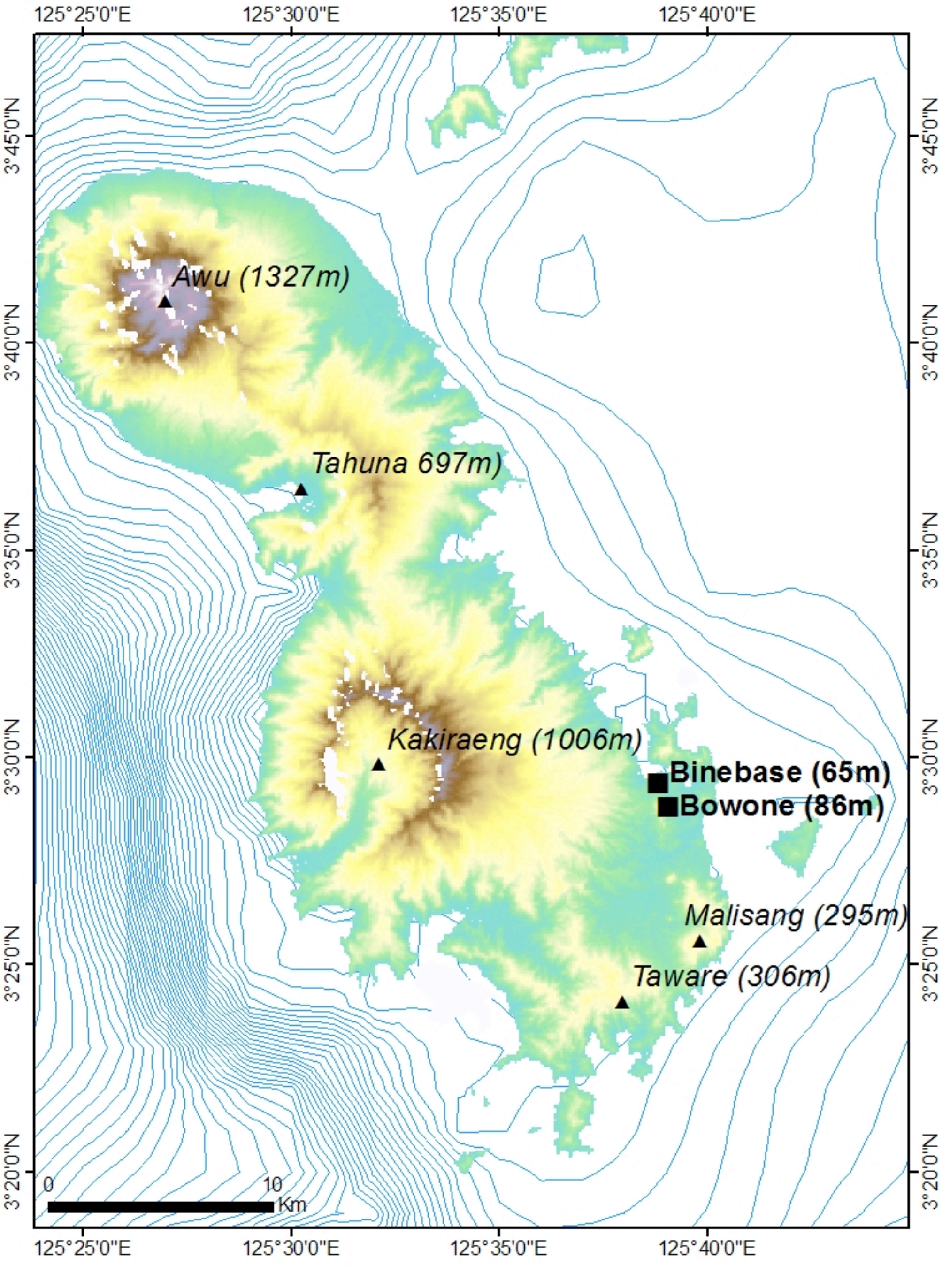

Figure I-1 Sangihe Island showing the location of the active volcano, Awu, the dormant/extinct volcanic centers (Tahuna, Kakiraeng, Malisang) and the Bowone and Binebase deposits. Bathymetry contours are at 50m intervals. Compiled in ArcGIS from SRTM data (USGS, 2004) and the General Bathymetric Chart of the Oceans (GEBCO_08 Grid, version 20091120, http://gebco.net) the exploration also led to the discovery of the Sede and Kupa low-sulphidation epithermal quartz vein prospects. Since the discovery of alluvial gold in the 1980s, the area has been worked by illegal/artisanal miners who have recovered an unknown amount of alluvial gold. The project is currently under the control of East Asia Minerals Ltd., the sponsor of this study. Over the course of their Contract of Work (CoW), East Asia Minerals Ltd. has drilled 79 diamond drill holes, run Induced Polarization (IP) and Ground Magnetic surveys, and conducted extensive trenching and sampling.

An evaluation in 2009 indicated a resource of 27 million tonnes averaging 0.95 g/t gold and 13.58 g/t silver for the oxide and sulphide (supergene and hypogene) zones (Stone, 2010). The highest concentrations of Au, Ag and Cu occur in the oxide zones where the original deposit underwent supergene enrichment. Although this zone is vital to eventual economic exploitation of the resource, the hypogene zone records the history of the high-sulphidation epithermal event and is the focus of this study.

Tectonic and Geological Setting

Sangihe Island is the largest island at the centre of the 500km long Sangihe Arc, which runs almost North-South from southern Mindanao, Phillipines to the northern arm of Sulawesi, and divides the Celebes and Molucca Seas (Hall and Wilson, 2000) (Fig. 1). Twenty-five Quaternary stratovolcanoes are located along the length of the arc; eight are active including Awu at the northern tip of Sangihe Island (Morrice and Gill, 1986). Since the middle Miocene, westerly subduction of the Molucca Sea plate under the Eurasian plate has been forming the Sangihe Arc, whereas the facing Halmahera Arc has been the product of easterly subduction of the Molucca Sea plate under the Philippine Sea Plate (Hall, 2000). This double subduction resulted in the closure of the Molucca Sea. Subduction is thought to have ceased with the “disappearance” of the Molucca Sea plate and the onset of obduction of the mélange (including the Halmahera Arc) westward onto the Sangihe Arc (Morrice et al., 1983; Morrice and Gill, 1986; Garwin, 1990; Hall, 1996; Hall and Wilson, 2000). To the east, westerly subduction of the Celebes Sea portion of the Eurasian plate under the Sangihe Arc is becoming more active (Hall, 2000).

There has been little work done on the Sangihe mineralization and mentions of it appear mostly in regional compilations (Carlile et al., 1990; Carlile and Mitchell, 1994; White et al., 1995; Garwin, 2000). More has been published on the geochemistry of the volcanic rocks that make up the arc, calc-alkaline volcanic sequences from strato volcanoes, (Morrice et al., 1983; Morrice and Gill, 1986; Gill and Williams, 1990; Elburg and Foden, 1998; MacPherson et al., 2003) and the tectonics (Hall, 2000; Macpherson and Hall, 2002; Widiwijayanti et al., 2004; Hinschberger et al., 2005). However, this research has ignored Sangihe Island.

Past company reports are the best source of geological information for Sangihe Island (Garwin, 1990). The stratigraphic sequence and geology of southern Sangihe was established by Steve Garwin in his report for P.T. Meares Soputan Mining (1990). Through mapping and sampling, he identified a volcano-sedimentary package on the southern lobe of the island dominated by five units (Fig. 2). At the base are the Taware (andesite flows and sub-intrusives, tuffs and breccias) and Binebase (andesitic ash and crystal tuff, hornblende-pyroxene flows; NE strike and moderate to steep SE dips) groups. Taware represents the proximal volcanic facies, whereas Binebase represents the distal facies. These units are conformably overlain by the Batunderang (andesitic lithic tuff, flows) and Malisang (hornblende andesite flows, sills, dykes) volcanics, with Malisang appearing to be the older of the two units (Garwin, 1990). The Tamako group of clinopyroxene andesite flows, lahars and lithic tuffs, breccias and rare intrusive bodies, covers most of southern Sangihe Island and unconformably overlies the Batunderang and Malisang groups. The Tamako group has a transgressive contact with the Pinterang Formation, which is the uppermost stratigraphic unit at Bowone but is not present at Binebase, and is a shallow marine sequence of reworked volcaniclastics, carbonates and organic rich units (Garwin, 1990).

Structurally, the southern portion of the island is dominated by NNE-NE, NNW-NW and N lineaments. These are not expressed as observable faults and are inferred to have formed during E-W compression; local structures are attributed to volcanic centres (Garwin, 1990). The NW and NE lineaments have multiple intersections in the Bowone and Binebase area, and likely exercised a control on the mineralization, though no direct structural connection has been recognized.

There has been some debate over the origin of the Bowone and Binebase deposits. Garwin (1990) interpreted them to be epithermal deposits but to have formed distal to a volcanic center in which sea water contributed to the hydrothermal fluid. Other authors subsequently concluded that these deposits have features of high sulphidation and exhalative massive sulphide deposits (Carlile et al., 1990; Carlile and Mitchell, 1994). A report by Royle (2007) refers to the deposits as being of VMS-type, with no mention of any epithermal characteristics.

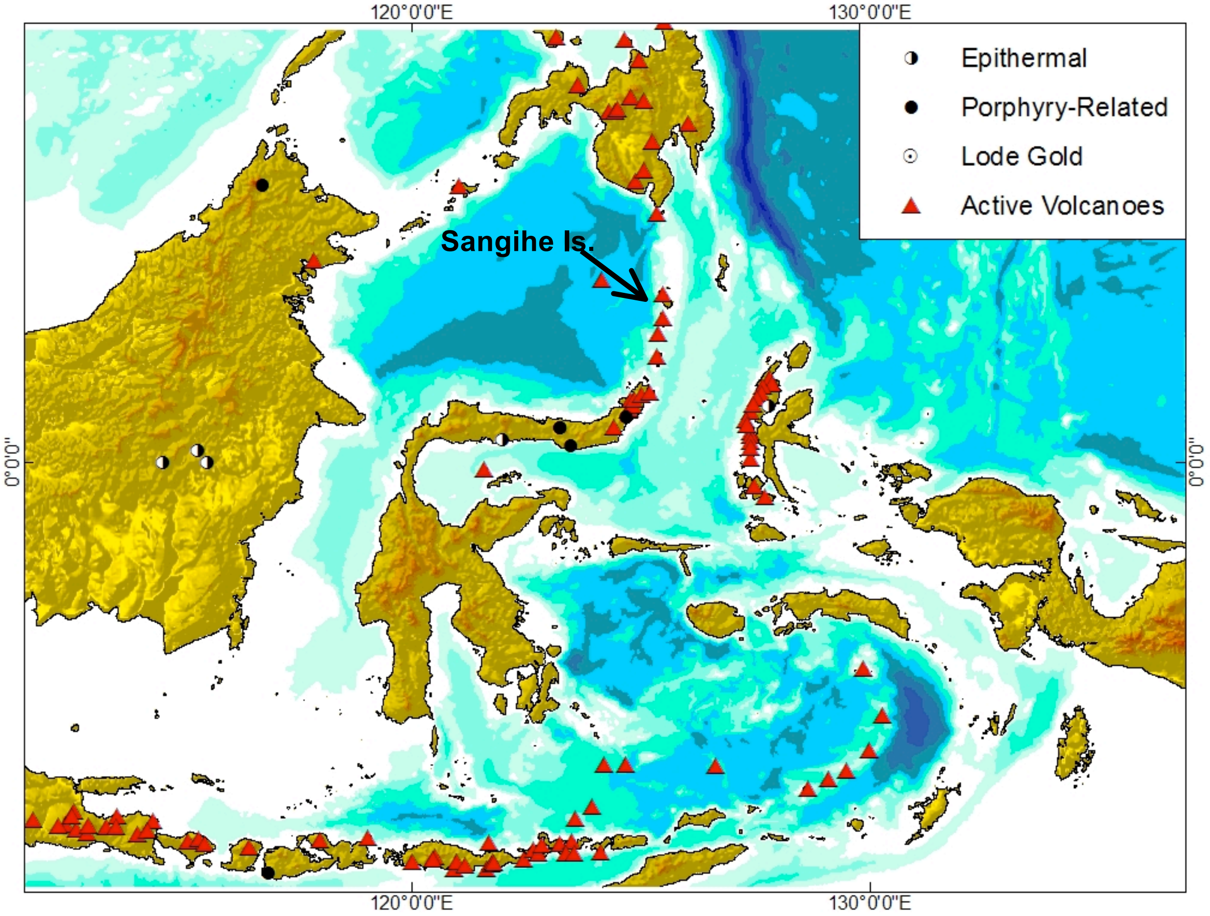

Figure I-2 Distribution of gold deposits and volcanism in northern Sulawesi, Indonesia and the southern Philippines. Compiled in ArcGIS from: 1) ore deposits datasets (Kirkham and Dunne, 2000; Gosselin and Dubé, 2005; Franklin et al., 2006); 2) the Smithsonian Institution Global Volcanism Program (Siebert and Simkin, 2002-2011); and 3) the General Bathymetric Chart of the Oceans (GEBCO_08 Grid, version 20091120, http://gebco.net).

Objectives

The primary objective of the research described in this thesis was to develop a genetic model for the Bowone and Binebase deposits by providing detailed descriptions of their geometry, geology, geochemistry and mineralization. These aspects have been thoroughly documented for many high-sulphidation epithermal systems but few studies have explored the mechanisms of gold concentration for high sulphidation epithermal deposits in which pyrite is the dominant host of the gold. This style of mineralization is of interest because the mechanisms for ore formation are poorly understood. The goal of this work is thus to contribute new understanding of the genesis of high-sulphidation epithermal deposits, particularly of the ore concentrating mechanisms.

Because of the nature of the Bowone and Binebase deposits, there were very few tools available to determine the conditions under which gold mineralization occurred. For example, there are no fluid inclusions suitable for microthermometric determinations. Inasmuch as the gold occurs almost exclusively in pyrite, a major focus of the research was the use of the crystallography and the trace element distribution in pyrite to determine the physicochemical conditions that might be favourable for the incorporation of gold in this mineral.

Methods

Sampling

Over two field seasons, the summers of 2008 and 2009, Dr. A.E. Williams-Jones, Dr. Glyn Williams-Jones and I travelled to the exploration camp, located in the village of Binebase within sight of both prospects, to meet with project geologists, log core and collect samples. Over the two seasons 67 holes were logged and 230 samples were taken from zones of interest to establish the spatial and temporal distribution of alteration and mineralization. Forty-five pulp samples, the fraction of sample remaining from assay, were also taken in 2009.

Owing to the high rainfall, extensive vegetation and warm climate, there is little to no outcrop visible at the prospects. Two outcrop samples were taken, one of the strongly oxidized showing at Binebase and one from the nearby coast where the rock type is the same as the principal host rock for both deposits (feldspar porphyry). No mapping was undertaken for the above-mentioned reasons.

Analysis

1. The results of the original East Asia Minerals (EAM) logging and our own relogging of core were compiled and cross-sections were made for the deposits using Target software obtained from Geosoft and hand-drawn cross-sections. This made it possible to constrain the geometry of the deposits.

2. Petrographic descriptions were made using transmitted and reflected light microscopic examination of 50 polished thin and thick sections showing different aspects of the mineralization and alteration of the two deposits. The samples were also examined for fluid inclusions and, although some were present in barite they were too small (< 2 μm) for microthermometric analysis.

3. Twenty six samples of the different rock and alteration types were analysed for bulk rock geochemistry (4 lithoresearch package, crushing RX2) at Actlabs in Vancouver (Appendix A). Samples were pulverized with mild steel to avoid contamination. Analysis of the major and trace elements was done using the lithium metaborate/tetraborate fusion Inductively Coupled Plasma -

Mass Spectrometer (ICP-MS) method and a Perkin Elmer Sciex ELAN instrument. Gold analysis was by Instrumental Neutron Activation Analysis (INAA).

4. The mineral composition of 45 pulp samples was determined using X-Ray Diffraction at the Geotop Facility at the University de Québec a Montreal. Diffractograms were prepared using a Siemens D 500 (Co Kα) and were interpreted at McGill using JADE software (Appendix B).

5. EMPA analyses were performed on selected polished thin sections that were coated with carbon prior to analysis. Preliminary analyses were conducted with an energy dispersive spectrometer (EDS) to identify unknown minerals. Systematic quantitative analyses of multiple generations and morphologies of pyrite (and enargite) were carried out with wavelength dispersive spectrometers (WDS) at 20 kV, a current of 50 nA and the smallest possible beam size, about 2 μm, for Fe, S, Cu, As, Sb, Co, Ni, Zn, Se and Te. A CANMET standard containing pyrite (Fe,S), chalcopyrite (Cu), AsNiCo (As, Ni, Co), CdTe (Cd, Te), sphalerite (Zn), stibnite (Sb)and AgSe (Se) was used to calibrate the instrument (Appendix C). Backscatter electron images were taken of each site analysed. Element maps ranging in size from 200 x 200 μm to 800 x 800 μm with 1-5 μm resolution and dwell times from 30 ms to 70 ms were prepared using a 20 kV and 50 nA current beam. Element maps were created for Cu, Fe and in some samples, Se, Ni and As. Finally quantitative point transects were run along paired sector zones for three samples showing strong sector and growth zoning.

6. LA-ICPMS was performed at the Geological Survey of Canada under the supervision of Dr. Simon Jackson. A Photon Machine Analyte 193 laser ablation system coupled to an Agilent 7700 with 2d rotary pump to increase the sensitivity was used. Fifteen polished thick sections were analysed for S^{34}, Fe^{57}, Co^{59}, Ni^{60}, Cu^{65}, Zn^{66}, As^{75}, Se^{77}, Ag^{107}, Sb^{121}, Te^{125}, Au^{197}, Pb^{206},

Pb^{208} as well as Al^{27}, Si^{29}, Ca^{42}, K^{39}, Ba^{137}, Ta^{181} and Bi^{209} to determine trace element compositions in pyrite and enargite and detect inclusions of other phases (Appendix D). In order to resolve matrix problems related to analysing sulphides, a number of standards were used: GSE-1G, NIST 610, Po 680 and an in-house standard.

7. One sample of drusy pyrite from sample BID34-84 was imaged for Au, Ag, Cu, Se, Te, S34, S32, using a PHI TRIFT III Tof SIMS in the Frederick Seitz Materials Research Laboratory at the University of Illinois.

Thesis Organization

This thesis in divided into four chapters; a general introduction followed by two chapters comprising manuscripts that will be submitted for peer-review journal publication, and a chapter describing the principal conclusions of the study and the contributions to knowledge. The first manuscript (Chapter 2) provides a geological overview of the Bowne and Binebase deposits and presents geochemical data relating to the alteration and mineralization. This information is used to develop a genetic model for the Bowone and Binebase deposits and, in turn, advance our understanding of the processes controlling the formation of high-sulphidation epithermal precious metal deposits.

As part of the study of the gold-bearing pyrite samples, a method was developed which makes use of the pyrite crystal structure and distribution of trace-elements to interpret the evolution of physicochemical conditions. The second manuscript (Chapter 3), describes this methodology and its potential application in mineral deposits. The method is employed in Chapter 2 to interpret the evolution of the hydrothermal environment during the crystallization of ore-stage pyrite at Bowone and Binebase.

The final chapter summarizes the results of my research and explains the importance of this work to the field of mineral deposit research.

Chapter II

High-Sulphidation Epithermal Au (Ag-Cu) Ore Formation by Condensed Magmatic Vapours on Sangihe Island, Indonesia

Julia King[1], A.E. Williams-Jones[1], Vincent van Hinsberg[1], Thomas Mulja[2] and Glyn Williams-Jones[3]

(1) Department of Earth and Planetary Sciences, McGill University, 3450 University Street,
Montreal, Quebec, Canada, H3A 2A7

(2) 3709 Rutherford Crescent, North Vancouver, British Columbia, Canada V7N 2C6

(3) Department of Earth Sciences, Simon Fraser University, 8888 University Drive, Burnaby,
British Columbia, Canada, V5A 1S6, Canada

Abstract

Although the gold in high sulpidation epithermal deposits generally occurs as the native metal or electrum, in some of these deposits a significant proportion of the gold is “invisible” within pyrite. Here we use a combination of petrography, pyrite mineralogy, trace-element geochemistry and crystallography to determine how gold is transported and incorporated into pyrite in two relatively young high sulpidation epithermal deposits, in which the gold occurs almost exclusively in solid solution or as nano-particles in pyrite.

The related Bowone and Binebase Au (Cu-Ag) deposits, located 1 km apart on the volcanic island of Sangihe, northeastern Indonesia, occur in andesitic-volcaniclastic rocks that have been altered to an advanced argillic assemblage of quartz + pyrite (Py I) ± pyrophyllite ± natroalunite ± alunite ± dickite ± kaolinite, and a more distal intermediate argillic assemblage of quartz + pyrite (Py I)± kaolinite ± dickite ± illite. The economic mineralization takes the form of multiple generations of auriferous pyrite, the first of which, Pyrite I, developed during advanced argillic alteration. Mass balance calculations show that almost all elements were mobile with the exception of Nb, Ti, HREEs and possibly Al.

The highest gold concentration is in Pyrite II, which occurs in veins that cut Pyrite I. This drusy variety of pyrite is characterized by complex growth and sector zoning, and contains 6.0 wt.% “invisible” Cu, which represents among the highest concentrations of Cu ever reported for pyrite. The elevated Cu concentration is accompanied by a high Au concentration, which correlates positively with As concentration. Silver concentration correlates strongly with Au concentration but poorly with Cu concentration. Later barite and enargite mineralization exploited Py II veins and vugs, and contains high concentrations of “invisible” Ag in enargite and significant Au although at lower concentration than in Py II or Py I.

A model is presented in which the fluid responsible for advanced argillic and intermediate argillic alteration and associated stage 1 gold mineralization was a condensed magmatic vapour derived from an oxidizing felsic magma. The gold and other metals were transported as hydrated species that ascended through the volcanic pile via fractures and zones of enhanced permeability to a depth between 920 and 1260 m, where the vapour condensed at a temperature between 250 and 340°C to form an acidic liquid with a pH of ~2.5; fO_2 ranged up to four log units above the hematite-magnetite buffer. Interaction of this liquid with the host andesites caused advanced argillic/intermediate argillic alteration including sulphidation of mafic minerals to form Py I. During crystallization of Py I, Au, Cu and Ag were adsorbed onto the surface of the pyrite and deposited as nanoparticles or were incorporated in the mineral structure. This adsorption of metals from the condensed vapour reached a peak during the crystallization of vein-hosted Py II and continued during the crystallization of later enargite, with the uptake of Ag and minor Au. From the distribution of metals among growth and sector zones in Py II, incorporation of gold and other metals appears to have been maximised when physicochemical conditions were relatively stable. This contrasts with the requirement for native gold precipitation that physicochemical gradients be steep to ensure maximum metal concentration.

Introduction

Although considerable progress has been made in understanding the formation of high sulphidation epithermal precious metal deposits, opinion is divided over the nature of the ore fluid. There is general agreement that the characteristic residual or vuggy silica and advanced argillic alteration are the result of interaction of the rocks with the condensates of highly acidic and oxidizing vapours (e.g., HCl, H_2S, and H_2SO_4, produced by reaction of H_2O with SO_2) from a proximal magma source (e.g., Hemley and Jones 1964; Stoffregen 1987; Arribas 1995). However, until recently, most researchers, noting that the ore minerals commonly fill vugs and therefore postdate the alteration, have concluded that the fluid responsible for the alteration did not transport the ore metals (Stoffregen, 1987; White and Hedenquist, 1990; Arribas, 1995; Hedenquist et al., 1998). Instead, these researchers have attributed the mineralization to collapse of the vapour-dominated system and transport of the metals by a magmatic hydrothermal liquid with a large meteoric water component. The discovery that gold mineralization in the Pascua deposit, Chile, was contemporaneous with advanced argillic alteration (Chouinard et al., 2005a), indicates, that for some high sulphidation epithermal deposits (see also Voudouris, 2010) the two-stage hydrothermal model does not apply. This, and a combination of fluid inclusion (Heinrich et al., 1999; Landtwing et al., 2010) and experimental (Archibald et al. 2001 and 2002; Williams-Jones et al. 2002; Zezin et al. 2011; Migdisov et al., accepted for publication) evidence showing that gold, silver and copper may be considerably more soluble in aqueous vapours than previously suspected, supports a model for these deposits in which hydrothermal alteration and economic mineralization were both products of a magmatic hydrothermal vapour (cf. Williams-Jones and Heinrich, 2005; Mavrogenes et al., 2010; Berger and Henley, 2011; Henley and Berger, 2011; Scher et al. in press).

Most studies of high sulphidation epithermal systems have focused on deposits in which the gold occurs as a discrete mineral or minerals (e.g., native gold, electrum or a telluride such as calaverite; Kesler et al., 1981; Stoffregen, 1987; Moritz et al., 2004; Deditius et al., 2008). However, in some high sulphidation deposits, notably the Pascua deposit in Chile, which was referred to above, a high proportion of the gold is “invisible” in sulphide minerals, particularly pyrite (e.g., Chouinard et al., 2005b; Deditius et al., 2009). In this paper, we report results of a study of two high sulphidation epithermal deposits, Bowone and Binebase, located on Sangihe Island, Indonesia, in which virtually all the hypogene gold is “invisible” in pyrite. Most significantly, over 50% of this gold is in pyrite, which forms part of the advanced argillic alteration mineral assemblage; the rest is concentrated in pyrite veins that cut the altered rocks. Thus, gold mineralization was both contemporaneous with and postdated alteration. Based on this and other observations, we develop a model designed to explain the genesis of the Bowone and Binebase deposits involving transport of the metals in a highly acidic vapour and the sorption of the gold onto the surfaces of growing pyrite crystals. Given the early timing of the mineralization and the nature of the host, we also propose that these deposits are representatives of a separate subclass of high sulphidation epithermal precious metal deposits, in which the bulk of the metal is hosted in pyrite and the ore fluid was likely a vapour.

Regional Geological Setting

The Bowone and Binebase Au (Ag-Cu) deposits are located in the south of Sangihe Island, the largest of the islands in the 500 km long Sangihe Arc, which runs North-South from southern Mindanao, Phillipines, to the north arm of Sulawesi, and separates the Celebes and Molucca Seas (Hall, 2000). The Sangihe Arc formed as a result of the westerly subduction of the Molucca Sea plate under the Eurasian plate, whereas the facing Halmahera Arc was produced by the easterly subduction of the Molucca Sea plate under the Philippine Sea Plate (Hall, 2000). This double subduction has been ongoing since the middle Miocene and, by the end of the Pliocene, resulted in the closure of the Molucca Sea and the thrusting of the Halmahera Arc over its own back arc

(Hall, 2000). Subduction is thought to have ceased with the “disappearance” of the Molucca Sea plate and the onset of obduction of the mélange (including the Halmahera Arc) westward onto the Sangihe Arc (Morrice et al., 1983; Morrice and Gill, 1986; Garwin, 1990; Hall, 1996, 2000). To the east, westerly subduction of the Celebes Sea portion of the Eurasian plate under the Sangihe Arc is more active (Hall, 2000). Twenty-five Quaternary stratovolcanoes are located along the length of the arc; eight of these are active, including Awu at the northern tip of Sangihe Island (Morrice and Gill, 1986)(Fig. 1). Previous studies of volcanism along the Sangihe Arc have shown that the arc is dominated by andesites, two-pyroxene andesites and hornblende andesites, but olivine basalts, dacites and rhyolites have also been observed (Morrice and Gill, 1986). Calc-alkaline suites predominate and vary from low- to high-K, depending on their distance from the volcanic front (Morrice and Gill, 1986).

Sangihe Island has a lobate form defined by the two most recent volcanic centres, the active stratovolcano, Awu, at the northern end and the dormant/extinct stratovolcano, Kakiraeng, in the south. The stratovolcanoes decrease in age to the northeast (Fig. 2). Given the heavy rainfall (over three metres per year), dense vegetation and inferred uplift due to the compressive tectonic regime, even the oldest volcanoes, in the south of the island where the Bowone and Binebase deposits are located, may be only a few tens of thousands of years in age.

South Sangihe Island is dominated by clinopyroxene andesite flows, breccias, lahars, and tuffs of the Tamako Group, except in the south and east where rocks of the Taware Group, Malisang Group, Binebase Group and Pinterang Formation predominate (Figs. 2 and 3). The Bowone and Binebase deposits are located 1 km apart with Binebase to the north, at the east coast, and Bowone to the south. Both deposits are hosted by rocks of the Binebase Group, although at

Bowone, the Binebase Group is overlain unconformably by the Pinterang Formation, which forms a cover over the deposit, whereas at Binebase, the deposit outcrops and is strongly oxidized to a depth of up to 60m. The Binebase Group has a northeasterly strike and moderate to steep southeasterly dip, and comprises andesitic ash and crystal tuff, hornblende-pyroxene andesite flows, biotite-hornblende-magnetite intrusives and minor dacite flows, interpreted to be volcanic and subvolcanic facies of the extinct and eroded Taware volcano (Garwin, 1990). To the east of the Binebase deposit, Binebase Group rocks are overlain by rocks of the Tamako Group (hornblende andesite flows, sills and dykes), the proximal facies of the now-dormant/extinct Kakiraeng volcano, and to the south by the Pinterang Formation. East of the Bowone deposit, the Pinterang Formation forms an irregular transgressive contact with the Tamako Group, which it overlies. The Pinterang Formation is thickest (<100m) in topographic lows, and consists of reworked cross-bedded volcanic silts and sands, carbonates and organic rich sediments, thereby providing a record of a marine incursion in southeast Sangihe Island (Garwin, 1990). The Pinterang Formation also contains slightly rounded, un-oxidized pyrite fragments, identical to the Bowone and Binebase hypogene ores. The Pinterang Formation and Tamako Group overlie the Malisang Group, which in turn unconformably overlies the Binebase Group in the south-east of the island. The Malisang Group consists of hornblende andesite flows, sills, dykes and diorite intrusives that form local highs related to the interpreted Malisang volcanic centre (Garwin, 1990).

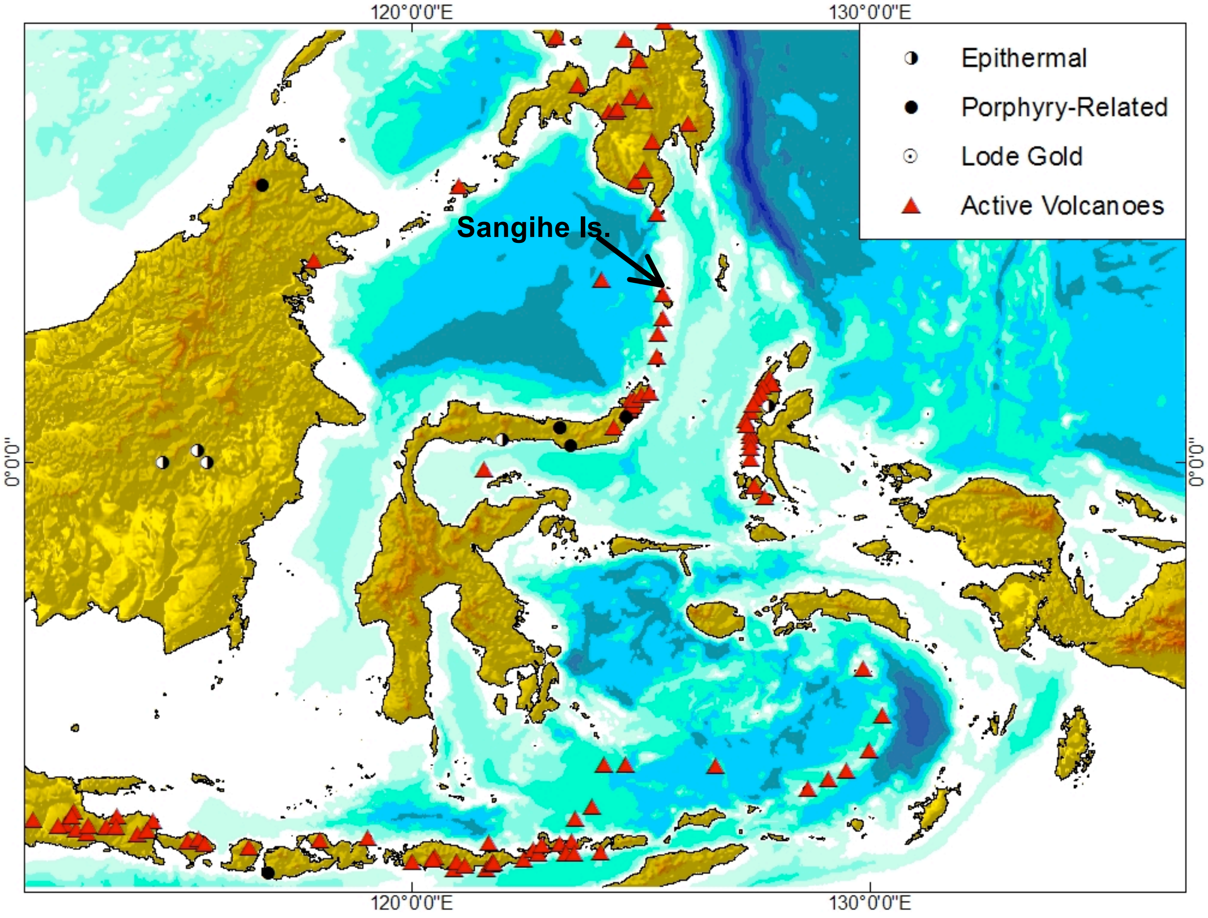

Figure II-1 Distribution of gold deposits and volcanism in northern Sulawesi, Indonesia and the southern Philippines. Compiled in ArcGIS from: 1) ore deposits datasets (Kirkham and Dunne, 2000; Gosselin and Dubé, 2005; Franklin et al., 2006); 2) the Smithsonian Institution Global Volcanism Program (Siebert and Simkin, 2002-2011); and 3) the General Bathymetric Chart of the Oceans (GEBCO_08 Grid, version 20091120, http://gebco.net).

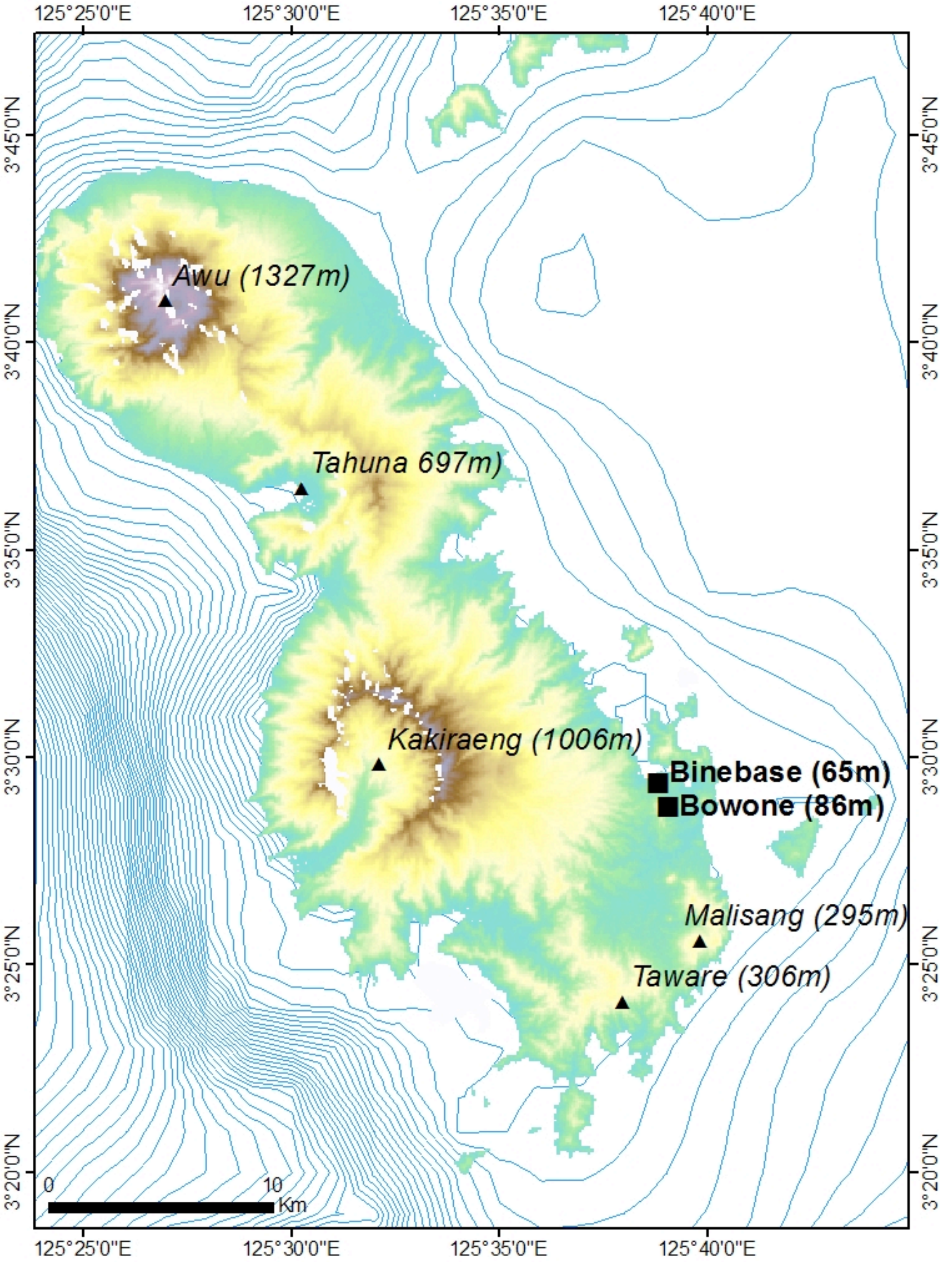

Figure II-2 Sangihe Island showing the location of the active volcano, Awu, the dormant/extinct volcanic centers (Tahuna, Kakiraeng, Malisang) and the Bowone and Binebase deposits. Bathymetry contours are at 50m intervals. Compiled in ArcGIS from SRTM data (USGS, 2004) and the General Bathymetric Chart of the Oceans (GEBCO_08 Grid, version 20091120, http://gebco.net)

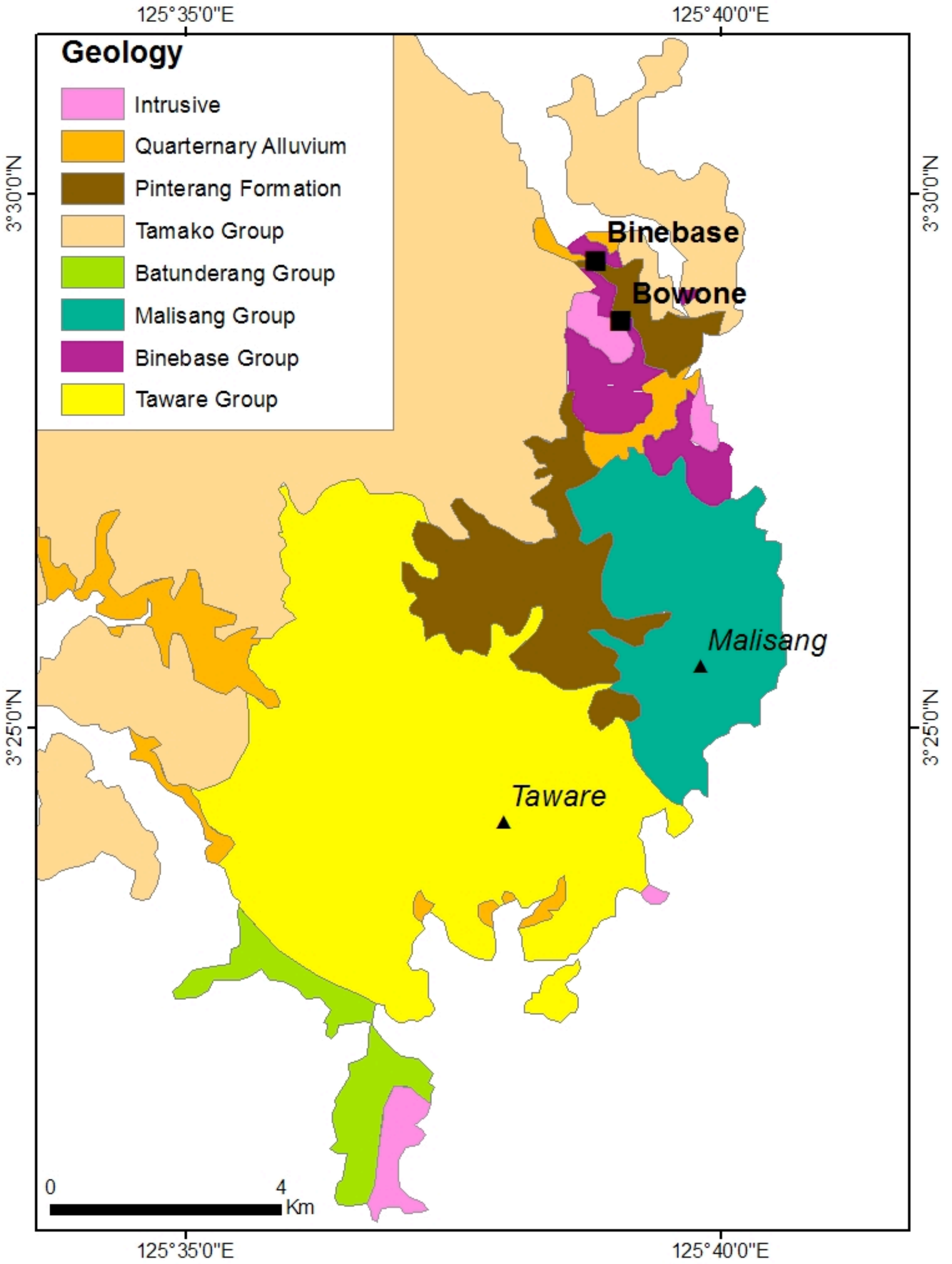

Figure II-3 The geology of south Sangihe Island and the location of the Bowone and Binebase deposits, modified from Garwin (1990).

Local Geological Setting

Locally at Bowone, a thick andesite layer overlies flow-banded plagioclase-quartz-phyric rhyolite, visible in cross-section (Fig. 4A). This unit is invariably intruded by hypabyssal andesitic porphyry. In least-altered samples, the andesite contains 5 to 30 vol.% white plagioclase laths (2 mm diameter) and rare, rounded quartz phenocrysts (2 mm in diameter) in an aphanitic matrix that is too fine-grained for minerals to be distinguished microscopically (Fig. 5).

Occasional conformable layers of welded crystal tuff can be recognized. These contain 10 volume % of < 3 mm long plagioclase laths and rare rounded < 3 mm diameter quartz grains. The hypabyssal porphyry contains 20 vol.%, 5 mm diameter subhedral to euhedral hornblende, magnetite, biotite and plagioclase phenocrysts and rare quartz eyes in an aphanitic matrix (Fig. 5). An intrusive breccia with subangular to subrounded, 1 to 10 cm diameter fragments of the host andesite and rhyolite generally defines the margins of the hypabyssal porphyry. At Bowone, the overlying Pinterang Formation (poorly consolidated volcaniclastic sandstones and siltstones, organic rich siltstones, and calcareous mudstones) is locally absent but ranges from 5 cm to 100 m thick, where present, and is separated from the Binebase Group rocks by a thin (a few cm thick) oxide layer. The Pinterang Formation is overlain by an unconsolidated oxidized soil profile that can be up to 4 m thick.

The Binebase deposit differs from the Bowone deposit in that it is exposed at surface and has been oxidised to a depth of 60 m below the erosional surface (Fig. 4B). The host andesite is a crystal-rich tuff containing 10 to 15 vol.% of plagioclase laths and quartz crystals (1 to 2 mm in length and diameter, respectively) and occasional lapilli, and lithic fragments (0.5 to 3 cm in

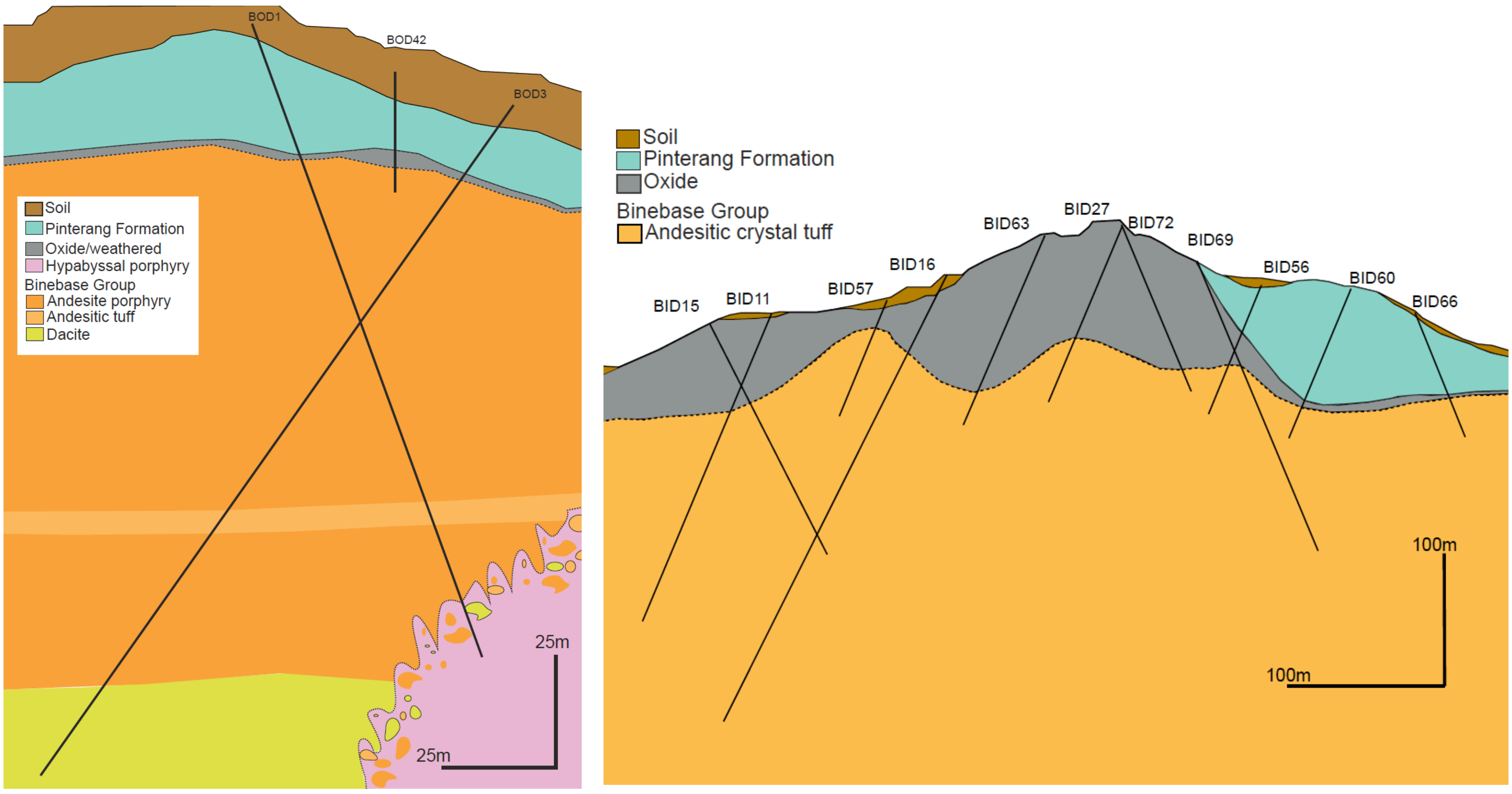

A

B

Figure II-4 Representative lithological cross-section A. through the Bowone deposit and B. through the Binebase deposit.

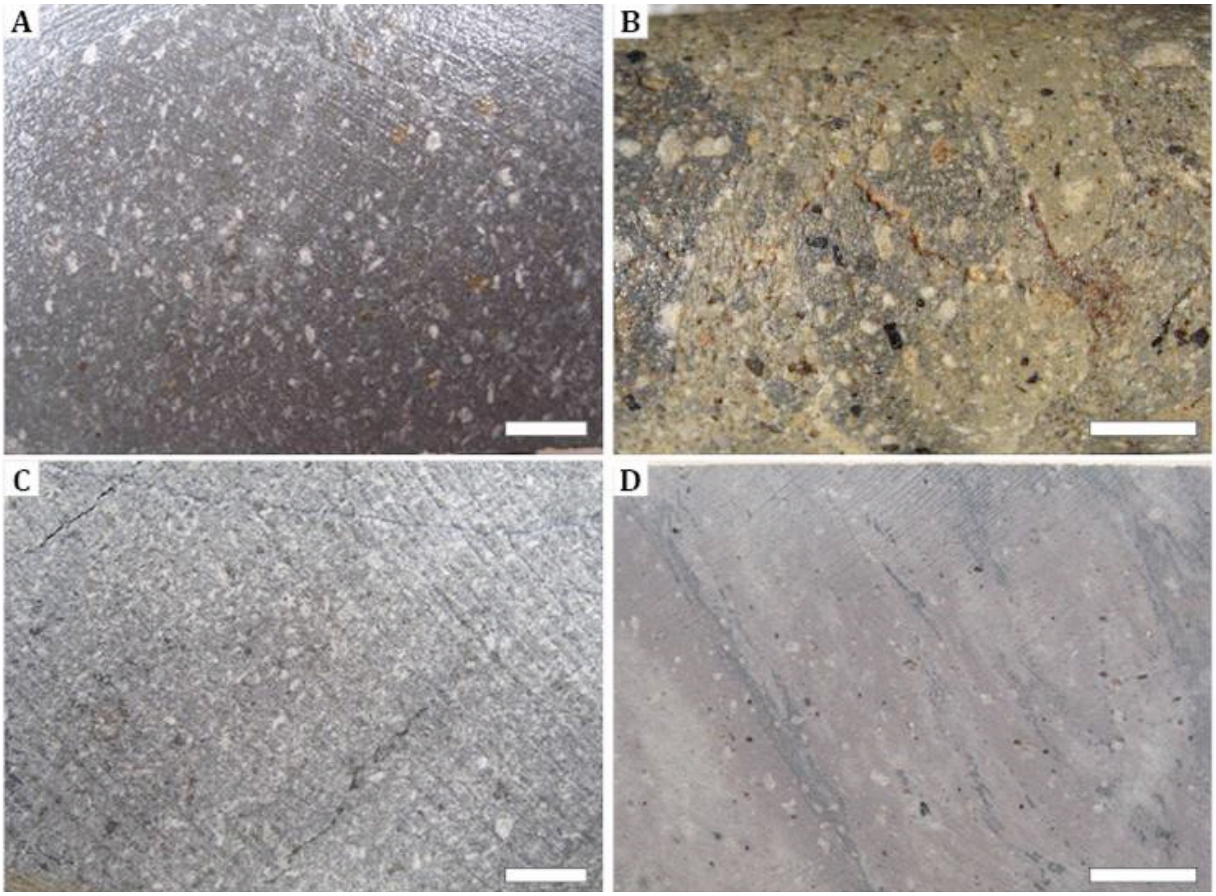

Figure II-5 Photographs of the host rocks at Bowone and Binebase. A. Plagioclase phyric andesite. B. Plagioclase-biotite-hornblende-magnetite andesitic porphyry. C. Andesite crystal tuff, the host rock to the ore at Bowone, with broken plagioclase crystals and rare lithic fragments D. Flow-banded rhyolite, the basal unit of the Binebase Gp. at Bowone. The scale is 1 cm.

Table II-1 Major element compositions of selected Bowone (BOD) and Binebase (BID) (the complete analyses can be found in Appendix A). Rock- and alteration-type are indicated based on petrographic observations, bulk rock geochemistry and/or X-ray diffraction analyses (IA= Intermediate Argillic, BaEn=barite-enargite veins, AA =Advanced Argillic, see text for description). Samples of the porphyritic dykes and associated igneous breccia were not classified by alteration type as they were emplaced post-alteration/mineralization.

Rock Type	Alteration	Sample	SiO_2 %	TiO_2 %	Al_2O_3 %	Fe_2O_3 %	MnO %	MgO %	CaO %	Na_2O %	K_2O %	P_2O_5 %	Total %	LOI %
			0.01	0.001	0.01	0.01	0.001	0.01	0.01	0.01	0.01	0.01	0.01	
Porphyry	IA I	BOD1-134.5	55.4	0.546	19.8	4.26	0.008	0.75	0.78	0.35	2.17	0.1	98.53	14.36
	IA I	BOD3-158.8	64.68	0.547	14.36	8.38	0.009	0.02	0.03	0.05	0.08	0.08	100.1	11.82
	IA I	BOD3-85.4	8.2	0.036	0.33	35.08	0.005	0.02	0.04	0.06	0.02	b.d.	66.75	23.02
	IA I	BOD3-74.1	58.66	0.528	9.13	13.45	0.006	0.01	0.06	0.56	0.69	0.06	99.83	16.69
	IA I	BOD3-106.4	51.41	0.484	2.91	27.98	0.007	0.02	0.05	0.06	0.02	0.04	100.3	17.33
	IA I	BOD3-83.3	48.19	0.541	2.85	30.09	0.006	0.02	0.04	0.07	0.04	0.05	100.3	18.38
	IA I/BaEn	BOD3-99.2	19.69	0.185	0.3	40.04	0.006	0.02	0.03	0.04	0.05	b.d.	82.61	22.25
	IA I/BaEn	BOD3-96.8	85.78	0.501	2.34	6.14	0.006	0.02	0.06	0.04	0.04	0.08	99.49	4.49
	AA I	BOD3-49.8	56.29	0.53	13.22	8.23	0.009	0.01	0.08	0.76	1.35	0.12	99.58	18.98
	AA I	BOD3-55	43.28	0.373	6.17	15.17	0.01	0.01	0.05	0.42	0.47	0.04	84.1	18.11
	AA I	BOD3-85.5	42.65	0.492	3.28	32.38	0.007	0.02	0.04	0.15	0.15	0.04	99.82	20.61
	AA I	BOD3-48.6	48.8	0.492	10.38	17.76	0.007	b.d.	0.06	0.48	0.71	0.1	99.86	21.06
	AA I	BOD3-100	29.11	0.377	0.26	46.64	0.009	0.02	0.04	0.05	0.03	0.02	100.1	23.58
	AA I	BOD3-78.7	8.74	0.22	1.25	59.44	0.014	0.03	0.05	0.06	0.02	0.02	100.8	31.01
	AA I/BaEn	BOD3-113.7	63.84	0.43	7.59	10.06	0.005	0.01	0.06	0.84	0.81	0.08	99.15	15.42
	AA II	BOD42-62.3	49.79	0.46	10.59	16.73	0.01	0.02	0.06	0.38	0.36	0.12	97.66	19.13
	AA II	BOD3-125.4	51.37	0.474	11.21	12.06	0.003	b.d.	0.07	0.92	1.21	0.08	97.92	20.52
	AA II	BOD3-46.9	53.65	0.603	12.29	12.72	0.008	0.02	0.12	0.71	0.71	0.2	100	19
	AA II	BOD3-34.4	20.65	0.684	19.21	30.85	0.012	0.03	0.07	0.17	0.18	0.22	99.21	27.12
	AA II	BOD3-27.3	7.08	1.029	24.05	19.86	0.005	0.03	0.12	1.22	3.49	0.43	98.86	41.55
	AA II	BOD3-79.5	65.52	0.485	6.24	14.38	0.006	b.d.	0.05	0.05	0.01	0.1	98.17	11.31
	AA II	BOD3-132.9	59.09	0.624	16.11	7.88	0.016	0.02	0.08	0.23	0.17	0.18	98.46	14.06
	AA II	BOD3-41	39.59	0.567	3.97	32.64	0.017	0.02	0.07	0.16	0.21	0.13	99.66	22.28
	AA II	BOD3-65.4	56.91	0.431	5.67	18.17	0.005	0.02	0.08	0.43	0.42	0.11	100	17.79
	AA II/BaEn	BOD3-65.8	17.64	0.082	0.81	31.27	0.003	0.02	0.04	0.06	b.d.	b.d.	77.25	22.94
	AA III	BOD1-115	59.72	0.61	16.49	7.98	0.014	0.02	0.11	0.07	0.03	0.21	98.39	13.13
	AA III	BOD1-124.9	61.62	0.773	16.96	5.73	0.022	0.03	0.1	0.14	0.03	0.11	99.98	14.47
	AA III	BOD3-122.6	39.9	0.298	3.6	32.09	0.006	0.02	0.04	0.31	0.29	0.04	98.21	21.62
Crystal Tuff	Least altered	PANTAI	58.37	0.546	15.2	5.59	0.132	2.86	7.02	2.79	1.1	0.2	99.55	5.74
	IA I	BID70-61.7	63.89	0.627	11.62	9.89	0.005	0.04	0.06	0.04	0.26	0.15	98.27	11.69
	IA I	BID24-101	65.1	0.706	12.71	8.13	0.005	0.03	0.07	0.04	0.02	0.16	98.77	11.81
	IA I	BID39-41.2	29.58	1.423	26.73	18.12	0.004	0.06	0.11	0.07	0.05	0.43	98.61	22.04
	IA II	BID43-39.5	66.18	0.587	12.6	5.45	0.017	0.99	0.33	0.04	3.55	0.16	99.88	9.97
	IA II	BID26-102.5	60.58	0.68	14.96	6.7	0.023	1.04	0.38	0.03	3.79	0.17	99.07	10.72
	IA II	BID15-84.2	58.02	0.771	16.24	7.15	0.018	0.96	0.14	0.07	4.29	0.15	99.25	11.44
	IA II	BID18-144.5	56.54	0.796	17.84	6.92	0.015	1.86	0.45	0.06	2.12	0.23	98.31	11.47
	IA II	BID18-183.2	56.83	0.852	18.21	6.79	0.027	0.84	0.8	0.06	2.41	0.2	99.5	12.49
	IA II	BID23-68.6	56.02	0.667	15.5	6.86	0.019	1.15	0.57	0.06	4.17	0.14	100.5	15.38
	IA II	BID26-58	47.52	0.902	19.49	6.34	0.025	0.68	0.62	0.09	6.09	0.23	98.29	16.31
Rhyolite	IA I	BOD3-159	63.25	0.236	16.53	1.65	0.061	0.86	2.13	1.14	8.13	0.07	99.55	5.49
	IA I	BOD3-153.5	73.15	0.176	13.82	0.86	0.032	0.56	0.53	0.51	5.96	0.09	99.88	4.19
	IA I	BOD3-165.5	69.48	0.165	13.5	1.09	0.058	0.79	2.15	1.78	4.47	0.07	98.27	4.72
	IA I	BOD3-167.3	69.69	0.178	13.8	1.48	0.05	0.89	1.6	1.85	6.19	0.17	100.3	4.39
Intrusive Porphyritic Dyke		BOD1-143.4	61.14	0.512	17.99	5.35	0.081	1.71	4.61	2.98	2.72	0.27	100.9	3.59
		BOD42-136.6	64.22	0.469	16.27	4.39	0.025	0.7	3.39	2.71	2.8	0.35	100.2	4.9
		BOD77-34.5	59.45	0.519	16.78	4.92	0.118	2.38	4.2	2.71	2.38	0.28	99.44	5.69
		BOD7-56.6	58.5	0.508	16.36	5.31	0.377	1.07	5.14	2.26	2.17	0.25	98.96	7.02
		BOD47-128.5	56.08	0.482	16.77	4.94	0.161	3.08	5.15	2.71	1.96	0.24	99	7.42
		BOD2-32.3	59.2	0.489	16.51	5.51	0.058	1.89	2.53	2.02	3.18	0.22	99.18	7.58
		BOD2-82	53.74	0.524	16.44	5.98	0.65	1.16	4.78	1.64	2.06	0.27	99.26	12
		BID24-144	44.72	0.672	14.97	6.21	0.401	4.58	7.43	0.05	1.93	0.19	98.41	17.26
Igneous Breccia		BOD10-141.5	58.31	0.486	16.38	4.42	0.364	0.96	5.78	2.15	2.01	0.24	99.7	8.62
		BOD2-72.3	59	0.5	16.15	4.54	0.033	1.09	2.36	1.52	2.15	0.27	98.67	11.04
		BOD7-43	55.47	0.725	21.25	3.44	0.01	0.22	0.23	0.06	0.34	0.08	96.04	14.21
		BOD47-34	14.51	0.886	25.56	14.82	0.016	0.02	0.06	1.71	2.67	0.21	98.97	38.5

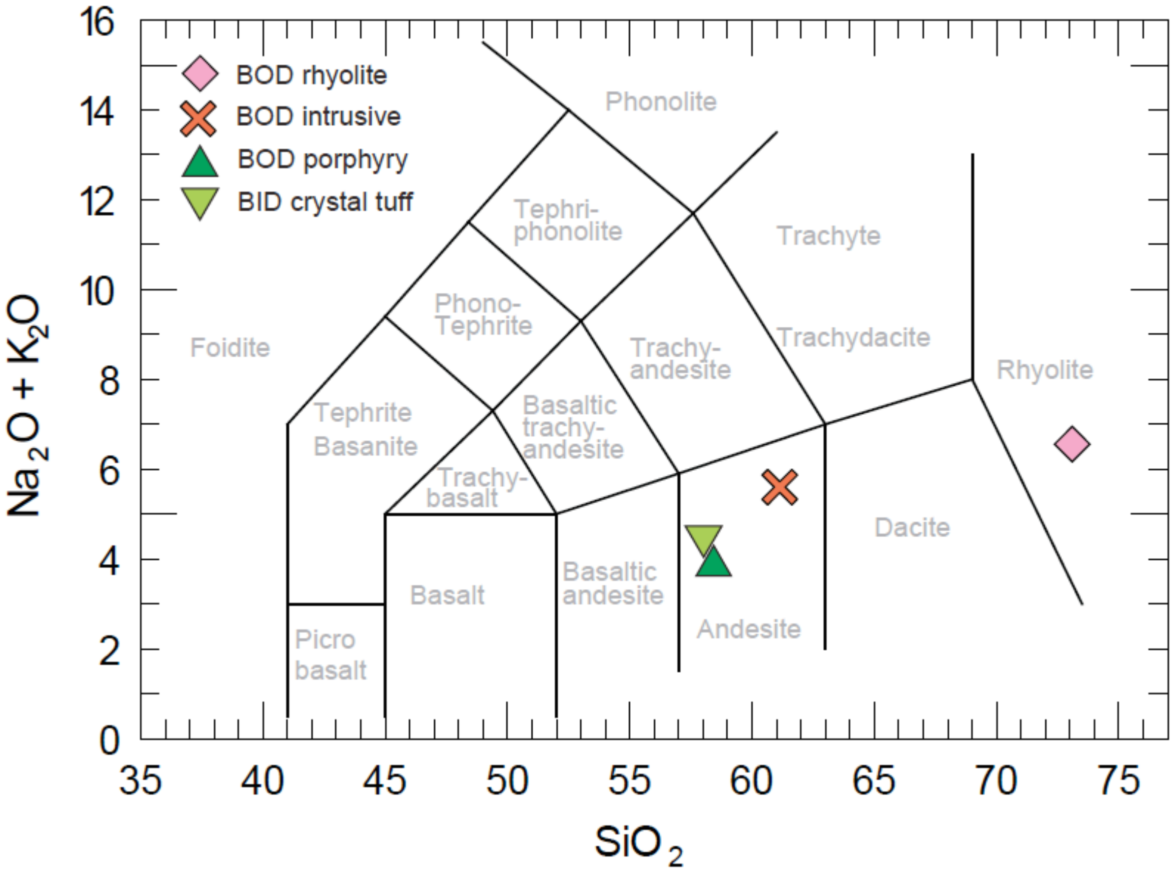

Figure II-6 A TAS (Total Alkali vs. Silica) diagram of unaltered (or least altered) samples from each of the main rock types at Bowone and Binebase. Diagram after Le Bas et al. (1986).

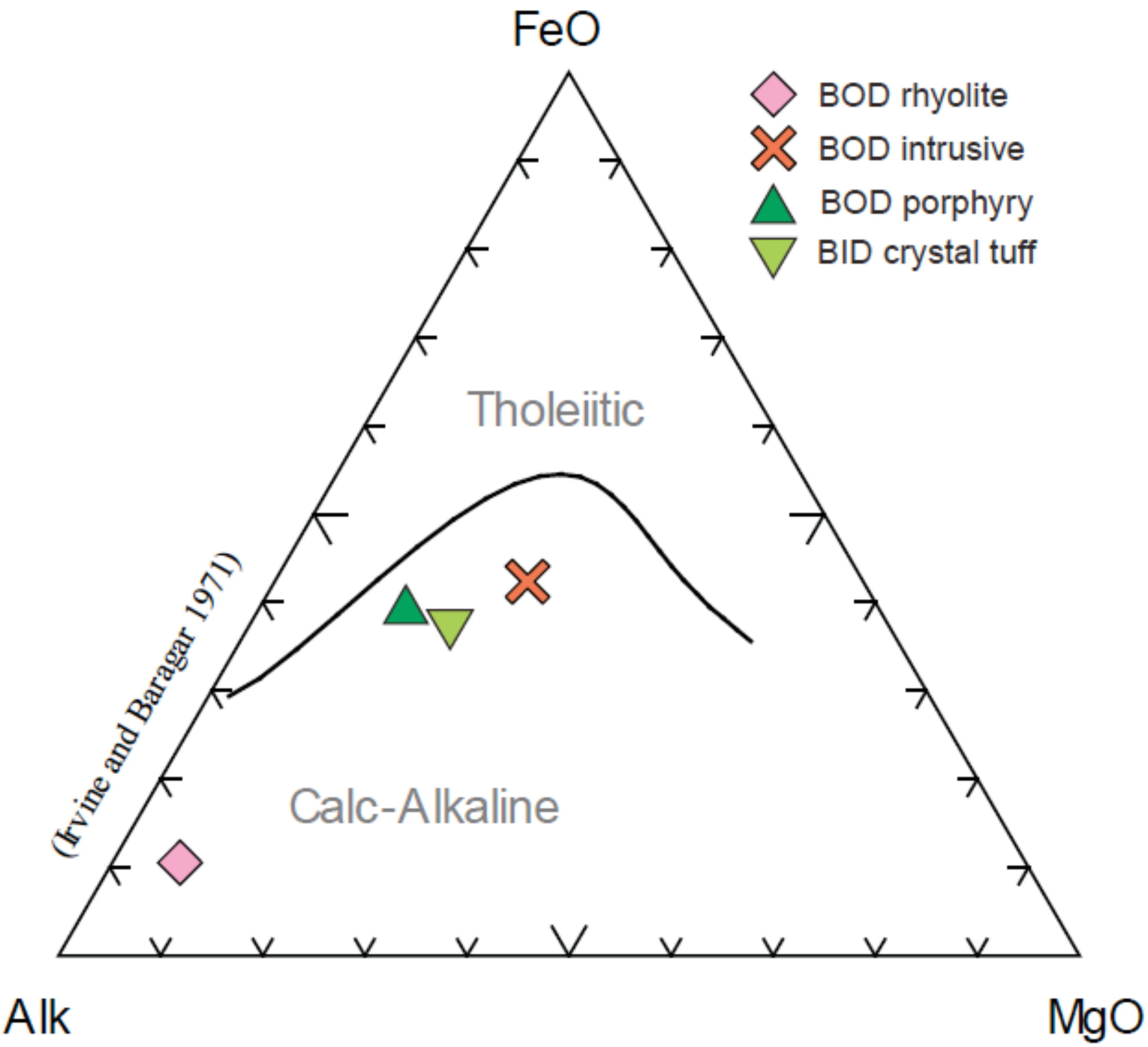

Figure II-7 AFM Diagram of unaltered (or least altered) samples from each of the main rock types at Bowone and Binebase showing their calc-alkaline affinity. Diagram after Irvine and Baragar, 1971.

diameter). Rare breccia zones containing a wide variety of fragments types are likely epiclastic units (Fig. 5B).

As mentioned above, the Bowone and Binebase deposits are hosted by andesites and rhyolites of the Binebase Group. These rocks are of calc-alkaline affinity, based on their whole-rock composition (Table 1; Figs. 6 and 7).

Recent oxidation has served to enrich both Au and Ag, and consequently much of the potentially economic mineralization of the Binebase deposit, and a small part of the Bowone deposit, is supergene in origin. However, both deposits have appreciable reserves of hypogene sulphide mineralization. The inferred resources, using a 0.25 g/t Au cut-off, are summarized in Table 2.

Hydrothermal Alteration

In hand sample, the altered rocks vary from dark grey to white in colour, depending on the pyrite content, and from very hard (quartz-dominated) to powdery (clay-dominated); in drill core, the latter variation commonly occurs over intervals of 10s of centimetres to metres (Fig. 8). The alteration intensity is variable. In some samples, the primary minerals have been completely replaced by secondary minerals, destroying all original textures, whereas in other samples, volcanic textures are preserved. Petrographic analysis revealed pervasive, and commonly, complete replacement of primary minerals by very small anhedral clay particles intergrown with fine-grained equigranular quartz and pyrite (generally anhedral) (Fig. 9). Less intensely altered samples commonly retain porphyritic textures, and in these samples, the phenocrysts commonly have been replaced by kaolinite or dickite. Intensely altered samples consist of a fine-grained mosaic of intergrown anhedral quartz, clay minerals (kaolinte, dickite, pyrophyllite), sulphate

Table II-2 Inferred resources for the Bowone and Binebase deposits (Stone, 2010). Some oxide ore is present at Bowone but the quantity is negligible compared to the sulphide body and has yet to be measured.

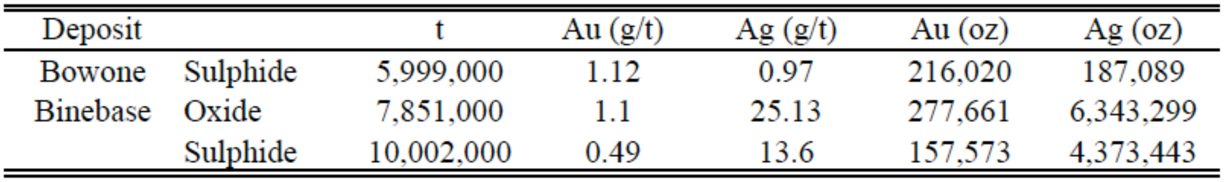

Deposit		t	Au (g/t)	Ag (g/t)	Au (oz)	Ag (oz)
Bowone	Sulphide	5,999,000	1.12	0.97	216,020	187,089
Binebase	Oxide	7,851,000	1.1	25.13	277,661	6,343,299
	Sulphide	10,002,000	0.49	13.6	157,573	4,373,443

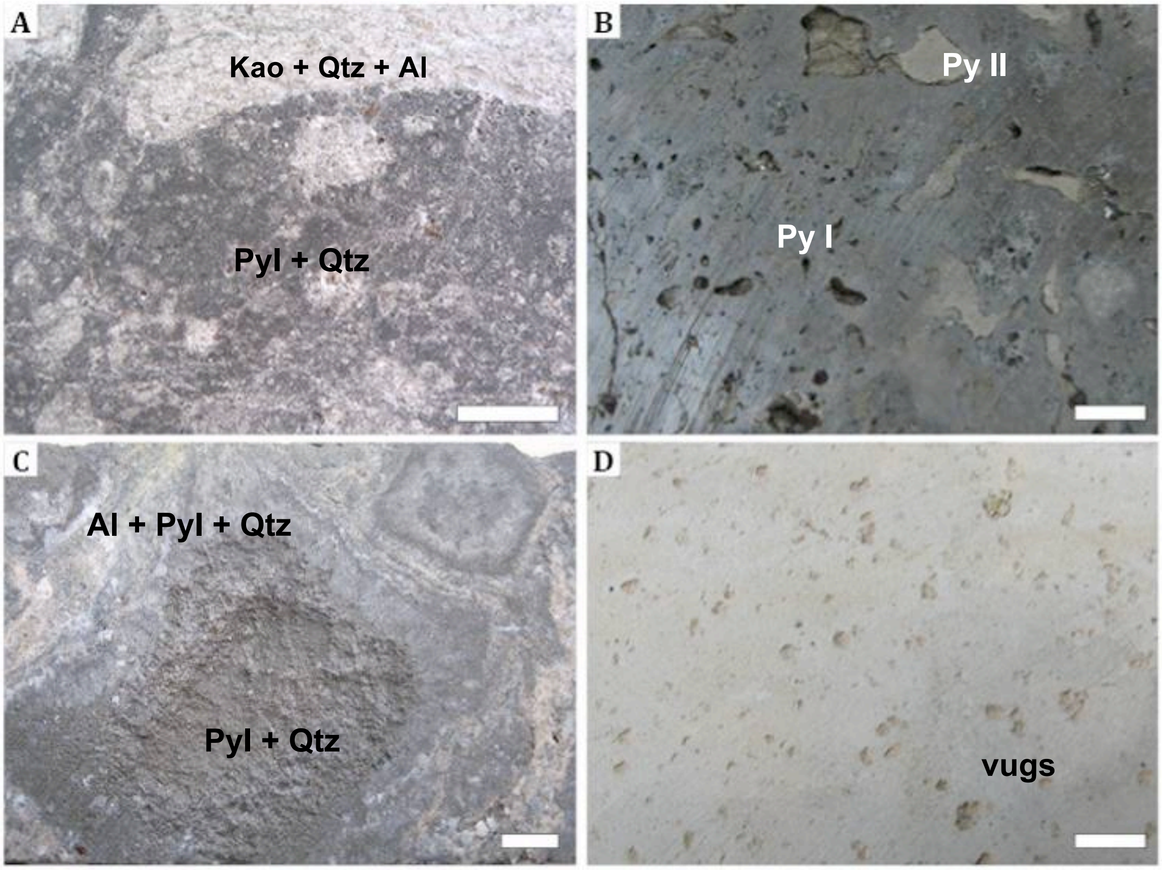

Figure II-8 Photographs of intensely altered core. A. Advanced argillic (quartz, pyrite, alunite) alteration of fragments (light grey) in a matrix of fine-grained quartz and pyrite (dark grey). B Massive pyrite breccias, showing complete replacement of the host rock by PyI, with PyII infilling vugs, and relic fragments of altered host rock with kaolinite replacing phenocrysts. C. Photograph of an advanced argillically altered sample showing a PyI-kaolinite-quartz core rimmed by quartz-alunite-PyI. D. Argillically altered rhyolite showing leached cavities of crystals and replacement of its matrix by kaolinite and quartz. The scale is 1 cm.

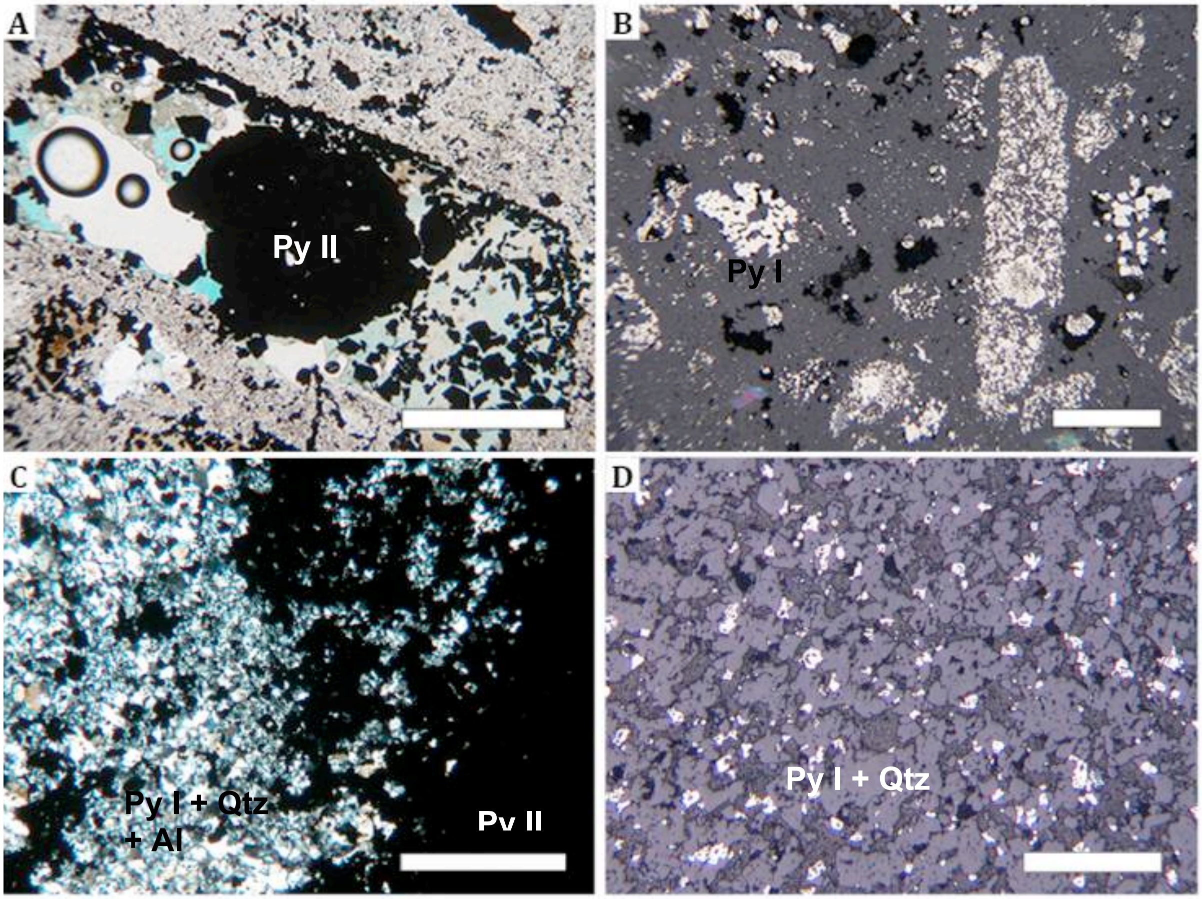

Figure II-9 Photomicrographs showing the textures of the altered rocks as observed in transmitted and reflected light (the scale is 10 µm). A. A relict phenocryst replaced by pyrite, quartz and kaolinite in a fine-grained argilically altered matrix (transmitted light). B. Amphibole phenocrysts replaced by PyI in a groundmass replaced by fine-grained quartz, kaolinite ± dickite (reflected light). C. Fine grained intergrowth of quartz, alunite and pyrite I in contact with massive pyrite II (transmitted light, crossed-polars). D. Fine-grained intergrowth of quartz, alunite and pyrite, typical of argillic alteration (reflected light).

minerals (alunite, natroalunite) and pyrite. Hereafter, fine-grained, anhedral pyrite associated with intermediate and/or advanced argillic alteration will be referred to as Pyrite I (PyI).

The alteration created secondary porosity in the form of mm-scale vugs (formed by the dissolution of phenocrysts), or irregular, centimetre-scale cavities. The latter commonly are infilled by subhedral alunite, and/or pyrophyllite, and/or euhedral pyrite, and/or subhedral chalcocite, and/or euhedral barite crystals (Fig. 8).

Alteration is most intense (few primary textures are preserved) along subvertical conduits that fan out horizontally at stratigraphic contacts (Fig. 10). Distal to the mineralized zones, the alteration is generally less intense, primary volcanic textures and minerals are preserved, and the rock is generally more competent. The matrix is altered preferentially and has a grey to light-brown hue.

Two main alteration facies have been recognized, advanced argillic and intermediate argillic, based on the occurrence of the assemblages quartz ± pyrite ± pyrophyllite ± natroalunite ± alunite ± dickite ± kaolinite and quartz ± pyrite ± kaolinite ± dickite ± illite, respectively. Quartz and pyrite are nearly ubiquitous alteration phases, but the proportions of these minerals and of the accompanying phases, which were used to define the alteration facies, vary significantly. In principle, the advanced argillic and intermediate argillic facies can be subdivided into sub-facies with fewer minerals that reflect different physicochemical conditions. For example, at conditions of quartz saturation (the case here), pyrophyllite is stable at higher temperature than dickite, and dickite is stable at higher temperature than kaolinite. Similarly, natroalunite is stable at higher temperature than alunite provided that the K/Na ratio of the fluid is relatively constant (Stoffregen and Cygan, 1990). Finally, illite is stable at higher pH than kaolinite, dickite and

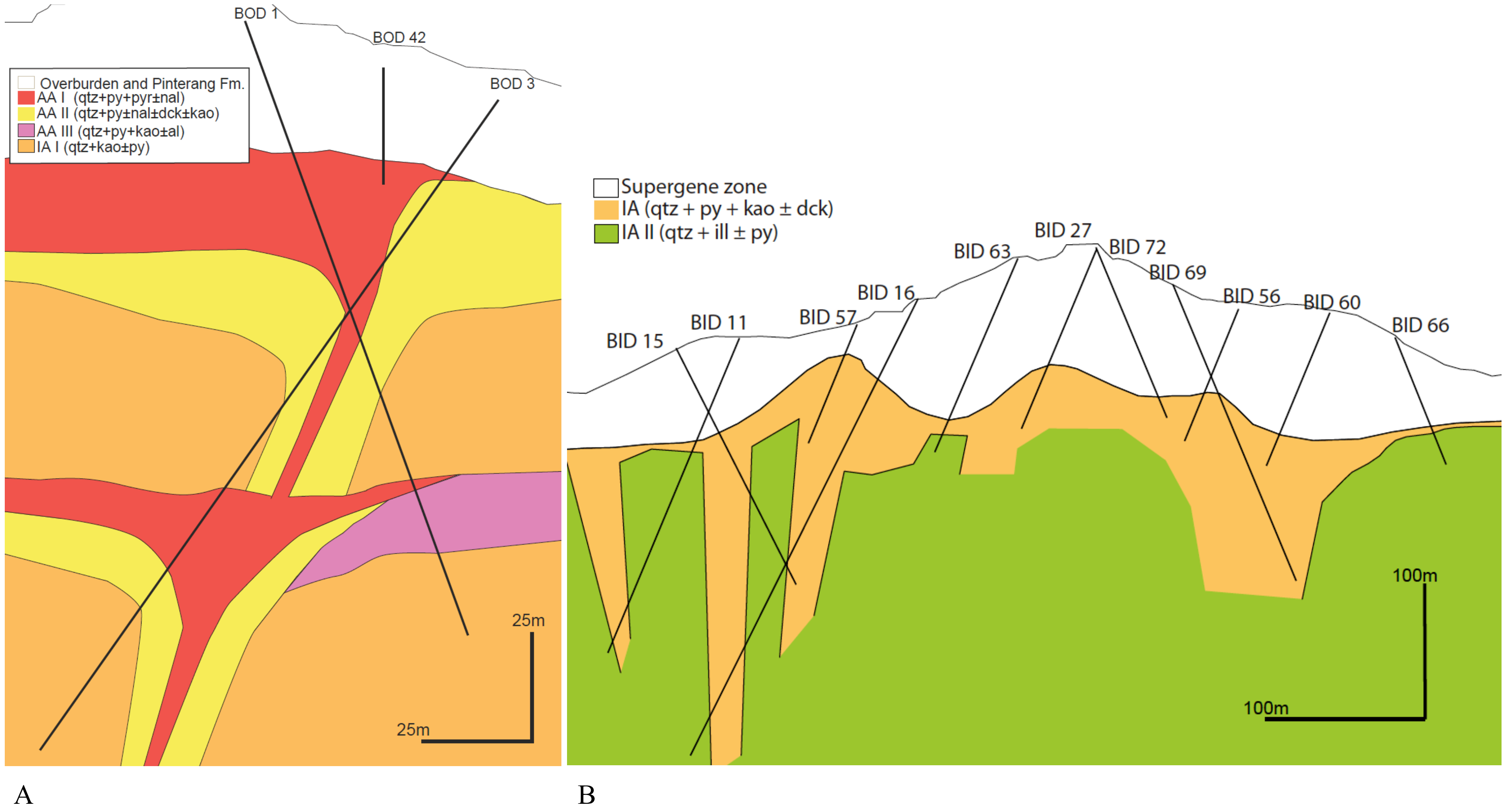

Figure II-10 Representative alteration cross-section A. through the Bowone deposit and B. through the Binebase deposit. Hypogene alteration facies established using X-Ray diffraction analysis and core logging.

pyrophyllite. In view of this, and X-ray diffraction evidence that subsets of the above assemblages form mappable units, we subdivided the advanced argillic assemblage into a high temperature sub-facies (advanced argillic I), quartz + pyrite + pyrophyllite ± natroalunite, an intermediate temperature sub-facies (advanced argillic II), quartz + pyrite ± natroalunite ± dickite ± kaolinite, and a low temperature sub-facies (advanced argillic III), quartz + pyrite + kaolinite + alunite. The intermediate argillic assemblage was subdivided into a low pH sub-facies (intermediate argillic I), quartz + kaolinite ± pyrite ± dickite and a higher pH sub-facies, quartz + illite ± pyrite (intermediate argillic II).

The alteration facies described above are zonally distributed, both vertically and horizontally, and the intensity of alteration decreases with depth. At Bowone, the upper part of the deposit is dominated by advanced argillic alteration, whereas at Binebase, the upper zone underwent intense oxidation due to exposure of the hypogene mineralization to weathering (Fig. 10). Consequently, advanced argillic alteration is not observed at Binebase; the Bowone deposit was protected from the effects of weathering by the overlying Pinterang Formation (Fig. 10A). Advanced argillic alteration in the Bowone deposit terminates abruptly at the contact with the overlying Pinterang formation. Locally, a thin (cm-scale) oxide layer is present at the contact, indicating that the uppermost part of the deposit was oxidized, suggesting in turn that some of it may have been removed by erosion prior to deposition of the Pinterang Formation.

The advanced argillic alteration at Bowone occurs as a subhorizontal zone below the Pinterang formation and a second zone lower in the stratigraphy just below a layer of andesitic tuff (Figs 4A and 10A). Both zones appear to flare out from a steeply inclined advanced argillic alteration zone that likely formed the conduit for the altering fluids. The upper parts of the sub-horizontal alteration zones and the central part of the inclined alteration zone are dominated by the high temperature, advanced argillic I alteration sub-facies. Below the sub-horizontal advanced argillic I alteration zones and adjacent to the inclined advanced argillic I alteration zone, this subfacies is replaced by advanced argillic II alteration and more distally by intermediate alteration I alteration. Low temperature advanced argillic III alteration is seen only at depth and locally may develop directly below advanced argillic I alteration without intervening advanced argillic II alteration (Fig. 10A). The advanced argillic III alteration may also be related to the hypabyssal porphyry intrusion.

At Binebase, the zone of supergene oxidation passes directly into intermediate argillic alteration. The latter comprises a blanket of intermediate argillic I alteration with several sub-vertical roots which pass downwards and laterally into intermediate argillic II alteration (Fig. 10B).

Hypogene Mineralization

Free gold or electrum is not observed in the hypogene zone of the Bowone deposit and very rarely in the Binebase deposit. Instead, the hypogene gold in both deposits is “invisible” in pyrite. Silver too is “invisible” in pyrite as is copper, although silver is also present in enargite. Copper occurs mainly in pyrite and enargite (volumetrically much less important than pyrite), and to a much lesser extent as chalcocite. Based on core logging, petrography and analyses of mineral chemistry, the main Au-(Ag-Cu) stages of gold mineralization are represented by: 1) the disseminated pyrite of advanced argillic and intermediate argillic (minor) alteration (pyrite I (Py I)); 2) multiple generations of lenses, veins and breccias of subhedral to euhedral, drusy, and massive to semi-massive pyrite II (Py II); and 3) late barite-enargite-pyrite veins. At Binebase, there is a fourth stage in the form of rare barite, base-metal sulphide and electrum veins (Fig. 11D).

The earliest gold mineralization is invisible in Py I, which is an ubiquitous alteration product intergrown with quartz and aluminous phases, and occurs as small (2 to 30 µm diameter), isotropic, anhedral grains, accounting for 2 to 20% of the rock (by volume); the gold grade corresponds directly to the amount of pyrite in the rock. As part of the advanced argillic and to a much lesser extent the intermediate argillic alteration, this stage of mineralization was focused along vertical structures and fanned out horizontally near the top of the deposit where fluids were confined by less-permeable strata or paleo-water tables. In the case of the Bowone deposit, it is also concentrated below an impermeable andesitic tuff in a subhorizontal zone of advanced argillic I alteration at a depth of ~75 m below the base of the Pinterang formation (Figs. 4 and 10)

The second stage of precious metal mineralization is characterized by veins, veinlets, blebs, breccias, lenses and massive bodies of coarse-grained, brassy Py II, which overprinted the advanced argillic alteration and intermediate argillic I alteration, exploited the secondary porosity created during this alteration and cross-cut fine-grained Py I. As is the case for Py I, the gold grade is controlled by the abundance of Py II, which makes up from 3 to 90% of the rock by volume, although not all the Py II shows the same level of gold enrichment. In thin section, Py II is coarse-grained (0.1 to 2 mm in diameter), massive, or net-textured and ranges in morphology from anhedral to euhedral (Figs. 11,12 and 13). Botryoidal and drusy textures (Figs. 11A, B and 12A) are common and many crystals are complexly zoned (Figs. 12A and C). Some pyrite II crystals have an anhedral blue anisotropic core, which chemically is indistinguishable from the

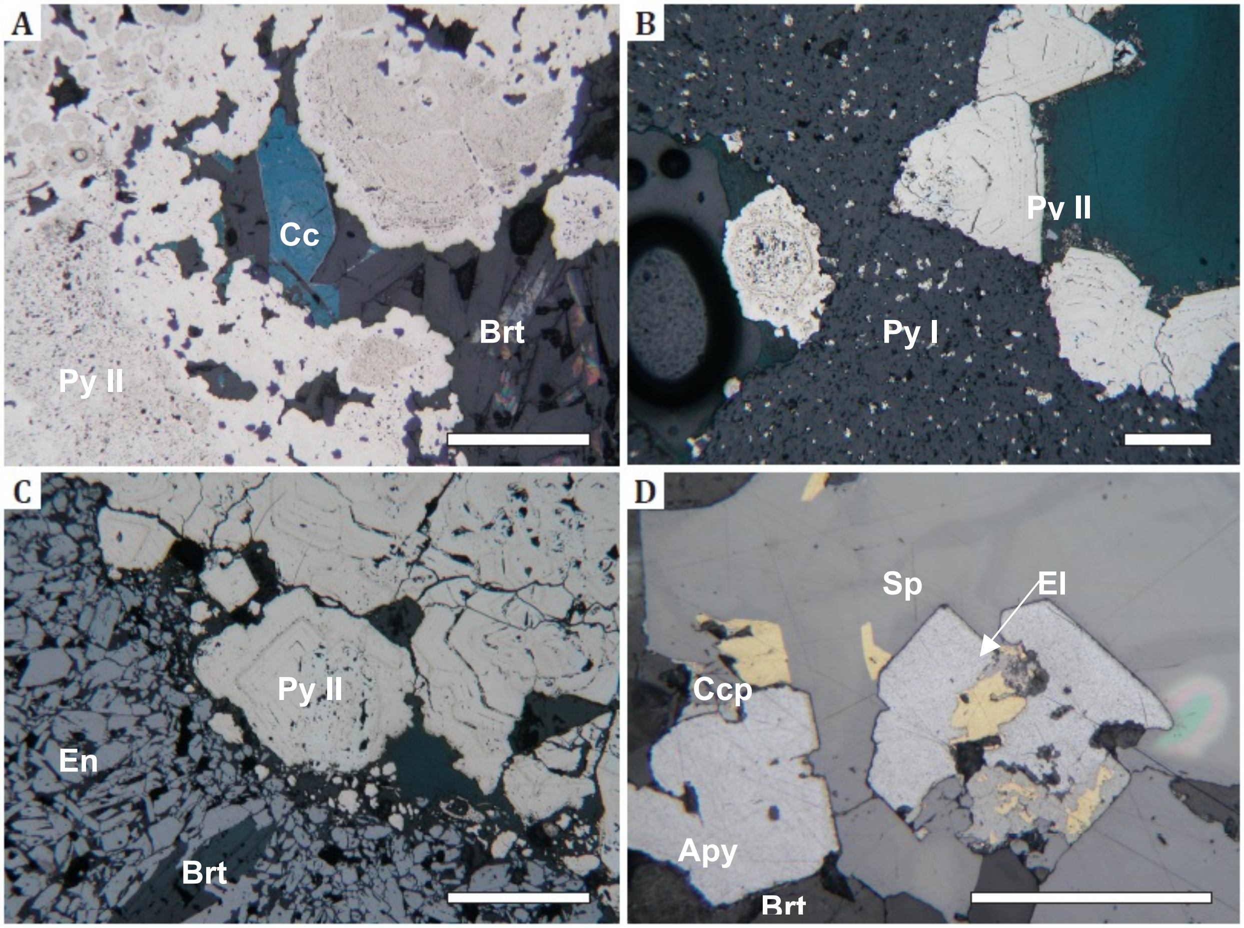

Figure II-11 Photomicrographs in reflected light showing textural features of the four stages of Au mineralization (the scale is 10 µm). A. Massive PyII with a vug containing rare chalcocite (Cc) and barite (Brt) crystals. B. Zoned drusy crystals of PyII infilling a vug in andesite altered to fine-grained PyI and quartz (blue-grey is epoxy). C. Fractured and zoned crystals of massive PyII cut by a barite-enargite (En) vein. D. Sphalerite (Sp), arsenopyrite (Apy), chalcopyrite (Ccp) and electrum (El) crystals in a barite vein.

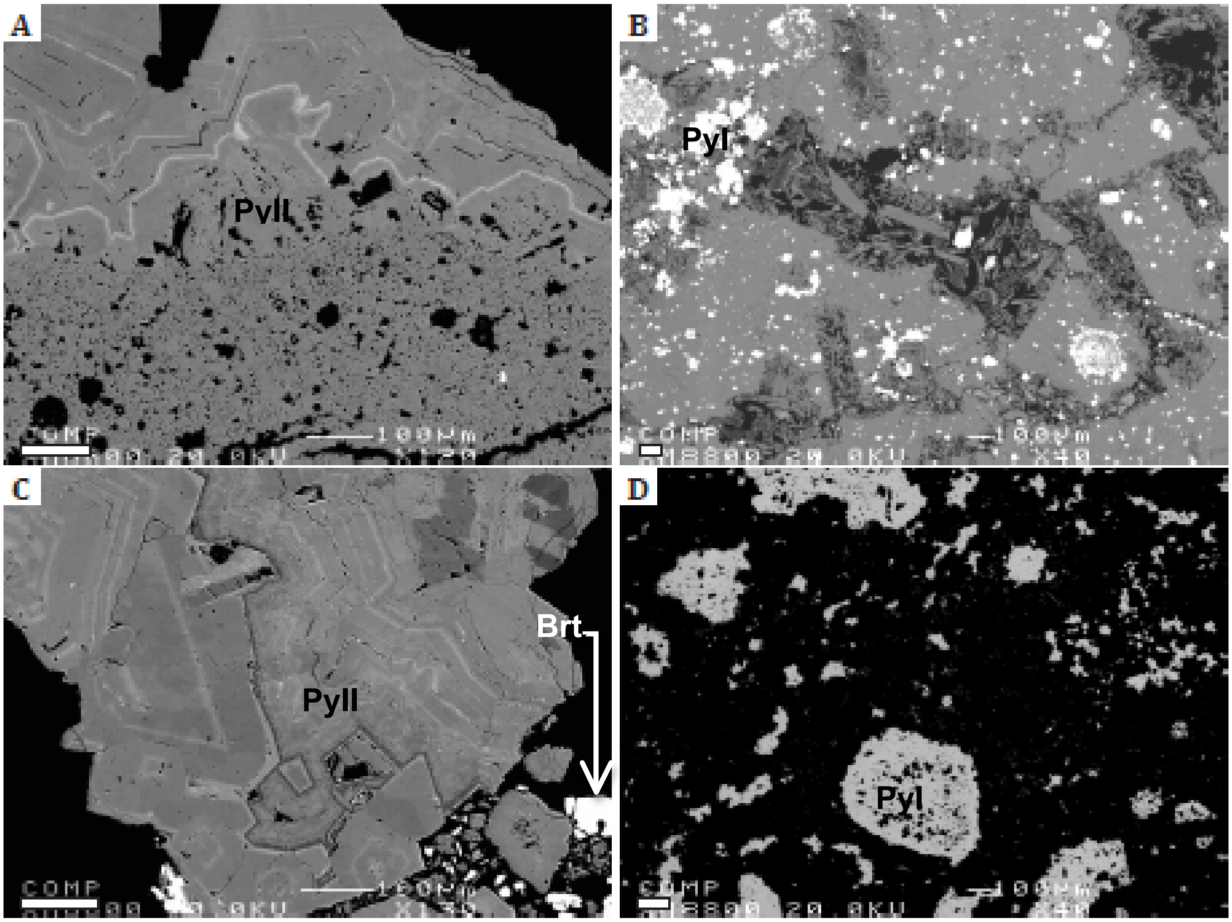

Figure II-12 BSE images of PyI and PyII (the scale is 100 µm). The brightness of each mineral correlates to relatively higher atomic weight than the surrounding material. A. Zoned drusy PyII overgrowing porous, massive PyII. B. Disseminated PyI (white) in a matrix of quartz and alunite, and a vug infilled by blades of an aluminosilicate phase. C. Zoned PyII (grey) in a vein with barite crystals (white). D. Disseminated porous PyI grains (grey) in a matrix of quartz and accessory phases.

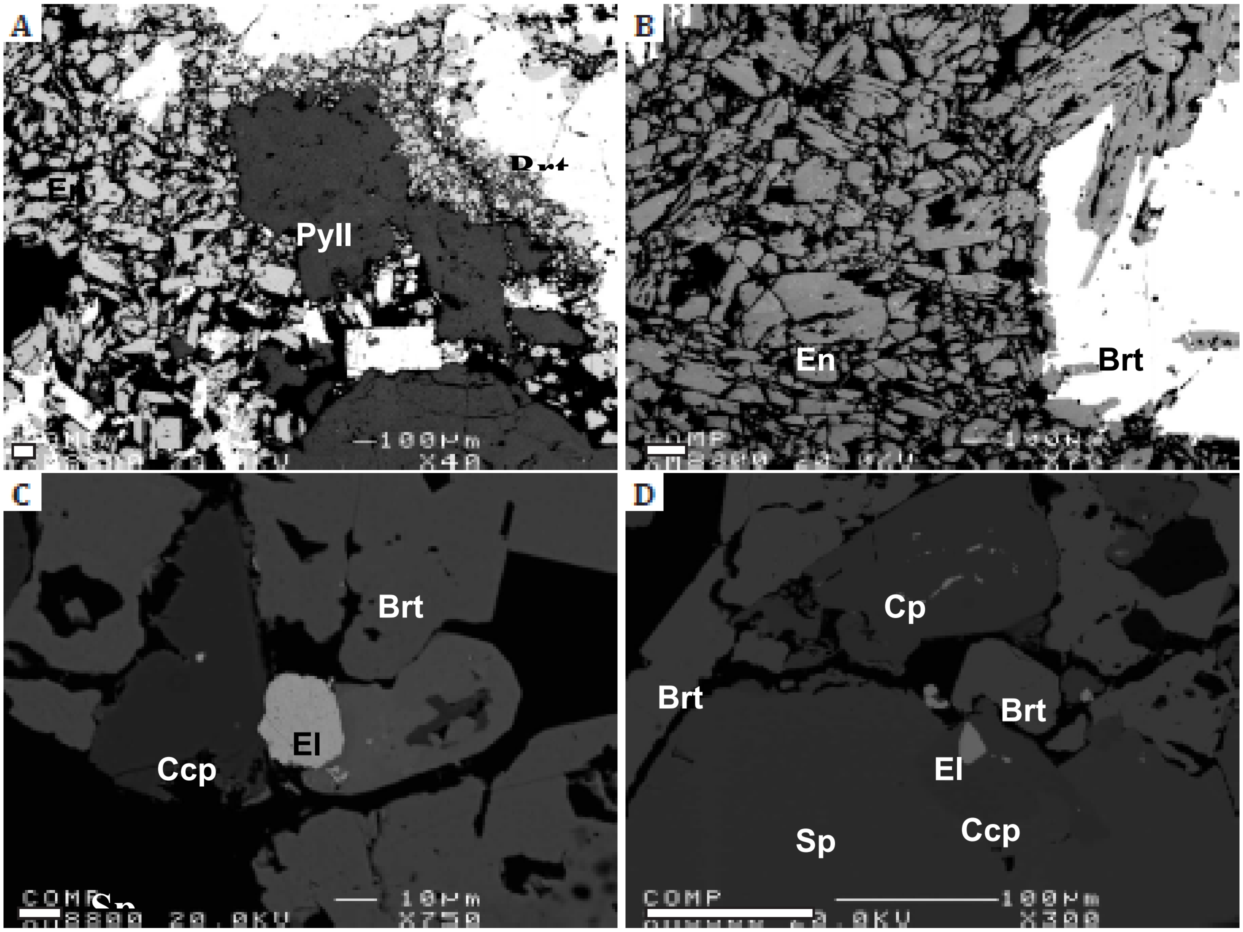

Figure II-13 BSE images of later generations of mineralization. Brighter areas correspond to relatively higher atomic weight than the surrounding material. A. and B. Barite-enargite veins with µm scale, homogeneous subhedral-euhedral enargite crystals intergrown with mm-scale subhedral barite (white crystals surrounding PyII fragments) (the scale is 100µm). C. Electrum (El) grain surrounded by subhedral chalcopyrite (Ccp), barite (Brt) and sphalerite (Sp) (the scale is 10 µm). D. Electrum grains in chalcopyrite, surrounded by barite and spalerite (the scale is 100 µm).

rest of the crystal (Fig. 11C). Rare, isolated anhedral chalcocite crystals (3 mm in diameter) are observed locally in vugs rimmed by drusy Py II (Fig. 12A). Growth zoning of Py II crystals on the µm scale is very common, particularly for drusy crystals which show a relatively stable growth history recorded by continuous growth surfaces, and for massive pyrite in which it is possible to make out crystals that grew separately and were annealed, resorbed, brecciated and overgrown (Fig. 12C).

Pyrite I and II are commonly cross-cut by later barite-enargite veins (0.2 to 5 cm wide), which appear to have exploited earlier Py II veins, as they are commonly lined by fractured Py II crystals and Py II commonly occurs as brecciated fragments in the veins, indicating that they have been incorporated mechanically (Fig. 11C). In the centres of these veins, blue-purple, intact, isotropic subhedral to euhedral (10 to 60 µm wide) rectangular or bladed enargite crystals and fractured Py II fragments are suspended in a matrix of coarse-grained, subhedral to drusy barite crystals. Texturally, enargite is homogeneous, unzoned and appears to have co-precipitated with barite (Figs. 11C and 13A, B). Barite and enargite also commonly occur in vugs. The density of barite-enargite veins (proportion of veins relative to host-rock) is variable but appears to correlate with that of Py II veins, suggesting that both vein stages exploited the same conduits.

Although the occurrence of electrum is volumetrically insignificant, the gold grade of these rare base-metal barite veins is twenty-times higher than that of the rest of the deposit. The rare base metal sulphide-electrum-barite veins in the Binebase deposit range from 0.5 to 8 cm in thickness and are observed in the centre of the hypogene mineralization. This rare vein assemblage was only observed at Binebase and cross-cuts all other mineralization except for the enargite-barite veins. The relative timing of these two vein generations therefore cannot be established. Mineralogically, the base metal sulphide-electrum-barite veins comprise small subhedral to euhedral crystals of spalerite, arsenopyrite, chalcopyrite, galena, pyrite, electrum and Sb-sulphides, which occur as aggregates in a coarse-grained matrix of euhedral barite crystals (Figs. 11 D, 13C and D).

Distribution of gold-silver mineralization

Gold and silver grades in the Bowone deposit are highest just below the contact with the Pinterang Formation, decrease with depth and then pick up again just below a thin tuffaceous andesite unit in a zone of argillic I altered rocks (Figs. 4 and 10). Metal concentrations correlate with the volume of Py II, pyrite breccias and/or barite-enargite veins. The same geometry is inferred for the hypogene mineralization at Binebase. However, as the upper part of the Binebase deposit was subjected to supergene oxidation, we infer that the high-grade hypogene mineralization in this deposit is now part of the supergene zone. This interpretation is consistent with the observation that the remaining hypogene mineralization has a much lower concentration of gold and silver than the Bowone deposit (Table 1).

Assay data for 1 m intervals of drill core for Bowone and Binebase, made available by East Asia Minerals Corp., show that there is a strong spatial correlation of concentrations of Au and Ag, with those of As and Cu, and a weaker correlation with Sb, Pb and Zn. Molybdenum concentrations are too low to discern a pattern. The distribution of Au, Ag, As and Cu is vertically zoned, with the highest concentrations of these elements occurring at the top of the hypogene zone. The highest of the Au peaks coincide with peaks in Cu, As and Sb, corresponding to barite-enargite veins, however, this is not the case for the second highest Au peak (Fig. 14). Furthermore the highest peaks in Cu, As and Sb, except in one case, are accompanied by minor to negligible enrichment in Au. We interpret these metal distributions to indicate that barite-enargite veins contributed minor amounts of gold and locally re-opened veins of pyrite II (coincident Au, Cu, As and Sb peaks).

Mass Changes During Alteration

Fifty-four drillcore samples of the different lithological units and alteration types were analysed for major, trace and rare earth elements (REE) by ICP-MS, and for gold by INAA, at Actlabs in Vancouver. The compositions of the altered rocks were compared to those of the least-altered rocks to evaluate the gains and losses of elements in the altered rocks. In order to assess the mass changes during alteration, it was first necessary to identify potentially immobile elements that could be used to normalize the compositions of the altered rocks to those of their least-altered equivalents. This was done by making binary plots of the data, and determining which of the element pairs were linearly distributed, as such a distribution would correspond to a relatively constant ratio for the elements and could indicate that they were immobile (e.g., MacLean and Kranidiotis, 1987; Warren et al., 2007; Agrawal et al., 2008). These plots show that pairs of the following elements, Zr, Ti, Nb, Hf and Ta are all linearly distributed. However, as Ti, Nb and Ta commonly occur together in rutile and Zr and Hf in zircon, only the linear distribution of Zr versus TiO_2 was taken as evidence of immobility (Fig. 15). Assuming that Zr and TiO_2 are immobile, the concentration of these elements in each altered sample was normalized to their concentration in a least altered sample for each rock-type, using the method of Grant (1986). To scale the changes for each element proportionally so that the mass change for an unaltered rock is zero (and the ratio of the mass change in the altered rock relative to the unaltered rock is

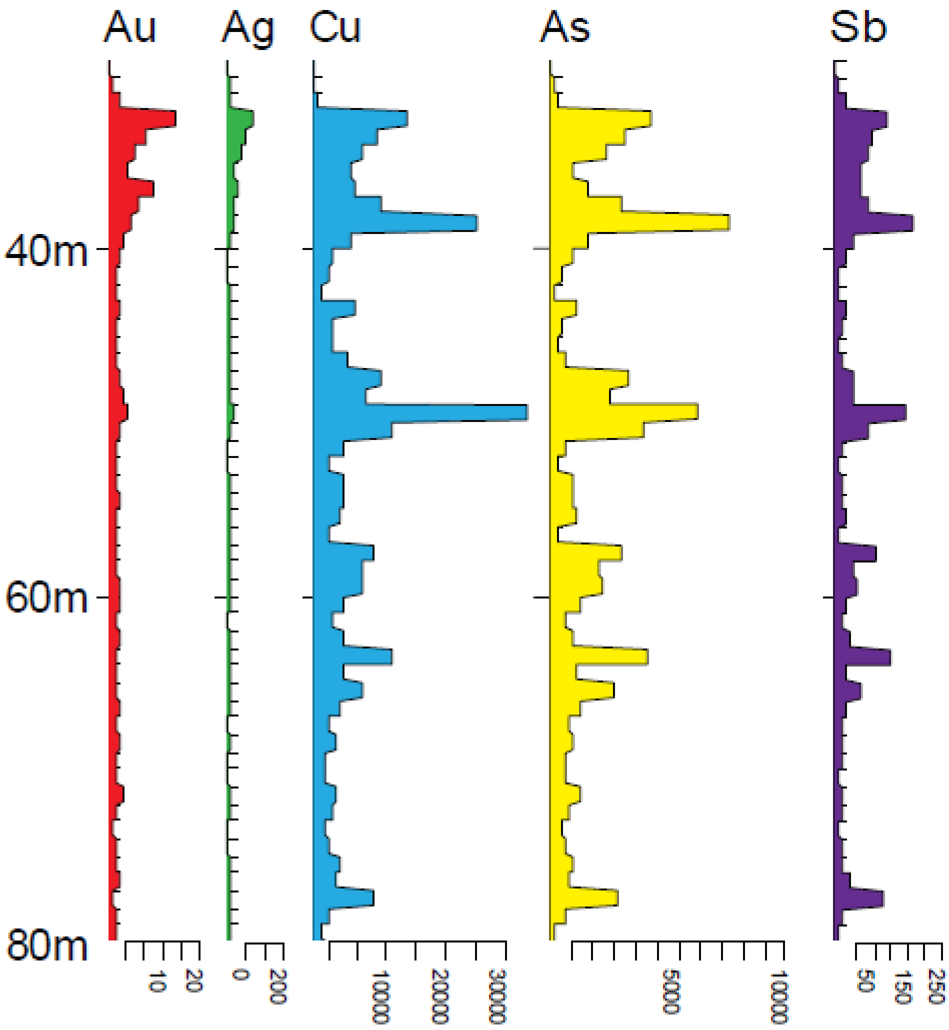

Figure II-14 The distribution of Au, Ag, Cu, As and Sb from a section of drillhole BOD1 (Pb, Zn levels were too low to be detected and Mo and Ba were not analysed).

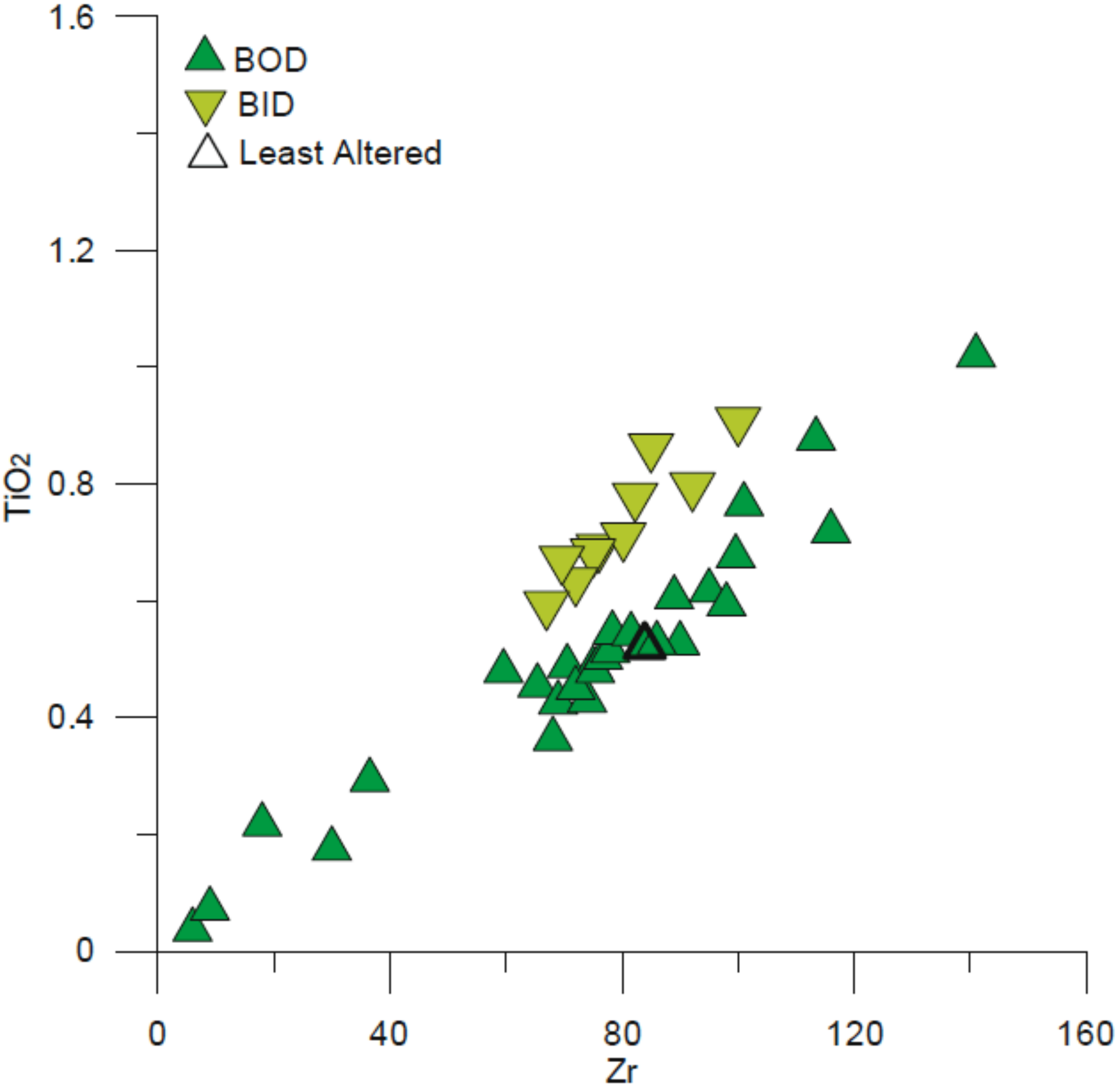

Figure II-15 A Binary plot showing the distribution of TiO_2 and Zr in variably altered rocks of the Bowone and Binebase deposits. See the text for an interpretation of the significance of these data.

unity), the concentration of each element was multiplied by the ratio of immobile element concentration (Zr and TiO_2) from the fresh rock to the altered rock in the Bowone and Binebase suites. Values below 1 indicate proportional losses of an element, relative to an unaltered sample, and values above 1 indicate gains.

Three distinct patterns of relative gains/losses are observed for advanced argillic alteration (the small size of the data set precluded separate treatment of advanced argillic alteration I, II and III) and intermediate argillic I (Bowone and Binebase) and II (Binebase) alteration (Fig. 16). As expected, given the mineralogy, the advanced argillic and intermediate argillic I samples were strongly depleted in the major elements Mn, Mg, Ca, and Na, moderately depleted in K, weakly depleted in Al and P, relatively undepleted in Si and strongly enriched in Fe. The intermediate argillic alteration II samples were also depleted in Mn, Mg, Ca and P, and particularly in Na, but appear to have conserved Al, Si and Fe. In contrast to advanced argillic and intermediate argillic I alteration, these samples are enriched in K. The overall distribution of trace metals and semi-metals (Au, Cu, As, Ag, Cr, Co, Ni, Zn, Mo, Sn, Sb, Tl, W and Pb) indicates they were added during all stages of alteration albeit in variable quantities. However, whereas Rb and Cs were depleted during advanced argillic and intermediate argillic I alteration and Sr added, the opposite occurred during intermediate II alteration; Sr was depleted and Rb and Cs enriched.

Both the advanced argillic and intermediate argillic I alteration underwent substantial mass losses in all the REE, but these mass losses were greatest for advanced argillic alteration, with the extent of depletion increasing progressively with atomic number from La to Dy and then decreasing progressively to Lu. (Fig. 16). In contrast to advanced argillic and intermediate argillic I alteration, the depletion of REE during intermediate argillic II alteration was greatest

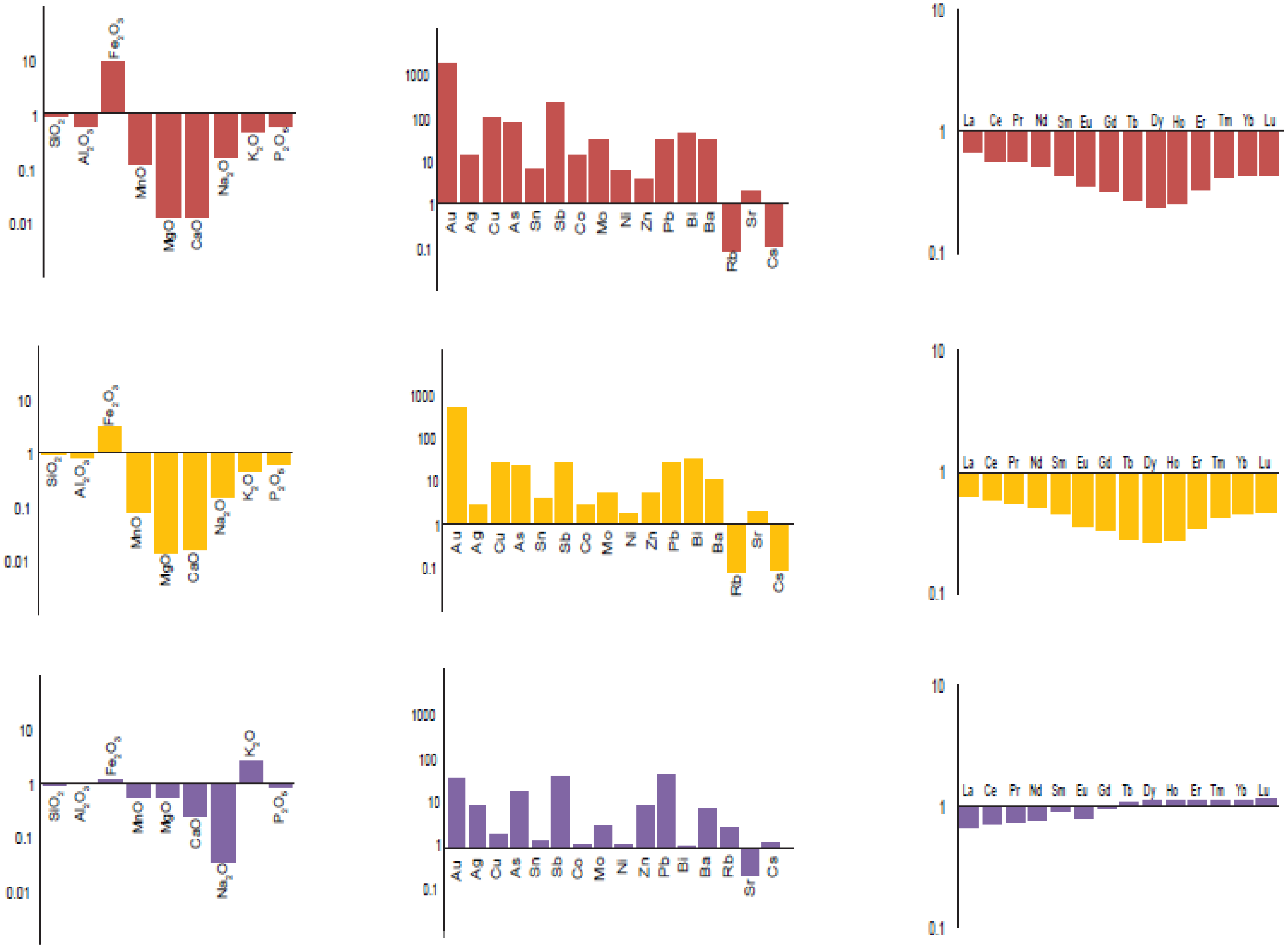

Figure II-16 Relative gains and losses of elements for advanced argillically altered rocks from Bowone (red), intermediate argillically altered I samples from selected porphyry and crystal tuffs from Bowone and Binebase (yellow) and intermediate argillically II altered (purple) rock samples from Binebase (crystal tuffs), calculated using the method of Grant (1986). A value of 1 indicates relative immobility, less than 1 indicates a relative loss and more than 1 indicates a gain.

for La and decreased with atomic number to Gd; we consider that the very small additions at higher atomic number of the REE reflect uncertainties in the mass transfer calculations and that these elements were immobile during alteration. The preferential leaching of the LREE during intermediate argillic II alteration is consistent with results of experiments showing that the LREE are more mobile in chloride-bearing hydrothermal fluids than the HREE (Migdisov et al. 2009). However, the reason for the preferential depletion of the MREE during advanced argillic and intermediate argillic I alteration is unclear. A possible explanation for this anomalous behaviour is that depletion of the LREE was inhibited because of their uptake by alunite and phyllosilicates (e.g., Miller et al., 1982; Hopf, 1993; Fulignati et al., 1999; Karakaya, 2009) and that without this uptake they would have been more depleted than the MREE, consistent with the experimental predictions (Migdisov et al., 2009). The differential behaviour of the REE reported above supports observations from active systems that REE chemistry offers a useful tool for distinguishing among alteration types (e.g., Michard, 1989; Lottermoser, 1992; Lewis et al., 1997; Fulignati et al., 1998, 1999).

Ore Mineral Chemistry

The composition of pyrite and enargite was analysed using a combination of electron microprobe (EMP) and laser ablation induced coupled mass spectrometry (LA-ICPMS). Quantitative electron microprobe analyses for Fe, S, Cu, As, Sb, Co, Ni, Zn, Se and Te were conducted on carbon-coated samples at McGill University using a JEOL 8900 instrument equipped with five wavelength dispersive spectrometers (WDS). The operating conditions were an excitation potential of 20 kV, a beam current of 50 nA and a spot-size of 2 μm. Analyses were standardized using pyrite (Fe, S), chalcopyrite (Cu), AsNiCo (As, Ni, Co), CdTe (Cd, Te), sphalerite (Zn), stibnite (Sb) and AgSe (Se) supplied by CANMET. In addition to quantitative spot analyses, the EMP was also used to prepare element maps for Cu, Fe, Se, and As. The operating conditions were an excitation voltage of 20 kV, an operating current of 90 nA, and a beam diameter of 2 µm. The counting time was 30 ms and the pixel size between 0.20 to 1.28 µm.

The LA-ICPMS analyses were conducted at the Geological Survey of Canada (pyrite) using a Photon Machines Nalyte 193 mm Excimer laser with an Agilent Technologies 7700 Series ICP MS and at Université de Chicoutimi (enargite) using an Excimer Resolution M-50 (Resonetics) Laser with an Agilent 7700x ICP MS. The concentration of Fe^{57}, S^{34}, Cu^{65}, Au^{197}, Se^{77}, Te^{125}, Ag^{107}, As^{75}, and Sb^{121} was measured in both pyrite and enargite. Pyrite was also analysed for Co^{59}, Ni^{60}Pb^{208}, Zn^{66}, and Bi^{209}. The ablation pits ranged from 14 µm to 54 µm in diameter, and the counting time was 100 s (30 s of background, 70 s of ablation) for pyrite and 90 s (30 s for background, 60 s of ablation) for enargite. The concentrations of Fe and S determined by EMP analysis were used as an internal standard for pyrite and enargite, respectively; GSE-IG, NIST 610 and Po689 were used as external standards for the analysis of pyrite and GSE-1G, PS1 and JB5 for enargite.

Pyrite

The following trace elements were detected in pyrite using the EMP: As, Co, Cu, Ni, Sb, Se, Te, Zn. Laser ablation ICPMS analyses yielded results for these elements similar to those obtained with the EMP (Appendix C) and in addition detected Ag, Au, Bi, and Pb (Appendix D). Copper is the principal trace element in both generations of pyrite followed by Co, As and Pb (Py I) or by Co, Pb, and As (Py II). Significantly, both generations of pyrite contain ppm levels of Au and Ag.

Pyrite I crystals are unzoned (Fig. 12 B, D) and have a wide range of Cu concentration (from 0.02 to 1.5 wt.%); the average Cu concentration is 0.45 wt% (σ = 0.4 wt %). Cobalt concentration is significantly lower, averaging 117 ppm (σ = 12.3ppm). The average As concentration is 95ppm (σ = 133 ppm) and that of Pb is 55 ppm (σ = 55 ppm). As discussed above, Py I is auriferous/argentiferous. The average concentrations of Au and Ag are 1.08 ppm (σ = 0.77 ppm) and 33.0 ppm (σ = 47.8 ppm), respectively. Somewhat surprisingly, the concentrations of Se and Te, elements that with As are commonly elevated in auriferous pyrite (e.g., Fleet et al., 1993; Reich et al., 2005), are relatively low, 32 ppm (σ = 42 ppm) and 10 ppm (σ = 13 ppm), respectively (Table 3).

The concentrations of all trace elements detected in Py I are higher in Py II. The average concentration of Cu in Py II is 1.12 wt%, (σ = 1.14 wt%) but can be as high as 5.3 wt% in individual crystals. On average, the concentration of Co is 3016 ppm, (σ = 6052 ppm), that of Pb is 512 ppm (σ = 1169 ppm) and that of As is 330 ppm (σ = 457 ppm). Unlike the case for Py I, the concentration of Te is relatively high, averaging 218 ppm (σ = 389 ppm) and that of Se is significant, averaging 121ppm (σ = 199 ppm). The Au concentration in Py II ranges up to 13.6 ppm and averages 3.0 ppm (σ = 3.1 ppm), and the Ag concentration ranges up to 1273 ppm and averages 80 ppm (σ = 228 ppm).

Although the concentrations of trace elements, on average, are lower in Py I than in Py II, the inter-element distributions are similar. Binary plots (Fig. 17) and element maps (Fig. 18) show that high Au concentration in Py I and II is generally associated with elevated Cu, As, Ag, and Te, but Au concentration may be high even if concentrations of these elements are relatively low; this is especially true for Ag and Te. Gold concentration is almost entirely independent of Se

Table II-3 Summary concentration data for PyI and PyII based on LA-ICPMS analyses.

	Ag (ppm)	As (ppm)	Au (ppm)	Bi (ppm)	Co (ppm)	Cu (wt %)	Fe (wt %)	Ni (ppm)	Pb (ppm)	S (wt %)	Sb (ppm)	Se (ppm)	Te (ppm)	Zn (ppm)
Py I mean	33.0	95.4	1.1	10.1	117.1	0.4	59.7	43.1	55.3	53.3	3.7	31.8	10.1	5.8
median	9.1	43.9	1.0	3.9	62.5	0.3	58.4	33.7	59.6	53.4	3.7	9.6	3.8	2.8
σ	47.8	133.0	0.8	14.2	123.9	0.4	68.9	50.0	55.6	68.8	3.4	41.7	12.5	7.4
min	0.3	2.3	d.l.	0.1	0.1	d.l.	52.3	0.5	0.5	51.7	0.3	1.2	0.7	0.6
max	145.8	467.3	2.5	47.9	404.3	1.5	71.7	182.9	199.8	54.6	11.0	118.6	35.5	22.9
Py II mean	80.6	329.7	3.0	9.4	3015.6	1.1	48.6	138.3	511.8	52.3	10.7	121.0	218.3	91.7
median	3.7	117.6	2.4	5.9	148.0	0.6	49.0	40.3	69.9	52.6	3.7	25.9	31.3	6.8
σ	228.2	457.0	3.1	9.4	6051.7	1.1	92.7	206.2	1168.8	17.9	24.9	199.0	389.1	319.4
min	d.l.	0.8	d.l.	d.l.	d.l.	d.l.	30.9	0.1	0.1	48.3	0.1	0.7	0.1	0.5
max	1273.2	1636.6	13.6	43.2	21417.7	4.4	76.1	800.2	7205.3	55.2	169.6	640.1	1430.9	1936.3

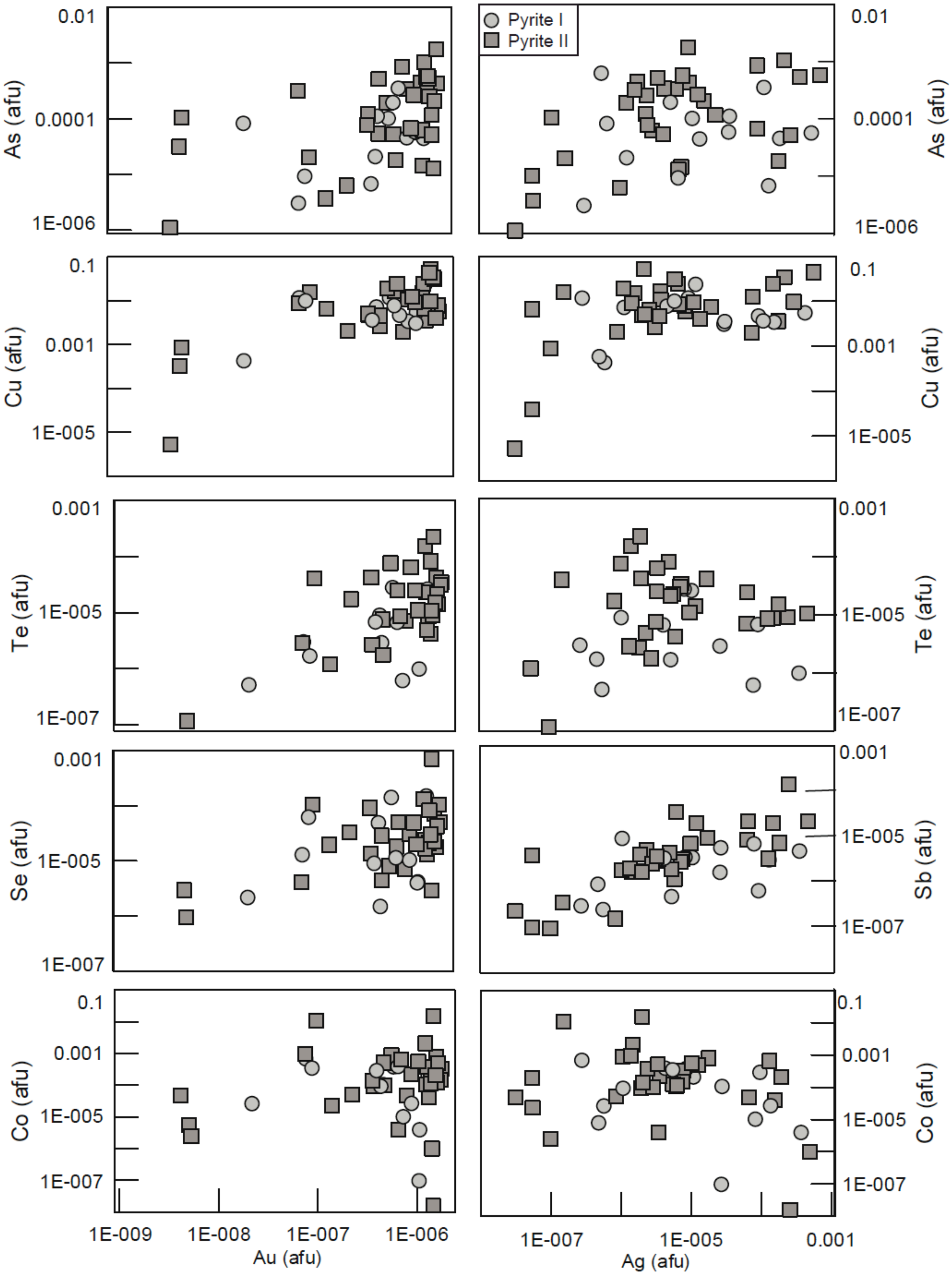

Pyrite I
Pyrite II
As (afu)
0.01
0.0001
1E-006
Cu (afu)
0.1
0.001
1E-005
Te (afu)
0.001
1E-005
1E-007
Se (afu)
0.001
1E-005
1E-007
Sb (afu)
0.001
1E-005
1E-007
Co (afu)
0.1
0.001
1E-005
1E-007
1E-009
1E-008
1E-007
1E-006
Au (afu)
1E-007
1E-005
0.001
Ag (afu)

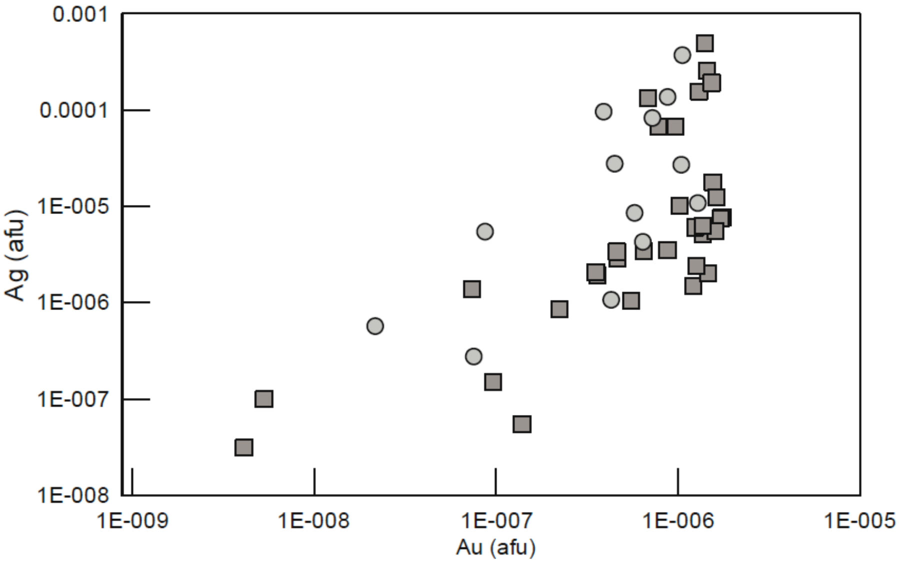

Figure II-17 Binary plots of trace element concentration in pyrite analysed by LA-ICPMS. The term afu refers to atomic force units.

concentration and shows no correlation with Co (or Ni, Sb, Zn, Pb or Bi, which are not shown) concentration. The inter-element correlations for Ag are similar to those for gold, except that high Ag concentration is associated with low Te concentration and vice versa.

As mentioned earlier and illustrated by reflected light (Fig. 11) and back scatter SEM images (Fig. 12), Py II is complexly zoned (this contrasts with Py I, which, as noted above, is unzoned). Moreover, the backscatter electron images (Fig. 12) indicate that this zonation reflects differences in the distribution of its trace elements. This was confirmed by quantitative spot analyses of Py II, which show that there are appreciable compositional variations among zones within single crystals

Copper concentrations show the largest compositional variations between zones, the distribution of which reveals a complex history of growth, overgrowth and resorption (Fig. 18, 19). In addition to this growth zoning, sector zoning is evident in the distribution of Cu (i.e., within single growth zones there are sharply defined sectors of higher and lower Cu concentration corresponding to differences in the crystal faces presented). The nature of the sector zoning varies considerably with the nature of the crystal and is most easily observed in drusy crystals (Fig. 19A, B and E, F).

Based on electron microprobe analyses, the Cu concentration of individual zones can vary from as low as 0.12 to as high as 5.3 wt.%, and inversely with the concentration of Fe. In some zones, high Cu concentration is matched by an elevated concentration of As but in others the concentrations of the two elements do not correlate positively (Fig. 19). In addition to As, the concentrations of Ni, Se and Te were measured across the transects. All three elements show

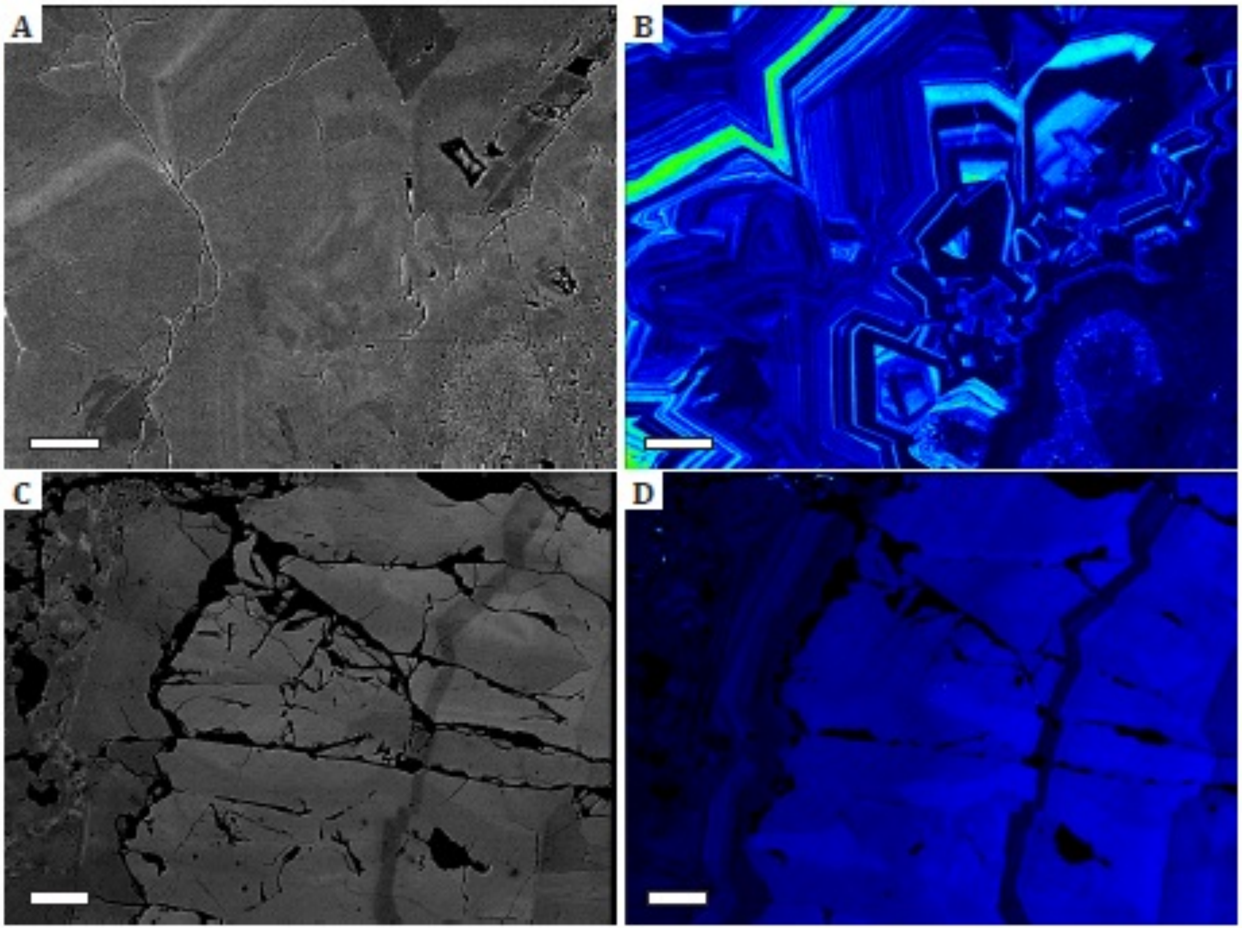

Figure II-18 BSE images (right) and corresponding copper maps (left) showing strong sector and growth zones in PyII (the scale is 50 µm). In the Cu maps, light blue-green represents higher Cu concentration and the darker the blue, the lower is the Cu concentration. A. and B. Complex, micron scale, strongly growth zoned drusy pyrite overgrown on massive, porous pyrite, also zoned. The growth zoning is perpendicular to the crystal growth direction and records the primary growth history. C. and D. Two morphological varieties of pyrite II showing growth zonation (banding), decreasing Cu concentration to the right, and sector zoning, crystallographically controlled zones delineated by variable copper content, perpendicular to the growth zones.

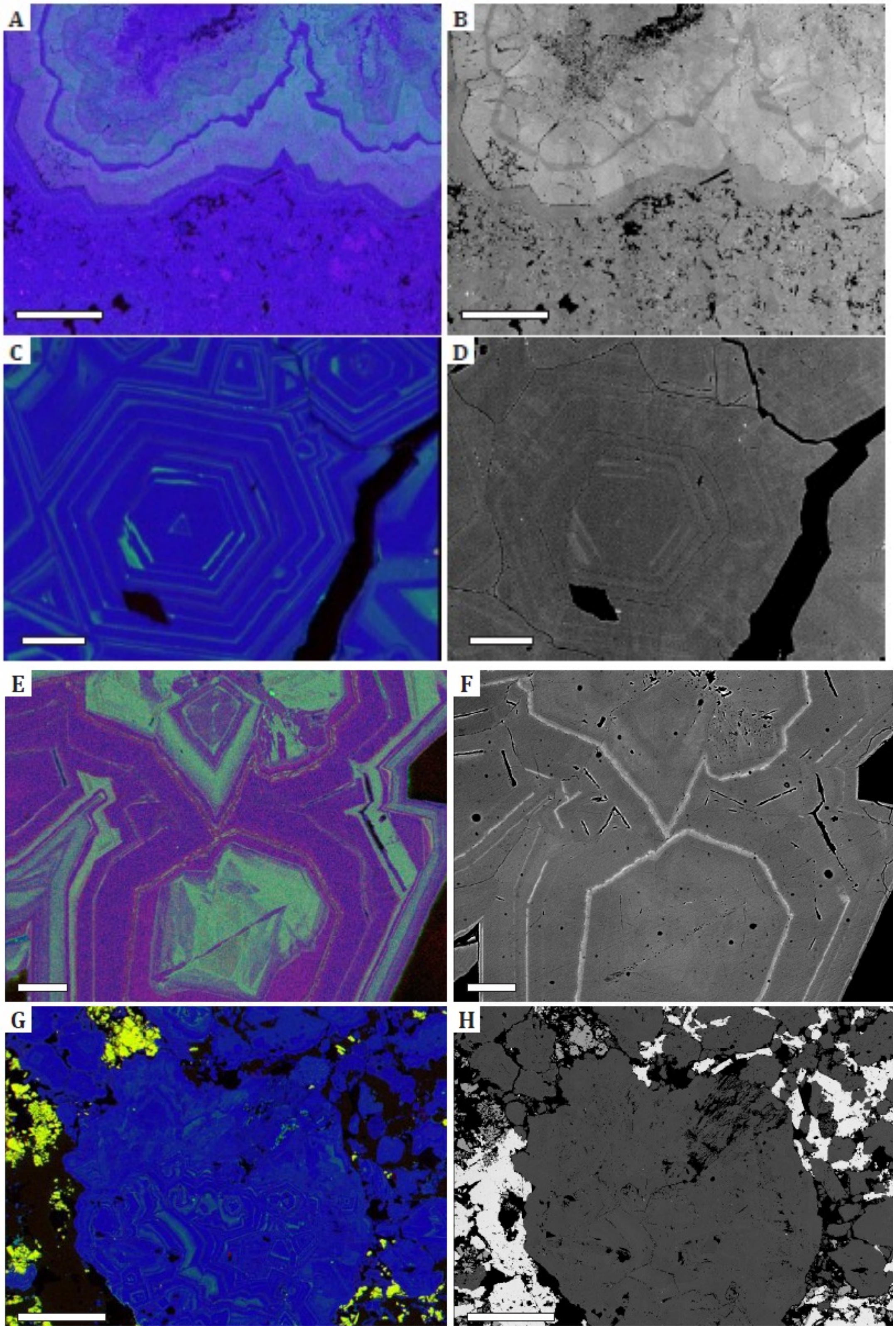
A
B
C
D
E
F
G
H

Figure II-19 Composite Cu (green), Fe (blue) and As or Se (red) maps (right) of PyII and the corresponding BSE images (right). Brighter colours correspond to higher concentrations of an element. A. and B. Drusy, PyII with growth and sector zones and very high Cu concentrations (green) and variably As-rich (red) bands transitioning into massive, porous PyII with lower Cu concentration and isolated zones of As enrichment (the scale is 50 µm). C. and D. Cross-section through a euhedral PyII crystal displaying growth zoning with alternating As (red) and Cu (green) enriched bands. Sector zoning presents most strongly as a Cu enrichment on three equivalent faces, about a three-fold axis (the scale is 500µm). E. and F. Drusy PyII crystals displaying complex growth zoning in either Cu (green) or Se (red) bands. Sector zoning in Cu is also present in the form of a cross at the center of a cubic pyrite grain, top-centre (the scale is 500 µm). F. and G. Broken PyII aggregate of subhedral crystals with growth zones surrounded by barite (white in BSEI) and enargite (light grey in BSEI, and yellow in map composite), taken from a late barite-enargite vein. Growth zoning is visible in enriched Cu growth zones (green), whereas enargite crystals with both high As (red) and Cu (green) appear yellow and are homogeneous and unzoned (the scale is 50 µm).

increases in concentration with elevated Cu concentration. In samples for which concentrations are high enough, Ni, Se and Te alternately covary with Cu and As. Further insight into how trace elements in Py II covary is provided by LA-ICPMS depth profiles through crystal growth zones. Overall, the profiles show that zones enriched in Cu are enriched in all trace elements, although individual elements covary in their concentrations with some but not all the elements analysed. This is illustrated in Figure 20, which shows the signal intensity (counts) for a suite of elements through three growth zones. From this figure, it is evident that the concentrations of Au, As and Te covary (they all decrease strongly in the central zone), that Cu, Co, Ni, Zn, Bi and Se covary and do so independently of Au, As and Te, and that Ag and Pb covary independently of the other two groups of elements. It should be noted, however, that these groupings are not observed in all crystals. For example, Te behaves independently of Au and As in some crystals and covaries with Se in others. Nonetheless, the “Cu group” of Cu, Ni and Co generally covary independently of the “Au group” of Au, As and Te (Se). Silver concentration is usually decoupled from those of both Au and Cu and commonly covaries with Pb, Bi and, rarely Se concentration.

Enargite

On the basis of quantitative EMP analyses, the enargite has close to an end member composition with an average As concentration of 18.3 wt% ($\sigma = 0.9$ wt%), an average S concentration of 32.7 wt% ($\sigma = 0.4$ wt%) and an average Cu concentration of 48.3wt% ($\sigma = 0.7$wt%). The trace element concentrations were analysed by a combination of EMP and LA-ICPMS methods and predictably, Sb was the trace element in highest concentration with an average of 8097 ppm ($\sigma =$ 1247 ppm). This is well below the concentration needed for it to be identified as stibioenargite

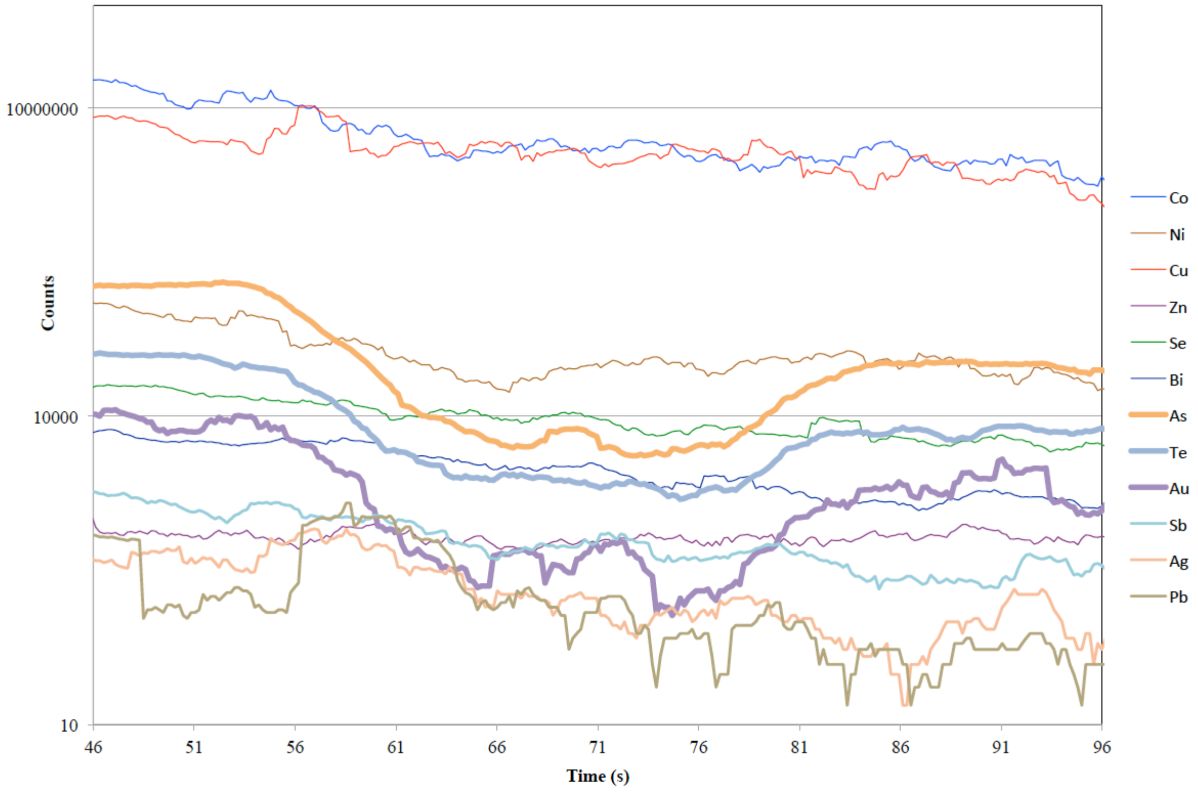

Figure II-20 An example of a processed depth profile through three growth zones of a Py II crystal produced by LA-ICPMS, showing counts vs. time for major and trace elements. Arsenic, Te, and Au covary through the three growth zones and are independent of Co, Cu, Ni, Zn, Se and Bi, whereas Ag, Pb and to some extent Sb covary independently of the other two trends.

Table II-4 Enargite composition, analysed by LAICP-MS

Sample	Ag (ppm)	As (wt%)	Au (ppm)	Cu (wt%)	Fe (ppm)	S (wt%)	Sb (ppm)	Se (ppm)	Te (ppm)
En-1	114.9	15.5	0.5	24.9	277.7	32.7	4987.7	2.6	189.2
En-2	214.5	11.8	0.7	38.5	548.6	32.7	4876.6	3.3	177.8
En-3	59.1	15	0.4	45.8	26.7	32.7	6525.8	1.8	188.9
En-4	108.5	13.4	0.6	37.2	82	32.7	9543.1	2.3	95.1
En-5	113	14.2	0.8	32.1	316.8	32.7	4574.5	3.2	211.3
En-6	48.9	13.9	0.1	33.2	117.8	32.7	8167.5	2.7	135.9
En-7	31.1	12.9	0.7	28.4	649.6	32.7	9220.2	3.4	108.5
En-8	171.7	12.5	0.7	28.8	1304.1	32.7	4273.7	5.5	82.6
En-9	52.7	12.3	0.3	34.9	786.5	32.7	5527.7	3.4	79.5

(Springer, 1969; Maske and Skinner, 1971; Posfai and Buseck, 1998). Iron is the next most important trace element with an average concentration of 348 ppm (σ = 254 ppm), followed by Te and Se, with average concentrations of 67 ppm (σ = 100 ppm) and 31 ppm (σ = 8 ppm), respectively (Table 4). The Au content is significantly lower than that of Py I or Py II, averaging 0.53 ppm (σ = 0.23 ppm), but the silver content, on average, is significantly higher than that of either generation of Py (101.6 ppm, σ = 61.2 ppm). Despite the presence of a number of trace elements in significant concentration in the enargite, none of them display a systematic correlation with another trace element.

From BSE images, the enargite appears to be unzoned, but LA-ICPMS depth profiles show small variations in the signals of some trace elements and of Cu (Fig. 21). Moreover, the counts for some elements covary but track independently of those for other trace elements. For example, the counts for Ag and Te covary over the first 80% of the profile displayed in Figure 21 before converging, but vary antithetically with those for Fe and Sb; in the last part of the profile, the signal for Ag covaries with that for Cu.

Sulphur Isotopes

Isotopic compositions of pyrite and sulphates (alunite and barite) were measured to better understand the physiochemical conditions of ore formation.

Method

As it is impossible to physically separate the fine grained, intergrown pyrite and alunite, separation was achieved chemically in two stages. In the first stage, finely ground altered rock

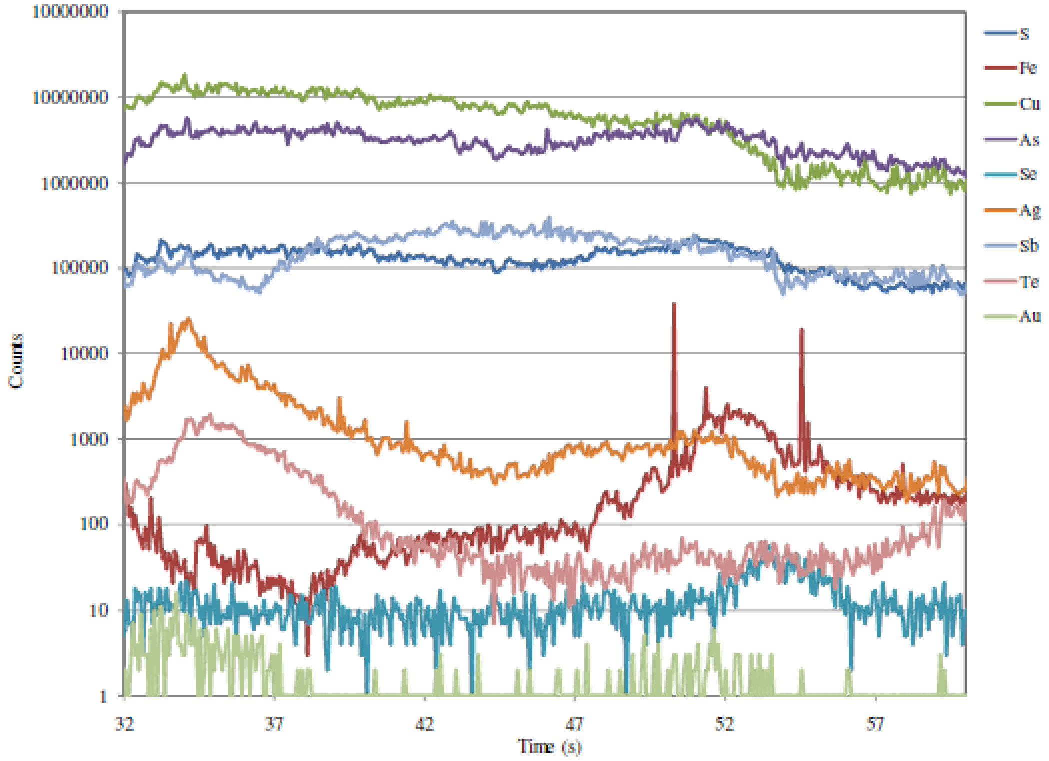

Figure II-21 A plot of counts vs. time (s) in a depth profile through an enargite crystal analysed by LA-ICPMS. Silver and Te covary and are roughly antithetic to Fe and Sb. Copper, As, S Se remain relatively constant and Au values are near the detection limit, although from 32 to 37s they may correspond to the increased Ag and Te signal.

was reacted with a Cr-reducing solution to liberate H_2S from the sulphides (Canfield et al., 1986). This procedure stripped the sample of sulphide, allowing the solid residue to be filteredand reacted with thode solution (Thode et al., 1961) to convert the remaining sulphur (sulphate) to H_2S. In both cases, the resulting H_2S was trapped using a zinc-acetate solution and reacted with a solution of $AgNO_3$ to produce solid Ag_2S that was purified and reacted with SF_6 (Thode and Rees, 1979) prior to introduction into a Thermo Finnigan MAT 253 dual-inlet gas-source mass spectrometer at McGill University for measurement of sulphur isotopic ratios, with IAEA-S-1 as an internal standard (Sharman, 2011). The ratios are reported relative to V-CDT in δ notation.

Results

Two samples of the argillically and advanced argillically altered material and one sample of the pyrite and barite from the late barite-enarite veins were selected for analysis for their sulphur isotopic composition (Table 5). Preliminary analysis gave inconclusive results for sulphate but consistent $\delta^{34}S$ values were obtained for pyrite. The $\delta^{34}S$, $\delta^{35}S$ and $\delta^{36}S$ values for pyrite have average values of: -2.65 (σ =0.25), -5.17 (σ =0.48) and -9.93 (σ =0.77), respectively. The standard deviations are small considering that the pyrite represents different generations of mineralization.

Discussion

Geological Setting

The Bowone and Binebase deposits occur at the southwestern end of a young volcanic island

Table II-5 Sulphur isotope compositions of PyI and PyII from Bowone and Binebase.

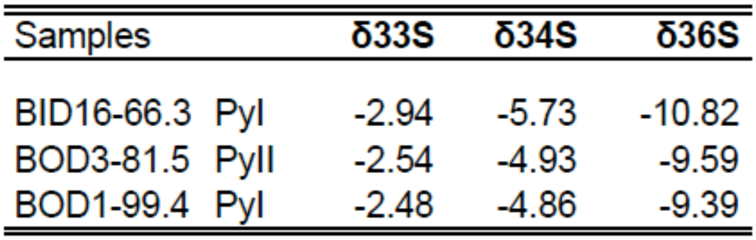

Samples		δ33S	δ34S	δ36S
BID16-66.3	PyI	-2.94	-5.73	-10.82
BOD3-81.5	PyII	-2.54	-4.93	-9.59
BOD1-99.4	PyI	-2.48	-4.86	-9.39

with an active volcano to the northeast and a chain of extinct/dormant volcanic edifices in between. Both deposits are hosted by rocks of the Binebase Group, a thick andesitic sequence of alternating porphyritic-epiclastic flows and crystal tuffs that were probably nearly coeval and in close proximity to a volcanic centre, though none is visible today. There has been no dating of the volcanoes on Sangihe Island. However, if, as seems likely, a volcano was located above the Binebase and Bowone deposits (and was thus close to the coast), its erosion would have been very rapid due to a combination of rising sea level (as indicated by the marine deposits of the overlying Pinterang Formation), thermal subsidence as the magmatic centre moved north-west and the hot wet tropical climate. Consequently, all traces of the volcanic edifice could have disappeared in a few tens of thousands of years.

Pressure

A rough estimate of the depth and pressure of emplacement of the Bowone and Binebase deposits can be made by comparing their current elevation to that of Awu volcano, the only active volcano on Sangihe Island. The summit of this volcano is at an elevation of 1327 m abovesea level; the elevations of the dormant/extinct volcanoes range from 1006 m for Kakiraeng, which lies to the west of the deposits, to 295m for Malisang situated near the south end of the island. By contrast, the Bowone and Binebase deposits are exposed on the erosional surface at elevations of 86m and 65m, respectively. Thus, if the summit of the volcano above the deposits was at an elevation similar to those of Awu and Kakiraeng volcanoes, it follows that the deposits would have been emplaced at depths between 1260 and 920 m below the paleosurface. These depths fall within the range of depths (150 to 1500m below the paleosurface) estimated for other high-sulphidation epithermal deposits (Jannas et al., 1990; Arribas, 1995; Cooke and

Simmons, 2000). The depths inferred for Bowone and Binebase (1260 to 920 m) correspond to lithostatic pressures of 252 to 345 bar or hydrostatic pressures of 90 to 123 bar, respectively. As much of the mineralization is disseminated and there is no evidence of large through-going fractures that might have intersected the paleosurface, pressure was probably intermediate between the two extremes. In the discussion that follows, we therefore assume that the pressure accompanying hydrothermal alteration and gold mineralization was ~200 bar.

Temperature and pH

Earlier in this paper, we showed that advanced argillic (AA) and intermediate argillic (IA) alteration in the Bowone and Binebase deposits were characterised by the following assemblages: AA I (quartz+ pyrite+ pyrophyllite± natroalunite), AA II (quartz+ pyrite± natroalunite± dickite± kaolinite), AA III (quartz+ pyrite+ kaolinite+ alunite), IA I (quartz+ kaolinite± pyrite± dickite) and IA II (quartz+ illite± pyrite). Here, we use stability relationships among these minerals in the system Al-Si-O-K-Na-Fe-H-S to make inferences about temperature and pH (Fig. 22 and 23). The total S concentration was assumed to be 0.01m, consistent with that inferred for other high sulphidation epithermal systems (e.g., Muntean et al., 1990). At a pH below 2, aluminum is mobile, an observation confirmed by our mass balance calculations, which provide evidence for some Al mobility. For such conditions, Al activity was assumed to be 0.1 (Knight, 1977; Fulignati et al., 1999). At higher pH, Al was assumed to be immobile and its activity buffered by the aluminum minerals (Stoffregen, 1987; Salvi et al., 1998).The Na/K ratio was constrained to be 10 by the observed coexistence of natroalunite and alunite, and the conclusion that alunite transformed to natroalunite at a temperature of ~275°C (see below). Oxygen fugacity was inferred from the $\delta^{34}S$ values for pyrite to be that of the hematite-magnetite buffer (see below). The activity of Fe and Si were assumed to have been buffered by pyrite and quartz, respectively, which are ubiquitous in the deposits.

At the conditions for which Figures 22 and 23 were constructed, pyrite is stable above 250°C (hematite is stable below 250°C), making this the lower temperature limit for all alteration facies. As kaolinite and quartz react to form pyrophyllite at a temperature of 275ºC (Fig. 22), the coexistence of quartz and kaolinite in AA II, AA III and IA I alteration zones constrains their temperature to have been below 275ºC. Conversely, the presence pyrophyllite in the AA I alteration zone indicates that this alteration occurred at a temperature above 275ºC (Holland, 1998). Natroalunite is the stable form of the alunite group minerals in the AA I alteration zone and alunite its stable form in the AA III alteration zone. Unexpectedly, however, given the coexistence of quartz and kaolinite (implying a temperature below 275ºC), natroalunite is also the stable member of the alunite family in the AA II alteration zone. We interpret this to indicate that AA II alteration occurred at ~275ºC, an interpretation that is supported by the presence of dickite in the AA II alteration zone (kaolinite is widely inferred to convert to dickite above 150°C (Hemley et al., 1969; Stoffregen and Alpers, 1987; Stoffregen and Cygan, 1990). In view of the distribution of alunite group minerals among the AAI, AAII and AAIII zones, we conclude that alunite was replaced by natroalunite at ~275 ºC.

An upper temperature limit for AA I alteration is provided by the absence of andalusite, which forms from the reaction of pyrophyllite and quartz at ~340ºC (Fig. 22 and 23). In summary, we conclude that AA I alteration occurred at a temperature between 275 and 340ºC, AA II alteration at ~ 275ºC and AA III and IA I alteration at between 250 and 275ºC. As the IA II alteration assemblage includes pyrite, it occurred at >250ºC and, although we cannot constrain the upper

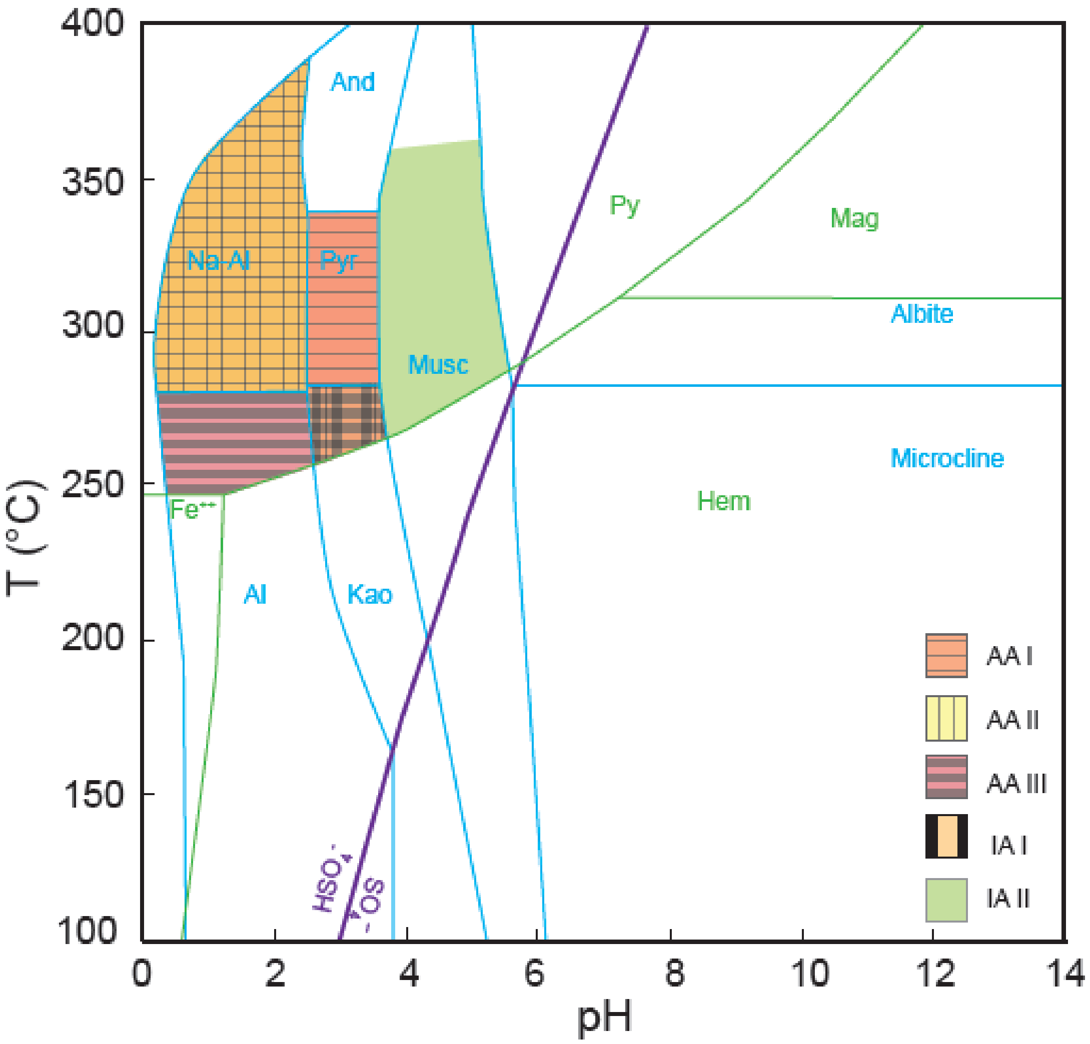

Figure II-22 Stability relationships among minerals in the systems K-Na-Al-Si-O-H and Fe-S-O as a function of temperature and pH. Also shown on the diagram are the fields of stability of the five main alteration facies, advanced argillic I (AA I), advanced argillic II (AA II), advanced argillic III (AA III), intermediate argillic I (IA I) and intermediate argillic II (IA II). Calculations were made for 200 bar (SVP), logfO_2 = -30 (suggested by the δ^{34}S of pyrite, assuming a magmatic source, at a temperature between 250°C and 300°C), quartz and pyrite saturation, $Na^+/K^+=10$ (see text for details), $a\Sigma S=0.01$ (see text for details) and $aAl^{3+}= 0.1$. Silicate and sulphate species are blue, sulphur species are purple, and sulphides are green.

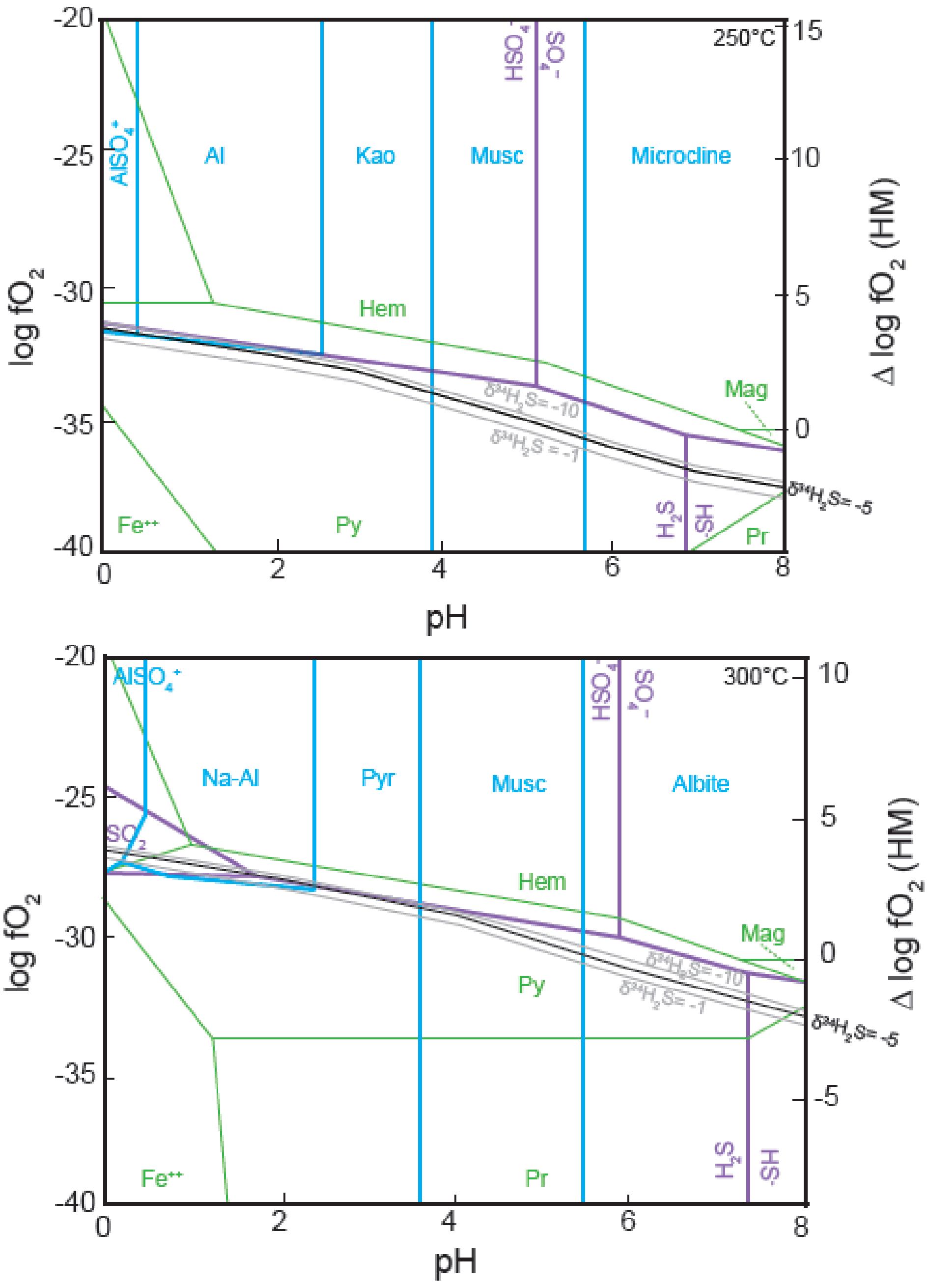

Figure II-23 Log fO_2-pH diagrams showing stability relationships for minerals in the K-Na-Al-Si-O-H and Fe-S-O systems A) at 250°C, and B) at 300°C, the mid- to high-temperature case. The diagrams were created assuming a pressure of 200 bar (SVP), logfO_2 = -30, quartz and pyrite saturation, $Na^+/K^+=10$, $a\Sigma S=0.01$ and $aAl^{3+}= 0.1$ (see text for details). Silicates and sulphate species are blue, sulphur species are purple, and sulphides are green. The black lines are $\delta^{34}S$ contours for pyrite at -1, -5 (the measured $\delta^{34}S_{H2S}$ value for Sangihe pyrite) and -10, and constrain the logfO_2 values to between -35 and -27.

temperature of this alteration from its mineralogy, it is reasonable to conclude that this limit was less than or similar to that for IA I alteration, i.e., ≤ 275ºC.

On the basis of the stability relationships illustrated in Figure 22, specifically the presence of both natroalunite and pyrophyllite in the AA I assemblage, natroalunite and kaolinite/dickite in the AA II assemblage and alunite and kaolinite in the AA III assemblage, we interpret the pH of advanced argillic alteration to have been ~ 2.5. In principle, the pH could have been significantly lower, if natroalunite and pyrophyllite or alunite and kaolinite were not in equilibrium (Hemley and Jones, 1964; Knight, 1977). If, however, the pH was below 2, aluminum would have been highly mobile (Stoffregen, 1987), which based on our analysis of mass changes (Fig. 16) was not the case; aluminum experienced minor depletion. This supports a conclusion that the pH was at least 2 and more likely 2.5. The presence of kaolinite in the IA I alteration assemblage constrains its pH to have been between 2.5 and 4, and the presence of illite, but absence of K-feldspar in the IA II assemblage, constrains its pH to have been between ~ 4 and 6.

fO_2

High sulphidation ore-forming epithermal systems are characteristically oxidizing with oxygen fugacity straddling or just below that of the hematite-magnetite buffer. For example, values for $\Delta \log fO_2$ (HM) reported for some other high sulphidation deposits have ranges of +4.24 to -1.32 (Thiersch et al., 1997), +2.4 to +0.07 (Muntean et al., 1990) and <+2.5 (Voudouris, 2011). If the sulphur source is assumed to be dominantly magmatic, which is considered to be the case for most high sulphidation deposits (e.g., Muntean et al., 1990; Rye et al., 1992; Rye, 1993; Arribas, 1995; Hedenquist et al., 1998b; Bethke et al., 2005; Deyell et al., 2005a,b; Fifarek and Rye, 2005; Taylor, 2007), $\Sigma\delta^{34}S$ is approximately zero, and it is possible to calculate $\delta^{34}S$ from the measured pyrite values and in turn log fO_2 for given values of pH (Zhang, 1993). The negative $\delta^{34}S$ values interpreted for the reduced sulphur (H_2S) at Bowone and Binebase, assuming a temperature between 250 and 340ºC are similar to those of other high sulphidation deposits (Muntean et al., 1990; Hedenquist et al., 1994; Voudouris, 2010), and are consistent with fractionation between sulphides/sulfosalts and sulphates in an oxidizing environment (Arribas, 1995; Cooke and Simmons, 2000). Given the $\delta^{34}S_{H2S}$ values, the Δ logfO_2 (HM) values for advanced and intermediate argillic alteration are between +4 and -1 (Fig.23, Table 6) (Rye, 1993, 2005; Cooke and Simmons, 2000).

Metal Transport

According to many researchers, there is a "ground preparatory stage" or "pre-ore" stage of hydrothermal alteration in high-sulphidation epithermal systems, which precedes gold mineralization (Stoffregen, 1987; Hedenquist et al., 1994; Arribas, 1995; Hedenquist et al., 1998; Hedenquist et al., 2000). There is also a consensus among these researchers that the extreme acidity required to produce the advanced argillic alteration that characterizes much of this ground preparation stage can only be explained by interaction of the rocks with a condensed acidic vapour (e.g. Hedenquist et al., 1994; Hedenquist et al., 2000). With few exceptions, these researchers have attributed metal transport to a liquid of magmatic or mixed magmatic and meteoric origin (Stoffregen, 1987; White and Hedenquist, 1990; Arribas, 1995; Hedenquist et al., 1998). At Bowone and Binebase, the "ground preparatory stage" of intermediate and advanced argillic alteration was accompanied by gold mineralization in the form of pyrite (Pyrite I) containing "invisible gold". This gold represents between 30% and 50% of the hypogene mineralization, and occurs with appreciable copper and silver, also "invisible" in pyrite. It

Table II-6 Table showing physicochemical conditions for each alteration facies as determined by mineral stability and $\delta^{34}S$ values for Py I and Py II.

	T	pH	$\log fO_2$	$\Delta \log fO_2$ (HM buffer)
IA I	260-275	3-4	-34 to -31	+1 to +3
IA II	>265	4-6	-35 to -33	-1 to +2
AA I	275-330	0.5-4	-28 to -27	+2 to +4
AA II	270-275	0.5-4	-28 to -27	+1 to +4
AA III	250-270	0.5-4	-33 to -32	+1 to +3

therefore follows that gold and the other metals must also have been introduced into the deposits in the form metallic species dissolved in vapour. Higher grade veins and replacement bodies of Pyrite II and enargite were introduced later, but likely drew their metals from vapour, given the similar trace element and isotopic compositions of Pyrite I and II.

Evidence that metals can be transported in high concentrations in magmatic vapours has been provided by analyses of the compositions of vapor inclusions, which have yielded concentrations at the ppm and in some cases percentage level (Audétat et al., 1998, 2008; Ulrich et al., 1999; Williams-Jones and Heinrich, 2005; Seo et al., 2009). In the case of Cu and gold, the metals have even been reported to partition preferentially into the vapour phase (Heinrich et al., 1992; Ulrich et al., 1999; Audétat et al., 2000), although recently this evidence for Cu has been placed in question by experiments showing that it readily diffuses through quartz, the mineral hosting these inclusions (Lerchbaumer and Audétat, 2012). Because of its large radius, however, diffusion is not a factor in the concentration of gold in quartz-hosted vapour inclusions.

In addition to the fluid inclusion and volcanic gas data, there is also evidence from experiments that copper and precious metals can be transported in appreciable concentrations in aqueous vapour (Migdisov et al., 1999, n.d.; Archibald et al., 2001, 2002; Hurtig et al., 2012). Indeed, Migdisov et al. (accepted for publication) have shown for Ag, that at the conditions of entrapment of the vapour inclusions referred to above, these concentrations are similar to those reported for the inclusions. They have shown, moreover, that this metal solubility increases exponentially with increasing fH_2O (see also Hurtig et al., 2012). At the temperature and pressure predicted for formation of the Bowone and Binbase deposits, i.e., close to those of the H_2O vapour-liquid boundary and critical point, conditions would have been optimal for the transport of gold in ore-forming concentrations by magmatic vapour. Other studies have documented gold mineralization associated with early advanced argillic alteration (e.g., Muntean et al., 1990; Voudouris, 2011), but this is the first time that "invisible gold" in pyrite in an ore deposit has been attributed to a condensed vapour (our Py I). However, the phenomenon has recently been observed to be occurring in the crater of Kawah Ijen volcano, also located in Indonesia (Scher et al., in press). Auriferous pyrite from Kawah Ijen shows similar patterns of distribution of As, Au, Ag and Cu to those of Py I and Py II at Bowone and Binebase (Fig. 24). Moreover, the Kawah Ijen pyrite has similar Au/Cu and Au/Ag ratios to Py I and Py II, although the absolute metal concentrations in the Bowone and Binebase pyrite are much higher; the As concentration range for Kawah Ijen is similar to that for Bowone and Binebase.

Ore Deposition

For the reasons presented above, we propose that the fluid responsible for the formation of the Bowone and Binebase deposits was a vapour. However, we consider it likely that this vapour encountered a physicochemical barrier, such as the water table or an impermeable cap rock (this seems to have been the case for the deeper mineralization at Bowone (Figs. 4 and 10), and condensed to a low pH liquid from which the ore mineral (pyrite) precipitated or formed by replacement of primary iron-bearing minerals. According to this interpretation, the ore metals were transported in the vapour as hydrated species, e.g., $MeCl{\bullet}H_2O$ or $MeHS{\bullet}H_2O$ (Migdisov et al., 1999, accepted for publication.; Williams-Jones and Heinrich, 2005; Zezin et al., 2011b), whereas after condensation of the vapour to liquid, they would have been transported as charged

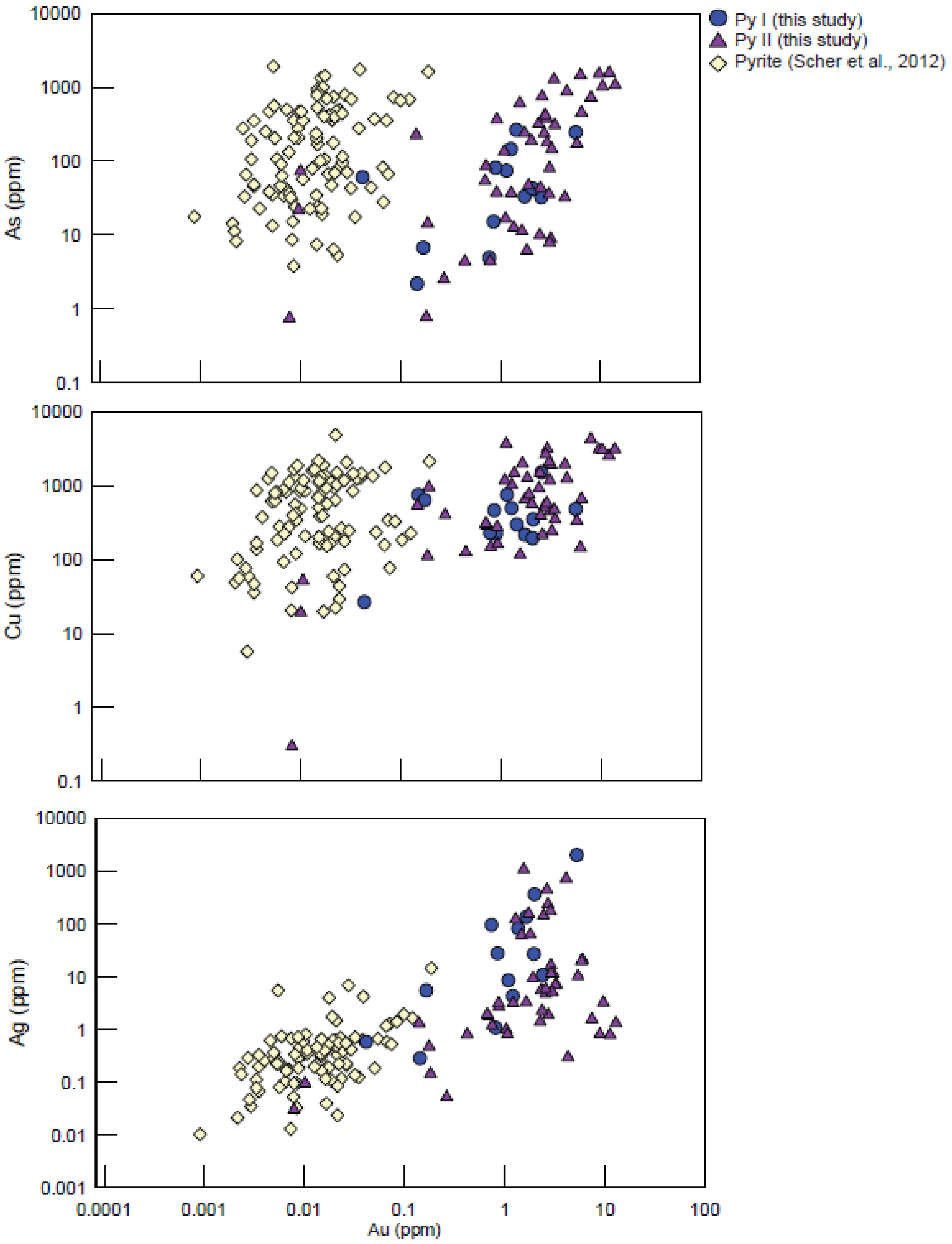

Figure II-24 Log-log plots of the composition of pyrite from Kawah Ijen, an actively-forming high sulphidation epithermal system (Scher et al. (in press)) and this study.

or neutral aqueous species like $MeCl_2^-$ or $MeHS^o$ (Crerar and Barnes, 1976; Gammons and Barnes, 1989; Zotov et al., 1990; Gammons and Williams-Jones, 1997; Xiao et al., 1998; Mountain and Seward, 2003; Stefánsson and Seward, 2003, 2004; Williams-Jones et al., 2009).

If saturation of the fluid with the metal had occurred, ore deposition would have been controlled by reactions such as

$$Au(HS)^o + \frac{1}{2} H_2O_{(l)} = Au_{(s)} + H_2S + \frac{1}{4} O_2 \qquad (1)$$

$$AuCl_2^- + H_2O_{(l)} = Au_{(s)} + 2HCl_{(aq)} + \frac{1}{2} O_{2(g)} \qquad (2)$$

However, as native gold does not occur in the deposits and, instead, the gold occurs with other metals as invisible particles in pyrite or within the structure of that mineral, it follows that gold was undersaturated in the liquid. Copper on the other hand, although present in high concentrations in pyrite, also occurs as enargite, albeit only in the later stages of the mineralization.

Deposition of gold and other metals is interpreted to have occurred as a result of their adsorption onto the faces of pyrite during crystal growth. This deposition began at the onset of advanced argillic alteration with the precipitation of Pyrite I and continued with the precipitation of Pyrite II. Adsorption of gold onto pyrite has been proposed previously as a mechanism to explain the occurrence of “invisible gold” in other epithermal deposits (e.g. Simon et al., 1999; Wilder and Seward, 2002; Pals et al., 2003). It also has been investigated experimentally at ambient pressure and temperature for pH values from 2 to 10. Results of these experiments for pyrite having negatively charged crystal faces (pyrite can also have positively charged faces, if arsenic-bearing; Favorov et al., 1974; the effects of high concentrations of Cu on the surface properties of pyrite are unknown) show that over 90% of the gold in solution is adsorbed at a pH <5 (Widler and Seward, 2002).

Pyrite I is in textural equilibrium with the advanced and intermediate argillic alteration, and accounts for 60% of the gold in the deposit with an average grade of 1.1 ppm Au, 33 ppm Ag and 0.4 wt% Cu. The texturally complex Pyrite II contains an average of 3ppm Au, 80.6 ppm Ag and 1.1 wt% Cu, and accounts for most of the remaining gold. Some gold and even more silver are present in enargite (0.53 ppm Au; 102 ppm Ag).

Insights into the conditions favourable for the uptake of gold by pyrite in the Bowone and Binebase deposits were afforded by the presence of both growth and sector zoning in Pyrite II. The latter zoning reflects differences in the concentrations of elements on two non-equivalent faces within single growth zones, and enables partition coefficients to be calculated for these faces that record the relative changes in physicochemical conditions during crystal growth (Van Hinsberg and Schumacher, 2007). We have used sector and growth zones in Pyrite II (see Chapter III for a full description of the method and its limitations) to determine the conditions favourable for the incorporation of gold and other trace elements into pyrite. The element concentrations in two adjacent non-equivalent faces were measured for a series of growth zones and the partition coefficients (Kd) were calculated (see Chapter III for a detailed discussion of the applicability of this technique to pyrite). We observed that the highest gold concentrations coincided with periods of growth marked by relatively constant Kd, and lower gold values coincided with sharp increases and decreases in the Kd (Fig. 25). Thus, in contrast to mineralization produced by saturation of an ore mineral, which is favoured by rapid changes in the physicochemical conditions due to processes like mixing and boiling, concentration of gold

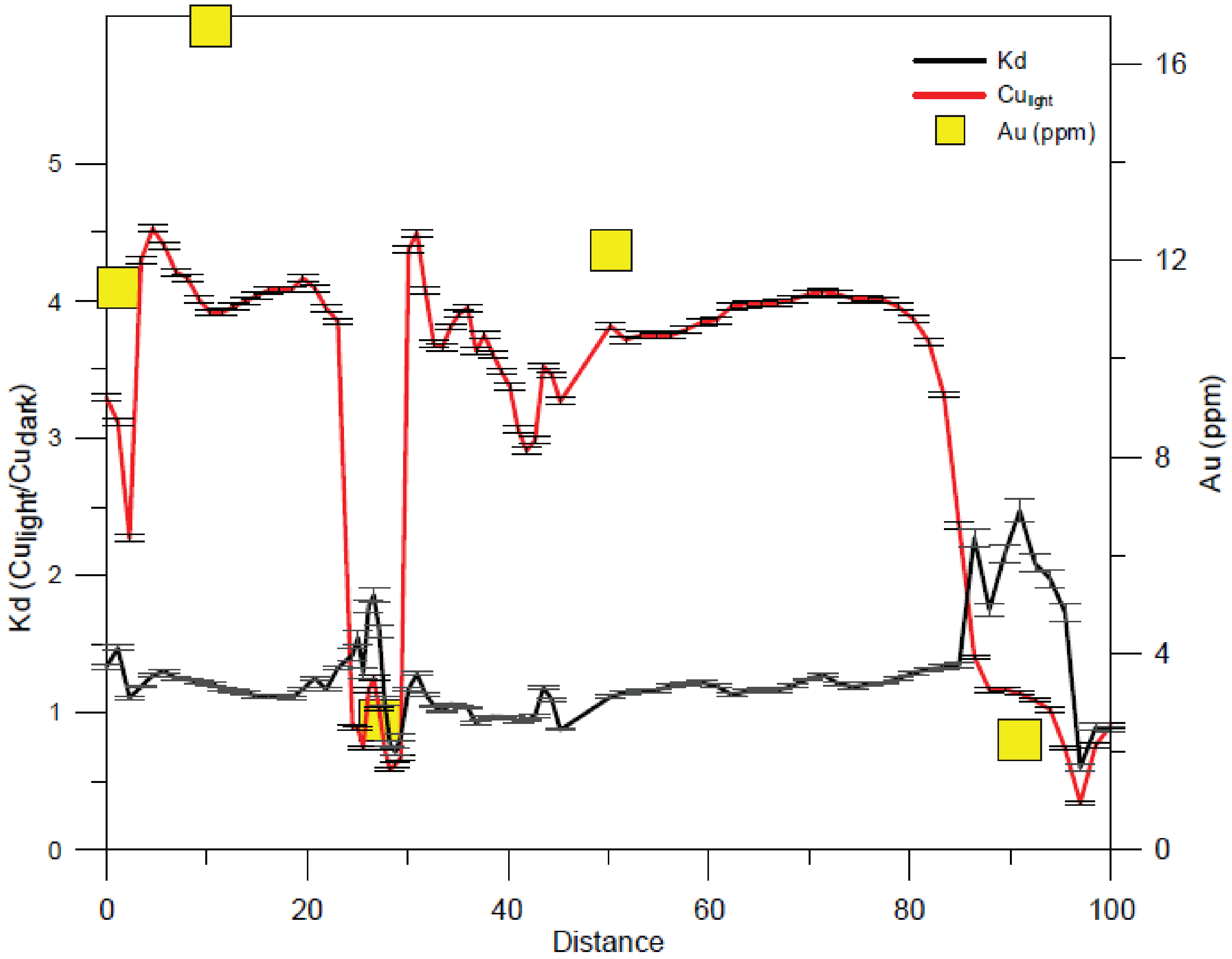

Figure II-25 Plot of Kd vs. % distance from core to rim for a single pyrite crystal (BID34-84). In black is the variation in Kd: an increase in inferred to reflect an decrease in temperature and a decrease an increase in temperature; see Chapter III for additional explanation. The yellow squares represent analysis by LA-ICPMS of the gold concentration with the width of the square showing the diameter of the pit in relation to the growth zones; the Au concentration is indicated by the vertical scale on the right hand side of the diagram. The highest gold concentrations correspond to regions where the Kd is stable, whereas lower gold concentrations correspond to intervals over which there is a rapid change in Kd values; Cu concentrations (Chapter III) show the same behaviour.

in the Bowone and Binebase deposits was favoured when physicochemical conditions were relatively stable.

Incorporation of Trace Elements in Pyrite

Unlike many examples of deposits in which pyrite contains “invisible gold”, the pyrite in the Bowone and Binbase deposits only contains trace quantities of As (Table 3). Despite this low concentration of As relative to that in auriferous pyrite from other deposits (e.g., Reich et al., 2005), Au concentration correlates positively with the concentration of As (Fig. 17, 20 and 24); the latter is a hundred times higher than the concentration of Au in Py I and Py II. This correlation suggests that Au+As substituted for Fe, as has been proposed previously for other deposits containing invisible gold in pyrite (Cook and Chryssoulis, 1990; Fleet et al., 1993; Huston et al., 1995). It is also possible, however, that some or all of this gold occurs as nanoparticles within the pyrite. Although our data do not allow us to determine whether the gold was incorporated into the pyrite structure or is present as nanoparticles, Reich et al. (2005) have observed that in pyrite with an Au/As ratio over 0.02, gold occurs as micro-inclusions, whereas if the ratio is lower than this, it is substituted into the pyrite structure. The average Au/As ratio for pyrite in the Bowone and Binebase deposits is 0.019, suggesting that much of the gold may have been incorporated in the structure of this mineral.

Incorporation of Au in the pyrite structure is also favoured by the presence of Te, which substitutes for the smaller S ion, thereby expanding the lattice and providing space for the large Au ion (Chouinard, et al., 2005a; Bi et al., 2011). The presence of appreciable Te (concentrations of Te are tens (Py I) to a hundred (Py II) times higher than that of Au) and its positive correlation with Au (Fig. 20) suggests that this substitution was also important in the uptake of Au.

Although the As concentration in Pyrite II is low compared to that of auriferous pyrite elsewhere, the Cu concentration is anomalously high, up to 6 wt % Cu (Appendix X). Significantly, most of the other examples of auriferous pyrite with high copper contents are also from high sulphidation epithermal deposits, e.g., Pascua Lama (up to 1.5 wt.% Cu; Chouinard et al., 2005a), Pueblo Viejo (up to 3.0 wt.% Cu; Deditius et al., 2011) and Chelopech (up to 4.5 wt.% Cu; Pacevski et al., 2008). Moreover, the exceptions, such as pyrite from the Coka Marin polymetallic deposit (up to 8 wt. % Cu; Pacevski et al., 2008) have many characteritics of high sulphidation deposits.

It has been shown that copper can be incorporated in the pyrite structure as nanoparticles and by substitution for Fe, even within a single ore deposit such as Peublo Viejo (Huston et al., 1995; Oberthür et al., 1997; Deditius et al., 2011). At Bowone and Binebase, it is also likely that Cu was incorporated by a combination of both mechanisms. In comparison, some studies have shown that Cu-rich pyrite is the result of recrystallization of Cu-phases (Pacevski et al., 2008), but we know this is not the case because of the well-documented growth zoning that records the growth history of the crystals.

There is no agreed upon mechanism to explain the rare and anomalous Cu concentrations in pyrite. Some researchers have suggested oxidation of aqueous Cu^+ and direct substitution of Cu^{2+} for Fe^{2+} (e.g., Chouinard et al., 2005; Pacevski et al., 2008) accompanied by the incorporation of other trace elements to cause distortion of the lattice (e.g., Radcliff and McSween, 1970). In any case, it seems likely that the highly oxidizing conditions that are characteristic of high sulphidation deposits play a role in the incorporation of Cu in the pyrite structure.

The reason for the high concentration of Cu in the pyrite at Bowone and Binebase, and whether it is incorporated in the pyrite structure or occurs as nanoparticles is unknown. However, it seems likely that the mechanism controlling its incorporation was similar to that in other high sulphidation epithermal deposits and that this mechanism takes advantage of the similar chemical behaviour of copper and gold, and the high concentration of Cu in the fluid forming these deposits.

Genetic Model

We propose that the metals forming the Bowone and Binebase deposits originated from an oxidizing felsic magma that was emplaced at high crustal levels and exsolved a low density supercritical fluid (that subsequently evolved to vapour) into which the metals partitioned preferentially. The gold and other metals were transported as hydrated species that ascended through the volcanic pile via fractures and zones of enhanced permeability to a depth between 920 and 1260 m, where the vapour condensed at a temperature between 250 and 340°C to form an acidic liquid with a pH of ~2.5; fO_2 ranged up to four log units above the hematite-magnetite buffer.

The acidic condensate altered the host andesite, replacing primary mafic minerals, such as hornblende, biotite and magnetite, with auriferous Py I (sulphidation), and converting feldspars to an advanced argillic assemblage that includes kaolinite, pyrophyllite, alunite, natroalunite, and dickite. At lower fluid/rock ratios, the alteration led to an intermediate argillic I alteration assemblage of kaolinite, quartz, and pyrite, and a distal intermediate argillic II alteration assemblage of illite, quartz and pyrite. The alteration also created porosity through the dissolution of minerals. During alteration, all major elements, except for Zr and Ti were depleted proximal to the main alteration/mineralization conduits (Al and particularly Si experienced minor depletion) (Fig. 16). Iron and all trace elements, except for the REE, Rb and Cs were enriched, in some cases by orders of magnitude relative to their orginal abundance.

Auriferous Py II was deposited in veins and exploited the secondary porosity. These same veins were fractured and the fractures later filled by barite and enargite. Rare, late auriferous (electrum) barite-base metal (sphalerite and chalcopyrite) veins formed at Binebase.

Pyrite I (associated with advanced and intermediate alteration) and Pyrite II precipitated under conditions for which metals, including gold, were undersaturated in the fluid and were adsorbed onto the surfaces of the growing pyrite crystals, to be incorporated in the pyrite either as a solid solution or as nanoparticles. Some gold and silver was incorporated in enargite by the same mechanisms. The Bowone and Binbase deposits were subsequently exhumed and partially oxidized, creating an upper zone of enriched oxide ore and exposing lower-grade hypogene ores (Fig. 26)

Conclusions

Textural and geochemical observations provide compelling evidence that the Bowone and Binebase gold deposits were the products of an acidic condensed magmatic vapour. This fluid produced the advanced argillic and intermediate argillic alteration that is characteristic of high sulphidation epithermal systems and deposited gold, as well as copper and silver, either within the structure of pyrite or as nanoparticles within this mineral. As the fluid did not deposit native gold or electrum (except in very late veins at Binebase), we conclude that it was undersaturated in respect to these metals. Instead of precipitating directly from the fluid, gold and silver were concentrated by adsorbing onto the surfaces of growing pyrite (and to a much lesser extent

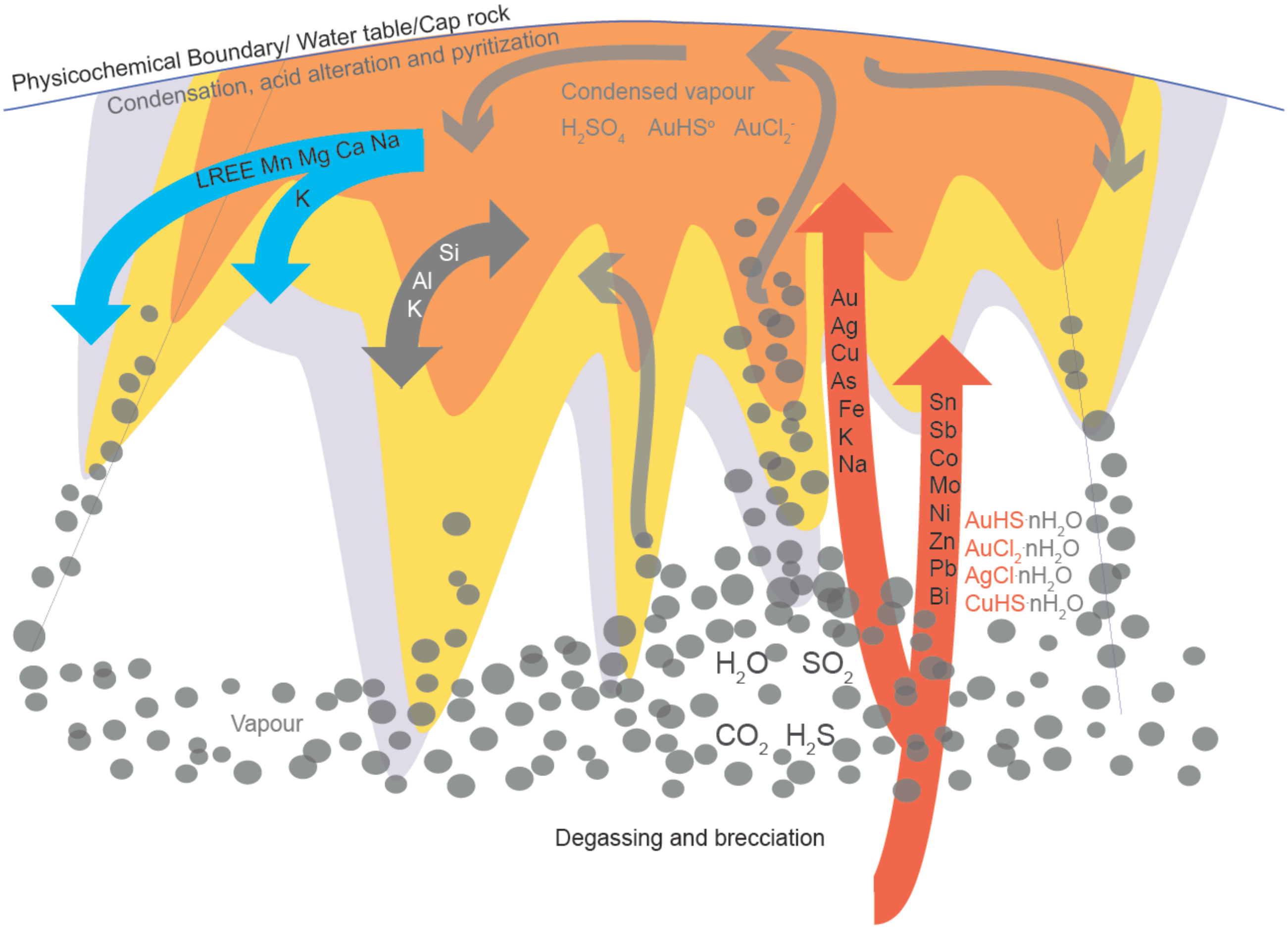

Figure II-26 Schematic diagram showing the transition from vapour to condensed liquid in the alteration and Au-Ag-Cu depositional environment at Bowone and Binebase with the gas species (H_2O, SO_2, CO_2 and H_2S) and addition of metals (in red) and loss of major elements and LREEs (blue) enargite) crystals, where they either formed nanoparticles or substituted for iron in the structure of the mineral. Much of the auriferous pyrite formed during advanced and intermediate argillic alteration as a result of the sulphidation of primary mafic minerals (significant Fe was also introduced by the fluid). Auriferous pyrite (Py II), formed later, filling fractures in the earlier formed pyrite, and was joined even later by Au-Ag-bearing enargite that deposited in reopened pyrite II veins. Although the later pyrite is richer in Au than Pyrite I and the enargite richer in Ag than both pyrite generations, the precious metals in Pyrite II and enargite are also “invisible” in these minerals, and as in pyrite I are interpreted to have concentrated from a condensed magmatic vapour by adsorption during crystal growth. The Bowone and Binebase deposits represent an important, newly recognized subclass of high sulphidation deposit formed exclusively from a condensed magmatic vapour, and record a mineralizing process that likely has contributed to the formation of many other high sulphidation deposits.

Chapter III

Physicochemical Inferences from Growth and Sector Zoning in Pyrite of the Bowone and Binebase Au (Ag-Cu) High-Sulphidation Epithermal Deposits, Indonesia

Julia J. King[1], A.E. Williams-Jones[1], Vincent van Hinsberg[1]

(1) Department of Earth and Planetary Sciences, McGill University, 3450 University Street,
Montreal, Quebec, Canada, H3A 2A7

Abstract

Pyrite is a common mineral in a large variety of geologic environments, including those of metallic mineral deposits, and forms over a wide range of physicochemical conditions. If, as is frequently reported (Radcliff and McSween, 1970; Fleet et al., 1993; Craig et al., 1998; Krinov, 2008; Barker et al., 2009; Cook, Ciobanu, and Mao, 2009; Tauson et al., 2009) pyrite is compositionally zoned, changes in trace element concentrations between zones can be used to reconstruct the chemical evolution of the ore fluid, and potentially determine changes in physicochemical conditions, including temperature. Gold-bearing pyrite in the Bowone and Binebase high-sulphidation epithermal Au deposits on Sangihe Island, Indonesia, display evidence of both growth and sector zoning. Here we report the results of a study of pyrite from these deposits, and document the distribution of trace elements among growth and sector zones in this mineral with the goal of gaining insights into the physicochemical conditions of trace element uptake.

Compositional variations among growth zones in pyrite are controlled by changes in fluid composition, pressure and temperature. We have mapped trace element compositions for elements that are zonally distributed (Cu, Se, Te, Ni, Zn, As, Au, Ag) in the Bowone and Binebase pyrite. Copper is the dominant trace element and its distribution is strongly zoned; the average concentration is 0.83 wt.% and the maximum concentration 6.0 wt.%.

In addition to growth zoning, pyrite of the Bowone and Binebase deposits displays intense sector zoning, in which the above trace elements were taken up preferentially onto different crystallographic surfaces. Sector differences are also most evident for copper. Inter-sector partition coefficients for Cu were calculated for three pyrite crystals by measuring Cu

concentrations for adjacent sector zones over multiple growth zones from core to rim. In each case, relatively constant Kd values correlate with higher trace element concentrations. Whether the control on Kd is temperature, pH or some other parameter, the principal finding of this study is that the maximum uptake of Cu and other trace elements occurred when physicochemical conditions were stable (constant Kd)

Introduction

Pyrite (FeS_2) occurs in many ore- and non-ore-forming geological environments, and is stable over a wide range of temperatures (from atmospheric conditions to about 800°C and pressures greater than 8,000 bars (Kullerud and Yoder, 1959). The face-centered cubic structure can accommodate a variety of minor and trace (<1 wt%) elements, including Ag, As, Au, Bi, Cd, Co, Cu, Hg, Mo, Ni, O, Pb, Pd, Ru, Sb, Se, Sb, Sn, Te, Tl and Zn (Cook and Chryssoulis, 1990; Fleet and Mumin, 1997; Maddox et al., 1998; Ashley et al., 2000; Abraitis et al., 2004; Palenik et al., 2004; Chouinard, et al., 2005a; Reich et al., 2005). These elements can be present in solid solution (both stoichiometric and non-stoichiometric) and also in nano-inclusions that are invisible using an optical microscope or even a scanning electron microscope (Simon et al., 1999; Deditius et al., 2011; Su et al., 2011). As economic concentrations of “invisible gold” have been found in pyrite from ore deposits, much of the research that has been carried out on the minor and trace element chemistry has focussed on how gold is incorporated into the pyrite structure (e.g., Cook and Chryssoulis, 1990; Maddox et al., 1998; Hanlie et al., 1999; Chouinard et al., 2005a; Barker et al., 2009). This research has suggested that As, Cu,Te and Se may play an important role in gold incorporation through coupled substitution (Chouinard et al., 2005a; Reich et al., 2005).

Imaging and quantitative analysis of gold-bearing pyrite during the late 1980s helped identify substitution mechanisms and other means of incorporation of gold in pyrite (e.g., Chryssoulis et al., 1989; Fleet et al., 1989). More recently, imaging has been used to determine the spatial relationships of the gold to other trace elements (Cook and Chryssoulis, 1990; Fleet and Mumin, 1997; Maddox et al., 1998; Ashley et al., 2000; Steele et al., 2000; Chouinard et al., 2005a; Deditius et al., 2008, 2011b). With few exceptions, these studies have investigated pyrite formed under near-neutral pH conditions. Only the studies of (Einaudi, 1968; Chouinard et al., 2005; Pacevski et al., 2012) have considered pyrite formed in the extremely low pH environment of high-sulphidation epithermal gold deposits. Consequently, there is still a limited understanding of the uptake and incorporation of trace elements in pyrite in this environment.

In high-sulphidation epithermal deposits, the common trace elements in pyrite are Ag, As, Au, Cu, Se, Te (Einaudi, 1968; Chouinard et al., 2005; Pacevski et al., 2008). Although this mineral is reported to have elevated concentrations of As in some high sulphidation epithermal deposits, Cu is the most abundant minor element. For example, pyrite in the Chelopech high-sulphidation epithermal deposit (Bulgaria) contains up to 4.5 wt% Cu (Pacevski et al., 2008). The highest reported concentration of Cu thought to be in solid solution in pyrite, is 10 wt.% in the intermediate sulphidation, Nukundamu epithermal deposit, Fiji (Frenzel and Ottemann, 1967; Colley and Rice, 1975), followed by 8 wt% Cu in pyrite from the Coka Marin polymetallic deposit, Serbia (Pacevski et al., 2008). It is likely that Cu in the pyrite occurs as a solid solution and/or as nanoparticles of the native metal or sulphides including Fe-bearing varieties (Deditius et al., 2011; Pacevski, 2012). In either case, it is the differences in crystallography lead to differences in both nanoparticle and element sorption. The research reported here builds on the ideas presented in the papers referred to above, and uses trace element geochemistry, and strong sector and growth zoning to infer physicochemical conditions during trace element uptake by auriferous pyrite in the Bowone and Binebase high-sulphidation epithermal deposits on Sangihe Island, Indonesia.

A striking feature of the most auriferous pyrite in the Bowone and Binebase deposits is its strong growth and sector zonation, with the greatest compositional differences being in Cu concentration. These compositional features reflect differences in physicochemical conditions and partitioning of elements between adjacent non-equivalent faces, respectively. In principle, they can be used to make inferences about the conditions that promote the uptake of trace elements in during crystal growth. Growth zoning preserves a record of changes in temperature, pressure, chemistry, fO_2, and pH of the fluid as a series of compositionally different zones developed perpendicular to the growth direction (Reeder and Paquette, 1989) (Fig. 1). This style of zonation has been observed in many minerals and, for plagioclase, has been used to extrapolate the growth history of single crystals to the crystallization history of entire magma chambers (e.g., Anderson, 1984). In hydrothermal systems, zoned garnets have been used to constrain the evolution of complex fluid-rock systems (Crowe et al., 2008). Sector zoning reflects differences in the trace element compositions of coeval, adjacent non-equivalent faces (e.g., cubic vs. octahedral faces), and is less commonly reported than growth zoning; it has been observed in, amongst others, calcite, tourmaline, staurolite, arsenopyrite and pyrite (Hollister, 1970; Reeder, 1991; Vesselinov and Kerestedjian, 1995; van Hinsberg et al., 2011) (Fig. 1). This type of zoning develops within growth zones at the contact between a growing crystal and its host medium, and has been attributed to selective adsorption of elements due to kinetic differences (e.g., Tiller, 1986) and/or differences in the geometry of the non-equivalent faces

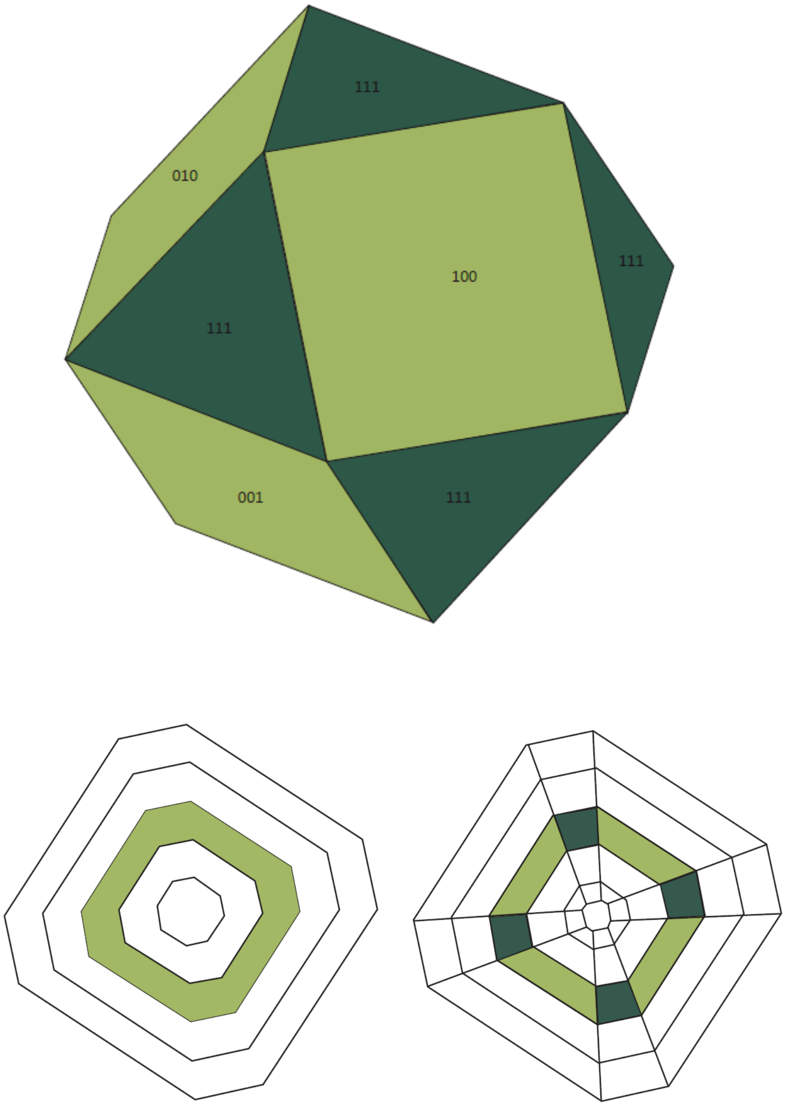

Figure III-1. Example of a pyritohedron cut parallel to the 001 face showing a) growth zoning and b) sector zoning between the octahedral and cubic faces.

(e.g., Hollister, 1970; Chakhmouradian et al., 2007a; Shtukenberg et al., 2009). In the case of pyrite, the preference is systematic, if poorly constrained, with Ag, As and Te concentrating selectively on the {111} face (Chouinard et al., 2005a). The difference in concentration of an element between two sectors allows an effective partition coefficient to be determined that depends on the conditions in the fluid at a given stage in the crystal growth (Rakovan et al., 1997; van Hinsberg and Schumacher, 2007; Shtukenberg et al., 2009). Sector zoned crystals can be produced by slow lattice diffusion (Watson and Liang, 1995) but diffusion is more likely to destroy sector zoning and given the primary growth zones and the young age of the deposit (likely <100 000 years), the sector zoning in the Bowone and Binebase deposits is interpreted to be primary.

Changes in the effective partition coefficient can be used to make inferences about growth rates, substitution mechanisms fluid compostion, and even temperature (van Hinsberg and Schumacher, 2007). As temperature increases and bonds become more flexible, and the lattice is less able to differentiate between elements at high temperatures. Consequently, for reasons similar to those governing the decrease in isotopic fractionation with increasing temperature, the trace element fractionation between two adjacent non-equivalent faces decreases with increasing temperature to a point at which the two faces are compositionally indistinguishable. The fractionation between the two non-equivalent faces is given by the partition coefficient (Kd) and, for tourmaline, has been shown to be dependent only on temperature (Henry and Dutrow, 1992; van Hinsberg et al., 2006) (Fig. 2). Thus, an increase in Kd between growth zones represents a decrease in temperature (non-equivalent faces are more selective), whereas a decrease in Kd represents an increase in temperature (non-equivalent faces are less selective). However, such

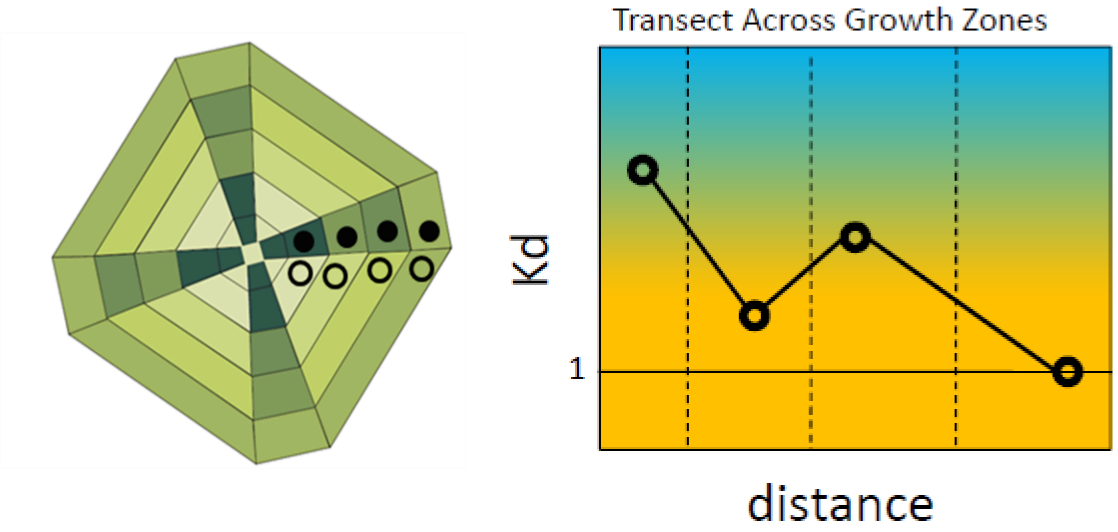

$$Kd = \frac{\text{element } X_{\bullet}}{\text{element } X_{\circ}}$$

Figure III-2. The relationship between crystallography and element fractionation. A) Schematic crystal showing sector and growth zoning – different shades of green represent different compositions. Within each growth zone, there are compostional differences between non-equivalent faces; a strong difference in the shade of green represents strong fractionation and a small differences little or no frationation. The shade differences between sector zones decrease away from the core, coresponding to decreaseing fractionation and, by inference, increased temperature. B) The corresponding Kd vs. distance from the core. Open and filled circles show analysis locations.

changes could also reflect differences in the selective adsorption of metals on the non-equivalent faces due to changes in other physicochemical conditions, and superimposed kinetic effects due changes in growth rate (Shtukenberg et al., 2009). Despite the uncertainty over the controls of sector zoning in pyrite, it is possible, nevertheless, to track Kd changes over the growth history of a crystal and relate them to general changes in physicochemical conditions. We have used the changes in Kd of growth- and sector-zoned pyrite in the Bowone and Binebase deposits to interpret the evolving physicochemical environment and elucidate its role in metal concentration.

Geologic Setting

The Bowone (BOD) and Binebase (BID) Au (Ag) deposits of south Sangihe Island, northern Sulawesi, Indonesia, have recently been identified as a subtype of the high sulphidation epithermal group of deposits in which gold is "invisible" in pyrite (King et al., in preparation). The two deposits are located 1km apart, and are hosted in recently emplaced volcaniclastic rocks. The hypogene zone of both deposits is dominated by advanced argillic and intermediate argillic alteration assemblages that include pyrite (Py I). Late, pyrite veins, massive bodies and drusy crystals cross-cut and overprint earlier, pyrite-rich, alteration. This later generation of pyrite, PyII, exhibits strong sector and growth zoning.

Pyrite II comprises morphologically varied massive pyrite with crystals up to 5mm wide, which appear brassy in hand sample and occur as veins, vug fillings, lenses and massive bodies. The morphologies are highly variable and their paragenesis is difficult to establish, given the many generations of pyrite that overprint and replace each other (Fig. 3). Pyrite II commonly infills cavities as sub-euhedral, drusy crystals that display strong growth and sector zoning.

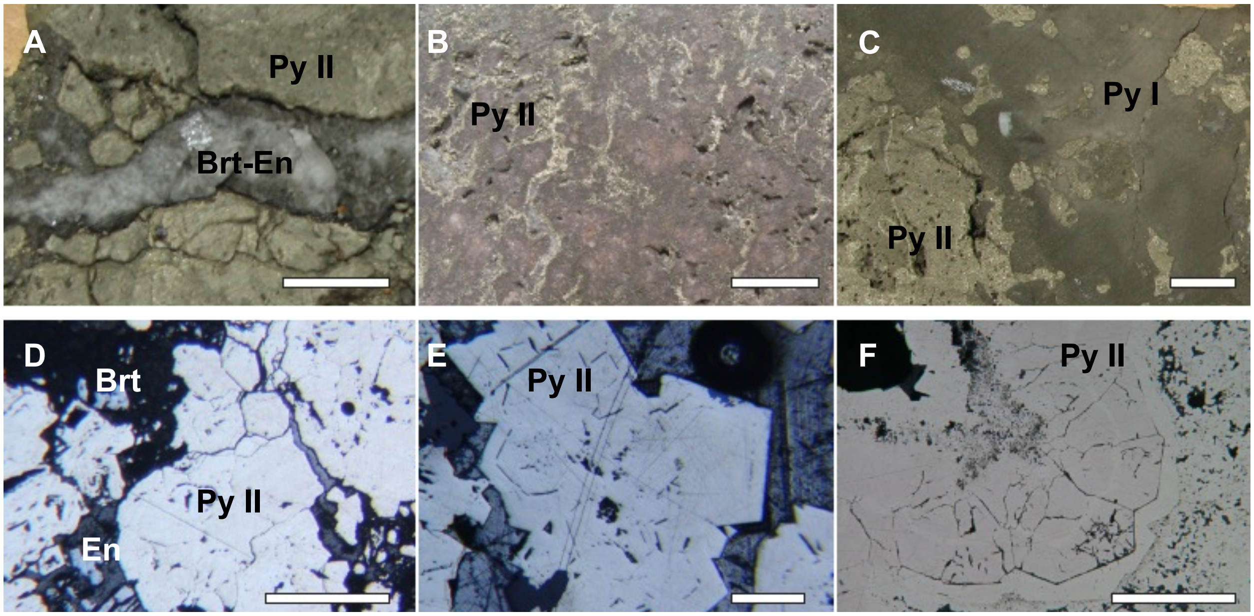

Figure III-3. Photographs of core showing A) a barite-enargite (Brt-En) vein crosscutting massive PyII, B) veinlets of brassy Py II, and C) massive Py II and Py I (dark grey). The scale is 1cm. Photomicrographs showing D) fractured Py II crystals in a matrix of barite, E) euhedral Py II infilling a vug, F) multiple generations of Py II. The scale is 1mm.

Methods

The composition of pyrite was analysed for Fe, S, Cu, As, Sb, Co, Ni, Zn, Se and Te in carbon-coated samples at McGill University using a JEOL 8900 electron microprobe (EMP) equipped with five wavelength dispersive spectrometers (WDS). The operating conditions were an excitation potential of 20 keV, a beam current of 50 nA and a spot-size of 2µm. Analyses were standardized using pyrite (Fe, S), chalcopyrite (Cu), AsNiCo (As, Ni, Co), CdTe (Cd, Te), sphalerite (Zn), stibnite (Sb) and AgSe (Se) supplied by CANMET.

Element maps were prepared of parts of polished thin sections that showed strong zonation in reflected light and in BSE images to aid in the selection of sector pairs for detailed analysis of partition coefficients. The maps for Cu, Fe, Se and As were prepared from carbon-coated samples at McGill University using the EMP referred to above. The operating conditions were an excitation voltage of 20 kV, an operating current of 90 nA, and a beam diameter of 2 µm. The counting time was 30 ms and the pixel size between 0.20 to 1.28 µm. If the maps showed evidence of sector zonation, high-resolution quantitative analyses of transects were made across each of the paired sector zones using the EMP. A BSE image was made after the quantitative analysis to show the location of the analysis spots. As the growth zones are almost invisible in BSE images, the original Cu element map and the BSEI showing the analysis spots were imported into GIS software, given an artificial coordinate system using pixel size, and were georeferenced to each other. The spot outlines were overlain on the detailed Cu element map showing individual growth zones, and each analysis pair was visually located (Fig. 4). The Kd for each zone was calculated using the method of van Hinsberg and Schumacher (2007). Given

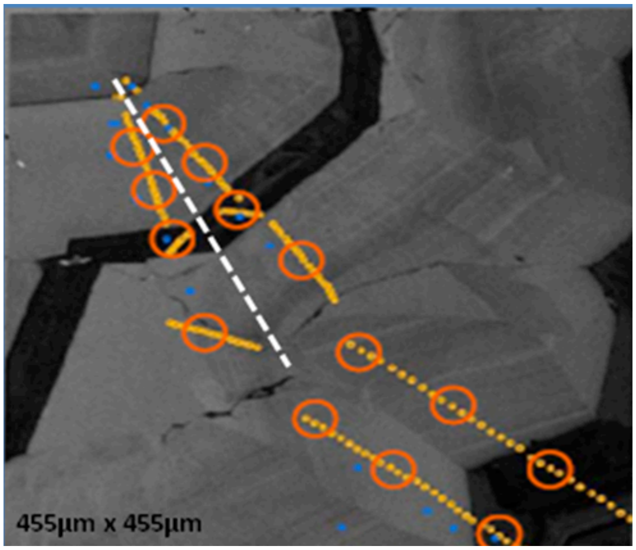

Figure III-4. Example of paired EMPA transects in BID34-84 showing analysis locations in orange taken through each sector zone with the “light” transect on the right and the “dark” on the left. The white dashed line represents the sector zone boundary. Individual pairs were matched by hand (red circles) and lines were normalized as described.

that it was not possible to identify the particular crystallographic orientation of the pyrite (e.g., the 111 and 100 faces, Chouinard et al., 2005a and Pacevski et al., 2012), the Kd for each element was calculated by taking the concentration of that element in the sector zone with the highest Cu concentration (and thus brighter or "light" in the element maps) and dividing it by the corresponding element concentration for the adjacent "dark" sector.

Samples and Analysis

Petrography

Sector zoning is commonly too subtle to observe under reflected light or even in BSE images but can be clearly seen in maps showing the distribution of copper, which is the element most strongly partitioned between the two faces. Several different styles of sector zoning were observed, three examples of which were analysed quantitatively using the electron microprobe. One of these sector pairs is in a brecciated pyrite crystal aggregate located at the centre of a barite-enargite vein in sample BOD3-97 from the Bowone deposit (Figs. 5A-D). Images of this pair are presented in Figs. 5C, D and represent a section through a euhedral PyII crystal forming part of a complex aggregate of similarly zoned pyrite crystals. The crystal displays strong regular concentric growth zoning with rare defects or breaks in the zonation. This crystallographic continuity shows that the texture formed during crystal growth. The sector zoning occurs between two non-equivalent faces related by a 3-fold rotation axis.

The second sector pair analysed is in sample BID32-16 from the Binebase deposit, and is in a crystal that forms part of a drusy vug-filling aggregate comprising multiple generations of zoned

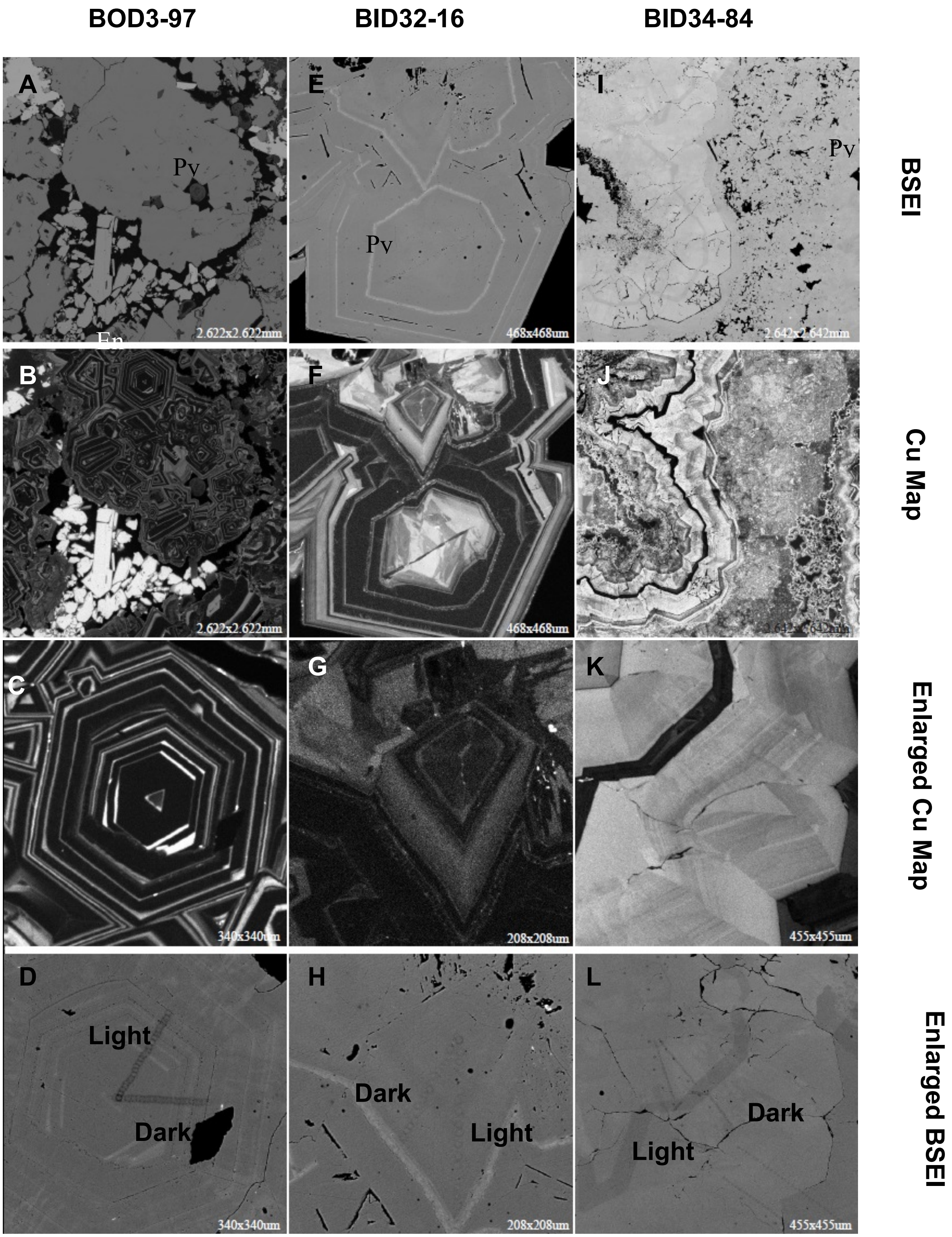
BOD3-97
BID32-16
BID34-84
BSEI
Cu Map
Enlarged Cu Map
Enlarged BSEI
A
Py
En
2.622x2.622mm
E
Py
468x468um
I
Py
2.642x2.642mm
B
2.622x2.622mm
F
468x468um
J
2.642x2.642mm
C
340x340um
G
208x208um
K
455x455um
D
Light
Dark
340x340um
H
Dark
Light
208x208um
L
Dark
Light
455x455um

Figure III-5 Images of three pyrite samples (BOD3-97, BID32-16 and BID34-84) displaying growth and sector zoning. Row 1 (A, E and I) shows BSE images of each sample; evidence of zoning is weak. Row 2 (B, F and J) illustrates the distribution of Cu for the same field of view as A, E and I. These maps show that Cu in the pyrite crystals is distributed in strongly contrasting complex growth and sector zones (the lighter shades of grey correspond to higher Cu concentrations). Row 3 (C, G, and K) shows high-resolution Cu element maps of the specific crystals in images B, F and J that were subject to quantitative EMP analysis (see text for further detail). Row 4 (D, H, and L) provides BSE images of the fields of view of images C, G, and K showing the location of the analytical spots used to calculate Kd values. The spots in each image are distributed along two transects at right angles to the growth zones in adjacent sectors. Values of Kd were obtained by dividing concentrations in the "light" sectors by the corresponding concentrations in the adjacent "dark" sectors. Sample BOD3-97 shows strongly zoned aggregates of pyrite (Py) surrounded by euhedral enargite (En) crystals. The sector zoning in the analysed crystal (C) is visible about a 3-fold axis in growth zones near its centre. Sample BID32-16 comprises drusy pyrite crystals infilling a vug. Image F reveals a complex history of growth zoning, sector zoning and intersectoral zoning. Sector zoning is evident as a cross at the centre of the analysed crystal (G). Sample BID34-84 displays colloform growth zonation in pyrite overgrown by massive, porous and unzoned pyrite (I and J). In the former, sector zoning is evident as wedge shapes of contrasting shades of grey that cross growth bands (J and K).

crystals overgrowing complex cores (Figs. 5E-H). Both sector and inter-sectoral zoning were observed; intra-sectoral zoning is evident in the complexly zoned copper-rich cores. The sector zones analysed are at the centre of a trapezoid located between two non-equivalent faces, creating a cross pattern (Figs. 5G, H).

The final pair considered in this study is in sample BID34-84, also from the Binebase deposit, and is of drusy, colloform pyrite (Figs. 5I-L). Growth zoning is visible as a series of semi-continuous, parallel, micron-scale bands with variable Cu concentrations. Sector zoning is evident within the growth zones as contrasting wedges between the non-equivalent faces, which vary in Cu concentration according to the growth zone in which they are located (Figs. 5K, L). However, because of the lack of symmetry, it is not possible to determine the number of non-equivalent crystallographic faces.

Chemistry

Quantitative analysis for Cu, As, Te, Se, Fe and S in parallel transects through adjacent non-equivalent faces across each growth zone provided information on the absolute concentrations of these elements in the different sectors and growth zones of samples BOD3-97, BID32-16 and BID34-84, and enabled calculation of Kd values. These compositional data are reported in Table 1.

Sample BOD3-97

All the growth zones in the hexagonal section of the pyrite crystal in BOD3-97 (Fig. 5C) display evidence of fractionation of Cu between non-equivalent faces. Copper concentrations reach up to 6.00 wt.% (among the highest reported in pyrite anywhere) in the “light” sector, and up to 2.02

Table III-1 Concentrations of trace elements in adjacent dark and light sectors of pyrite.

BID32-16

Dark (wt %)								Light (wt %)							
Point	Cu	As	Ni	Se	Te	Fe	S	Point	Cu	As	Ni	Se	Te	Fe	S
247	0.61	0	0	<0.028	0	45.78	52.87	227	0.507	<0.025	0	<0.028	0	46.22	53.51
248	1.105	<0.025	0	<0.028	<0.015	45.58	52.75	228	0.437	<0.025	<0.001	<0.028	0	46.30	52.94
249	0.518	0	0	<0.028	0	46.17	52.98	229	0.404	<0.025	0	<0.028	0	46.38	53.46
250	0.612	0	0	<0.028	<0.015	46.13	53.06	230	0.509	<0.025	<0.001	<0.028	<0.015	46.16	53.31
251	0.579	<0.025	0	<0.028	0	46.15	53.29	231	0.705	0	0	<0.028	<0.015	46.03	53.16
252	0.565	0	0	<0.028	0	46.13	53.14	232	0.819	0	0	0	0	45.87	52.93
253	0.583	<0.025	<0.001	<0.028	<0.015	46.16	53.24	233	0.267	0	0	<0.028	0	46.44	53.24
254	0.431	<0.025	0	0	<0.015	46.23	52.90	234	0.266	<0.025	<0.001	<0.028	<0.015	46.43	53.11
255	0.585	<0.025	<0.001	<0.028	0	46.14	52.88	235	0.727	0	0	0	0	45.96	53.16
256	0.45	<0.025	0	0	0	46.31	53.02	236	1.474	<0.025	0	<0.028	0	45.32	53.19
257	0.773	0	0	<0.028	0	45.98	53.17	237	1.849	0	0	<0.028	<0.015	44.90	53.16
258	1.161	0	0	<0.028	0	45.58	53.09	238	1.694	0	<0.001	<0.028	<0.015	45.13	53.06
259	1.742	<0.025	0	<0.028	0	44.93	52.88	239	1.638	<0.025	0	<0.028	0	45.13	53.30
260	1.599	0	0	<0.028	<0.015	45.17	53.05	240	1.423	0	<0.001	0	0	45.28	53.07
261	1.401	<0.025	<0.001	<0.028	0	45.33	52.48	241	1.15	<0.025	0	<0.028	0	45.63	53.12
262	1.082	0	<0.001	<0.028	<0.015	45.73	52.92	242	0.584	0	<0.001	<0.028	0	46.13	53.05
263	0.899	0	0	<0.028	0	45.85	53.25	243	0.08	0	<0.001	0.049	<0.015	46.55	53.37
264	0.13	0	0	0.039	0	46.64	52.87	244	0.143	0.184	0	0	<0.015	46.13	53.26
265	0.396	0.192	<0.001	0	0	45.81	53.06	245	1.07	0.323	0	<0.028	<0.015	44.64	52.57
266	0.138	0.603	<0.001	0.03	<0.015	44.86	52.94	246	0.556	0.531	0	0.039	0.05	44.20	53.16
ave	**0.768**	**0.066**	**0.000**	**0.014**	**0.000**	**45.83**	**52.99**	**ave**	**0.815**	**0.087**	**0.000**	**0.015**	**0.004**	**45.74**	**53.16**
std dev	**0.449**	**0.178**	**0.000**	**0.019**	**0.000**	**0.47**	**0.19**	**std dev**	**0.549**	**0.173**	**0.000**	**0.023**	**0.014**	**0.67**	**0.20**
min	**0.130**	**0.000**	**0.000**	**0.000**	**0.000**	**44.86**	**52.48**	**min**	**0.080**	**0.000**	**0.000**	**0.000**	**0.000**	**44.20**	**52.57**
max	**1.742**	**0.603**	**0.000**	**0.039**	**0.000**	**46.64**	**53.29**	**max**	**1.849**	**0.531**	**0.000**	**0.049**	**0.050**	**46.55**	**53.51**

BOD3-97

Dark (wt %)								Light (wt %)							
Point	Cu	As	Ni	Se	Te	Fe	S	Point	Cu	As	Ni	Se	Te	Fe	S
202	0.481	0	<0.001	<0.028	<0.015	45.68	52.62	177	0.569	<0.025	<0.001	0	0	45.99	52.98
203	0.56	0	<0.001	0	<0.015	45.82	52.97	178	0.527	0	0	0	0	46.04	53.17
204	1.266	0	0	<0.028	<0.015	45.16	53.18	179	0.441	0	<0.001	<0.028	<0.015	46.25	53.12
205	0.026	<0.025	<0.001	0	<0.015	46.67	53.22	180	1.868	0	0	0	0	44.66	52.85
206	0.015	0	0	0	0	46.44	53.05	181	0.09	<0.025	<0.001	0	<0.015	46.21	52.93
207	0.021	<0.025	0	0	0	46.57	52.99	182	0.014	0.033	<0.001	0	0	46.31	53.29
208	0.009	0	0	0	0	46.69	53.19	183	0.012	<0.025	0	0	0	46.25	53.17
209	<0.007	0	<0.001	0	0	46.63	53.30	184	0.015	<0.025	<0.001	<0.028	<0.015	46.46	53.10
210	0.009	<0.025	<0.001	0	<0.015	46.46	53.09	185	0.016	0.028	<0.001	<0.028	<0.015	46.51	53.35
211	0.013	0	0	0	0	46.42	53.31	186	0.012	0.036	<0.001	<0.028	0	46.29	53.32
212	<0.007	<0.025	<0.001	0	0	46.38	53.10	187	0.024	<0.025	0	0	0	46.55	53.05
213	0.014	<0.025	<0.001	0	0	46.60	53.12	188	0.044	0	<0.001	0	0	46.50	53.31
214	0.448	0	0	0	0	46.05	52.94	189	0.643	<0.025	0	<0.028	<0.015	45.89	53.34
215	0.033	0	0	<0.028	0	46.53	52.91	190	6.001	<0.025	<0.001	<0.028	<0.015	40.62	52.46
216	0.034	<0.025	0	0	0	46.47	52.94	191	0.168	<0.025	<0.001	<0.028	<0.015	46.09	52.98
217	0.61	<0.025	<0.001	0	0	45.86	53.05	192	0.061	0	0	<0.028	<0.015	46.36	53.31
218	0.055	<0.025	0	0	0	46.47	53.03	193	4.769	<0.025	0	0	<0.015	41.88	52.99
219	0.064	<0.025	0	0	0	46.26	53.30	194	0.163	0.035	<0.001	<0.028	0	46.50	53.03
220	0.873	0	0	0	0	45.59	53.09	195	0.123	0.039	0	<0.028	<0.015	45.80	53.28
221	2.021	0	<0.001	<0.028	0	44.60	53.17	196	1.374	<0.025	0	0	<0.015	45.36	52.86
222	0.791	0.127	0	0	0	44.68	53.01	197	0.494	<0.025	<0.001	<0.028	0	45.93	52.96
223	0.022	0	0	0	0	46.48	53.27	198	0.426	0.123	0	0	<0.015	44.69	52.96
224	0.108	0.193	0	0	0	45.66	53.49	199	0.065	<0.025	<0.001	<0.028	0	46.38	52.90
225	1.181	0	<0.001	<0.028	0	45.36	52.94	200	0.288	0.124	0	0	0	45.47	52.90
226	0.433	0.111	0	0	0	45.11	53.42	201	0.543	<0.025	<0.001	<0.028	<0.015	46.10	53.23
ave	**0.395**	**0.027**	**0.000**	**0.000**	**0.000**	**46.02**	**53.11**	**ave**	**0.750**	**0.035**	**0.000**	**0.000**	**0.000**	**45.64**	**53.07**

BID34-84

Dark (wt %)								Light (wt %)							
Point	Cu	As	Ni	Se	Te	Fe	S	Point	Cu	As	Ni	Se	Te	Fe	S
d.l.	0.007	0.025	0.001	0.028	0.015	0.30	0.20	d.l.	0.007	0.025	0.001	0.028	0.015	0.30	0.20
7	2.478	0.171	0.086	0.160	0.109	41.67	52.74	32	3.297	b.d.	0.052	0.168	b.d.	42.23	52.86
8	2.373	0.156	0.082	0.150	0.105	41.47	52.32	33	3.108	b.d.	0.048	0.158	b.d.	42.52	52.89
9	1.107	0.045	b.d.	0.034	0.032	45.14	53.20	34	2.214	b.d.	0.022	0.087	b.d.	44.07	53.06
10	3.467	0.197	0.097	0.160	0.154	40.42	52.60	35	4.250	b.d.	0.056	0.164	b.d.	41.14	52.88
11	3.715	0.194	0.092	0.132	0.136	40.34	52.63	36	4.544	b.d.	0.052	0.171	b.d.	41.14	52.83
12	3.528	0.169	0.085	0.164	0.142	40.02	52.08	37	4.504	b.d.	0.047	0.160	b.d.	41.17	52.72
13	3.378	0.183	0.089	0.159	0.123	40.76	52.74	38	4.340	b.d.	0.044	0.158	b.d.	41.17	52.82
14	3.366	0.171	0.078	0.152	0.112	40.86	52.68	39	4.185	b.d.	0.047	0.163	b.d.	41.36	52.84
15	3.365	0.161	0.086	0.148	0.114	41.05	52.89	40	4.177	b.d.	0.043	0.173	b.d.	41.51	52.78
16	3.356	0.136	0.081	0.158	0.116	40.98	52.50	41	4.032	b.d.	0.045	0.161	b.d.	41.60	52.85
17	3.219	0.156	0.083	0.154	0.117	40.33	52.04	42	3.958	b.d.	0.042	0.164	b.d.	41.51	52.90
18	3.228	0.170	0.079	0.171	0.122	41.05	52.61	43	3.872	b.d.	0.036	0.164	b.d.	41.66	52.91
19	3.338	0.155	0.071	0.175	0.115	41.13	52.53	44	3.935	b.d.	0.044	0.166	b.d.	41.69	52.99
20	3.411	0.158	0.078	0.168	0.137	41.01	52.65	45	3.958	b.d.	0.049	0.171	b.d.	41.61	52.82
21	3.447	0.173	0.072	0.168	0.119	40.89	52.64	46	3.987	b.d.	0.044	0.169	b.d.	41.66	52.85
22	3.56	0.137	0.074	0.172	0.118	41.02	52.62	47	4.035	b.d.	0.040	0.149	0.020	41.64	52.80
23	3.626	0.159	0.068	0.172	0.109	41.01	52.82	48	4.044	b.d.	0.036	0.167	b.d.	41.63	52.91
24	3.667	0.134	0.066	0.174	0.088	41.02	52.75	49	4.097	b.d.	0.033	0.171	0.019	41.55	52.61
25	3.664	0.139	0.072	0.167	0.111	41.14	52.81	50	4.083	b.d.	0.035	0.164	b.d.	41.64	52.61
26	3.697	0.115	0.054	0.172	0.106	41.11	52.58	51	4.075	b.d.	0.033	0.163	b.d.	41.69	52.82
27	3.666	0.124	0.061	0.174	0.105	41.20	52.68	52	4.181	b.d.	0.039	0.172	b.d.	41.58	52.83
28	3.391	0.127	0.062	0.171	0.105	41.35	52.61	53	4.136	b.d.	0.037	0.165	b.d.	41.73	53.06
29	3.193	0.142	0.058	0.197	0.129	41.64	52.67	54	4.060	b.d.	0.033	0.178	b.d.	41.80	52.69
30	3.419	0.140	0.048	0.215	0.135	41.74	52.77	55	3.911	b.d.	0.036	0.169	b.d.	41.95	52.82
31	2.909	0.075	0.024	0.171	0.079	43.02	52.97	56	3.853	b.d.	0.032	0.184	b.d.	41.98	52.60
67	0.854	b.d.	b.d.	b.d.	b.d.	45.65	53.11	57	0.890	b.d.	b.d.	b.d.	b.d.	45.70	53.34
68	0.858	b.d.	0.017	b.d.	b.d.	45.21	52.85	58	0.885	b.d.	b.d.	b.d.	b.d.	45.61	53.27
69	0.576	b.d.	0.042	b.d.	b.d.	44.93	52.95	59	0.710	0.026	b.d.	b.d.	b.d.	45.90	53.42
70	0.569	b.d.	0.046	b.d.	b.d.	45.03	52.80	60	1.356	0.026	b.d.	b.d.	0.026	45.31	53.17
71	0.693	b.d.	0.066	b.d.	b.d.	44.75	53.21	61	1.186	b.d.	b.d.	b.d.	b.d.	44.89	53.04
72	0.638	b.d.	0.069	b.d.	b.d.	44.76	52.97	62	0.860	0.049	0.069	b.d.	0.019	44.05	53.12
73	0.714	b.d.	0.071	b.d.	b.d.	44.74	53.10	63	0.562	0.045	0.114	b.d.	b.d.	43.42	52.96
74	0.898	b.d.	0.074	b.d.	b.d.	44.37	53.05	64	0.632	0.046	0.121	b.d.	0.020	43.38	52.90
75	0.735	b.d.	0.08	b.d.	b.d.	44.57	53.01	65	0.579	0.041	0.118	b.d.	b.d.	43.49	53.09
76	0.706	b.d.	0.073	b.d.	b.d.	44.48	52.77	66	1.473	0.097	0.148	0.069	0.040	42.14	52.68
137	3.734	0.226	0.08	0.124	0.103	40.63	52.68	157	4.377	b.d.	0.042	0.133	b.d.	41.75	52.77
138	3.497	0.248	0.093	0.121	0.093	40.63	52.27	158	4.404	b.d.	0.032	0.137	b.d.	41.76	52.70
139	3.597	0.206	0.082	0.142	0.101	40.66	52.44	159	4.573	b.d.	0.029	0.145	0.046	41.53	52.45
140	3.497	0.208	0.092	0.150	0.095	40.72	52.44	160	4.105	0.067	0.043	0.145	0.038	41.46	52.77
141	3.673	0.201	0.084	0.140	0.082	40.86	52.63	161	3.709	0.213	0.075	0.127	0.090	41.07	52.52
142	3.566	0.213	0.077	0.138	0.091	40.88	52.42	162	3.615	0.213	0.066	0.131	0.091	40.95	52.13
143	3.79	0.210	0.074	0.138	0.089	40.85	52.41	163	3.797	0.176	0.057	0.150	0.083	41.10	52.35
144	3.83	0.159	0.069	0.142	0.078	40.83	52.51	164	3.854	0.190	0.074	0.132	0.080	41.00	52.41
145	3.997	0.159	0.067	0.148	0.075	40.91	52.53	165	4.061	0.126	0.064	0.116	0.069	40.96	52.59
146	3.83	0.178	0.072	0.144	0.068	41.01	52.57	166	3.596	0.191	0.064	0.144	0.076	41.34	52.63
147	3.619	0.184	0.068	0.152	0.073	40.98	52.20	167	3.780	0.138	0.050	0.144	0.061	41.42	52.39
148	3.588	0.151	0.08	0.147	0.088	41.21	52.56	168	3.644	0.160	0.048	0.151	0.077	41.31	52.49
149	3.384	0.168	0.071	0.170	0.078	41.27	52.78	169	3.499	0.185	0.052	0.146	0.084	41.48	52.56
150	3.08	0.215	0.087	0.146	0.088	41.27	52.34	170	3.435	0.162	0.071	0.154	0.096	41.25	52.88
151	3.079	0.169	0.083	0.165	0.095	41.37	52.48	171	2.977	0.223	0.069	0.154	0.083	41.54	52.62
152	2.967	0.187	0.084	0.166	0.087	41.36	52.40	172	b.d.	0.146	0.041	b.d.	b.d.	35.23	44.53
153	3.059	0.188	0.065	0.151	0.093	41.41	52.51	173	3.633	0.028	0.029	0.149	b.d.	41.76	51.25
154	3.75	0.096	0.071	0.114	0.058	41.18	52.81	174	3.358	0.153	0.035	0.148	0.071	41.84	52.54
155	3.658	0.096	0.059	0.118	0.076	41.25	52.80	175	3.136	0.163	0.039	0.143	0.078	41.90	52.40
77	3.618	0.130	0.04	0.140	0.062	41.80	52.33	176	3.337	0.163	0.033	0.141	0.062	41.85	52.80
78	3.236	0.196	0.061	0.128	0.074	41.73	52.42	107	3.819	0.089	0.056	0.106	0.058	41.34	52.61
79	3.243	0.187	0.056	0.119	0.078	41.78	52.61	108	3.703	0.098	0.068	0.090	0.064	41.20	52.95
80	3.231	0.223	0.038	0.129	0.070	41.98	52.62	109	3.765	0.099	0.059	0.097	0.057	41.27	52.65
81	3.111	0.223	0.045	0.122	0.079	42.05	52.79	110	3.735	0.121	0.067	0.103	0.053	41.33	52.79

82	3.145	0.188	0.039	0.122	0.077	42.00	52.53	111	3.763	0.109	0.055	0.086	0.062	41.33	52.68
83	3.172	0.188	0.041	0.121	0.092	42.09	52.45	112	3.844	0.088	0.045	0.097	0.044	41.32	52.52
84	3.539	0.133	0.039	0.122	0.063	41.97	52.43	113	3.850	0.066	0.054	0.075	0.047	41.43	52.76
85	3.392	0.184	0.034	0.112	0.076	42.07	52.49	114	3.968	0.094	0.043	0.078	0.054	41.57	52.88
86	3.441	0.160	0.035	0.113	0.061	42.07	52.54	115	3.978	0.092	0.051	0.073	0.046	41.56	52.85
87	3.299	0.174	0.033	0.113	0.062	42.12	52.73	116	3.983	0.089	0.045	0.081	0.054	41.62	52.87
88	3.184	0.209	0.043	0.111	0.079	42.23	52.43	117	3.985	0.069	0.039	0.087	0.059	41.59	52.76
89	3.409	0.164	0.038	0.107	0.065	42.10	52.38	118	4.038	0.061	0.035	0.075	0.043	41.64	52.90
90	3.345	0.166	0.028	0.110	0.057	42.22	52.50	119	4.071	0.062	0.036	0.080	0.050	41.62	52.84
91	3.285	0.172	0.035	0.099	0.074	42.26	52.69	120	4.052	0.064	0.034	0.075	0.044	41.55	52.80
92	3.03	0.189	0.037	0.111	0.083	42.29	52.63	121	4.011	0.069	0.032	0.084	0.045	41.81	52.73
93	2.774	0.185	0.041	0.121	0.083	42.33	52.57	122	4.022	0.045	0.026	0.070	0.053	41.75	52.80
94	2.218	0.130	0.064	0.152	0.089	42.28	52.40	123	4.001	0.042	0.030	0.066	0.044	41.70	52.91
95	0.587	b.d.	b.d.	b.d.	b.d.	46.09	53.55	124	3.917	0.044	0.027	0.075	0.062	41.80	53.01
96	0.698	b.d.	b.d.	b.d.	b.d.	45.91	53.31	125	3.791	0.048	0.035	0.079	0.054	41.89	52.75
97	0.586	b.d.	b.d.	b.d.	b.d.	46.02	53.32	126	3.470	0.066	0.047	0.089	0.060	41.79	52.81
98	0.445	0.029	b.d.	b.d.	b.d.	46.00	53.39	128	1.276	b.d.	b.d.	b.d.	b.d.	45.35	53.27
99	0.497	0.028	0.015	b.d.	b.d.	45.87	53.15	129	1.127	b.d.	b.d.	b.d.	b.d.	45.37	53.46
100	0.571	0.026	0.024	b.d.	b.d.	45.67	53.44	130	1.193	b.d.	b.d.	b.d.	b.d.	45.38	53.23
101	0.411	b.d.	0.051	0.034	b.d.	45.47	52.97	131	1.085	b.d.	b.d.	b.d.	b.d.	45.33	52.91
102	0.456	b.d.	b.d.	0.116	b.d.	46.35	53.51	132	1.094	b.d.	0.016	b.d.	b.d.	45.21	53.06
103	0.775	b.d.	b.d.	b.d.	b.d.	45.97	53.51	133	0.782	b.d.	0.025	b.d.	b.d.	45.20	53.01
104	0.991	0.085	b.d.	b.d.	0.022	45.73	53.59	134	0.328	b.d.	0.078	b.d.	b.d.	44.62	53.09
105	1.085	b.d.	b.d.	0.040	b.d.	45.83	53.79	135	0.844	b.d.	b.d.	b.d.	b.d.	45.87	53.30
106	0.829	b.d.	b.d.	0.058	b.d.	46.00	53.34	136	0.928	0.092	b.d.	b.d.	0.017	45.70	53.06
mean	**2.638**	**0.159**	**0.063**	**0.139**	**0.092**	**42.47**	**52.74**	**mean**	**3.196**	**0.103**	**0.049**	**0.131**	**0.056**	**42.25**	**52.71**
median	**0.441**	**0.182**	**0.001**	**0.029**	**0.015**	**45.84**	**53.05**	**median**	**0.511**	**0.091**	**0.001**	**0.034**	**0.015**	**45.91**	**53.06**
std dev	**1.231**	**0.047**	**0.021**	**0.035**	**0.026**	**1.92**	**0.36**	**std dev**	**1.293**	**0.057**	**0.023**	**0.037**	**0.021**	**1.69**	**0.95**
min	**0.411**	**0.026**	**0.015**	**0.034**	**0.022**	**40.02**	**52.04**	**min**	**0.328**	**0.026**	**0.016**	**0.066**	**0.017**	**35.23**	**44.53**
max	**3.997**	**0.248**	**0.097**	**0.215**	**0.154**	**46.35**	**53.79**	**max**	**4.573**	**0.223**	**0.148**	**0.184**	**0.096**	**45.90**	**53.46**

wt.% Cu in the “dark” sector (Figs. 5C and 6A); the terms “light” and “dark” refer to the back scattered electron density and reflect the relative masses of material analysed, with “light” corresponding to greater mass. The “light” sector also contains significant arsenic (up to 0.12 wt.% versus 0.19 wt.% in the “dark” sector; Table 1). Concentrations of Se, Te and Ni are low but detectable in the “light” sectors and are below their detection limits in the dark sectors (Table 1). Within both dark and light sectors, the concentrations of As and Cu are inversely correlated, and this effect is enhanced in the “light” sector. Selenium, Te and Ni appear to mimic the behaviour of As, rather than that of Cu (Table 1).

The Kd between the two sectors displays considerable variability across the growth zones, consistent with the strong contrast observed between sectors in the Cu map (Figs. 5C and 6B). In the first 10% of the distance outwards from the core, there is effectively no fractionation, but at 15% of the distance to the rim, the Kd reaches a peak value of 36, the highest value on the transect (although this peak is defined by a single point, it coincides with a sharp greyscale contrast between sectors in the Cu map, Fig. 5C). Between 20 and 45% of the distance to the rim, there is very little fractionation between sectors, whereas between 45 and 75% of this distance, the fractionation is relatively strong. Beyond this, there is no fractionation between sectors except for a single point 90% of the distance to the rim with a Kd of 7.

Sample BID32-16

The concentrations of all trace elements, except Cu and As, in the sector zones within the trapezoid-shaped section of the pyrite crystal from sample BID32-16 (Figs. 5G and 7A) are below 0.05 wt% and at, or near, the detection limit over the length of the transect. Copper

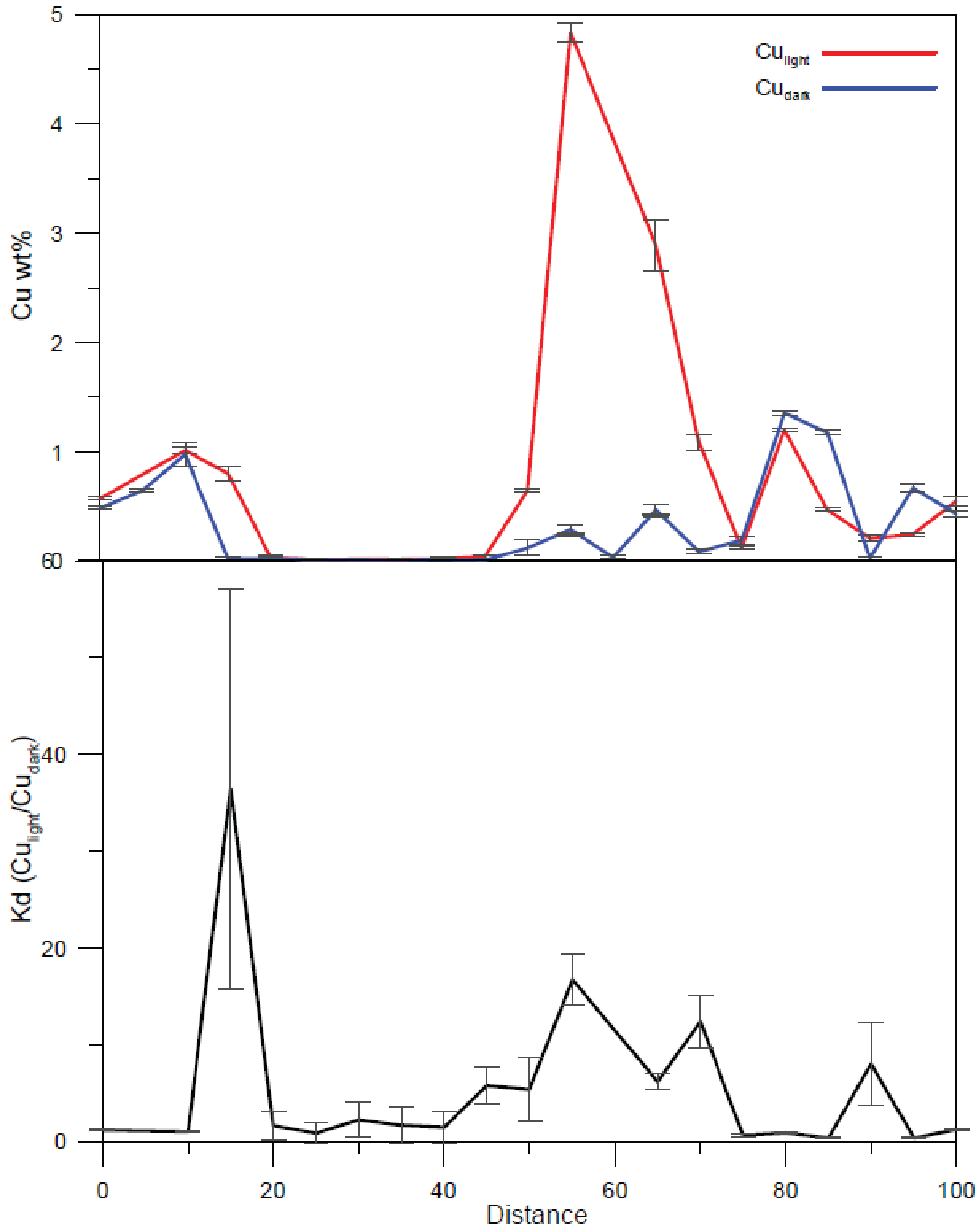

Figure III-6 Top: Concentration of Cu along transects in adjacent "light" and "dark" sectors crossing growth zones in pyrite from sample BOD3-97 (Fig. 5C and D). The distance has been normalized to a scale of 100 units with 0 representing the beginning of a transect in the core of the crystal and 100 its end at the rim. Bottom: Kd values for the transects represented in the upper figure. Error bars were calculated from the analytical error.

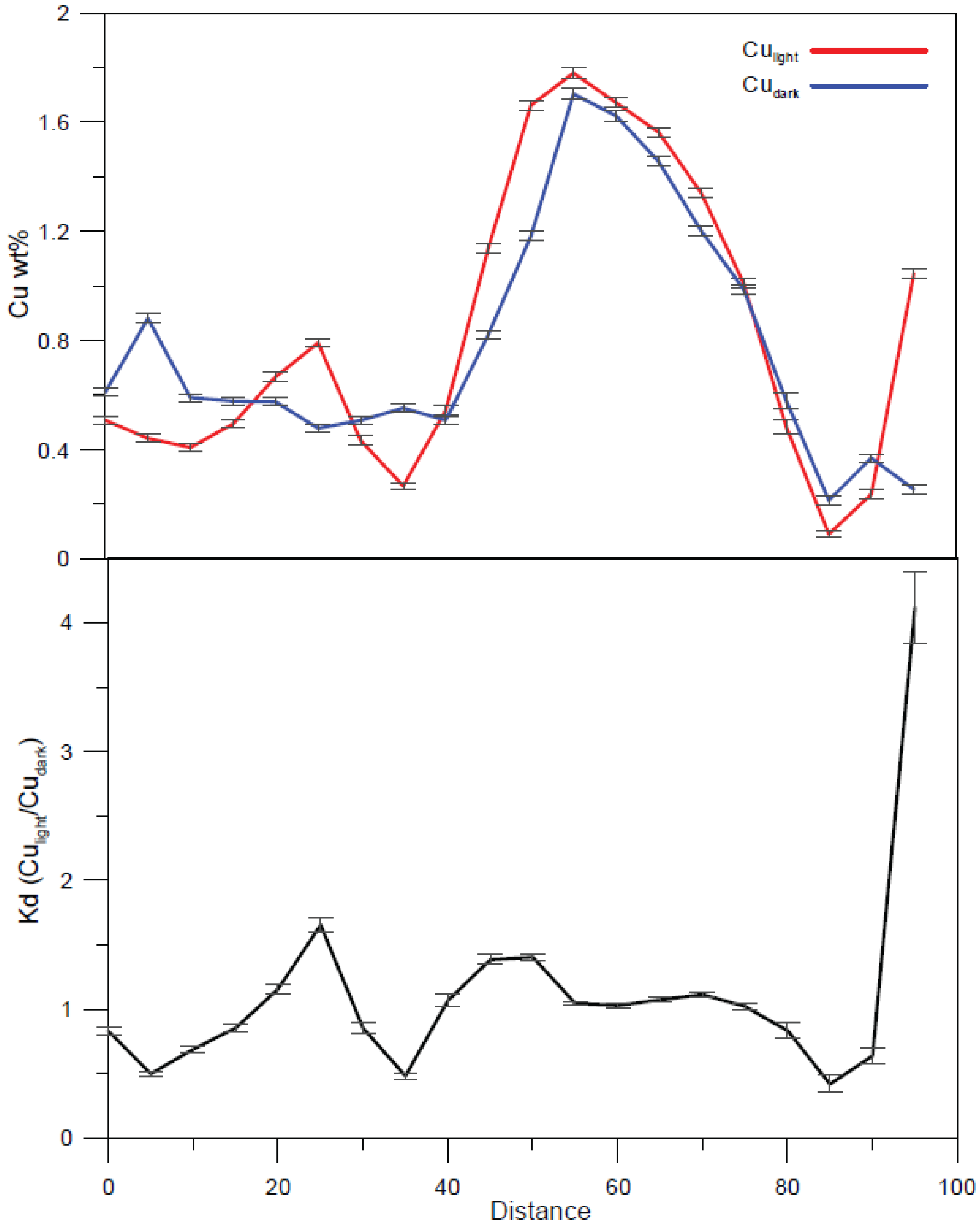

Figure III-7 Top: Concentration of Cu along transects in adjacent “light” and “dark” sectors crossing growth zones in pyrite from sample BID32-16 (Fig. 5G and H). The distance has been normalized to a scale of 100 units with 0 representing the beginning of a transect in the core of the crystal and 100 its end at the rim. Bottom: Kd values for the transects represented in the upper figure. Error bars were calculated from the analytical error.

concentrations range from 0.08 to 1.85 wt. % and track very closely in the two sectors (Fig. 7a). The highest Cu concentrations occur in growth zones between 50 and 75% of the distance to the crystal rim and at 95% of this distance. In other growth zones, the concentration is < 1 wt% Cu. In the light sector, Se concentrations (up to 0.05 wt.%), As concentrations (up to 0.60 wt.%) and Te concentrations show a rough positive correlation (Table 1). At the end of the transect, the As and Se concentrations increase in both sectors (up to 0.60 wt.% As and 0.04 wt.% Se). Concentrations of Ni are too low (< 0.001 wt.%) to discern a pattern to their distribution (Table 1).

The Kd values for sample BID32-16 are close to unity, consistent with the observation that copper concentrations in the two sectors are similar (Figs.7A and B). Between 0 and 40% of the distance to the rim of the crystal, the Kd values vary from 0.5 to 1.6 (the local occurrence of Kd values < 1 reflects a reversal in the relative preference of Cu for a particular sector), whereas between 40% and 75% of this distance, the Kd values are between 1 and 1.4. Beyond this distance, the Kd climbs to a value of 4. These variations in Kd are reflected in the Cu map shown in Fig. 5G, in which the degree of greyscale contrast for adjacent sectors correlates positively with the size of the Kd.

Sample BID34-84

The drusy, banded pyrite of sample BID34-84 has the highest average concentration of Cu of the three samples of pyrite crystals considered in this study, although Cu concentration in one growth zone in the pyrite from BOD3-97 is higher than in any growh zone from the pyrite in BID34-84 (Figs. 6A and 8A). This pyrite also has much higher concentrations of As, Ni, Se and

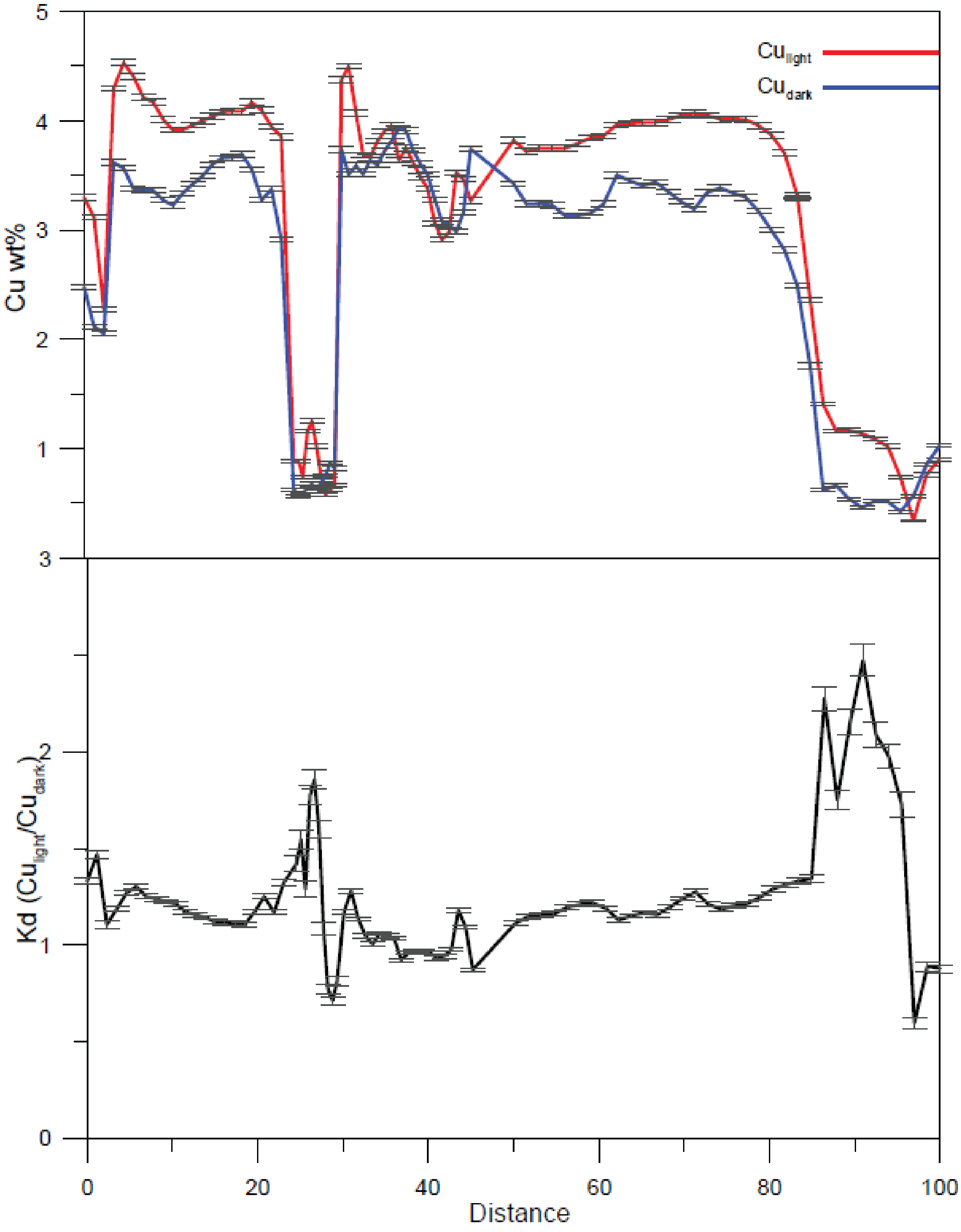

Figure III-8 Top: Concentration of Cu along transects in adjacent “light” and “dark” sectors crossing growth zones in pyrite from sample BID34-84 (Fig. 5K and L). The distance has been normalized to a scale of 100 units with 0 representing the beginning of a transect in the core of the crystal and 100 its end at the rim. Bottom: Kd values for the transects represented in the upper figure. Error bars were calculated from the analytical error.

Te than the other pyrite crystals analysed. The Cu concentration in individual "light" sector growth zones ranges between 0.3 wt.% and 4.6 wt.% and in "dark" sector growth zones ranges between 0.4 and 4.0 wt.% (Fig. 8A). Concentrations of Cu in the two sectors generally covary closely. Between 0 and 25% of the distance from the core, Cu concentrations are generally between 3.5 and 4.2 wt%, and the light sector is enriched in Cu relative to the dark sector by between 0.5 and 0.75 wt% (Fig. 8A). By contrast, the dark sector is preferentially enriched in As, Ni and Te, and the Se concentration varies little between the two sectors (Table 1). In the interval between 25% to 30% of the distance to the rim, concentrations of Cu and Se are sharply lower than in the preceding interval and their concentrations are relatively constant in the dark sector (Fig. 8A). Tellurium concentrations are similar to those of the preceding interval, whereas Ni and As concentrations are markedly higher. Between 30% and 85% of the distance to the rim, the Cu concentration returns to levels similar to those preceding the 25 to 30% interval and is consistently higher in the "light" sector than in the "dark" sector. In this interval (30 and 85%), concentrations of As, Ni, Se and Te are higher in the dark sector and, except for Se, correlate positively with Cu. Beyond this interval, concentrations of all elements, including Cu, are markedly lower.

The Kd values decrease from 1.5 in the core to 1 approximately 20% of the distance along the transect, and increase sharply to a value of ~ 2 at 27% of the distance. At 30% of the distance to the rim the Kd plunges to a value of 0.7 (Fig. 8B). Sharp changes in Kd correspond to a decrease in the concentration of most trace elements and are easily visible in the Cu map (Fig. 5K). From 30 to 85% of the distance to the rim, the Kd gradually rises in a series of steps to a value of 1.3. Between 85 and 95% of this distance, there is a sharp increase in Kd to a value of 2.7 followed by a precipitous drop between 95 and 98% to a value of 0.5. There is a small increase in Kd at the end of the transect, which is matched by a corresponding increase in the concentration of all the trace elements analysed. Except for short intervals between 25 and 30% and between 85 and 97% of the distance along the transect, the partitioning of Cu between the sectors was relatively constant.

The Kd for each transect shows irregular changes (Figs. 6-8) The concentration of copper does not appear to be directly related to either increases or decreases in Kd, but higher copper concentrations correspond to periods when the Kd was relatively constant, rather than increasing or decreasing. This is best illustrated by sample BID34-84 (Fig. 8). Although the association of high metal concentration with periods of relatively constant Kd is most evident for Cu, it is also observed for the other elements analysed.

Error Analysis

Analyses of the type described above have two distinct sources of error: 1) analytical error and 2) error due to normalization and placement of the transects. Error bars for each element were calculated using the JOEL electron microprobe routine for 1σ in X-Ray counting. The detection limits were calculated using the average pooled standard deviation and a 95% confidence interval for the student-t test.

The second set of error calculations estimated the error due to placement of points. The pairing of analyses from each growth zone was done manually using georeferenced BSE images and Cu maps and, due to variations in the width of growth zones, caused transects to be non-uniformly stretched or compressed. We accounted for this error by comparing the relative peak positions on

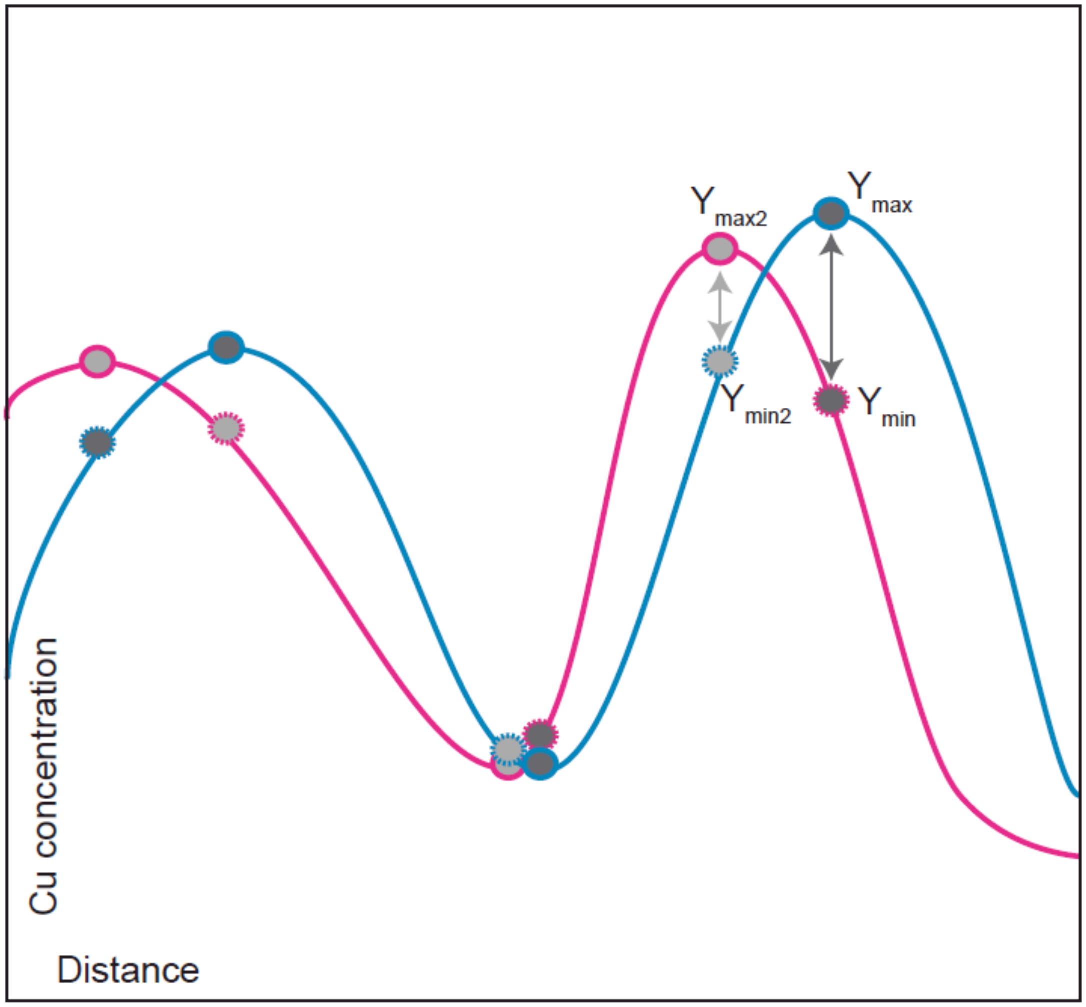

$$\text{Error} = \frac{\left(\frac{Y_{max}}{Y_{min}}\right) - \left(\frac{Y_{max2}}{Y_{min2}}\right)}{\left(\frac{Y_{max}}{Y_{min}}\right)} \times 100$$

Figure III-9 Schematic diagram showing how error associated with matching peaks from two paried transects was calculated.

the dark and light transects (Fig. 9). This method yielded an average error of 30% for the transects. Although it may seem that the error due to placement limits discrimination between zones, this is not the case because we used mean values for Kd and the error on the mean is much smaller than on individual points (Fig. 10).

Fractionation between non-equivalent sector zones is strongest for copper. Not only is the concentration great enough to create high-resolution maps (vital for matching growth zones), but the total error (including the calculated statistical error as well as error in calibration, propagated error, the error in positioning, and natural interferences, which are not quantified), it is much lower at higher concentration. The wedge shape of the Kd vs. Cu plot demonstrates the convergence of Kd values at higher Cu concentration as the error in Kd decreases with increasing Cu concentration (Fig. 11). However, this shape may also reflect differences in the incorporation mechanism at high Cu concentration. Additional chemical analysis by methods with lower detection limits (e.g., laser ablation inductively coupled mass spectrometry or SIMS) would help discriminate between the effect of increasing error with decreasing Cu concentration and that of changes in incorporation mechanisms.

Multiple sources of error are inherent in this technique but the error can be mitigated by comparing the calculated values to the original, high-resolution element map. This visual technique makes it possible to determine if a spike in Kd is an artefact (due, for example, to point density or normalization) by comparing the Cu concentrations to the Cu maps. Thus, if the image shows a contrast between sectors within a growth zone where there is a spike in Kd, then the latter is not an artefact. The symmetry of the crystals also offers the opportunity to make multiple paired transects through the same crystal and use the average of these transects to calculate Kd

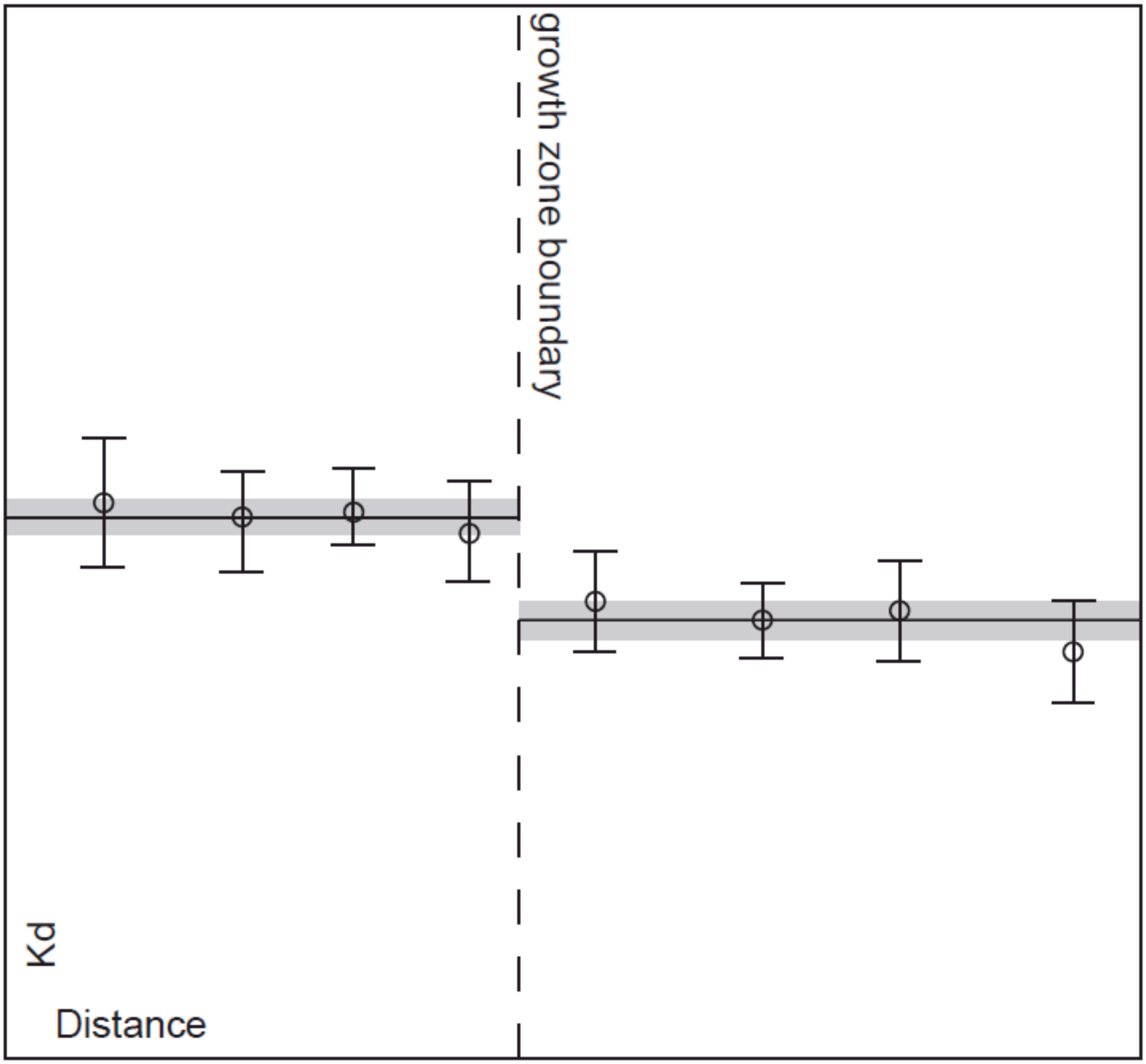

Figure III-10 Schematic diagram comparing the error on individual points with the error on the mean (grey boxes), for two growth zones.

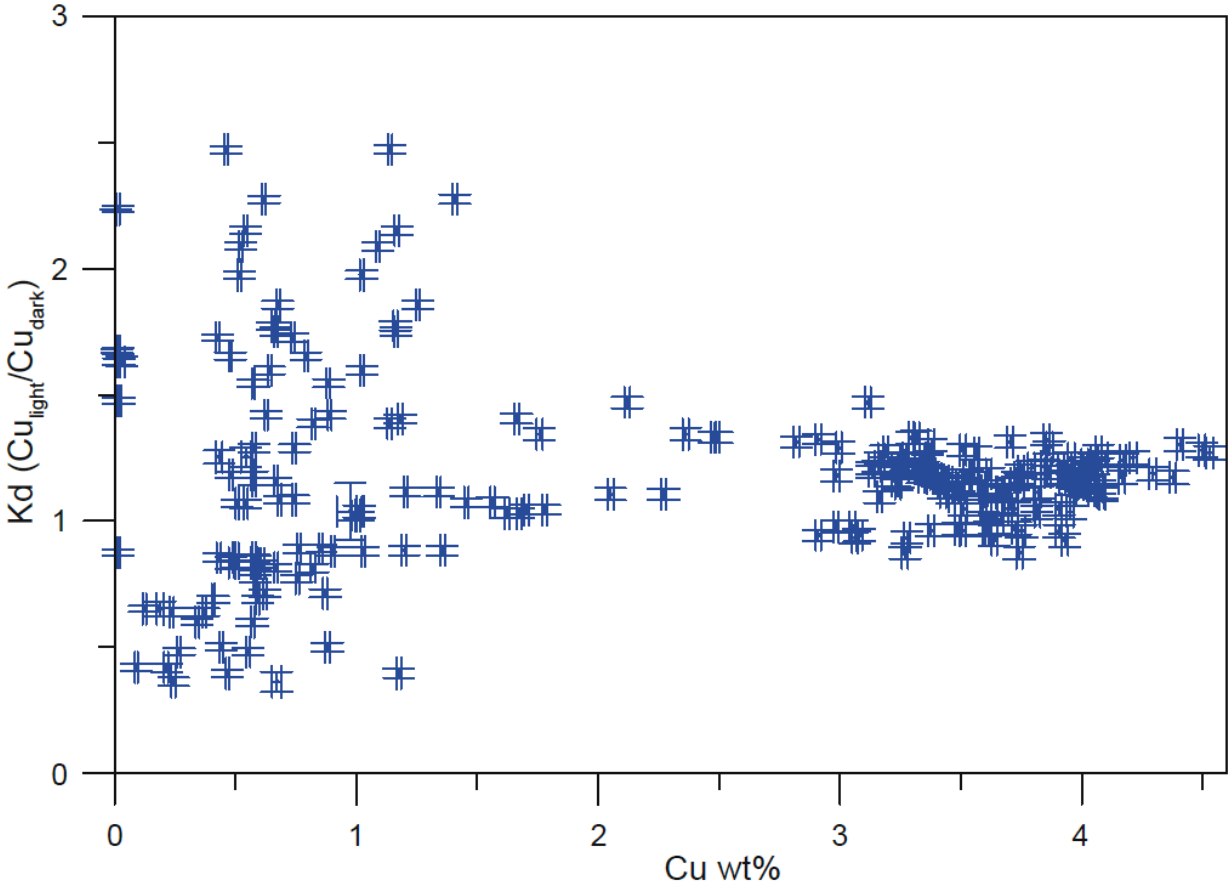

Figure III-11 A plot of Kd vs. Cu concentration for all samples, demonstrating convergence at higher concentration or a relationship between Kd and Cu concentration.

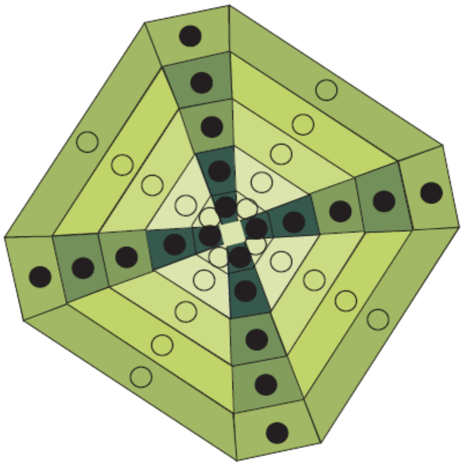

Figure III-12 A schematic diagram showing how multiple transects can be made through multiple sector zones.

values for individual growth zones (Fig. 12). Finally, the resolution could be improved with a precise cross-reference of the analysis location to the corresponding location on the element map.

Discussion

Although sector zoning has been investigated in a number of minerals, including calcite, tourmaline, staurolite, arsenopyrite and pyrite (Hollister, 1970a; Reeder, 1991; Vesselinov and Kerestedjian, 1995; Chouinard et al., 2005; van Hinsberg et al., 2006), the partitioning of elements between sectors has only been related to physicochemical conditions for tourmaline. In the case of this mineral, it was shown that the partitioning (measured by the Kd) depends mainly on temperature and thus sector zoning in tourmaline can be used as a geothermometer (van Hinsberg and Schumacher, 2007). Whether or not sector zoning in pyrite is also temperature-dependent is unknown. In principle, this zoning could reflect changes in other physicochemical parameters, e.g., pH and fO_2, concentration (as discussed above; Fig. 11), pressure, and also in growth rate, with the latter affecting the adsorption mechanism and in turn Kd (Watson and Liang, 1995; Shtukenberg et al., 2009). If the growth rate of a particular face is fast, the concentration of an element on that face may be controlled kinetically rather than by the properties of the face. In such cases, values of Kd calculated using such a sector may not reflect the prevailing physicochemical conditions. Indeed, Dowty (1976) recommended caution when applying element partitioning “as indicators of temperature and pressure, especially when growth is rapid”. It is unlikely that the growth rate is a strong controlling variable for the three crystals studied here since large variations in Kd are observed. Moreover, there is almost no variation in the angle between the two sectors, which should change if growth rate were an important control on Kd; the angle should vary with Kd.

Pressure is not likely to affect sector zoning in pyrite, particularly if the differences in element uptake are controlled by the charge of species rather than the geometry. Nonetheless, in the context of this study, it is clear that the sector zoning observed in pyrite at Binebase and Bowone, provides a record of physicochemical change; even a change in growth rate would reflect a change in the physicochemical gradient.

An important characteristic of pyrite is that it is a semi-conductor, with the nature of the conductivity depending in part on deviations from stoichiometry and in part from the presence of trace elements in the lattice. Thus, pyrite with a deficit of sulphur will tend to be n-type and with an excess of sulphur will tend to be p-type, but this is not always the case (Abraitis et al., 2004). These two types of pyrite will tend to adsorb positively and negatively charged aqueous species, respectively. Among the trace elements in pyrite that affects its electrical properties, the effect of As is best known. This element imparts p-type conduction to the pyrite. There are no data for Cu, however, which as discussed earlier is a major constituent of the pyrite at Binebase and Bowone. Significantly for this study, low temperature pyrite, including the colloform varieties common in these deposits is typically p-type (Pridmore and Shuey, 1976). Of particular importance is that different zones within a single pyrite crystal may have different semi-conducting properties (Favorov et al., 1974). If p-type and n-type sectors were both present in the pyrite considered in this study, or if the conductivity of the different sectors varied, this could have influenced element uptake through adsorption (i.e., one face might have been more receptive to positively or negatively charged species than another face). Changes in pH could have amplified or dampened this effect, causing a change in Kd values. It is also possible that the fO_2 of the fluid could similarly have affected the partitioning of the elements between sectors. Changes in fO_2 would promote the stability of one species over another (e.g., $AuHS^-$ and AuS°), and differences in surface polarity would influence the selection of species, element uptake and thus Kd.

Regardless of whether the sector zoning was due to changes in pH, fO_2 or temperature, it is still possible to make preliminary observations about the physicochemical history of each grain discussed in this study. All three samples analyzed show, independent of the size or sign of the Kd value, that trace element uptake reached a maximum when the Kd was relatively constant, i.e., when physicochemical conditions (whether temperature, pH or fO_2) were stable. This is an important observation, as most mineral deposit models invoke sudden changes in physicochemical conditions (e.g., through boiling or fluid mixing) to explain ore formation.

Conclusions

Even though the controls on sector zoning in pyrite are not fully understood at this point and the corresponding Kd values have not been directly related to specific physicochemical parameters such as temperature, analysis of this zoning provided valuable information about the evolution of the studied mineral deposits. It allowed us to gain insights into the conditions that favoured uptake of Cu and other elements in an unusual high-sulphidation epithermal environment and showed that these elements were concentrated to potentially economic levels under stable physiochemical conditions, rather than during rapid changes in these conditions as is generally inferred for most hydrothermal systems.

Chapter IV

General Conclusions

The Bowone and Binebase hypogene Au (Ag-Cu) deposits are the products of an acidic condensate of magmatic origin that caused intermediate and advanced argillic alteration of the volcanic/volcaniclastic host rocks, mobilized most elements and concentrated Au, Ag and Cu in pyrite. The ore metals were undersaturated in the condensate and accumulated by adsorbing onto the surface of pyrite and enargite. They were incorporated in these minerals either by solid solution or by precipitating as nano-inclusions.

This work adds to the body of literature devoted to the understanding of high-sulphidation deposits. Bowone and Binebase belong to a group of high-sulphidation epithermal deposits that formed by the vapour transport of the metals along with such deposits as Pascua (Chouinard et al., 2005b) and Monte Negro (Muntean et al., 1990). A feature of these systems observed at Bowone and Binebase is the stratigraphically controlled, sub-horizontal geometry of the ore zones that develops from subvertical conduits. Another feature of these deposits is the occurrence of a significant proportion of "invisible gold" (and Ag) in pyrite and enargite. At Bowone and Binebase, the gold is hosted almost entirely in pyrite and to a much lesser extent in enargite. The auriferous (1.1 ppm Au) Pyrite I is in textural equilibrium with advanced and intermediate argillic alteration (quartz, pyrophyllite, natroalunite, alunite, kaolinite, dickite), indicating that the fluid responsible for this alteration was also the ore fluid. The temperature and pH of the different alteration assemblages were determined using stability relationships among the minerals. Oxygen fugacity was estimated from a combination of these stability relationships and $\delta^{34}S$ values for pyrite. These analyses show that hydrothermal alteration and ore formation occurred at temperatures ranging from 250 to 340°C, a pH between 0.5 and 4 and oxygen fugacity from 4 log units above the hematite-magnetite buffer to 1 log unit below it.

The later, Pyrite II generation has higher concentrations of Au (3.0 ppm Au) and Cu (up to 6.0 wt%) than Pyrite I and occurs in veins and as replacement bodies filling voids created by the early alteration. Later barite and enargite were deposited along fractures that reopened veins of Pyrite II. These later veins contain higher concentrations of Ag than Pyrite II veins and significant Au concentrations. It was not possible to constrain the physicochemical conditions of these later generations of mineralization. However, it seems likely that the conditions for Pyrite II were very similar to those for Pyrite I mineralization.

The development of growth and sector zoning in Pyrite II made it possible to document relative changes in physicochemical conditions during the growth of this mineral. Quantitative and qualitative analysis of the concentration of Cu and other elements of paired sector zones from successive growth zones yielded partition coefficients (Kd) for copper. The analyses showed that trace element concentrations were highest for intervals of growth for which the partition coefficient remains constant. This implies that instead of gold being concentrated along a sharp gradient of changing physicochemical conditions, as is typically the case when native gold is deposited, uptake of gold was optimised when these conditions remained constant for protracted periods of time.

Contributions to Knowledge

This study fills a gap in the research into high-sulphidation epithermal systems and shows that deposits formed from condensed vapours are part of the epithermal spectrum. This has important implications for both exploration and genetic models.

This study describes the first example of a gold deposit which demonstrably and unequivocably formed from condensed vapour. The elevated concenrations of gold, copper and silver in Pyrite I, which formed during advanced and intermediate argillic alteration, provides evidence that the condensed vapours responsible for the alteration also concentrated the metals. This has important implications for programs designed to explore for high sulphidation epithermal deposits, and may explain why the altereed rocks are commonly mineralized in these systems.

On the deposit scale, I successfully identified the hosts for the economic metals in the hypogene zone, which is important to the refining process. The study also furnished the sponsoring company with a new model for predicting the geometry of the mineralized zones, establishing the nature of the alteration and evaluating the relationship of the alteration to the (invisible) mineralization.

Another important contribution was the demonstration that sector and growth zoning in pyrite can be used to determine relative changes in physicochemical conditions, and the implications of these changes for gold mineralization. This is an important contribution for ore deposits geochemistry that will find practical application in mineral exploration. Given the poor preservation of many ore deposits and the limited number of minerals that are available to supply data on physicochemical conditions, analysis of the zoning in pyrite could be particularly useful in constraining ore-forming conditions.

The Sangihe Arc has a great potential for the discovery of epithermal mineralization that has not been realized because of a paucity of geological investigation. This work adds to the body of knowledge of this poorly studied area and hopefully will contribute to a better understanding of ore deposits in the region.

Suggestions for Future Study

There are many avenues for additional research on this project and the samples that have already been collected. As noted in this thesis, much of the gold in the Binebase deposit is concentrated in a high-grade supergene zone. The study of this mineralization was beyond the scope of the present study, although some unsuccessful preliminary scanning electron microscopy was conducted to try and find the source. This work needs to be continued with the objective of tracking the gold from its origins in the pyrite of the hypogene zone to the supergene zone. Additional X-Ray Diffraction analyses to identify the exact nature and proportions of silicate and sulphate minerals in both the supergene and hypogene zones will improve understanding of both the primary high-sulphidation processes and supergene enrichment. From a mineralogical perspective there are also a variety of water-soluble sulphate minerals that remain unidentified.

Isotopic analysis of O, S and K from alunite would be useful in identifying the fluid sources and degree of mixing, and additional analyses for $\delta^{34}S$ of sulphide-sulphate pairs would better constrain the temperature of alteration and mineralization. An investigation of the pyrite structure to determine how the trace elements are incorporated would add to the discussion of economic concentrations of invisible gold as well as inform research on sector zoning and trace-element uptake.

The research described in Chapter III represents the first steps in the development of pyrite as a single-crystal tool for evaluating physicochemical conditions in ore-forming systems. In the future, experiments designed to evaluate element partitioning under carefully controlled physicochemical conditions and gradients will be needed to allow the process to be properly understood and quantified. A database of studies of sector-zoned natural samples that formed at a known temperature, would also be an important in eventually calibrating and testing this application of sector zoning in pyrite

References

Abraitis, P.K., Pattrick, R.A.D., Vaughan, D.J., 2004. Variations in the compositional, textural and electrical properties of natural pyrite: A review. International Journal of Mineral Processing 74, 41–59.

Agrawal, S., Guevara, M., Verma, S., 2008. Tectonic Discrimination of Basic and Ultrabasic Volcanic Rocks through Log-Transformed Ratios of Immobile Trace Elements. International Geology Review 50, 1057–1079.

Anderson, A.T., 1984. Probable relations between plagioclase zoning and magma dynamics, Fuego Volcano, Guatemala. American Mineralogist 69, 660–676.

Archibald, S., Migdisov, A.A., Williams-Jones, A.E., 2001. The stability of Au-chloride complexes in water vapor at elevated temperatures and pressures. Geochimica et Cosmochimica Acta 65, 4413–4423.

Archibald, S.M., Migdisov, A.A., Williams-Jones, A.E., 2002. An experimental study of the stability of copper chloride complexes in water vapor at elevated temperatures and pressures. Geochimica et Cosmochimica Acta 66, 1611–1619.

Arehart, G.B., Chryssoulis, S.L., Kesler, S.E., 1993. Gold and Arsenic in Iron Sulfides from Sediment-Hosted Disseminated Gold Deposits: Implications for Depositional Processes. Economic Geology 88, 171–185.

Arodji, W., Johnedy, S., 2008. East Asia Minerals Corp Annual Report: Sangihe Project 2008 Exploration Progress Report.

Arribas, A.R., 1995. Characteristics of High-Sulphidation Epithermal Deposits, and their Relation to Magmatic Fluid, in: Thompson, J.F.H. (Ed.), Magmas, Fluids, and Ore Deposits. pp. 419–454.

Ashley, P.M., Creagh, C.J., Ryan, C.G., 2000. Invisible gold in ore and mineral concentrates from the Hillgrove gold-antimony deposits, NSW, Australia. Mineralium Deposita 35, 285–301.

Audétat, A., Günther, D., Heinrich, C.A., 1998. Formation of a magmatic-hydrothermal ore deposit: Insights with LA-ICP-MS analysis of fluid inclusions. Science 279, 2091–2094.

Audétat, A., Günther, D., Heinrich, C.A., 2000. Causes for large-scale metal zonation around mineralized plutons: Fluid inclusion LA-ICP-MS evidence from the Mole Granite, Australia. Economic Geology 95, 1563–1581.

Audétat, A., Pettke, T., Heinrich, C.A., Bodnar, R.J., 2008. Special Paper: The Composition of Magmatic-Hydrothermal Fluids in Barren and Mineralized Intrusions. Economic Geology 103, 877–908.

Barker, S.L.L., Hickey, K.A., Cline, J.S., Dipple, G.M., Kilburn, M.R., Vaughan, J.R., Longo, A.A., 2009. Uncloaking Invisible Gold: Use of Nanosims to Evaluate Gold, Trace Elements, and Sulfur Isotopes in Pyrite from Carlin-Type Gold Deposits. Economic Geology 104, 897–904.

Le Bas, M.J., Le Maitre, R.W., Streckeisen, A., Zanettin, B., 1986. A Chemical Classification of Volcanic Rocks Based on the Total Alkali-Silica Diagram. Journal of Petrology 27, 745–750.

Benzaazoua, M., Marion, P., Robaut, F., Pinto, A., 2007. Gold-bearing arsenopyrite and pyrite in refractory ores : analytical refinements and new understanding of gold mineralogy. Mineralogical Magazine 71, 123–142.

Berger, B.R., Henley, R.W., 2011. Magmatic-vapor expansion and the formation of high-sulfidation gold deposits : Structural controls on hydrothermal alteration and ore mineralization. Ore Geology Reviews 39, 75–90.

Bethke, P.M., Rye, R.O., Stoffregen, R.E., Vikre, P.G., 2005. Evolution of the magmatic-hydrothermal acid-sulfate system at Summitville, Colorado: integration of geological, stable-isotope, and fluid-inclusion evidence. Chemical Geology 215, 281–315.

Bi, S.-J., Li, J.-W., Zhou, M.-F., Li, Z.-K., 2011. Gold distribution in As-deficient pyrite and telluride mineralogy of the Yangzhaiyu gold deposit, Xiaoqinling district, southern North China craton. Mineralium Deposita 46, 925–941.

Bonham, H.F., 1984. Three major types of epithermal precious metal deposits, in: Geological Society of America Abstracts. p. 449.

Boyce, A.J., Fulignati, P., Sbrana, A., Fallick, A.E., 2007. Fluids in early stage hydrothermal alteration of high-sulfidation epithermal systems: A view from the Vulcano active hydrothermal system (Aeolian Island, Italy). Journal of Volcanology and Geothermal Research 166, 76 – 90.

Cabri, L.J., Newville, M., Gordon, R.A., Crozier, E.D., Sutton, S.R., Mcmahon, G., Jiang, D., 2000. Chemical speciation of gold in arsenopyrite. Canadian Mineralogist 38, 1265−1281.

Canfield, D.E., Raiswell, R., Westrich, J.T., Reaves, C.M., Berner, R.A., 1986. The use of chromium reduction in the analysis of reduced inorganic sulfur in sediments and shales. Chemical Geology 54, 149–155.

Carlile, J.C., Davey, G.R., Kadir, I., Langmead, R.P., Rafferty, W.J., 1998. Discovery and exploration of the Gosowong epithermal gold deposit, Halmahera, Indonesia. Journal of Geochemical Exploration 60, 207–227.

Carlile, J.C., Digdowirogo, S., Darius, K., 1990. Geological setting, characteristics and regional exploration for gold in the volcanic arcs of North Sulawesi, Indonesia, in: Hedenquist, J.W., White, N.C., Siddeley, G. (Eds.), Epithermal Gold Mineralization of the Circum-Pacific Geology: Geochemistry, Origin and Exploration. Journal of Geochemical Exploration, pp. 105–140.

Carlile, J.C., Mitchell, A.H.G., 1994. Magmatic arcs and associated gold and copper mineralization in Indonesia. Journal of Geochemical Exploration 50, 91–142.

Cepedal, A., Fuertes-Fuente, M.E., Martin-Izard, A., 2008. Gold-Bearing As-Rich Pyrite and Arsenopyrite from the El Valle Gold Deposit, Asturias, Northwestern Spain. The Canadian Mineralogist 46, 233–247.

Chakhmouradian, A.R., Halden, N.M., Mitchell, R.H., Horváth, L., 2007. Rb-Cs-rich rasvumite and sector-zoned "loparite-(Ce)" from Mont Saint-Hilaire (Québec, Canada) and their petrologic significance. European Journal of Mineralogy 19, 533–546.

Chambefort, I., Moritz, R., 2006. Late Cretaceous structural control and Alpine overprint of the high-sulfidation Cu–Au epithermal Chelopech deposit, Srednogorie belt, Bulgaria. Mineralium Deposita 41, 259–280.

Chouinard, A., Paquette, J., Williams-Jones, A.E., 2005. Crystallographic Controls on Trace-Element Incorporation in Auriferous Pyrite from the Pascua Epithermal High-Sulphidation Deposit, Chile-Argentina. The Canadian Mineralogist 43, 951–963.

Chouinard, A., Williams-Jones, A.E., Leonardson, R.W., Hodgson, C.J., Silva, P., Tellez, C., Vega, J., Rojas, F., 2005. Geology and Genesis of the Multistage High-Sulfidation Epithermal Pascua Au-Ag-Cu Deposit, Chile and Argentina. Economic Geology 100, 463–490.

Chryssoulis, S.L., Cabri, L.J., Lennard, W., 1989. Calibration of the Ion Microprobe for Quantitative Trace Precious Metal Analyses of Ore Minerals. Economic Geology 84, 1684–1689.

Clark, J.R., Williams-Jones, A.E., 1990. Analogues of epithermal gold-silver deposition in geothermal well scales. Nature 346, 644–645.

Colley, H., Rice, C.M., 1975. A Kuroko-Type Ore Deposit in Fiji. Economic Geology 70, 1373–1386.

Cook, N.J., Chryssoulis, S.L., 1990. Concentrations of "Invisible Gold" in the Common Sulfides. The Canadian Mineralogist 28, 1–16.

Cook, N.J., Ciobanu, C.L., Mao, J., 2009. Textural control on gold distribution in As-free pyrite from the Dongping, Huangtuliang and Hougou gold deposits, North China Craton. Chemical Geology 264, 101–121.

Cook, N.J., Ciobanu, C.L., Pring, A., Skinner, W., Shimizu, M., Danyushevsky, L., Saini-Eidukat, B., Melcher, F., 2009. Trace and minor elements in sphalerite: A LA-ICPMS study. Geochimica et Cosmochimica Acta 73, 4761–4791.

Cooke, D.R., McPhail, D.C., 2001. Epithermal Au-Ag-Te Mineralization, Acupan, Baguio District, Philippines: Numerical Simulations of Mineral Deposition. Economic Geology 96, 109–131.

Cooke, D.R., Simmons, S.F., 2000. Characteristics and Genesis of Epithermal Gold Deposits. Reviews in Economic Geology 13, 221–244.

Craig, J.R., Vokes, F.M., Solberg, T.N., 1998. Pyrite: Physical and chemical textures. Mineralium Deposita 34, 82–101.

Crerar, D.A., Barnes, H.L., 1976. Chemistry of Chalcopyrite and Assemblages in Hydrothermal Solution at 200 to 350C. Economic Geology 71, 772–794.

Crowe, D.E., Riciputi, L.R., Bezenek, S., Ignatiev, A., 2008. Oxygen isotope and trace element zoning in hydrothermal garnets : Windows into large-scale fluid-flow behavior. Geology 29, 479–482.

Davies, A.G.S., Cooke, D.R., Gemmell, J.B., Simpson, K.A., 2008. Diatreme Breccias at the Kelian Gold Mine, Kalimantan, Indonesia: Precursors to Epithermal Gold Mineralization. Economic Geology 103, 689–716.

Deditius, A.P., Utsunomiya, S., Ewing, R.C., Chryssoulis, S.L., Venter, D., Kesler, S.E., 2009. Decoupled geochemical behavior of As and Cu in hydrothermal systems. Geology 37, 707–710.

Deditius, A.P., Utsunomiya, S., Reich, M., Kesler, S.E., Ewing, R.C., Hough, R., Walshe, J., 2011. Trace metal nanoparticles in pyrite. Ore Geology Reviews 42, 32–46.

Deditius, A.P., Utsunomiya, S., Renock, D., Ewing, R., Ramana, C., Becker, U., Kesler, S.E., 2008. A proposed new type of arsenian pyrite: Composition, nanostructure and geological significance. Geochimica et Cosmochimica Acta 72, 2919–2933.

Deyell, C.L., 2005. Alunite in the Pascua-Lama High-Sulfidation Deposit: Constraints on Alteration and Ore Deposition Using Stable Isotope Geochemistry. Economic Geology 100, 131–148.

Deyell, C.L., Rye, R.O., Landis, G.P., Bissig, T., 2005. Alunite and the role of magmatic fluids in the Tambo high-sulfidation deposit, El Indio–Pascua belt, Chile. Chemical Geology 215, 185 – 218.

Dowty, E., 1976. Crystal Structure and Crystal Growth: II. Sector Zoning in Minerals. The American Mineralogist 61, 460–469.

Einaudi, M.T., 1968. Copper Zoning in Pyrite from Cerro de Pasco, Peru. The American Mineralogist 53, 3–7.

Einaudi, M.T., 1977. Environment of Ore Deposition at Cerro De Pasco, Peru. Economic Geology 72, 893–924.

Elburg, M., Foden, J., 1998. Temporal changes in arc magma geochemistry, northern Sulawesi, Indonesia. Earth and Planetary Science Letters 163, 381–398.

Emmons, W.H., 1918. The Principles of Economic Geology. McGraw-Hill, New York.

Favorov, V.A., Krasnikov, V.I., Sychugov, V.S., 1974. Variations in semiconductor properties of pyrite and arsenpyrite and their determinants. International Geology Reviews 16, 385–394.

Fifarek, R.H., Rye, R.O., 2005. Stable-isotope geochemistry of the Pierina high-sulfidation Au–Ag deposit, Peru: influence of hydrodynamics on SO42−H2S sulfur isotopic exchange in magmatic-steam and steam-heated environments. Chemical Geology 215, 253–279.

Fleet, M.E., Chryssoulis, S.L., MacLean, P.J., Davidson, R., Weisener, C.G., 1993. Arsenian Pyrite from Gold Deposits: Au and As Distribution Investigated by SIMS and EMP, and Color Staining and Surface Oxidation by XPS and LIMS. The Canadian Mineralogist 31, 1–17.

Fleet, M.E., MacLean, P., Barbier, J., 1989. Oscillatory-zoned As-bearing pyrite from strata-bound and stratiform gold deposits: an indicator of ore fluid evolution. Economic Geology Monograph 6, 356–362.

Fleet, M.E., Mumin, A.H., 1997. Gold-bearing arsenian pyrite and marcasite and arsenopyrite from Carlin Trend gold deposits and laboratory synthesis. The American Mineralogist 82, 182–193.

Franklin, J.M., Gibson, H.L., Jonasson, I.R., Galley, A.G., 2006. Update to Supplement to Volcanogenic Massive Sulphide Deposits, in: Economic Geology and Bulletin of the Society of Economic Geologists, 100th Anniversary Edition. pp. 523–560.

Frenzel, G., Ottemann, J., 1967. Eine Sulfidparagenese mit kupferhaltigem Zonarpyrit von Nukundamu/Fiji. Mineralium Deposita 1, 307–316.

Fulignati, P., Gioncada, A., Sbrana, A., 1998. Geologic model of the magmatic-hydrothermal system of Vulcano (Aeolian Islands, Italy). Mineralogy and Petrology 62, 195–222.

Fulignati, P., Gioncada, A., Sbrana, A., 1999. Rare-earth element (REE) behaviour in the alteration facies of the active magmatic-hydrothermal system of Vulcano (Aeolian Islands Italy). Journal of Volcanology and Geothermal Research 88, 325–342.

Gammons, C.H., Barnes, H.L., 1989. The solubility of Ag2S in near-neutral aqueous sulfide solutions at 25 to 300°C. Geochimica et Cosmochimica Acta 53, 279–290.

Gammons, C.H., Williams-Jones, A.E., 1997. Chemical mobility of gold in the porphyry-epithermal environment. Economic Geology 92, 45–59.

Garwin, S.L., 1990. South Sangihe Regional Reconnaissance Program.

Garwin, S.L., 2000. The Setting, Geometry and Timing of Intrusion-Related Hydrothermal Systems in the Vicinity of the Batu Hijau Porphyry Copper-Gold Deposit, Sumbawa, Indonesia.

Gemmell, J.B., 2007. Hydrothermal Alteration Associated with the Gosowong Epithermal Au-Ag Deposit, Halmahera, Indonesia: Mineralogy, Geochemistry, and Exploration Implications. Economic Geology 102, 893–922.

Gill, J.B., Williams, R.W., 1990. Th isotope and U-series studies of subduction-related volcanic rocks. Geochimica et Cosmochimica Acta 54, 1427–1442.

Gosselin, P., Dubé, B., 2005. Gold Deposits of the World: Distribution, Geological Parameters and Gold Content. Geological Survey of Canada Open File , 271.

Grant, A., 1986. The Isocon Diagram - A Simple Solution to Gresens' Equation for Metasomatic Alteration. Economic Geology 81, 1976–1982.

Hall, R., 1996. Reconstructing Cenozoic SE Asia, in: Hall, R., Blundell, D. (Eds.), Tectonic Evolution of Southeast Asia. London, pp. 153–184.

Hall, R., 2000. Neogene History of Collision in the Halmahera Region, Indonesia, in: Proceedings of the Indonesian Petroleum Association 27th Annual Convention. pp. 487–493.

Hall, R., Wilson, M.E.J., 2000. Neogene sutures in eastern Indonesia. Journal of Asian Earth Sciences 18, 781–808.

Hanlie, H., Qinyan, W., Jianping, C., Shirong, L., Ruizhong, H., 1999. Occurrence and Distribution of Invisible Gold in the Shewushan Supergene Gold Deposit, Southeastern Hubei, China. The Canadian Mineralogist 37, 1525–1531.

Heald, P., Foley, N.K., Hayba, D.O., 1987. Comparative Anatomy of Volcanic-Hosted Epithermal Deposits : Acid-Sulfate and Adularia-Sericite Types. Economic Geology 82, 1–26.

Hedenquist, J.W., 1990. The Thermal and Geochemical Structure of the Broadlands-Ohaaki Geothermal System, New Zealand. Geothermics 19, 151–185.

Hedenquist, J.W., Arribas, A.R., Gonzalez-Urien, E., 2000. Exploration for Epithermal Ore Deposits. Reviews in Economic Geology 13, 245–277.

Hedenquist, J.W., Arribas, A.R., Reynolds, J.T., 1998. Evolution of an Intrusion-Centered Hydrothermal System: Far Southeast-Lepanto Porphyry and Epithermal Cu-Au Deposits, Philippines. Economic Geology 93, 373–404.

Hedenquist, J.W., Matsuhisa, Y., Izawa, E., White, N.C., Giggenbach, W.F., Aoki, M., 1994. Geology, geochemistry origin of high sulfidation Cu-Au mineralization in the Nansatsu district, Japan. Economic Geology 89, l–30.

Heinrich, C.A., Günther, D., Audétat, A., Ulrich, T., Frischknecht, R., 1999. Metal fractionation between magmatic brine and vapor , determined by microanalysis of fluid inclusions. Geology 27, 755–758.

Heinrich, C.A., Ryan, C.G., Mernagh, T.P., Eadington, P.J., 1992. Segregation of ore metals between magmatic brine and vapor; a fluid inclusion study using PIXE microanalysis. Economic Geology 87, 1566–1583.

Hemley, J.J., Hostetler, P.B., Gude, A.J., Mountjoy, W.T., 1969. Some Stability Relations of Alunite. Economic Geology 64, 599–612.

Hemley, J.J., Jones, W.R., 1964. Chemical Aspects of Hydrothermal Alteration with Emphasis on Hydrogen Metasomatism. Economic Geology 59, 538–569.

Henley, R.W., Berger, B.R., 2011. Magmatic-vapor expansion and the formation of high-sulfidation gold deposits : Chemical controls on alteration and mineralization. Ore Geology Reviews 39, 63–74.

Henry, D.J., Dutrow, B.L., 1992. Tourmaline in a low grade clastic metasedimentary rock: an example of the petrogenetic potential of tourmaline. Contributions to Mineralogy and Petrology 112, 203–218.

Hinchey, J.G., Wilton, D.H.C., Tubrett, M.N., 2003. a LAM-ICP-MS Study of the Distribution of Gold in Arsenopyrite From the Lodestar Prospect, Newfoundland, Canada. The Canadian Mineralogist 41, 353–364.

Van Hinsberg, V.J., Henry, D.J., Marschall, H.R., 2011. Tourmaline: An ideal indicator of its Host Environment. The Canadian Mineralogist 49, 1–16.

Van Hinsberg, V.J., Schumacher, J.C., 2007. Intersector element partitioning in tourmaline : a potentially powerful single crystal thermometer. Contributions to Mineral Petrology 153, 289–301.

Van Hinsberg, V.J., Schumacher, J.C., Kearns, S., Mason, P.R.D., Franz, G., 2006. Hourglass sector zoning in metamorphic tourmaline and resultant major and trace-element fractionation. The American Mineralogist 91, 717–728.

Hinschberger, F., Malod, J.-A., Rehault, J.-P., Villeneuve, M., Royer, J.-Y., Burhanuddin, S., 2005. Late Cenozoic geodynamic evolution of eastern Indonesia. Tectonophysics 404, 91 – 118.

Hollister, L.S., 1970. Origin, Mechanism, and Consequences of Compositional Sector-Zoning in Staurolite. The American Mineralogist 55, 742–766.

Hopf, S., 1993. Behaviour of rare earth elements in geothermal systems of New Zealand. Journal of Geochemical Exploration 47, 333–357.

Hurtig, N., Migdisov, A.A., Williams-Jones, A.E., 2012. The effect of different metal species on the evolution with pressure of hydration clusters in water vapour, in: Goldschmidt Conference Abstracts.

Huston, D.L., Sie, S.H., Suter, G.F., Cooke, D.R., Both, R.A., 1995. Sulfide Deposits: Part I. Proton Microprobe Analyses of Pyrite, and Part II. Selenium Levels in Pyrite: Comparison with del34S Values and Implications for the Source of Sulfur in Volcanogenic Hydrothermal Systems. Economic Geology 90, 1167–1196.

Irvine, T.N., Baragar, W.R.A., 1971. A Guide to the Chemical Classification of the Common Volcanic Rocks. Canadian Journal of Earth Sciences 8, 523–548.

Jannas, R.R., Beane, R.E., Ahler, B.A., 1990. Gold and Copper mineralization at the El Indio deposit, Chile. Journal of Geochemical Exploration 36, 233–266.

Jobson, D.H., Boulter, C.A., Foster, R.P., 1994. Structural controls and genesis of epithermal gold-bearing breccias at the Lebong Tandai mine, Western Sumatra, Indonesia. Journal of Geochemical Exploration 50, 409–428.

Karakaya, N., 2009. REE and HFS element behaviour in the alteration facies of the Erenler Dağı Volcanics (Konya, Turkey) and kaolinite occurrence. Journal of Geochemical Exploration 101, 185–208.

Kerrich, R., Goldfarb, R.J., Richards, J.P., 2005. Metallogenic Provinces in an Evolving Geodynamic Framework. Economic Geology 100, 1097–1136.

Kesler, S.E., Deditius, A.P., 2007. Geochemistry of Se and Te in Arsenian Pyrite : New Evidence for the Role of Se and Te Hydrothermal Complexes in Carlin and Epithermal-type Deposits. Geologian tutkimuskeskus, Opas 53 – Geological Survey of Finland, Guide 53 57–59.

Kesler, S.E., Russell, N., Seaward, M., Rivera, J., McCurdy, K., Cumming, G.L., Sutter, J.F., 1981. Geology and Geochemistry of Sulfide Mineralization Underlying the Pueblo Viejo Gold-Silver Oxide Deposit , Dominican Republic. Economic Geology 76, 1096–1117.

King, J.J., Williams-Jones, A.E., Van Hinsberg, V.J., Mulja, T., Williams-Jones, G., n.d. High-Sulphidation Epithermal Au (Ag-Cu) Ore Formation by Condensed Magmatic Vapours on Sangihe Island, Indonesia.

Kirkham, R. V, Dunne, K.P.E., 2000. World Distribution of Porphyry, Porphyry-Related Skarn, and Bulk-mineable Epithermal Deposits, Geological Survey of Canada, unpublished. Geological Survey of Canada Open File, 26 p.

Knight, J.E., 1977. A thermochemical Study of Alunite, Enargite, Luzonite, and Tennantite Deposits. Economic Geology 72, 1321–1336.

Krinov, D.I., 2008. Geochemical Zoning of Pyrite and Arsenopyrite Individuals from the Klyuchevskoe Gold Deposit , Eastern Transbaikalia. Geochemistry International 46, 1005–1015.

Kullerud, G., Yoder, S., 1959. Pyrite Stability Relations in the Fe-S System. Economic Geology 54, 533–572.

Landtwing, M.R., Furrer, C.F., Redmond, P.B., Pettke, T., Guillong, M., Heinrich, C.A., 2010. The Bingham Canyon Porphyry Cu-Mo-Au Deposit. III. Zoned Copper-Gold Ore Deposition by Magmatic Vapor Expansion. Economic Geology 105, 91–118.

Large, R., Danyushevsky, L., Hallmeier, Hollit, C., Maslennikov, V., Meffre, S., Gilbert, S., 2009. Gold and Trace Element Zonation in Pyrite Using a Laser Imaging Technique: Implications for the Timing of Gold in Orogenic and Carlin-Style Sediment-Hosted Deposits. Economic Geology 104, 635–668.

Lerchbaumer, L., Audétat, A., 2012. High Cu concentrations in vapor-type fluid inclusions: An artifact? Geochimica et Cosmochimica Acta 88, 255–274.

Lewis, A.J., Palmer, M.R., Sturchio, N.C., Kemp, A.J., 1997. The rare earth element geochemistry of acid-sulphate and acid-sulphate-chloride geothermal systems from Yellowstone National Park, Wyoming, USA. Geochimica et Cosmochimica Acta 61, 695–706.

Lindgren, W., 1933. Mineral Deposits. McGraw-Hill, New York.

Lottermoser, B.G., 1992. Rare earth elements and hydrothermal ore formation processes. Ore Geology Reviews 7, 25–41.

MacLean, W.H., Kranidiotis, P., 1987. Immobile Elements as Monitors of Mass Transfer in Hydrothermal Alteration: Phelps Dodge Massive Sulphide Deposit, Matagami, Quebec. Economic Geology 82, 951–962.

MacPherson, C.G., Forde, E.J., Hall, R., Thirlwall, M.F., 2003. Geochemical evolution of magmatism in an arc-arc collision: the Halmahera and Sangihe arcs, eastern Indonesia, in: Intra-Oceanic Subduction Systems: Tectonic and Magmatic Processes. pp. 207–220.

Macpherson, C.G., Hall, R., 2002. Timing and tectonic controls in the evolving orogen of SE Asia and the western Pacific and some implications for ore generation, in: Blundell, D.J., Neubauer, F., von Quadt, A. (Eds.), The Timing and Location of Major Ore Deposits in an Evolving Orogen. Geological Society of London, London, pp. 1–19.

Maddox, L.M., Bancroft, G.M., Scaini, M.J., Lorimer, J.W., 1998. Invisible gold: comparison of Au deposition on pyrite and arsenopyrite. The American Mineralogist 83, 1240–1245.

Marcoux, E., Milesi, J., 1994. Epithermal gold deposits in West Java, Indonesia: geology, age and crustal source. Journal of Geochemical Exploration 50, 393–408.

Maske, S., Skinner, B.J., 1971. Studies of the sulfosalts of copper; I, Phases and phase relations in the system Cu-As-S. Economic Geology 66, 901–918.

Mavrogenes, J., Henley, R.W., Reyes, A.G., Berger, B., 2010. Sulfosalt Melts: Evidence of High-Temperature Vapor Transport of Metals in the Formation of High-Sulphidation Lode Gold Deposits. Economic Geology 105, 257–262.

Michard, A., 1989. Rare Earth element systematics in hydrothermal fluids. Geochimica et Cosmochimica Acta 53, 745–750.

Migdisov, A.A., Williams-Jones, A.E., Hurtig, N., n.d. A predictive model for metal transport by vapor in ore-forming magmatic-hydrothermal systems 1–20.

Migdisov, A.A., Williams-Jones, A.E., Suleimenov, O.M., 1999. Solubility of chlorargyrite (AgCl) in water vapor at elevated temperatures and pressures. Geochimica et Cosmochimica Acta 63, 3817–3827.

Migdisov, A.A., Williams-Jones, A.E., Wagner, T., 2009. An experimental study of the solubility and speciation of the Rare Earth Elements (III) in fluoride- and chloride-bearing aqueous solutions at temperatures up to 300°C. Geochimica et Cosmochimica Acta 73, 7087–7109.

Miller, S.E., Heath, G.R., Gonzalez, R.D., 1982. Effects of Temperature on the Sorption of Lanthanides by Montmorillonite. Clays and Clay Minerals 30, 111–122.

Moritz, R., Kouzmanov, K., Petrunov, R., 2004. Late Cretaceous Cu – Au epithermal deposits of the Panagyurishte district, Srednogorie zone, Bulgaria. Swiss Bulletin of Mineralogy and Petrology 84, 79–99.

Morrice, M.G., Gill, J.B., 1986. Spatial Patterns in the Mineraloogy of Island Arc Magma Series: Sangihe Arc, Indonesia. Journal of Volcanology and Geothermal Research 29, 311–353.

Morrice, M.G., Jezek, P.A., Gill, J.B., Whitford, D.J., Monoarfa, M., 1983. An Introduction to the Sangihe Arc: Volcanism Accompanying Arc - Arc Collision in the Molucca Sea Indonesia. Journal of Volcanology and Geothermal Research 19, 135–165.

Mountain, B.W., Seward, T.M., 2003. Hydrosulfide/sulfide complexes of copper (I): Experimental confirmation of the stoichiometry and stability of Cu (HS)2- to elevated temperatures. Geochimica et Cosmochimica Acta 67, 3005–3014.

Muntean, J.L., Kesler, S.E., Russell, N., 1990. Evolution of the Monte Negro Acid Sulfate Au-Ag Deposit, Pueblo Viejo, Dominican Republic: Important Factors in Grade Development. Economic Geology 85, 1738–1758.

Oberthür, T., Weiser, T., Amanor, J., Chryssoulis, S., 1997. Mineralogical setting and distribution of gold in quartz veins and sulfide ores of the Ashanti mine and other deposits in the Ashanti belt of Ghana: genetic implications. Mineralium Deposita 32, 2–15.

Pacevski, A., 2012. Texture and Composition of Pb-bearing Pyrite from the Coka Marin Polymetallic Deposit, Serbia, Controlled by Nanoscale Inclusions. The Canadian Mineralogist 50, 1–20.

Pacevski, A., Libowitzky, E., Zivkovic, P., Dimitrijevic, R., Cvetkovic, L., 2008. Copper-Bearing Pyrite from the Coka Marin Polymetallic Deposit, Serbia: Mineral Inclusions or True Solid-Solution? The Canadian Mineralogist 46, 249–261.

Pacevski, A., Moritz, R., Kouzmanov, K., Marquardt, K., Zivkovic, P., Cvetkovic, L., 2012. Texture and composition of Pb-bearing pyrite from the Coka Marin Polymetallic Deposit, Serbia, Controlled by Nanoscale Inclusions. The Canadian Mineralogist 50, 1–20.

Palenik, C.S., Utsunomiya, S., Reich, M., Kesler, S.E., Wang, L., Ewing, R.C., 2004. "Invisible" gold revealed: Direct imaging of gold nanoparticles in a Carlin-type deposit. The American Mineralogist 89, 1359–1366.

Pals, D.W., Spry, P.G., Chryssoulis, S.L., 2003. Invisible Gold and Tellurium in Arsenic-Rich Pyrite from the Emperor Gold Deposit, Fiji: Implications for Gold Distribution and Deposition. Economic Geology 98, 479–493.

Posfai, M., Buseck, P.R., 1998. Relationships between microstructure and composition in enargite and luzonite. The American Mineralogist 83, 373–382.

Pridmore, D.F., Shuey, R.T., 1976. The electrical resistivity of galena, pyrite, and chalcopyrite. The American Mineralogist 61, 248–259.

Radcliff, D., McSween, H.T., 1970. Copper Zoning in Pyrite from Cerro de Pasco, Peru: Reply. The American Mineralogist 55, 527–528.

Rakovan, J., Mcdaniel, D., Reeder, R., 1997. Use of surface-controlled REE sectoral zoning in apatite from Llallagua, Bolivia, to determine a single-crystal SmNd age. Earth and Planetary Science Letters 146, 329–336.

Ransome, F.L., 1907. The Association of Alunite with Gold in the Goldfield District, Nevada. Economic Geology 2, 667–692.

Reeder, R., Paquette, J., 1989. Sector zoning in natural and synthetic calcites. Sedimentary Geology 65, 239–247.

Reeder, R.J., 1991. An Overview of Zoning in Carbonate Minerals, in: Barker, C.E., Kopp, O.C. (Eds.), Luminescence Microscopy and Spectroscopy: Qualitative and Quantitative Applications. Society for Sedimentary Geology, pp. 77–82.

Reich, M.R., Kesler, S.E., Utsunomiya, S., Palenik, C.S., Chryssoulis, S.L., Ewing, R., 2005. Solubility of gold in arsenian pyrite. Geochimica et Cosmochimica Acta 69, 2781–2796.

Royle, D.Z., 2007. Project Review, Indonesian Gold Projects.

Rye, R.O., 1993. The evolution of magmatic fluids in the epithermal environment; the stable isotope perspective. Economic Geology 88, 733–752.

Rye, R.O., 2005. A review of the stable-isotope geochemistry of sulfate minerals in selected igneous environments and related hydrothermal systems. Chemical Geology 215, 5–36.

Rye, R.O., Bethke, P.M., Wasserman, M.D., 1992. The stable isotope geochemistry of acid sulfate alteration. Economic Geology 87, 225–262.

Salvi, S., Pokrovski, G.S., Schott, J., 1998. Experimental investigation of aluminum-silica aqueous complexing at 300C. Chemical Geology 151, 51–67.

Scher, S., Williams-Jones, A.E., Williams-Jones, G., n.d. Fumarolic Activity, Acid-Sulphate Alteration and High-Sulphidation Epithermal Precious Metal Mineralization in the Crater of Kawah Ijen Volcano, Java, Indonesia. Economic Geology.

Seo, J.H., Guillong, M., Heinrich, C.A., 2009. The role of sulfur in the formation of magmatic–hydrothermal copper–gold deposits. Earth and Planetary Science Letters 282, 323–328.

Sharman, E.R., 2011. Application of multiple sulfur isotope analysis to Archean ore-forming processes.

Shtukenberg, A.G., Punin, Y.O., Artamonova, O.I., 2009. Effect of crystal composition and growth rate on sector zoning in solid solutions grown from aqueous solutions. Mineralogical Magazine 73, 385–398.

Siebert, L., Simkin, T., 2002. Volcanoes of the World: an Illustrated Catalog of Holocene Volcanoes and their Eruptions. Smithsonian Institution, Global Volcanism Program Digital Information Series, GVP-3, (http://volcano.si.edu/world/) 297–8.

Sillitoe, R.H., Angeles, C.A., Comia, G.M., Antioquia, E., Abeya, R.B., 1990. An acid-sulphate-type lode gold deposit at Nalesbitan, Luzon, Philippines. Journal of Geochemical Exploration 35, 387–411.

Simmons, S.F., Browne, P., 1990. Mineralogic, alteration and fluid-inclusion studies of epithermal gold-bearing veins at the Mt. Muro Prospect, Central Kalimantan (Borneo), Indonesia. Journal of Geochemical Exploration 35, 63–103.

Simmons, S.F., White, N.C., John, D., 2005. Geological characteristics of epithermal precious and base metal deposits, in: Hedenquist, J.W. (Ed.), Economic Geology 100th Anniversary Volume. Society of Economic Geologists, Denver, Colorado, pp. 485–522.

Simon, G., Huang, H., Penner-Hahn, J.E., Kesler, S.E., Kao, L.-S., 1999. Oxidation state of gold and arsenic in gold-bearing arsenian pyrite. American Mineralogist 84, 1071–1079.

Springer, G., 1969. Compositional Variations in Enargite and Luzonite. Mineralium Deposita 4, 72–74.

Steele, I.M., Cabri, L.J., Gaspar, J.C., McMahon, G., Marquez, M.A., Vasconcellos, M.A.Z., 2000. Comparative Analysis of Sulfides for Gold Using SXRF and SIMS. The Canadian Mineralogist 38, 1–10.

Stefánsson, A., Seward, T.M., 2003. Stability of chloridogold(I) complexes in aqueous solutions from 300 to 600°C and from 500 to 1800 bar. Geochimica et Cosmochimica Acta 67, 4559–4576.

Stefánsson, A., Seward, T.M., 2004. Gold(I) complexing in aqueous sulphide solutions to 500°C at 500 bar. Geochimica et Cosmochimica Acta 68, 4121–4143.

Stoffregen, R.E., 1987. Genesis of acid-sulfate alteration and Au-Cu-Ag mineralization at Summitville, Colorado: Economic Geology 82, 1575–1591.

Stoffregen, R.E., Alpers, C.N., 1987. Woodhouseite and svanbergite in hydrothermal ore deposits; products of apatite destruction during advanced argillic alteration. The Canadian Mineralogist 25, 201–211.

Stoffregen, R.E., Cygan, G.L., 1990. An experimental study of Na-K exchange between alunite and aqueous sulfate solutions. The American Mineralogist 75, 209–220.

Stone, M., 2010. Independent Technical Report: Sangihe Property, Sangihe Island, North Sulawesi, Indonesia, Structure.

Su, W., Zhang, H., Hu, R., Ge, X., Xia, B., Chen, Y., Zhu, C., 2011. Mineralogy and geochemistry of gold-bearing arsenian pyrite from the Shuiyindong Carlin-type gold deposit, Guizhou, China: implications for gold depositional processes. Mineralium Deposita 47, 653–662.

Tauson, V.L., Kravtsova, R.G., Grebenshchikova, V.I., Lustenberg, E.E., Lipko, S. V, 2009. Surface Typochemistry of Hydrothermal Pyrite : Electron Spectroscopic and Scanning Probe Microscopic Data . II . Natural Pyrite. Geochemistry International 47, 231–243.

Taylor, B.E., 2007. Epithermal Gold Deposits, in: Goodfellow, W.D. (Ed.), Mineral Deposits of Canada: A Synthesis of Major Deposit-Types, District Metallogeny, the Evolution of Geological Provinces, and Exploration Methods. Geological Association of Canada, Mineral Deposits Division, St. John's, pp. 113–139.

The GEBCO_08 Grid, version 20091120, http://gebco.net, 2011. .

Thiersch, P.C., Williams-Jones, A.E., Clark, J.R., 1997. Epithermal mineralization and ore controls of the Shasta Au-Ag deposit, Toodoggone District, British Columbia, Canada. Mineralium Deposita 32, 44–57.

Thode, H.G., Monster, J., Dunford, H.B., 1961. Sulphur isotope geochemistry. Geochimica et Cosmochimica Acta 25, 150–174.

Thode, H.G., Rees, C., 1979. Sulphur isotopes in lunar and meteorite samples. Proceedings of Lunar Planetary Science Conference 10th 1629–1636.

Thompson, J.F.H., Abidin, H.Z., Both, R.A., Martosuroyo, S., Rafferty, W.J., T, A.J.B., 1994. Alteration and epithermal mineralization in the Masupa Ria volcanic center, Central Kalimantan, Indonesia. Journal of Geochemical Exploration 50, 429–456.

Tiller, W.A., 1986. Thermodynamic and kinetic considerations for crystal growth of complex molecules from solution. Journal of Crystal Growth 76, 607–617.

Turner, S.J., Flindell, P.A., Hendri, D., Hardjana, I., Lauricella, P.F., Lindsay, R.P., Marpaung, B., White, G.P., 1994. Sediment-hosted gold mineralisation in the Ratatotok district, North Sulawesi, Indonesia. Journal of Geochemical Exploration 50, 317–336.

Ulrich, T., Gunther, D., Heinrich, C.A., 1999. Gold concentrations of magmatic brines and the metal budget of porphyry copper deposits. Nature 399, 676–679.

USGS, 2004. Shuttle Radar Topography Mission, 1 Arc Second scene SRTM_n03e125, Unfilled Unfinished 2.0, February 2. ed, Processing. Global Land Cover Facility, University of Maryland, College Park, Maryland.

Vesselinov, I., Kerestedjian, T., 1995. Mineralogy Petrology Kinetic aspects of sector zoning in arsenopyrite: a case study. Mineralogy and Petrology 52, 85–106.

Voudouris, P.C., 2010. Conditions of formation of the Mavrokoryfi high-sulfidation epithermal Cu–Ag–Au–Te mineralization (Petrota Graben, NE Greece). Mineralogy and Petrology 101, 97–113.

Warren, I., Simmons, S.F., Mauk, J.L., 2007. Whole-Rock Geochemical Techniques for Evaluating Hydrothermal Alteration, Mass Changes , and Compositional Gradients Associated with Epithermal Au-Ag Mineralization. Economic Geology 102, 923–948.

Watson, E.B., Liang, Y., 1995. A simple model for sector zoning in slowly grown crystals : Implications for growth rate and lattice diffusion , with emphasis on accessory minerals in crustal rocks. The American Mineralogist 80, 1179–1187.

White, N.C., Hedenquist, J.W., 1990. Epithermal environments and styles of mineralization: variations and their causes, and guidelines for exploration. Journal of Geochemical Exploration 36, 445–474.

White, N.C., Leake, M.J., McCaughey, S.N., Parris, B.W., 1995. Epithermal gold deposits of the southwest Pacific. Journal of Geochemical Exploration 54, 87–136.

Widiwijayanti, C., Tiberi, C., Deplus, C., Diament, M., Mikhailov, V., 2004. Geodynamic evolution of the northern Molucca Sea area (Eastern Indonesia) constrained by 3-D gravity field inversion. Tectonophysics 386, 203 – 222.

Wilder, A.M., Seward, T.M., 2002. The Adsorption of Gold(I) Hydrosulfide Complexes by Iron Sufide Surfaces. Geochimica et Cosmochimica Acta 66, 383–402.

Williams-Jones, A.E., Bowell, R.J., Migdisov, A.A., 2009. Gold in Solution. Elements 5, 281–287.

Williams-Jones, A.E., Heinrich, C.A., 2005. Vapor Transport of Metals and the Formation of Magmatic-Hydrothermal Ore Deposits. Economic Geology 100, 1287–1312.

Williams-Jones, A.E., Migdisov, A.A., Archibald, S.A., Xiao, Z., 2002. Vapor-transport of ore metals, in: Hellmann, R., Wood, S.A. (Eds.), Water-Rock Interactions, Ore Deposits, and Environmental Geochemistry A Tribute to David A. Crerar. The Geochemical Society, pp. 279–306.

Xiao, Z., Gammons, C.H., Williams-Jones, A.E., 1998. Experimental study of copper (I) chloride complexing in hydrothermal solutions at 40 to 300 C and saturated water vapor pressure. Geochimica et Cosmochimica Acta 62, 2949–2964.

Zezin, D., Migdisov, A.A., Williams-Jones, A.E., 2011a. PVTx properties of H2O–H2S fluid mixtures at elevated temperature and pressure based on new experimental data. Geochimica et Cosmochimica Acta 75, 5483–5495.

Zezin, D., Migdisov, A.A., Williams-Jones, A.E., 2011b. The solubility of gold in H2O–H2S vapour at elevated temperature and pressure. Geochimica et Cosmochimica Acta 75, 5140–5153.

Zhang, X., 1993. SULF34: A QUICKBASIC program for calculating sulfur isotope distribution in log fO2-pH diagram. Computers & Geosciences 19, 817–823.

Zotov, N., Petrov, K., Dimitrova-Pankova, M., 1990. Infrared spectra of Cu (II)-Co (II) mixed hydroxide nitrates. Journal of Physics and Chemistry of Solids 51, 1199–1205.

Appendix A Bulk Rock Geochemistry

Appendix A Bulk rock compositions of selected Bowone (BOD) and Binebase (BID) samples. Rock- and alteration-type are indicated based on petrographic observations, bulk rock geochemistry and/or X-ray diffraction analyses (IA= Intermediate Argillic, BaEn=barite-enargite veins, AA =Advanced Argillic, see text for description). Samples of the porphyritic dykes and associated igneous breccia were not classified by alteration type as they were emplaced post-alteration/mineralization.

			IA I	IA I	IA I	IA I	IA I	IA I	IA I/BaEn	IA I/BaEn
		d.l.	BOD1-134.5	BOD3-158.8	BOD3-85.4	BOD3-74.1	BOD3-106.4	BOD3-83.3	BOD3-99.2	BOD3-96.8
SiO2	%	0.01	55.4	64.68	8.2	58.66	51.41	48.19	19.69	85.78
TiO2	%	0.001	0.546	0.547	0.036	0.528	0.484	0.541	0.185	0.501
Al2O3	%	0.01	19.8	14.36	0.33	9.13	2.91	2.85	0.3	2.34
Fe2O3	%	0.01	4.26	8.38	35.08	13.45	27.98	30.09	40.04	6.14
MnO	%	0.001	0.008	0.009	0.005	0.006	0.007	0.006	0.006	0.006
MgO	%	0.01	0.75	0.02	0.02	0.01	0.02	0.02	0.02	0.02
CaO	%	0.01	0.78	0.03	0.04	0.06	0.05	0.04	0.03	0.06
Na2O	%	0.01	0.35	0.05	0.06	0.56	0.06	0.07	0.04	0.04
K2O	%	0.01	2.17	0.08	0.02	0.69	0.02	0.04	0.05	0.04
P2O5	%	0.01	0.1	0.08	b.d.	0.06	0.04	0.05	b.d.	0.08
Total	%	0.01	98.53	100.1	66.75	99.83	100.3	100.3	82.61	99.49
LOI	%		14.36	11.82	23.02	16.69	17.33	18.38	22.25	4.49
La	ppm	0.05	15.8	8.91	11	5.52	5.38	6.03	8.38	13.9
Ce	ppm	0.05	32.1	16.5	7.29	8.67	8.77	10	8.03	26
Pr	ppm	0.01	3.83	1.94	0.49	0.96	1.17	1.33	0.79	2.97
Nd	ppm	0.05	14	8	1.21	3.95	4.15	4.67	2.55	12.1
Sm	ppm	0.01	2.66	1.64	0.34	0.81	0.78	0.84	0.61	2.31
Eu	ppm	0.005	0.791	0.596	b.d.	0.197	0.155	0.185	0.472	0.649
Gd	ppm	0.01	2.18	1.2	1.51	0.61	0.57	0.58	1.02	1.49
Tb	ppm	0.01	0.36	0.14	0.04	0.13	0.08	0.09	0.1	0.16
Dy	ppm	0.01	2.19	0.72	0.09	0.76	0.42	0.44	0.28	0.89
Ho	ppm	0.01	0.45	0.15	0.02	0.19	0.09	0.08	0.07	0.16
Er	ppm	0.01	1.41	0.52	0.09	0.75	0.43	0.39	0.23	0.73
Tm	ppm	0.005	0.237	0.103	0.014	0.157	0.08	0.067	0.042	0.146
Y	ppm	0.5	12.8	4	1.3	5.6	3	2.8	2.5	5.2
Yb	ppm	0.01	1.78	0.72	0.08	1.02	0.61	0.52	0.31	1.03
Lu	ppm	0.002	0.31	0.119	0.012	0.173	0.101	0.091	0.053	0.174
Ag	ppm	0.5	b.d.	0.5	11.5	b.d.	0.8	0.7	3.9	b.d.
As	ppm	5	487	64	1350	124	66	22	1180	19
Au	ppb	2	b.d.	306	1500	751	1110	1190	2000	723
Ba	ppm	3	327	129	178900	6822	3050	4094	98830	212
Bi	ppm	0.1	b.d.	8.4	26.7	0.6	1	1.4	3.6	5
Co	ppm	1	13	10	47	23	108	112	104	18
Cr	ppm	20	b.d.	b.d.	b.d.	b.d.	30	30	60	b.d.
Cs	ppm	0.1	0.5	b.d.	0.2	b.d.	0.2	b.d.	0.3	b.d.
Cu	ppm	10	40	170	4550	1780	490	2590	4540	270
Ga	ppm	1	18	28	4	7	10	7	3	8
Ge	ppm	0.5	1.8	2.8	0.6	b.d.	b.d.	b.d.	0.5	1.2
Hf	ppm	0.1	2.2	1.8	0.2	2.4	2	1.6	0.8	3.1
In	ppm	0.1	b.d.	b.d.	0.4	b.d.	b.d.	b.d.	0.2	0.1
Mo	ppm	2	b.d.	5	28	4	12	6	14	13
Nb	ppm	0.2	6.4	2.2	1.1	2.7	2.6	2.7	1.3	2.3
Ni	ppm	20	b.d.	b.d.	b.d.	b.d.	30	30	40	b.d.
Pb	ppm	5	8	49	174	12	38	25	57	18
Rb	ppm	1	36	b.d.	b.d.	1	3	b.d.	2	b.d.
Sb	ppm	0.2	b.d.	2.8	112	10	2.5	b.d.	70.5	4.8
Sc	ppm	1	11	13	b.d.	9	7	5	3	10
Sn	ppm	1	b.d.	b.d.	15	b.d.	1	b.d.	5	b.d.
Sr	ppm	2	248	702	1484	477	298	310	772	515
Ta	ppm	0.01	0.35	0.18	0.06	0.18	0.2	0.15	0.08	0.21
Th	ppm	0.05	2.79	1.53	0.5	1.51	1.19	1.96	0.5	2.05
Tl	ppm	0.05	2.28	1.34	4.56	0.68	1.31	0.48	0.16	0.36
U	ppm	0.01	1.02	0.59	0.14	0.47	0.87	0.55	0.38	1.68
V	ppm	5	128	158	8	80	46	39	11	33
W	ppm	0.5	b.d.	4.1	19.2	4	4.4	9.9	2.6	6.4
Zn	ppm	30	1060	140	b.d.	1030	360	100	b.d.	320
Zr	ppm	1	81	78	6	86	75	58	30	144

									Porphyry	
			AA I	AA I	AA I	AA I	AA I	AA I	AA I/BaEn	AA II
		d.l.	BOD3-49.8	BOD3-55	BOD3-85.5	BOD3-48.6	BOD3-100	BOD3-78.7	BOD3-113.7	BOD42-62.3
SiO2	%	0.01	56.29	43.28	42.65	48.8	29.11	8.74	63.84	49.79
TiO2	%	0.001	0.53	0.373	0.492	0.492	0.377	0.22	0.43	0.46
Al2O3	%	0.01	13.22	6.17	3.28	10.38	0.26	1.25	7.59	10.59
Fe2O3	%	0.01	8.23	15.17	32.38	17.76	46.64	59.44	10.06	16.73
MnO	%	0.001	0.009	0.01	0.007	0.007	0.009	0.014	0.005	0.01
MgO	%	0.01	0.01	0.01	0.02	b.d.	0.02	0.03	0.01	0.02
CaO	%	0.01	0.08	0.05	0.04	0.06	0.04	0.05	0.06	0.06
Na2O	%	0.01	0.76	0.42	0.15	0.48	0.05	0.06	0.84	0.38
K2O	%	0.01	1.35	0.47	0.15	0.71	0.03	0.02	0.81	0.36
P2O5	%	0.01	0.12	0.04	0.04	0.1	0.02	0.02	0.08	0.12
Total	%	0.01	99.58	84.1	99.82	99.86	100.1	100.8	99.15	97.66
LOI	%		18.98	18.11	20.61	21.06	23.58	31.01	15.42	19.13
La	ppm	0.05	8.79	9.01	4.95	7.79	2.93	2.58	6.53	8.76
Ce	ppm	0.05	16.3	14.8	8.42	14	4.48	3.36	11.5	17
Pr	ppm	0.01	1.92	1.96	1.14	1.62	0.57	0.41	1.63	2.08
Nd	ppm	0.05	7.94	7.17	3.91	6.71	2	1.35	5.76	8.38
Sm	ppm	0.01	1.49	1.56	0.75	1.36	0.37	0.26	1.13	1.8
Eu	ppm	0.005	0.442	0.349	0.176	0.377	0.086	0.058	0.318	0.453
Gd	ppm	0.01	1.13	1.55	0.53	0.98	0.27	0.2	0.82	1.23
Tb	ppm	0.01	0.18	0.16	0.07	0.16	0.04	0.03	0.14	0.15
Dy	ppm	0.01	1.04	0.69	0.39	0.82	0.26	0.16	0.75	0.77
Ho	ppm	0.01	0.25	0.15	0.08	0.19	0.08	0.03	0.15	0.16
Er	ppm	0.01	0.86	0.56	0.35	0.73	0.3	0.14	0.66	0.56
Tm	ppm	0.005	0.174	0.101	0.065	0.148	0.057	0.026	0.134	0.104
Y	ppm	0.5	6.6	5.2	2.5	5.5	2.1	1.1	4.5	4
Yb	ppm	0.01	1.16	0.78	0.45	1.04	0.46	0.17	0.9	0.84
Lu	ppm	0.002	0.189	0.13	0.085	0.177	0.075	0.029	0.154	0.162
Ag	ppm	0.5	b.d.	0.6	b.d.	b.d.	2.3	2.2	0.6	1
As	ppm	5	38	314	14	20	167	36	8	74
Au	ppb	2	166	666	1470	580	1710	1690	287	487
Ba	ppm	3	779	95970	1990	1344	1473	511	370	1865
Bi	ppm	0.1	b.d.	b.d.	0.3	b.d.	5.6	1.7	0.1	3.2
Co	ppm	1	10	22	115	10	157	188	25	9
Cr	ppm	20	20	50	b.d.	b.d.	20	20	30	b.d.
Cs	ppm	0.1	b.d.	0.1	b.d.	b.d.	0.2	b.d.	b.d.	0.3
Cu	ppm	10	230	1550	1450	1010	2870	2010	490	410
Ga	ppm	1	18	19	7	32	1	3	11	10
Ge	ppm	0.5	0.8	b.d.	b.d.	b.d.	b.d.	b.d.	b.d.	0.9
Hf	ppm	0.1	2.5	1.9	1.5	2	2.4	0.6	2.2	2
In	ppm	0.1	b.d.	0.2	b.d.	b.d.	0.1	b.d.	0.1	b.d.
Mo	ppm	2	b.d.	3	4	b.d.	21	29	3	2
Nb	ppm	0.2	2.6	2	2.6	2.2	1.9	1	2.1	2.1
Ni	ppm	20	b.d.	b.d.	30	b.d.	40	60	b.d.	b.d.
Pb	ppm	5	23	b.d.	47	62	84	15	14	354
Rb	ppm	1	b.d.	2	1	2	b.d.	1	b.d.	2
Sb	ppm	0.2	1	6.5	b.d.	b.d.	11.5	9.3	0.8	2.1
Sc	ppm	1	13	8	6	13	5	2	8	11
Sn	ppm	1	b.d.	b.d.	b.d.	b.d.	2	b.d.	b.d.	5
Sr	ppm	2	669	564	310	592	60	83	455	641
Ta	ppm	0.01	0.2	0.14	0.14	0.12	0.14	0.06	0.14	0.15
Th	ppm	0.05	1.61	1.3	1.08	1.38	0.72	0.31	1.05	1.24
Tl	ppm	0.05	0.72	0.33	0.75	4.03	0.61	0.82	0.6	2.7
U	ppm	0.01	0.51	0.45	0.79	0.68	0.77	0.35	0.56	0.57
V	ppm	5	132	73	42	148	21	32	88	94
W	ppm	0.5	3.3	1.6	20.3	0.8	1.7	6.1	46	0.5
Zn	ppm	30	430	260	360	460	80	50	270	120
Zr	ppm	1	95	68	59	70	87	18	69	65

			AA II	AA II	AA II	AA II	AA II	AA II	AA II	AA II
		d.l.	BOD3-125.4	BOD3-46.9	BOD3-34.4	BOD3-27.3	BOD3-79.5	BOD3-132.9	BOD3-41	BOD3-65.4
SiO2	%	0.01	51.37	53.65	20.65	7.08	65.52	59.09	39.59	56.91
TiO2	%	0.001	0.474	0.603	0.684	1.029	0.485	0.624	0.567	0.431
Al2O3	%	0.01	11.21	12.29	19.21	24.05	6.24	16.11	3.97	5.67
Fe2O3	%	0.01	12.06	12.72	30.85	19.86	14.38	7.88	32.64	18.17
MnO	%	0.001	0.003	0.008	0.012	0.005	0.006	0.016	0.017	0.005
MgO	%	0.01	b.d.	0.02	0.03	0.03	b.d.	0.02	0.02	0.02
CaO	%	0.01	0.07	0.12	0.07	0.12	0.05	0.08	0.07	0.08
Na2O	%	0.01	0.92	0.71	0.17	1.22	0.05	0.23	0.16	0.43
K2O	%	0.01	1.21	0.71	0.18	3.49	0.01	0.17	0.21	0.42
P2O5	%	0.01	0.08	0.2	0.22	0.43	0.1	0.18	0.13	0.11
Total	%	0.01	97.92	100	99.21	98.86	98.17	98.46	99.66	100
LOI	%		20.52	19	27.12	41.55	11.31	14.06	22.28	17.79
La	ppm	0.05	7.62	10.8	8.29	16.8	8.97	11.4	10.4	8.48
Ce	ppm	0.05	13.9	20.5	15.5	31.1	15.8	22.1	19.4	15.4
Pr	ppm	0.01	1.61	2.43	2.06	3.44	2.12	2.59	2.68	2.08
Nd	ppm	0.05	6.79	10.4	7.02	13.5	7.48	11.2	9.94	7.45
Sm	ppm	0.01	1.43	2.33	1.25	2.4	1.34	2.45	2.19	1.4
Eu	ppm	0.005	0.425	0.689	0.319	0.496	0.368	0.854	0.68	0.415
Gd	ppm	0.01	1.15	2.15	0.87	1.53	0.88	1.96	1.77	1
Tb	ppm	0.01	0.15	0.31	0.13	0.19	0.12	0.24	0.22	0.15
Dy	ppm	0.01	0.85	1.69	0.71	0.95	0.65	1.23	1.14	0.77
Ho	ppm	0.01	0.17	0.36	0.16	0.2	0.13	0.26	0.22	0.18
Er	ppm	0.01	0.62	1.21	0.59	0.71	0.6	0.99	0.83	0.74
Tm	ppm	0.005	0.122	0.237	0.115	0.14	0.123	0.184	0.144	0.151
Y	ppm	0.5	5.2	10.4	4	5.3	4.2	6.9	6.6	5.1
Yb	ppm	0.01	0.84	1.64	0.83	1.06	0.9	1.35	1.02	1.07
Lu	ppm	0.002	0.137	0.274	0.138	0.183	0.15	0.218	0.164	0.174
Ag	ppm	0.5	b.d.	b.d.	1.9	3.2	b.d.	b.d.	1.6	2.8
As	ppm	5	28	56	141	55	106	104	442	311
Au	ppb	2	300	396	1390	1240	717	345	1310	1080
Ba	ppm	3	688	1458	1736	1546	2354	1517	2519	4145
Bi	ppm	0.1	1.1	0.2	0.7	1.2	b.d.	1.5	0.7	0.3
Co	ppm	1	28	12	28	17	53	11	25	26
Cr	ppm	20	b.d.	b.d.	30	40	30	20	30	30
Cs	ppm	0.1	b.d.	b.d.	0.2	0.1	b.d.	b.d.	b.d.	b.d.
Cu	ppm	10	350	710	1460	640	1440	180	3500	2720
Ga	ppm	1	10	48	58	184	13	18	24	19
Ge	ppm	0.5	0.6	b.d.	b.d.	b.d.	1.7	0.7	0.6	1.2
Hf	ppm	0.1	1.7	2.8	3.3	4	3.6	2.1	2.1	2.2
In	ppm	0.1	0.2	b.d.	b.d.	0.2	b.d.	b.d.	b.d.	0.1
Mo	ppm	2	2	4	9	12	18	15	11	5
Nb	ppm	0.2	2	3	2.9	4.2	2.4	2.6	2.2	2.2
Ni	ppm	20	b.d.	b.d.	30	20	20	b.d.	30	b.d.
Pb	ppm	5	14	30	46	149	b.d.	17	11	181
Rb	ppm	1	b.d.	1	1	2	b.d.	b.d.	1	1
Sb	ppm	0.2	1.3	1.9	8.7	8.8	34.4	2.1	35.6	24.6
Sc	ppm	1	10	13	28	35	10	14	10	9
Sn	ppm	1	1	b.d.	4	5	3	b.d.	6	4
Sr	ppm	2	532	931	1717	2840	682	1060	655	571
Ta	ppm	0.01	0.15	0.19	0.21	0.3	0.21	0.2	0.17	0.16
Th	ppm	0.05	1.25	1.78	2.41	3.8	1.66	1.85	1.52	1.33
Tl	ppm	0.05	1.15	2.52	4.41	3.81	0.93	1.53	0.49	4.59
U	ppm	0.01	0.54	0.63	1.25	5.45	1.91	1.45	0.84	0.51
V	ppm	5	109	174	259	410	69	157	91	59
W	ppm	0.5	6.4	7.9	2.2	5.3	2.1	0.8	3.4	12.9
Zn	ppm	30	500	1070	290	310	40	120	70	300
Zr	ppm	1	75	98	99	141	109	95	55	73

			AA II/BaEn	AA III	AA III	AA III	Least altered	IA I	IA I	IA I
		d.l.	BOD3-65.8	BOD1-115	BOD1-124.9	BOD3-122.6	PANTAI	BID70-61.7	BID24-101	BID39-41.2
SiO2	%	0.01	17.64	59.72	61.62	39.9	58.37	63.89	65.1	29.58
TiO2	%	0.001	0.082	0.61	0.773	0.298	0.546	0.627	0.706	1.423
Al2O3	%	0.01	0.81	16.49	16.96	3.6	15.2	11.62	12.71	26.73
Fe2O3	%	0.01	31.27	7.98	5.73	32.09	5.59	9.89	8.13	18.12
MnO	%	0.001	0.003	0.014	0.022	0.006	0.132	0.005	0.005	0.004
MgO	%	0.01	0.02	0.02	0.03	0.02	2.86	0.04	0.03	0.06
CaO	%	0.01	0.04	0.11	0.1	0.04	7.02	0.06	0.07	0.11
Na2O	%	0.01	0.06	0.07	0.14	0.31	2.79	0.04	0.04	0.07
K2O	%	0.01	b.d.	0.03	0.03	0.29	1.1	0.26	0.02	0.05
P2O5	%	0.01	b.d.	0.21	0.11	0.04	0.2	0.15	0.16	0.43
Total	%	0.01	77.25	98.39	99.98	98.21	99.55	98.27	98.77	98.61
LOI	%		22.94	13.13	14.47	21.62	5.74	11.69	11.81	22.04
La	ppm	0.05	6.84	12.1	9.83	3.87	12.5	7.53	9.05	10.5
Ce	ppm	0.05	5.76	24.7	17.9	5.81	24.6	14.6	18.6	16.1
Pr	ppm	0.01	0.53	2.84	2.1	0.71	3.13	1.52	2.13	1.35
Nd	ppm	0.05	1.48	12	8.17	2.53	12.8	6.08	8.82	3.57
Sm	ppm	0.01	0.35	2.44	1.56	0.53	2.96	1.05	1.88	0.39
Eu	ppm	0.005	0.18	0.616	0.784	0.181	1.03	0.352	0.595	0.2
Gd	ppm	0.01	0.76	1.59	1.19	0.49	2.89	0.73	1.36	0.32
Tb	ppm	0.01	0.05	0.2	0.2	0.06	0.48	0.12	0.17	0.05
Dy	ppm	0.01	0.17	1.04	1.25	0.28	2.87	0.81	0.86	0.32
Ho	ppm	0.01	0.03	0.23	0.28	0.06	0.6	0.21	0.19	0.09
Er	ppm	0.01	0.13	0.78	0.99	0.24	1.81	0.75	0.71	0.37
Tm	ppm	0.005	0.022	0.142	0.18	0.044	0.283	0.136	0.135	0.079
Y	ppm	0.5	1.7	6.2	7.1	1.8	16.6	6.1	5.5	2.4
Yb	ppm	0.01	0.16	1.17	1.42	0.31	1.97	1.09	1.1	0.75
Lu	ppm	0.002	0.028	0.23	0.28	0.055	0.331	0.205	0.209	0.173
Ag	ppm	0.5	3.7	b.d.	1.1	4.5	b.d.	0.6	b.d.	1.9
As	ppm	5	2500	60	125	242	b.d.	10	19	25
Au	ppb	2	1280	273	130	1760	b.d.	57	66	391
Ba	ppm	3	106900	802	1609	13280	181	664	107	1837
Bi	ppm	0.1	0.3	0.4	1	0.6	b.d.	0.4	0.5	4.2
Co	ppm	1	54	8	10	111	14	8	21	80
Cr	ppm	20	30	30	20	30	20	b.d.	b.d.	200
Cs	ppm	0.1	b.d.	b.d.	0.3	0.3	1.5	b.d.	b.d.	0.3
Cu	ppm	10	15000	70	90	2470	30	200	100	490
Ga	ppm	1	6	13	19	8	14	8	12	16
Ge	ppm	0.5	1.2	3.7	2.1	0.6	1.5	1.4	1.7	2
Hf	ppm	0.1	0.3	2.4	2.8	1.1	2.3	2.1	2.2	4.2
In	ppm	0.1	0.2	b.d.	b.d.	0.1	b.d.	b.d.	b.d.	b.d.
Mo	ppm	2	21	58	49	38	b.d.	b.d.	10	19
Nb	ppm	0.2	0.6	4.2	2.9	1.5	2.7	2.7	2.4	4.9
Ni	ppm	20	20	b.d.	b.d.	50	b.d.	b.d.	b.d.	30
Pb	ppm	5	b.d.	74	120	28	b.d.	15	25	55
Rb	ppm	1	1	b.d.	b.d.	2	21	4	b.d.	3
Sb	ppm	0.2	120	4.5	10.4	27.7	b.d.	1.7	b.d.	4.1
Sc	ppm	1	2	14	23	5	18	14	14	18
Sn	ppm	1	6	4	2	3	b.d.	3	3	11
Sr	ppm	2	1109	685	295	411	367	1040	688	3854
Ta	ppm	0.01	0.04	0.19	0.2	0.1	0.17	0.15	0.17	0.3
Th	ppm	0.05	0.32	1.83	1.93	0.52	1.83	1.22	1.03	1.73
Tl	ppm	0.05	0.07	1.21	3.13	0.4	0.1	0.38	0.75	0.39
U	ppm	0.01	0.25	0.67	12.6	0.4	0.77	0.38	0.91	0.59
V	ppm	5	17	120	199	36	171	120	123	222
W	ppm	0.5	1.6	b.d.	b.d.	2.5	2.4	0.8	0.8	2.4
Zn	ppm	30	190	360	960	b.d.	60	b.d.	80	b.d.
Zr	ppm	1	9	89	101	36	89	72	80	130

				Crystal Tuff						
			IA II	IA II	IA II	IA II	IA II	IA II	IA II	IA I
		d.l.	BID43-39.5	BID26-102.5	BID15-84.2	BID18-144.5	BID18-183.2	BID23-68.6	BID26-58	BOD3-159
SiO2	%	0.01	66.18	60.58	58.02	56.54	56.83	56.02	47.52	63.25
TiO2	%	0.001	0.587	0.68	0.771	0.796	0.852	0.667	0.902	0.236
Al2O3	%	0.01	12.6	14.96	16.24	17.84	18.21	15.5	19.49	16.53
Fe2O3	%	0.01	5.45	6.7	7.15	6.92	6.79	6.86	6.34	1.65
MnO	%	0.001	0.017	0.023	0.018	0.015	0.027	0.019	0.025	0.061
MgO	%	0.01	0.99	1.04	0.96	1.86	0.84	1.15	0.68	0.86
CaO	%	0.01	0.33	0.38	0.14	0.45	0.8	0.57	0.62	2.13
Na2O	%	0.01	0.04	0.03	0.07	0.06	0.06	0.06	0.09	1.14
K2O	%	0.01	3.55	3.79	4.29	2.12	2.41	4.17	6.09	8.13
P2O5	%	0.01	0.16	0.17	0.15	0.23	0.2	0.14	0.23	0.07
Total	%	0.01	99.88	99.07	99.25	98.31	99.5	100.5	98.29	99.55
LOI	%		9.97	10.72	11.44	11.47	12.49	15.38	16.31	5.49
La	ppm	0.05	6.12	6.04	8.04	10.3	10.5	11.9	12.7	16.6
Ce	ppm	0.05	11.7	13.5	18.3	21.5	21.7	23.3	25.6	30.4
Pr	ppm	0.01	1.46	1.69	2.52	2.83	2.93	3.04	3.33	3.32
Nd	ppm	0.05	6.05	7.94	11.1	12.2	12.4	12.6	14.1	11
Sm	ppm	0.01	1.98	2.51	2.98	3.37	3.36	2.91	3.51	1.92
Eu	ppm	0.005	0.581	0.84	0.858	0.947	1.09	0.891	1.1	0.47
Gd	ppm	0.01	2.46	3.12	3.11	3.49	3.58	2.97	3.74	1.53
Tb	ppm	0.01	0.46	0.57	0.55	0.58	0.63	0.52	0.65	0.25
Dy	ppm	0.01	2.94	3.59	3.39	3.58	3.9	3.28	4.01	1.42
Ho	ppm	0.01	0.61	0.73	0.69	0.77	0.81	0.68	0.82	0.31
Er	ppm	0.01	1.79	2.19	2.04	2.38	2.36	2.04	2.42	1.03
Tm	ppm	0.005	0.277	0.344	0.324	0.37	0.379	0.319	0.382	0.178
Y	ppm	0.5	17.7	21.7	19.2	21.6	22.2	19.2	22.4	9.9
Yb	ppm	0.01	1.92	2.4	2.39	2.62	2.67	2.25	2.64	1.4
Lu	ppm	0.002	0.322	0.411	0.435	0.445	0.466	0.374	0.452	0.273
Ag	ppm	0.5	12.7	6.5	3.2	b.d.	b.d.	b.d.	b.d.	0.5
As	ppm	5	204	43	15	9	10	94	118	9
Au	ppb	2	317	27	54	21	13	b.d.	b.d.	b.d.
Ba	ppm	3	8105	2045	1381	130	139	749	744	889
Bi	ppm	0.1	b.d.	b.d.	b.d.	b.d.	b.d.	b.d.	b.d.	0.5
Co	ppm	1	16	14	14	21	21	16	18	1
Cr	ppm	20	20	b.d.	b.d.	20	b.d.	b.d.	b.d.	b.d.
Cs	ppm	0.1	1.1	2	1.7	1.2	1.3	3	4.4	1
Cu	ppm	10	160	40	50	60	80	60	70	30
Ga	ppm	1	14	14	15	16	17	15	19	14
Ge	ppm	0.5	0.8	0.6	0.5	1.5	1.7	0.7	0.8	1.4
Hf	ppm	0.1	1.9	2.2	2.4	2.6	2.4	2	2.7	3.3
In	ppm	0.1	b.d.	b.d.	b.d.	b.d.	b.d.	b.d.	b.d.	b.d.
Mo	ppm	2	16	3	b.d.	3	b.d.	b.d.	b.d.	5
Nb	ppm	0.2	2.1	2.3	2.8	2.7	3.1	2.3	3.3	6.4
Ni	ppm	20	b.d.	b.d.	b.d.	b.d.	b.d.	b.d.	b.d.	b.d.
Pb	ppm	5	1080	44	54	10	23	30	b.d.	7
Rb	ppm	1	79	82	93	42	52	80	105	106
Sb	ppm	0.2	12.7	9.7	1.8	b.d.	6.7	11.5	9.7	b.d.
Sc	ppm	1	21	26	29	25	32	25	32	3
Sn	ppm	1	2	b.d.	b.d.	b.d.	b.d.	b.d.	b.d.	b.d.
Sr	ppm	2	184	73	59	23	47	54	61	102
Ta	ppm	0.01	0.13	0.14	0.16	0.15	0.16	0.12	0.18	0.54
Th	ppm	0.05	1.29	1.23	1.63	1.59	5.43	1.31	1.85	5.14
Tl	ppm	0.05	4.04	0.9	1.07	0.35	0.28	3.85	2.83	0.63
U	ppm	0.01	5.01	0.74	0.61	0.52	1.84	0.6	0.65	1.54
V	ppm	5	178	201	248	245	285	221	283	21
W	ppm	0.5	3.6	5.6	8.7	2	1.3	b.d.	b.d.	4.9
Zn	ppm	30	3450	320	300	70	320	350	470	60
Zr	ppm	1	67	76	82	92	85	70	100	117

			Rhyolite			Intrusive Porph			
			IA I	IA I	IA I				
		d.l.	BOD3-153.5	BOD3-165.5	BOD3-167.3	BOD1-143.4	BOD42-136.6	BOD77-34.5	BOD7-56.6
SiO2	%	0.01	73.15	69.48	69.69	61.14	64.22	59.45	58.5
TiO2	%	0.001	0.176	0.165	0.178	0.512	0.469	0.519	0.508
Al2O3	%	0.01	13.82	13.5	13.8	17.99	16.27	16.78	16.36
Fe2O3	%	0.01	0.86	1.09	1.48	5.35	4.39	4.92	5.31
MnO	%	0.001	0.032	0.058	0.05	0.081	0.025	0.118	0.377
MgO	%	0.01	0.56	0.79	0.89	1.71	0.7	2.38	1.07
CaO	%	0.01	0.53	2.15	1.6	4.61	3.39	4.2	5.14
Na2O	%	0.01	0.51	1.78	1.85	2.98	2.71	2.71	2.26
K2O	%	0.01	5.96	4.47	6.19	2.72	2.8	2.38	2.17
P2O5	%	0.01	0.09	0.07	0.17	0.27	0.35	0.28	0.25
Total	%	0.01	99.88	98.27	100.3	100.9	100.2	99.44	98.96
LOI	%		4.19	4.72	4.39	3.59	4.9	5.69	7.02
La	ppm	0.05	17	18.4	19.5	17.8	15.5	15.8	14.7
Ce	ppm	0.05	30.4	31.6	36.5	33.5	29.7	30.2	28.7
Pr	ppm	0.01	2.88	3.34	3.59	4.05	3.31	3.64	3.59
Nd	ppm	0.05	9.75	11.1	12.8	15.7	13.6	14.5	14.2
Sm	ppm	0.01	1.58	1.78	2.11	3.25	2.86	3.04	3.04
Eu	ppm	0.005	0.42	0.499	0.628	1.07	0.949	0.95	0.93
Gd	ppm	0.01	1.22	1.39	1.74	3.07	2.66	2.69	2.73
Tb	ppm	0.01	0.19	0.22	0.27	0.49	0.43	0.45	0.44
Dy	ppm	0.01	1.12	1.29	1.55	2.89	2.6	2.7	2.6
Ho	ppm	0.01	0.25	0.27	0.31	0.61	0.54	0.55	0.52
Er	ppm	0.01	0.83	0.91	1	1.87	1.67	1.67	1.61
Tm	ppm	0.005	0.147	0.165	0.18	0.3	0.27	0.267	0.263
Y	ppm	0.5	8.2	9	10.7	18.3	17.2	16	15.5
Yb	ppm	0.01	1.15	1.3	1.42	2.12	1.93	1.94	1.9
Lu	ppm	0.002	0.218	0.246	0.266	0.375	0.344	0.343	0.344
Ag	ppm	0.5	0.5	b.d.	0.5	b.d.	b.d.	b.d.	b.d.
As	ppm	5	9	5	11	b.d.	b.d.	b.d.	20
Au	ppb	2	b.d.	b.d.	b.d.	b.d.	b.d.	b.d.	14
Ba	ppm	3	713	778	855	472	435	647	1054
Bi	ppm	0.1	0.3	0.1	0.5	b.d.	b.d.	b.d.	0.1
Co	ppm	1	b.d.	b.d.	1	10	9	8	8
Cr	ppm	20	b.d.	b.d.	b.d.	b.d.	b.d.	b.d.	b.d.
Cs	ppm	0.1	0.9	0.9	0.7	0.6	0.4	0.7	0.8
Cu	ppm	10	b.d.	b.d.	b.d.	70	10	b.d.	60
Ga	ppm	1	12	11	10	16	15	15	16
Ge	ppm	0.5	1.5	1.6	1.5	2.6	1.5	1.7	1.2
Hf	ppm	0.1	2.7	2.3	2.9	2.9	2.7	2.3	2.3
In	ppm	0.1	b.d.	b.d.	b.d.	b.d.	b.d.	b.d.	b.d.
Mo	ppm	2	b.d.	b.d.	6	b.d.	b.d.	b.d.	b.d.
Nb	ppm	0.2	5.3	5.1	5.6	5.9	4.6	4.6	4.2
Ni	ppm	20	b.d.	b.d.	b.d.	b.d.	b.d.	b.d.	b.d.
Pb	ppm	5	10	18	12	5	9	7	10
Rb	ppm	1	63	74	80	47	35	41	37
Sb	ppm	0.2	b.d.	b.d.	0.7	b.d.	b.d.	b.d.	b.d.
Sc	ppm	1	2	2	2	11	11	10	12
Sn	ppm	1	b.d.	b.d.	b.d.	b.d.	1	b.d.	b.d.
Sr	ppm	2	83	145	117	404	351	348	364
Ta	ppm	0.01	0.47	0.41	0.47	0.32	0.32	0.3	0.29
Th	ppm	0.05	4.55	4.15	4.51	2.78	2.5	2.49	2.41
Tl	ppm	0.05	0.38	0.43	0.68	0.17	0.29	0.18	0.62
U	ppm	0.01	1.35	1.23	1.42	0.85	1.42	0.78	0.67
V	ppm	5	8	7	9	111	102	106	118
W	ppm	0.5	b.d.	b.d.	0.9	b.d.	b.d.	b.d.	b.d.
Zn	ppm	30	120	50	60	190	130	50	50
Zr	ppm	1	94	83	107	118	98	78	90

			yritic Dyke				Igneous Breccia			
		d.l.	BOD47-128.5	BOD2-32.3	BOD2-82	BID24-144	BOD10-141.5	BOD2-72.3	BOD7-43	BOD47-34
SiO2	%	0.01	56.08	59.2	53.74	44.72	58.31	59	55.47	14.51
TiO2	%	0.001	0.482	0.489	0.524	0.672	0.486	0.5	0.725	0.886
Al2O3	%	0.01	16.77	16.51	16.44	14.97	16.38	16.15	21.25	25.56
Fe2O3	%	0.01	4.94	5.51	5.98	6.21	4.42	4.54	3.44	14.82
MnO	%	0.001	0.161	0.058	0.65	0.401	0.364	0.033	0.01	0.016
MgO	%	0.01	3.08	1.89	1.16	4.58	0.96	1.09	0.22	0.02
CaO	%	0.01	5.15	2.53	4.78	7.43	5.78	2.36	0.23	0.06
Na2O	%	0.01	2.71	2.02	1.64	0.05	2.15	1.52	0.06	1.71
K2O	%	0.01	1.96	3.18	2.06	1.93	2.01	2.15	0.34	2.67
P2O5	%	0.01	0.24	0.22	0.27	0.19	0.24	0.27	0.08	0.21
Total	%	0.01	99	99.18	99.26	98.41	99.7	98.67	96.04	98.97
LOI	%		7.42	7.58	12	17.26	8.62	11.04	14.21	38.5
La	ppm	0.05	16.5	21.2	15.5	9.3	16	16.1	14.2	13.7
Ce	ppm	0.05	31.8	41.4	29.3	19.3	29.7	32.1	25.7	25.1
Pr	ppm	0.01	3.45	5.27	3.51	2.53	3.55	3.59	2.9	2.9
Nd	ppm	0.05	14	20.8	13.8	10.9	14	15.1	10.3	10.8
Sm	ppm	0.01	2.86	4.42	2.76	2.86	2.91	3.49	2.08	1.64
Eu	ppm	0.005	0.931	1.26	0.961	0.924	0.925	1.3	0.629	0.377
Gd	ppm	0.01	2.61	4.13	2.64	2.89	2.63	3.68	2.46	0.91
Tb	ppm	0.01	0.41	0.64	0.44	0.51	0.44	0.6	0.49	0.12
Dy	ppm	0.01	2.42	3.73	2.62	3.19	2.63	3.56	3.13	0.71
Ho	ppm	0.01	0.5	0.75	0.54	0.65	0.55	0.73	0.65	0.18
Er	ppm	0.01	1.57	2.2	1.62	1.89	1.66	2.17	1.95	0.67
Tm	ppm	0.005	0.251	0.341	0.261	0.295	0.267	0.35	0.311	0.124
Y	ppm	0.5	15.4	22.9	16.1	18.9	16.2	21.1	18.7	4.7
Yb	ppm	0.01	1.82	2.39	1.87	2.07	1.88	2.53	2.27	0.98
Lu	ppm	0.002	0.327	0.41	0.327	0.356	0.329	0.449	0.409	0.184
Ag	ppm	0.5	b.d.	b.d.	b.d.	b.d.	0.5	b.d.	0.9	0.8
As	ppm	5	30	6	8	34	20	10	97	38
Au	ppb	2	9	4	21	3	22	31	59	502
Ba	ppm	3	681	535	1043	475	854	1014	16940	2539
Bi	ppm	0.1	b.d.	b.d.	0.2	b.d.	b.d.	0.2	0.2	0.6
Co	ppm	1	8	9	8	18	8	7	27	34
Cr	ppm	20	b.d.	b.d.	b.d.	100	b.d.	b.d.	20	30
Cs	ppm	0.1	0.3	0.6	0.9	2.1	0.5	0.6	0.3	b.d.
Cu	ppm	10	40	160	100	50	80	80	250	540
Ga	ppm	1	16	14	15	13	14	15	19	50
Ge	ppm	0.5	1.3	1.6	1.1	0.8	1.1	1.3	1.4	b.d.
Hf	ppm	0.1	2.8	2.1	2.3	2	2.1	2.1	3.2	3.2
In	ppm	0.1	b.d.	b.d.	b.d.	b.d.	b.d.	b.d.	b.d.	b.d.
Mo	ppm	2	b.d.	b.d.	b.d.	b.d.	b.d.	b.d.	4	3
Nb	ppm	0.2	4.5	4.6	4.7	3.2	5	4.6	6.1	3.5
Ni	ppm	20	b.d.	b.d.	b.d.	30	b.d.	b.d.	b.d.	b.d.
Pb	ppm	5	13	6	17	b.d.	17	17	29	82
Rb	ppm	1	29	48	27	33	31	44	12	b.d.
Sb	ppm	0.2	b.d.	b.d.	b.d.	b.d.	b.d.	0.8	4.4	3.2
Sc	ppm	1	11	10	12	25	12	11	18	18
Sn	ppm	1	b.d.	b.d.	1	b.d.	b.d.	b.d.	1	9
Sr	ppm	2	383	265	279	68	326	255	624	1633
Ta	ppm	0.01	0.36	0.26	0.3	0.16	0.29	0.32	0.39	0.21
Th	ppm	0.05	2.83	2.23	2.49	1.36	2.68	2.83	3.08	1.8
Tl	ppm	0.05	0.3	3.45	0.34	0.71	0.35	0.58	15.7	1.12
U	ppm	0.01	0.83	0.82	0.83	0.42	0.81	0.85	1.33	1.06
V	ppm	5	104	100	120	201	115	121	131	194
W	ppm	0.5	b.d.	b.d.	b.d.	b.d.	b.d.	b.d.	b.d.	b.d.
Zn	ppm	30	100	280	210	60	80	200	180	90
Zr	ppm	1	104	74	84	75	75	77	116	113

Appendix B Interpreted X-Ray Diffraction Patterns

Appendix B Interpreted X-Ray Spectra showing possible mineral matches made using JADE software.

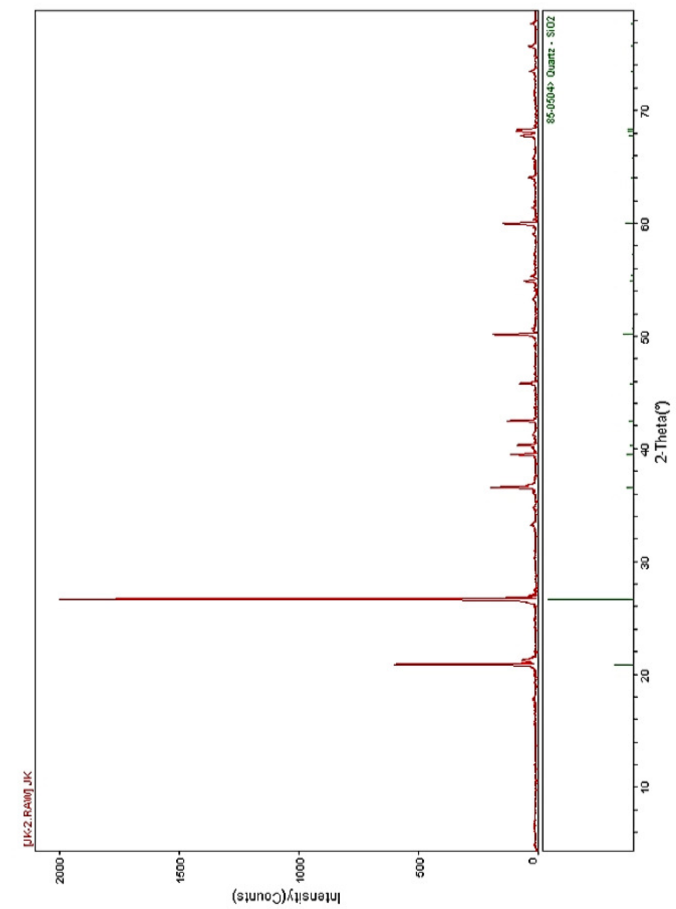
[JK-2.RAW] JK
Intensity(Counts)
0
500
1000
1500
2000
85-0504> Quartz - SiO2
10
20
30
40
50
60
70
2-Theta(°)

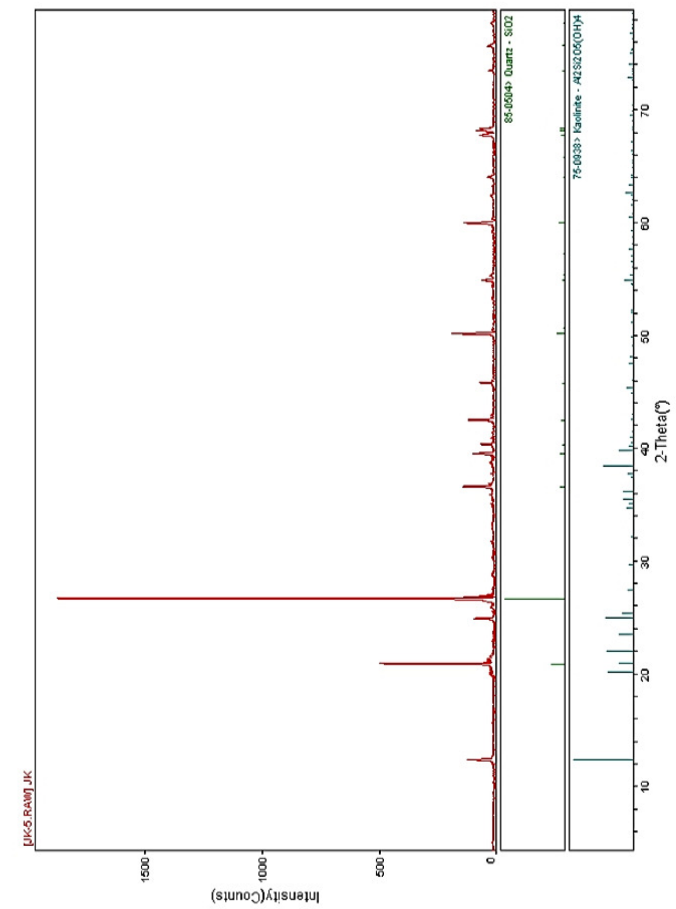
[JK-5.RAW] JK
Intensity(Counts)
0
500
1000
1500
85-0504> Quartz - SiO2
75-0938> Kaolinite - Al2Si2O5(OH)4
10
20
30
40
50
60
70
2-Theta(°)

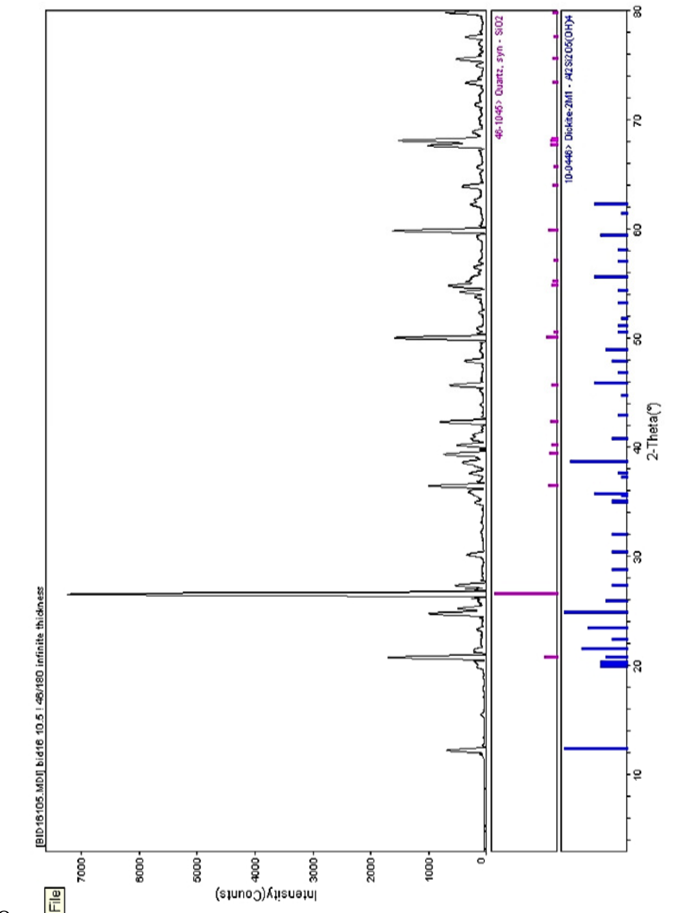
[BID16105.MDI] bid16 10.5 I 45/180 infinite thickness
Intensity(Counts)
0
1000
2000
3000
4000
5000
6000
7000
46-1045> Quartz, syn - SiO2
10-0446> Dickite-2M1 - Al2Si2O5(OH)4
10
20
30
40
50
60
70
80
2-Theta(°)

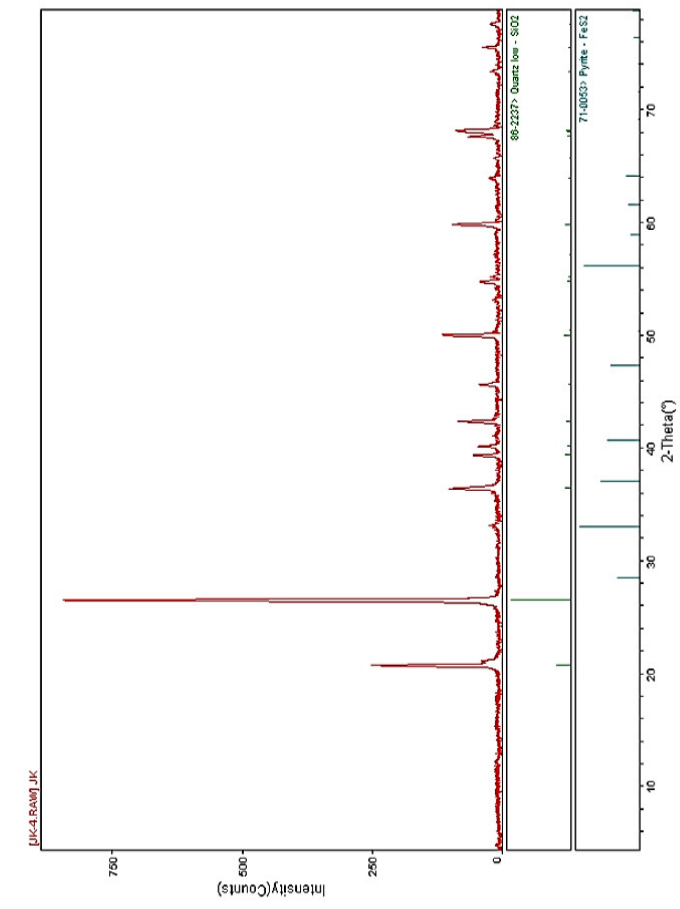
[JK-4.RAW] JK
Intensity(Counts)
0
250
500
750
86-2237> Quartz low - SiO2
71-0053> Pyrite - FeS2
10
20
30
40
50
60
70
2-Theta(°)

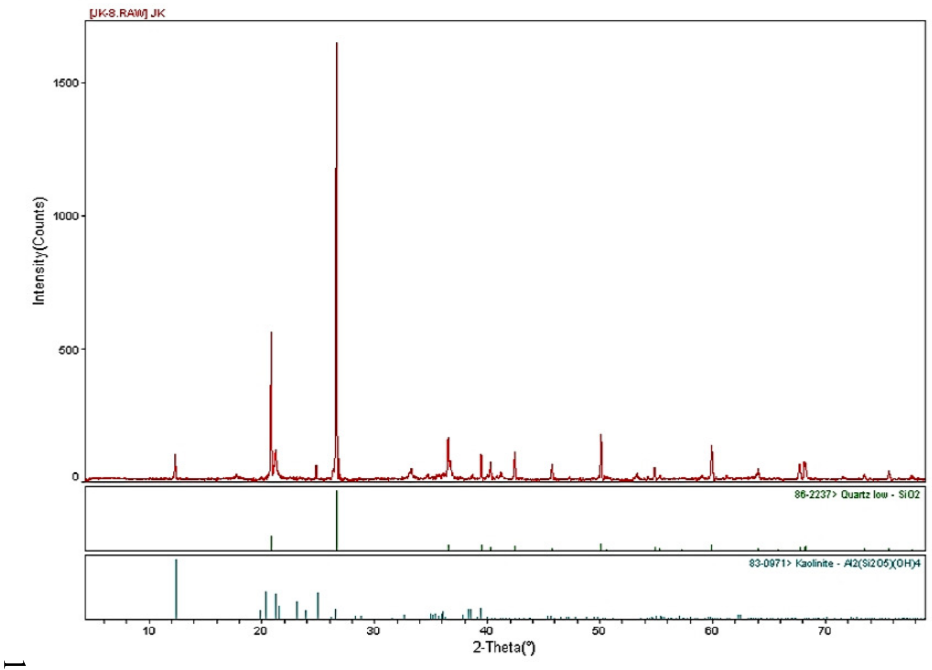
[JK-8.RAW] JK
Intensity(Counts)
1500
1000
500
0
86-2237> Quartz low - SiO2
83-0971> Kaolinite - Al2(Si2O5)(OH)4
10
20
30
40
50
60
70
2-Theta(°)

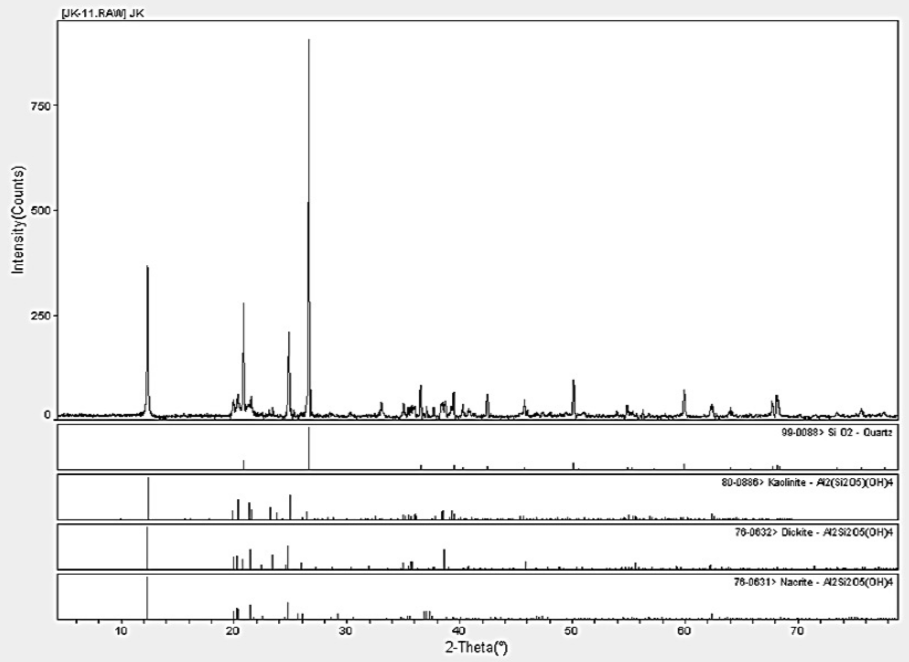
[JK-11.RAW] JK
Intensity(Counts)
750
500
250
0
99-0088> Si O2 - Quartz
80-0886> Kaolinite - Al2(Si2O5)(OH)4
76-0632> Dickite - Al2Si2O5(OH)4
76-0631> Nacrite - Al2Si2O5(OH)4
10
20
30
40
50
60
70
2-Theta(°)

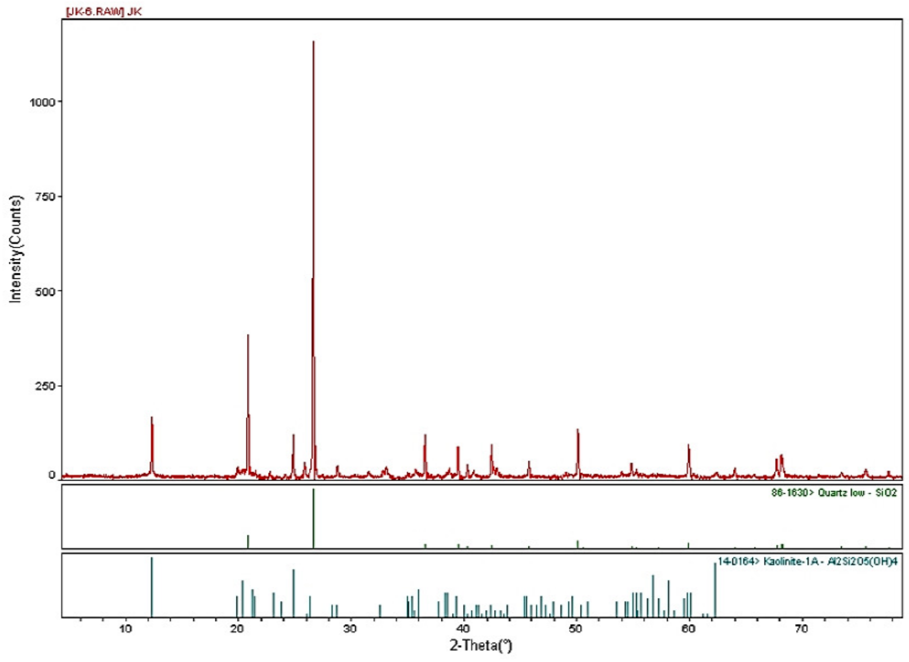
[JK-6.RAW] JK
Intensity(Counts)
1000
750
500
250
0
86-1630> Quartz low - SiO2
14-0164> Kaolinite-1A - Al2Si2O5(OH)4
10
20
30
40
50
60
70
2-Theta(°)

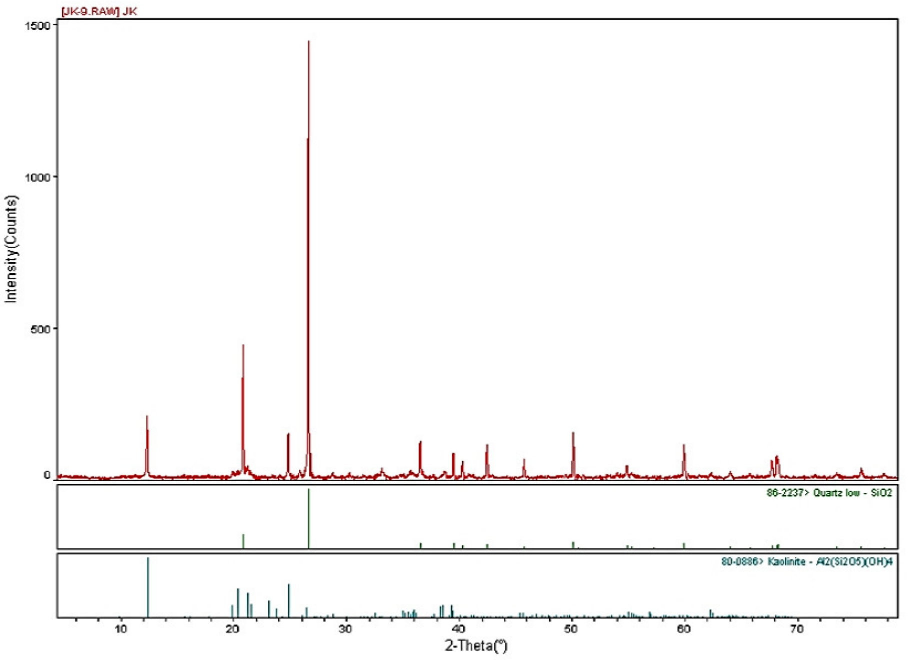
[JK-9.RAW] JK
Intensity(Counts)
1500
1000
500
0
86-2237> Quartz low - SiO2
80-0886> Kaolinite - Al2(Si2O5)(OH)4
10
20
30
40
50
60
70
2-Theta(°)

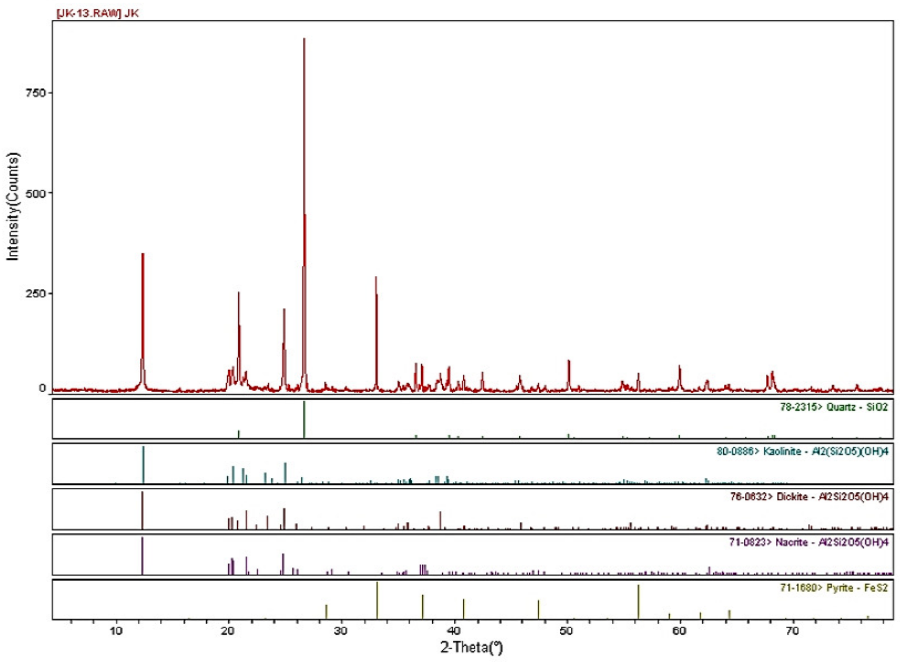
[JK-13.RAW] JK
Intensity(Counts)
750
500
250
0
78-2315> Quartz - SiO2
80-0886> Kaolinite - Al2(Si2O5)(OH)4
76-0632> Dickite - Al2Si2O5(OH)4
71-0823> Nacrite - Al2Si2O5(OH)4
71-1680> Pyrite - FeS2
10
20
30
40
50
60
70
2-Theta(°)

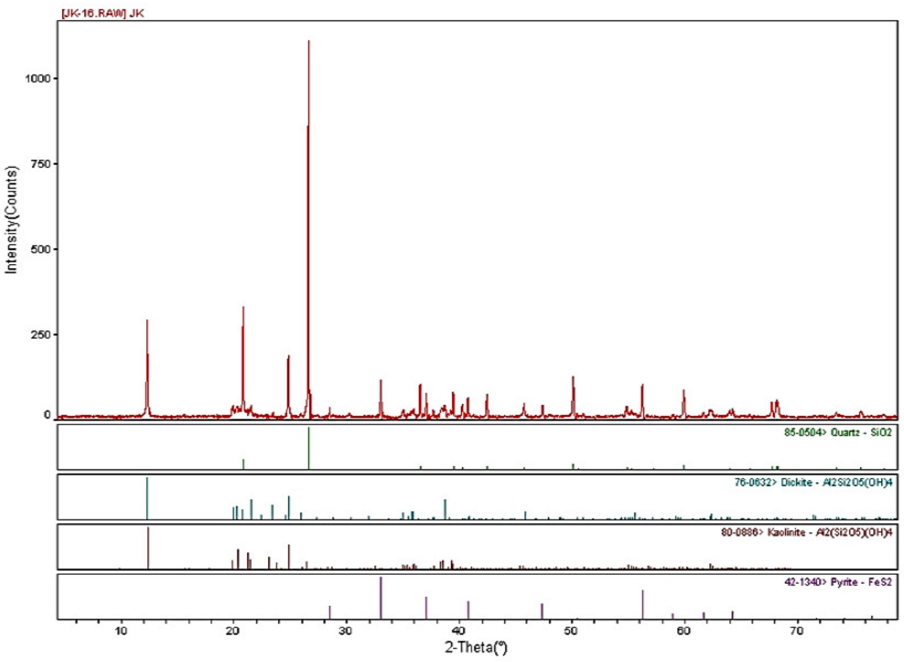
[JK-16.RAW] JK
Intensity(Counts)
1000
750
500
250
0
85-0504> Quartz - SiO2
76-0632> Dickite - Al2Si2O5(OH)4
80-0886> Kaolinite - Al2(Si2O5)(OH)4
42-1340> Pyrite - FeS2
10
20
30
40
50
60
70
2-Theta(°)

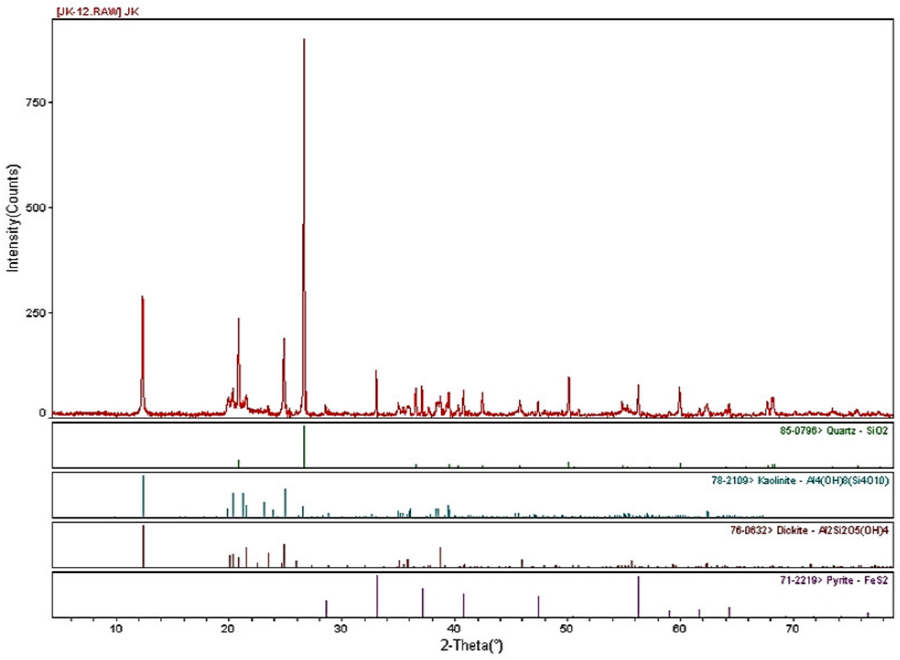
[JK-12.RAW] JK
Intensity(Counts)
750
500
250
0
85-0796> Quartz - SiO2
78-2109> Kaolinite - Al4(OH)8(Si4O10)
76-0632> Dickite - Al2Si2O5(OH)4
71-2219> Pyrite - FeS2
10
20
30
40
50
60
70
2-Theta(°)

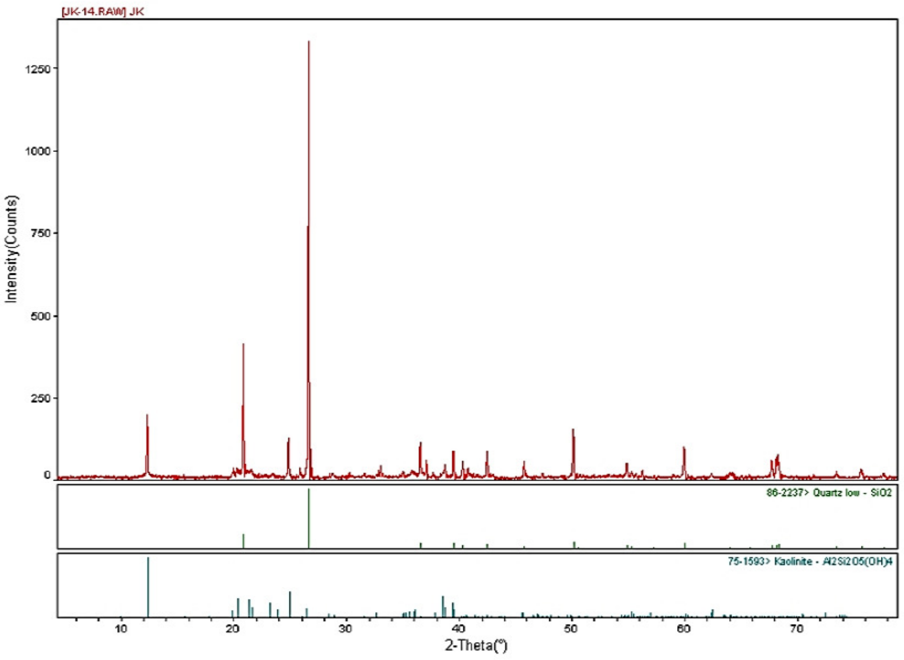
[JK-14.RAW] JK
Intensity(Counts)
1250
1000
750
500
250
0
86-2237> Quartz low - SiO2
75-1593> Kaolinite - Al2Si2O5(OH)4
10
20
30
40
50
60
70
2-Theta(°)

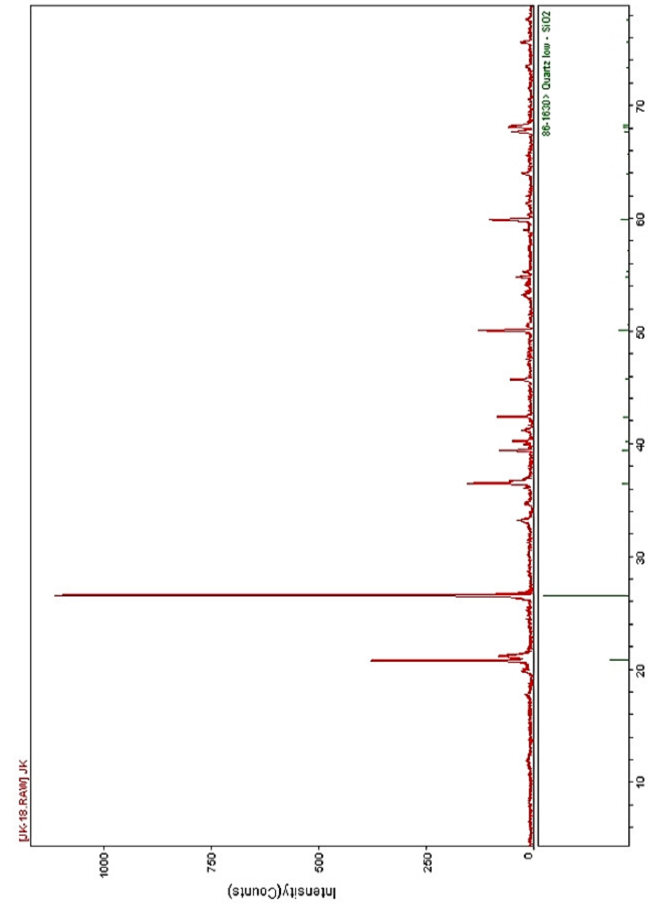
[JK-18.RAW] JK
Intensity(Counts)
0
250
500
750
1000
86-1630> Quartz low - SiO2
10
20
30
40
50
60
70
2-Theta(°)

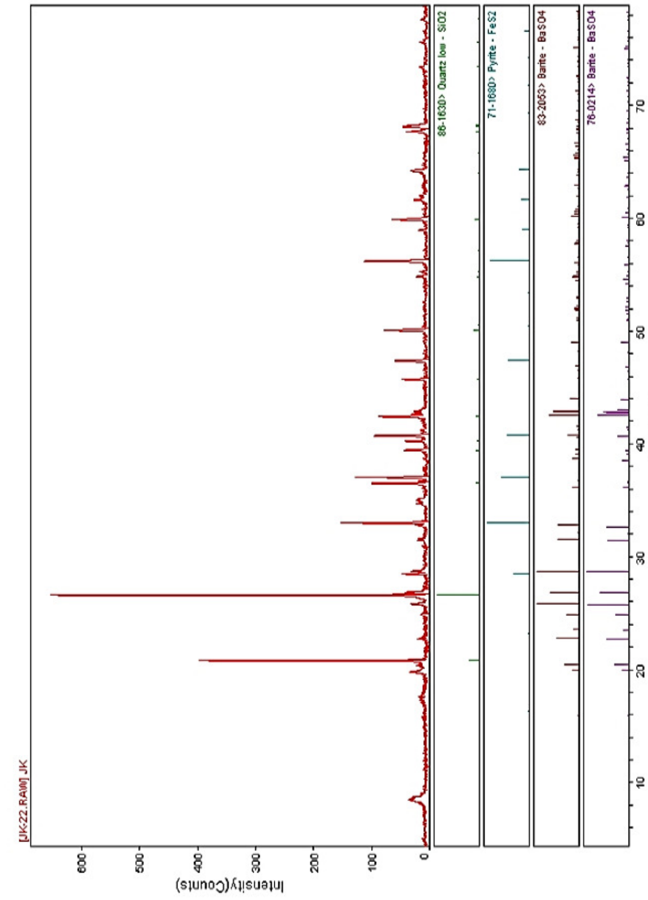
[JK-22.RAW] JK
Intensity(Counts)
0
100
200
300
400
500
600
86-1630> Quartz low - SiO2
71-1680> Pyrite - FeS2
83-2053> Barite - BaSO4
76-0214> Barite - BaSO4
10
20
30
40
50
60
70
2-Theta(°)

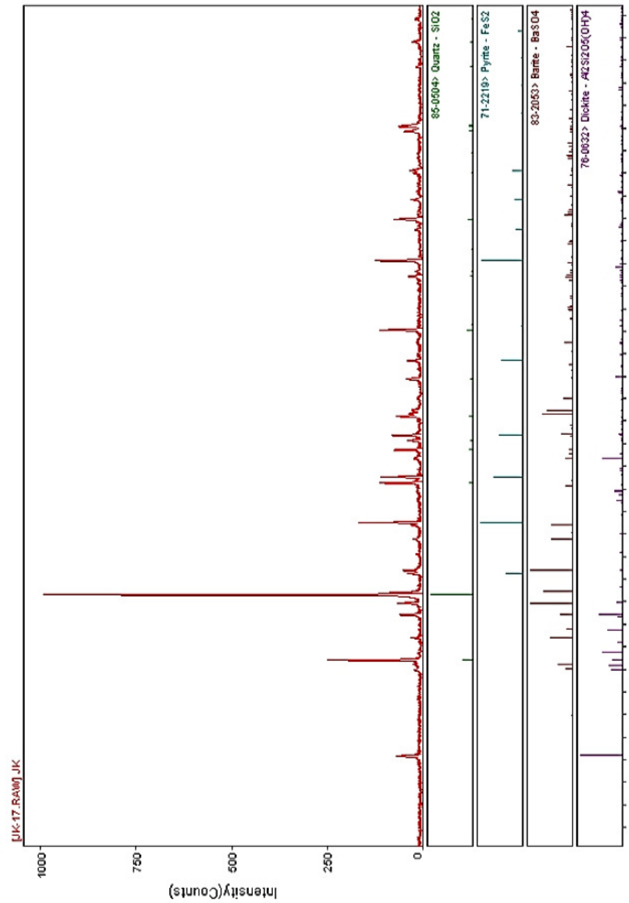
[JK-17.RAW] JK
Intensity(Counts)
0
250
500
750
1000
85-0504> Quartz - SiO2
71-2219> Pyrite - FeS2
83-2053> Barite - BaSO4
76-0632> Dickite - Al2Si2O5(OH)4
10
20
30
40
50
60
70
2-Theta(°)

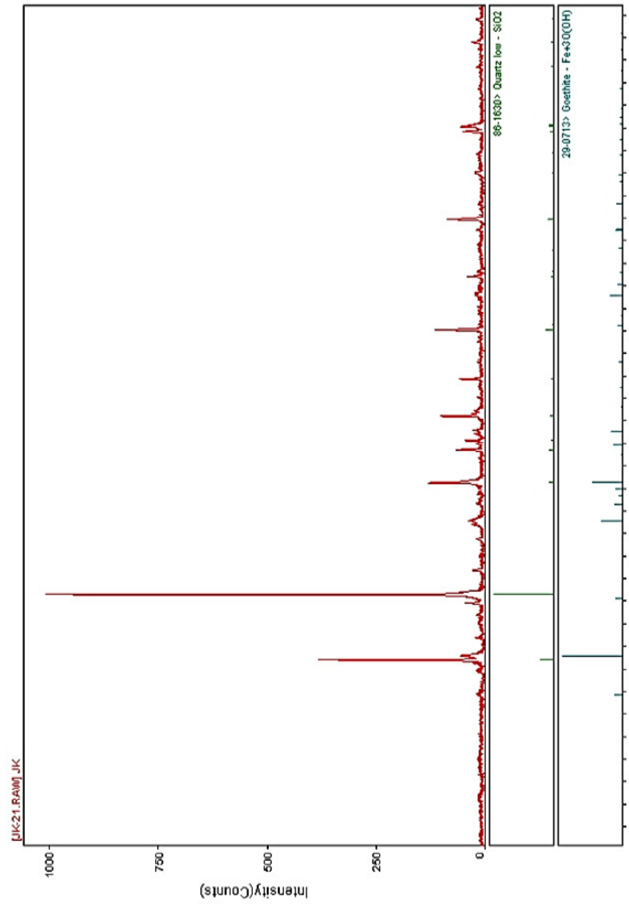
[JK-21.RAW] JK
Intensity(Counts)
0
250
500
750
1000
86-1630> Quartz low - SiO2
29-0713> Goethite - Fe+3O(OH)
10
20
30
40
50
60
70
2-Theta(°)

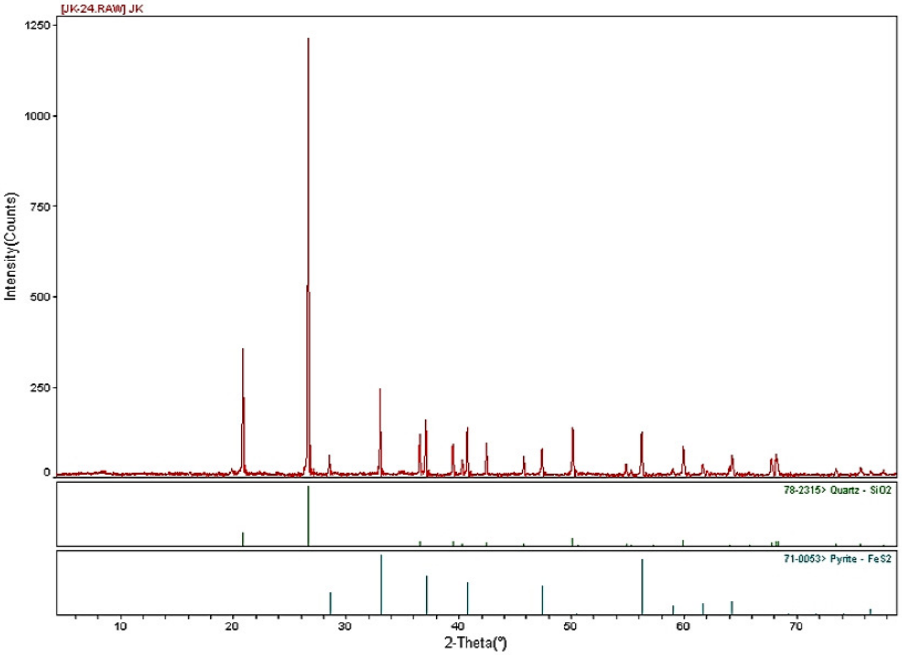
[JK-24.RAW] JK
Intensity(Counts)
1250
1000
750
500
250
0
78-2315> Quartz - SiO2
71-0053> Pyrite - FeS2
10
20
30
40
50
60
70
2-Theta(°)

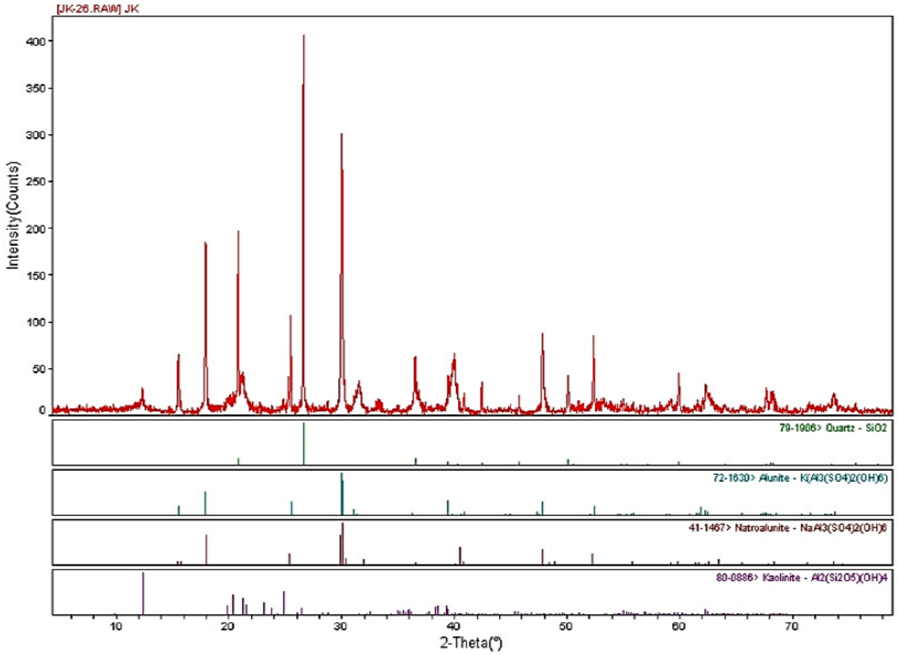
[JK-26.RAW] JK
Intensity(Counts)
400
350
300
250
200
150
100
50
0
79-1906> Quartz - SiO2
72-1630> Alunite - K(Al3(SO4)2(OH)6)
41-1467> Natroalunite - NaAl3(SO4)2(OH)6
80-0886> Kaolinite - Al2(Si2O5)(OH)4
10
20
30
40
50
60
70
2-Theta(°)

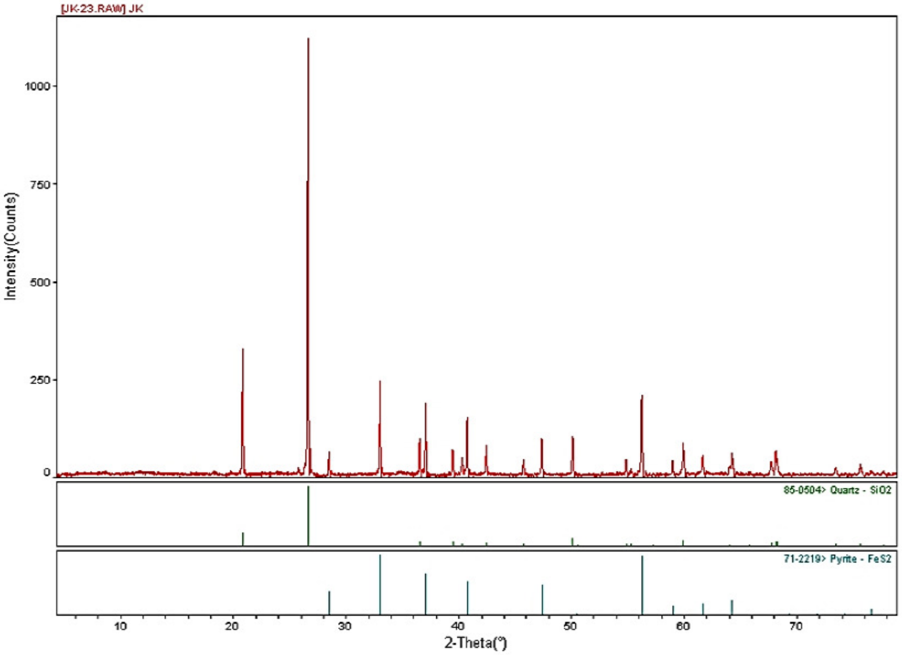
[JK-23.RAW] JK
Intensity(Counts)
1000
750
500
250
0
85-0504> Quartz - SiO2
71-2219> Pyrite - FeS2
10
20
30
40
50
60
70
2-Theta(°)

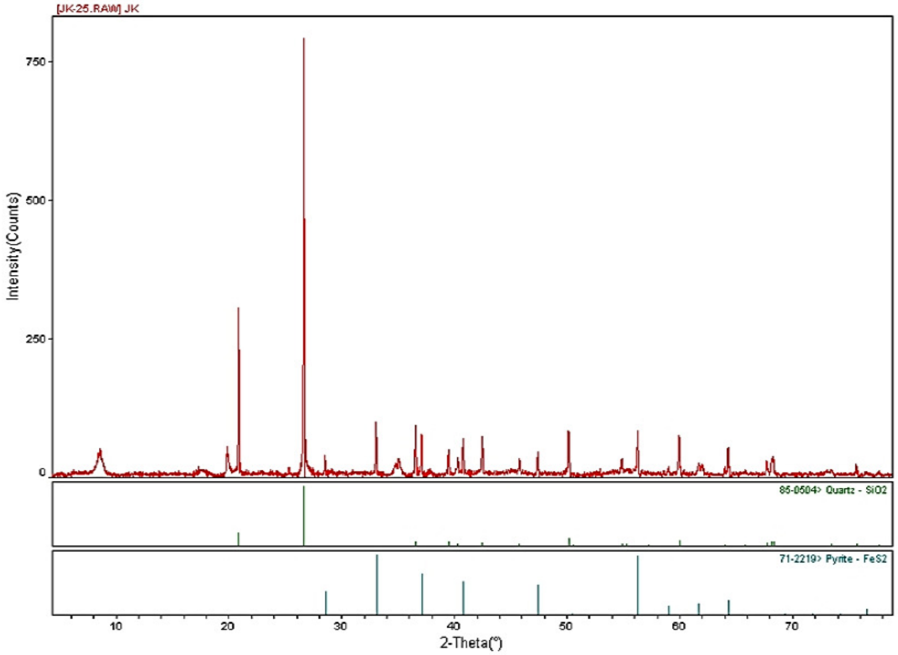
[JK-25.RAW] JK
Intensity(Counts)
750
500
250
0
85-0504> Quartz - SiO2
71-2219> Pyrite - FeS2
10
20
30
40
50
60
70
2-Theta(°)

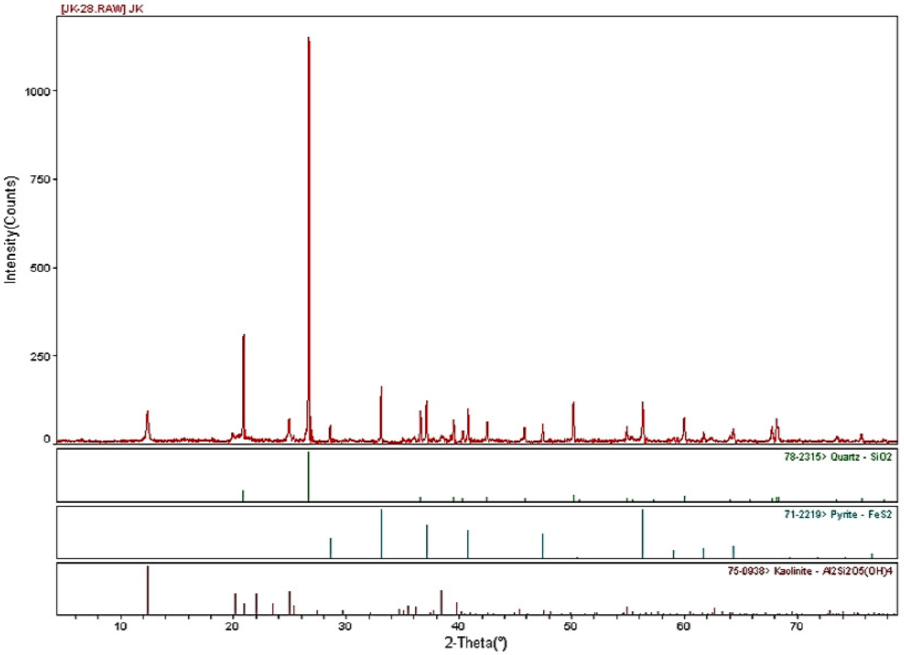
[JK-28.RAW] JK
Intensity(Counts)
1000
750
500
250
0
78-2315> Quartz - SiO2
71-2219> Pyrite - FeS2
75-0938> Kaolinite - Al2Si2O5(OH)4
10
20
30
40
50
60
70
2-Theta(°)

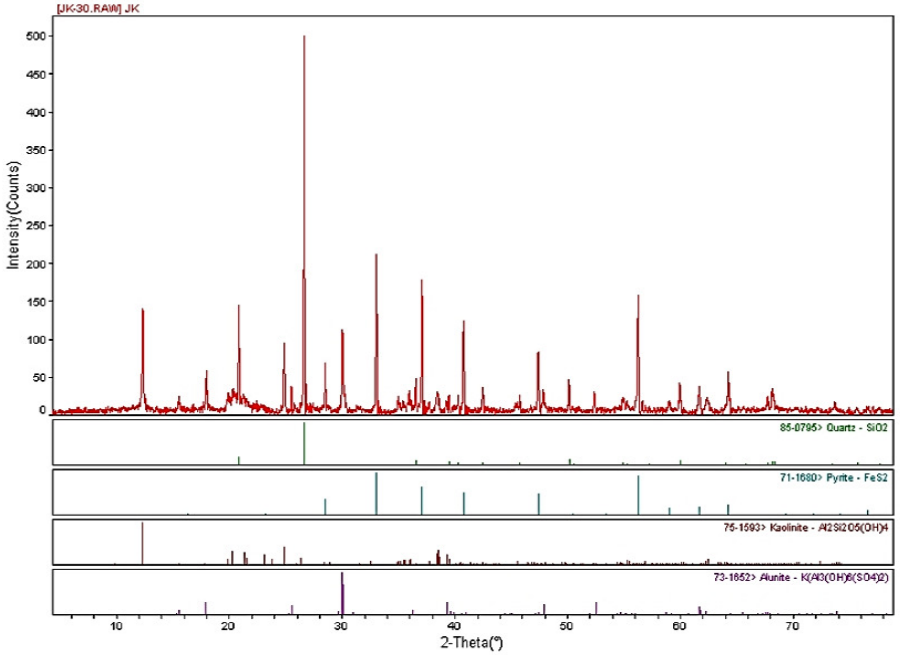
[JK-30.RAW] JK
Intensity(Counts)
500
450
400
350
300
250
200
150
100
50
0
85-0795> Quartz - SiO2
71-1680> Pyrite - FeS2
75-1593> Kaolinite - Al2Si2O5(OH)4
73-1652> Alunite - K(Al3(OH)6(SO4)2)
10
20
30
40
50
60
70
2-Theta(°)

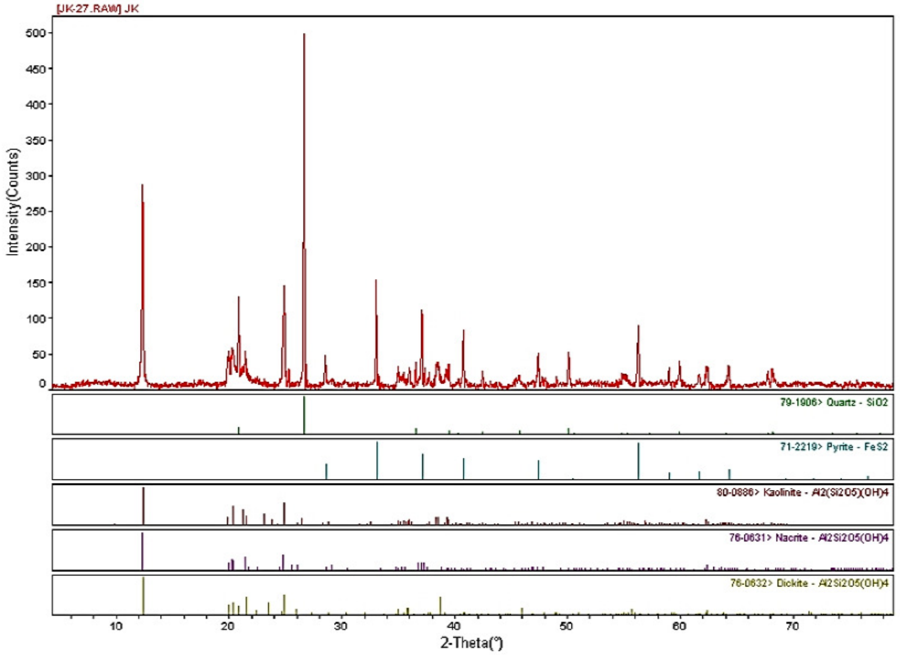
[JK-27.RAW] JK
Intensity(Counts)
500
450
400
350
300
250
200
150
100
50
0
79-1906> Quartz - SiO2
71-2219> Pyrite - FeS2
80-0886> Kaolinite - Al2(Si2O5)(OH)4
76-0631> Nacrite - Al2Si2O5(OH)4
76-0632> Dickite - Al2Si2O5(OH)4
10
20
30
40
50
60
70
2-Theta(°)

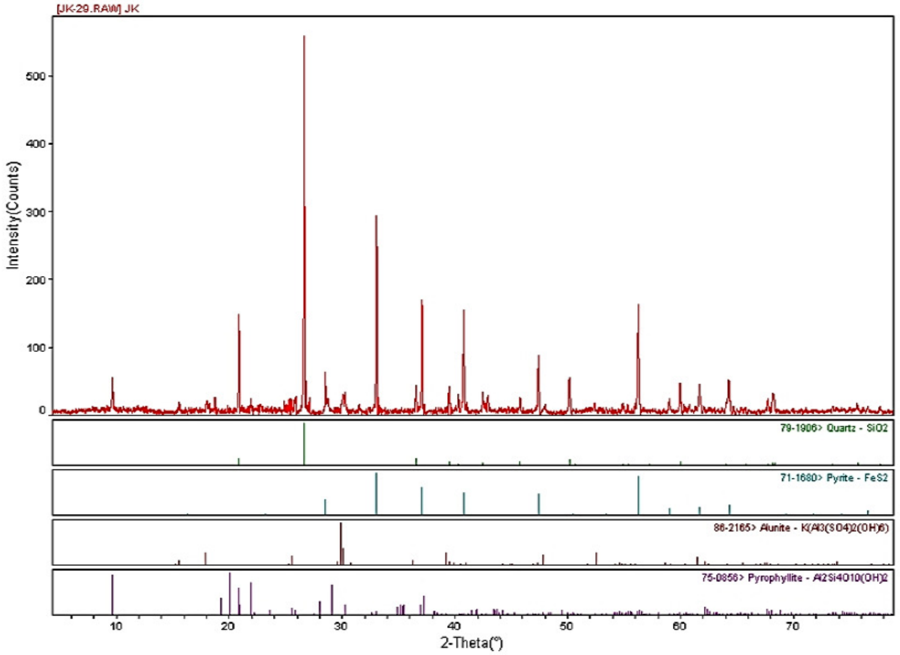
[JK-29.RAW] JK
Intensity(Counts)
500
400
300
200
100
0
79-1906> Quartz - SiO2
71-1680> Pyrite - FeS2
86-2165> Alunite - K(Al3(SO4)2(OH)6)
75-0856> Pyrophyllite - Al2Si4O10(OH)2
10
20
30
40
50
60
70
2-Theta(°)

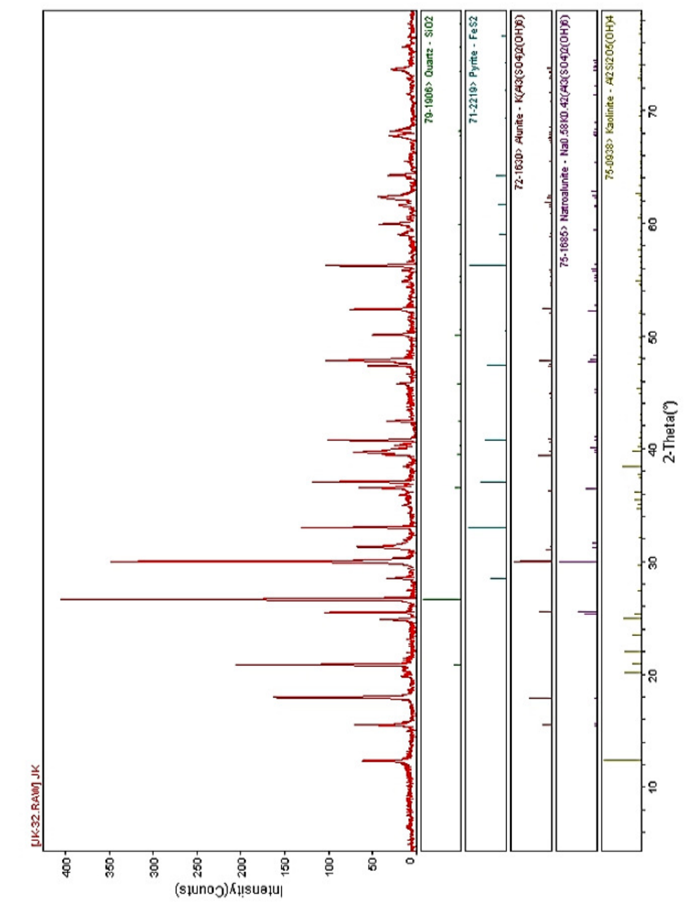
[JK-32.RAW] JK
Intensity(Counts)
0
50
100
150
200
250
300
350
400
2-Theta(°)
10
20
30
40
50
60
70
79-1906> Quartz - SiO2
71-2219> Pyrite - FeS2
72-1630> Alunite - K(Al3(SO4)2(OH)6)
75-1685> Natroalunite - Na0.58K0.42(Al3(SO4)2(OH)6)
75-0938> Kaolinite - Al2Si2O5(OH)4

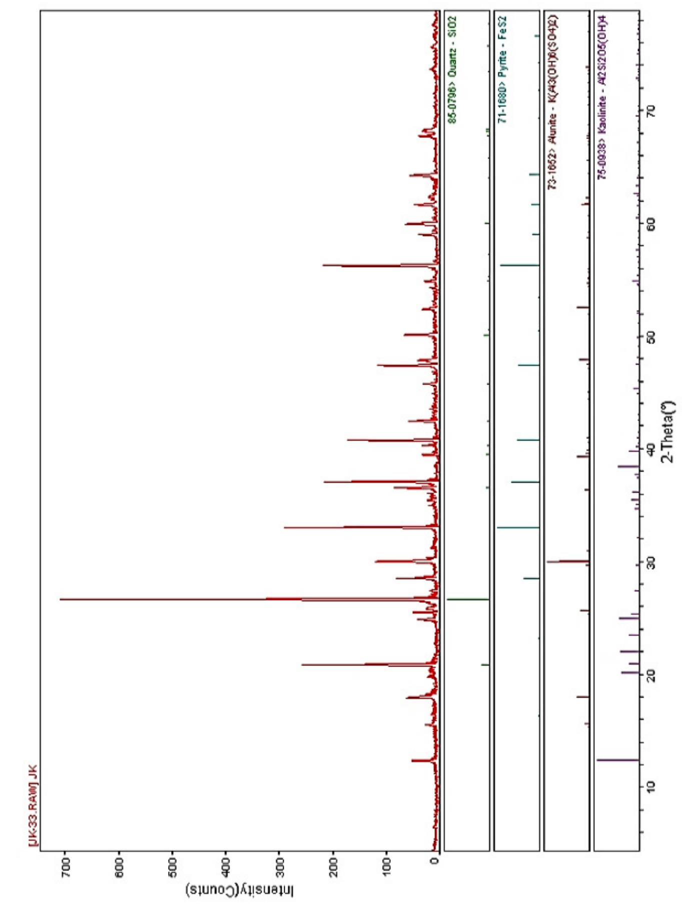
[JK-33.RAW] JK
Intensity(Counts)
0
100
200
300
400
500
600
700
2-Theta(°)
10
20
30
40
50
60
70
85-0796> Quartz - SiO2
71-1680> Pyrite - FeS2
72-1652> Alunite - K(Al3(OH)6(SO4)2)
75-0938> Kaolinite - Al2Si2O5(OH)4

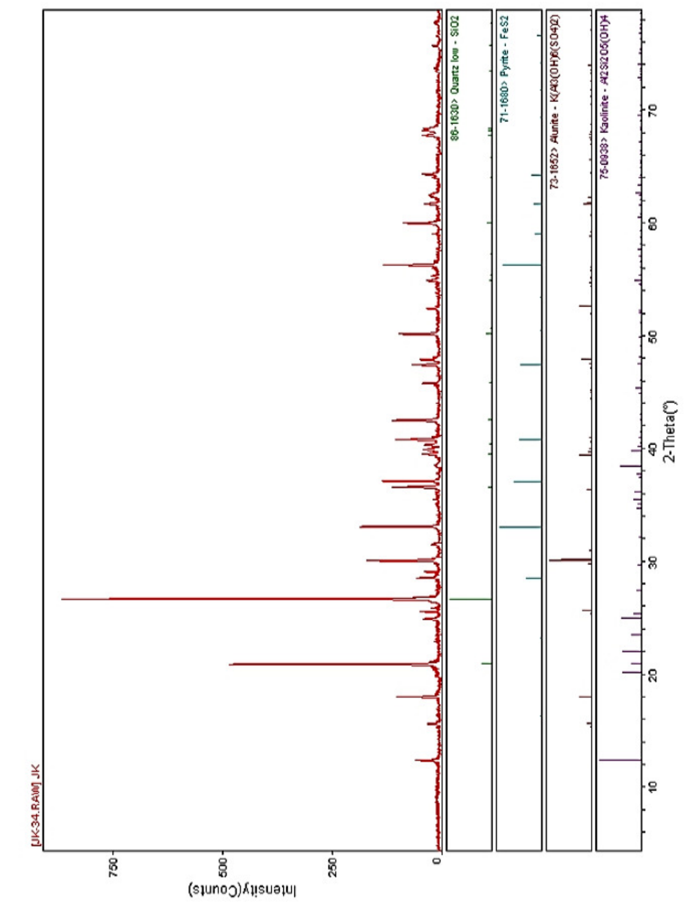
[JK-34.RAW] JK
Intensity(Counts)
0
250
500
750
2-Theta(°)
10
20
30
40
50
60
70
86-1630> Quartz low - SiO2
71-1680> Pyrite - FeS2
73-1652> Alunite - K(Al3(OH)6(SO4)2)
75-0938> Kaolinite - Al2Si2O5(OH)4

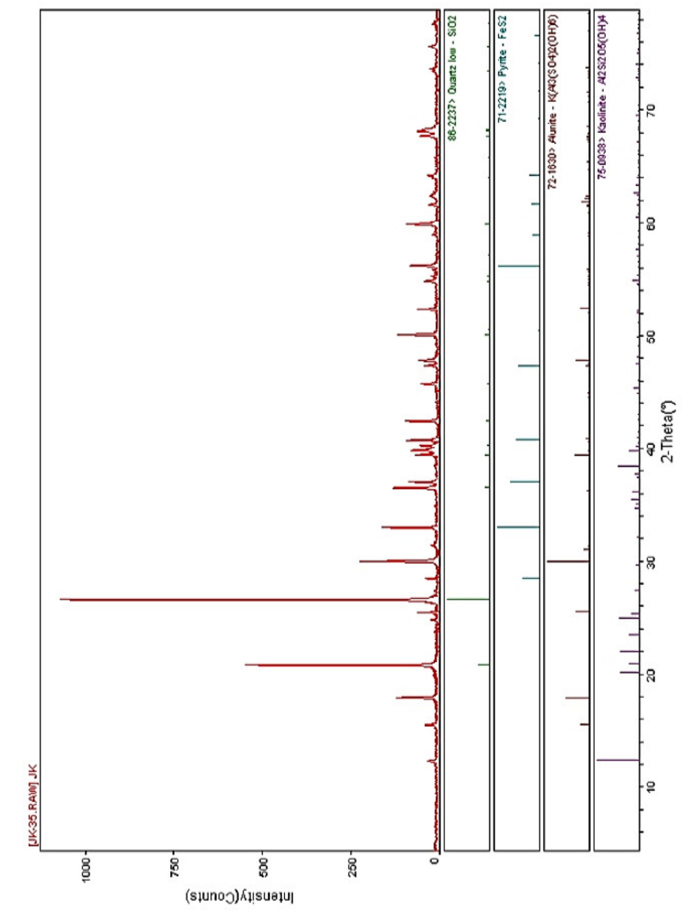
[JK-35.RAW] JK
Intensity(Counts)
0
250
500
750
1000
2-Theta(°)
10
20
30
40
50
60
70
86-2237> Quartz low - SiO2
71-2219> Pyrite - FeS2
72-1630> Alunite - K(Al3(SO4)2(OH)6)
75-0938> Kaolinite - Al2Si2O5(OH)4

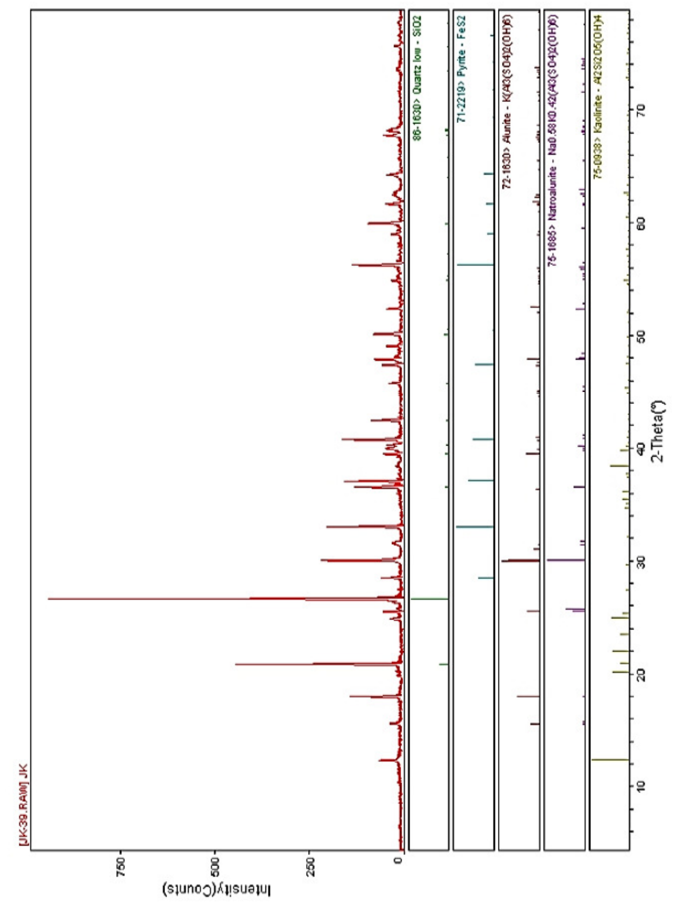
[JK-39.RAW] JK
Intensity(Counts)
750
500
250
0
86-1630> Quartz low - SiO2
71-2219> Pyrite - FeS2
72-1630> Alunite - K(Al3(SO4)2(OH)6)
75-1685> Natroalunite - Na0.58K0.42(Al3(SO4)2(OH)6)
75-0938> Kaolinite - Al2Si2O5(OH)4
10
20
30
40
50
60
70
2-Theta(°)

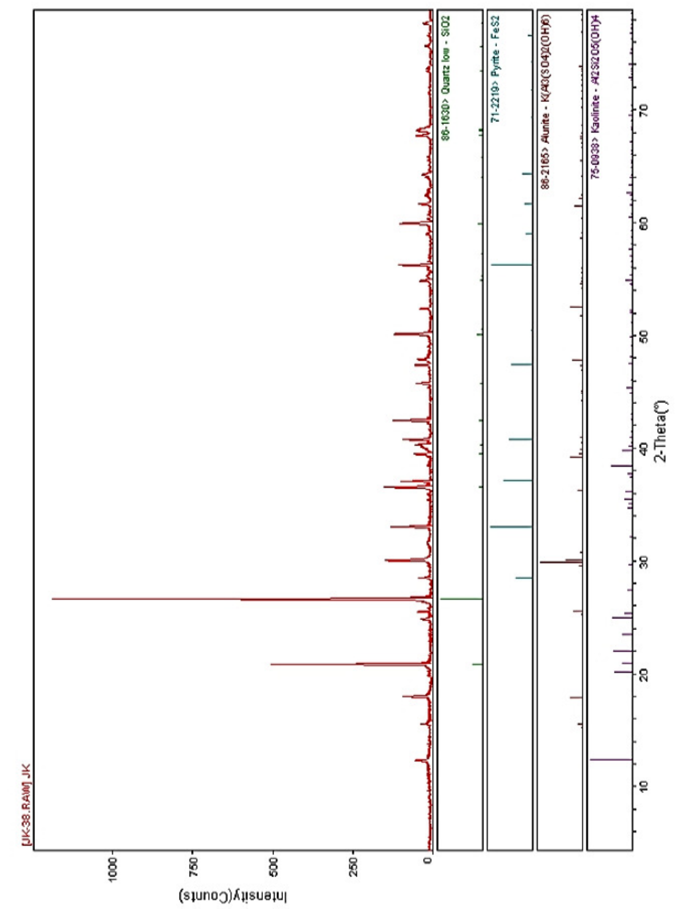
[JK-38.RAW] JK
Intensity(Counts)
1000
750
500
250
0
86-1630> Quartz low - SiO2
71-2219> Pyrite - FeS2
86-2165> Alunite - K(Al3(SO4)2(OH)6)
75-0938> Kaolinite - Al2Si2O5(OH)4
10
20
30
40
50
60
70
2-Theta(°)

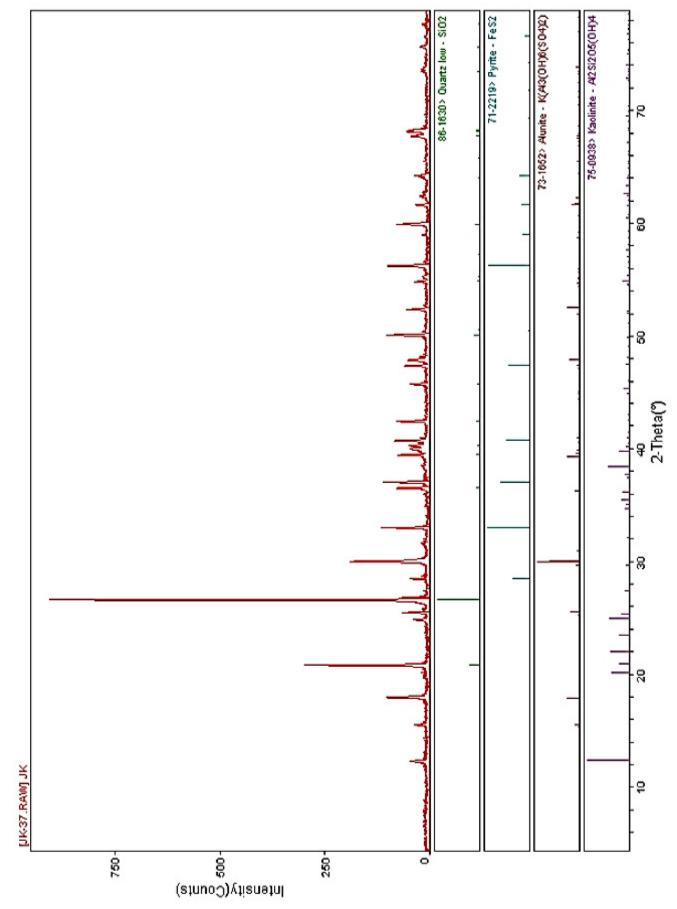
[JK-37.RAW] JK
Intensity(Counts)
750
500
250
0
86-1630> Quartz low - SiO2
71-2219> Pyrite - FeS2
73-1652> Alunite - K(Al3(OH)6(SO4)2)
75-0938> Kaolinite - Al2Si2O5(OH)4
10
20
30
40
50
60
70
2-Theta(°)

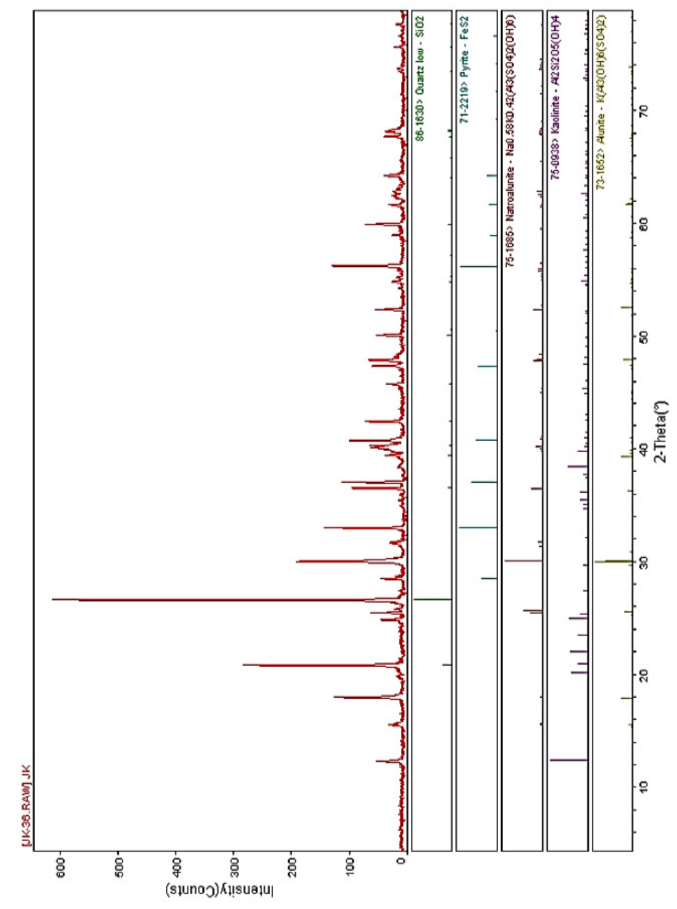
[JK-36.RAW] JK
Intensity(Counts)
600
500
400
300
200
100
0
86-1630> Quartz low - SiO2
71-2219> Pyrite - FeS2
75-1685> Natroalunite - Na0.58K0.42(Al3(SO4)2(OH)6)
75-0938> Kaolinite - Al2Si2O5(OH)4
73-1652> Alunite - K(Al3(OH)6(SO4)2)
10
20
30
40
50
60
70
2-Theta(°)

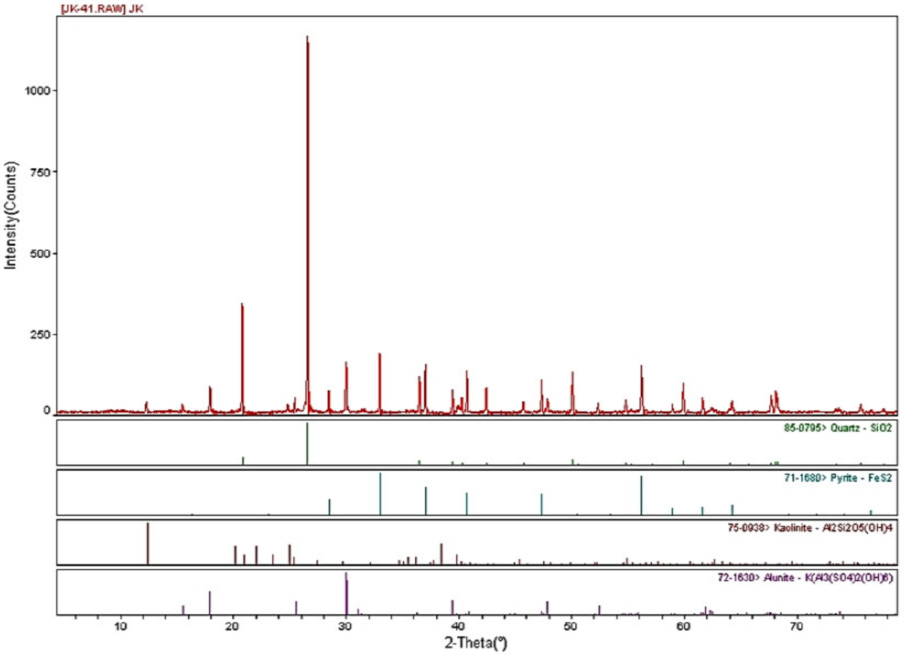
[JK-41.RAW] JK
Intensity(Counts)
1000
750
500
250
0
85-0795> Quartz - SiO2
71-1680> Pyrite - FeS2
75-0938> Kaolinite - Al2Si2O5(OH)4
72-1630> Alunite - K(Al3(SO4)2(OH)6)
10
20
30
40
50
60
70
2-Theta(°)

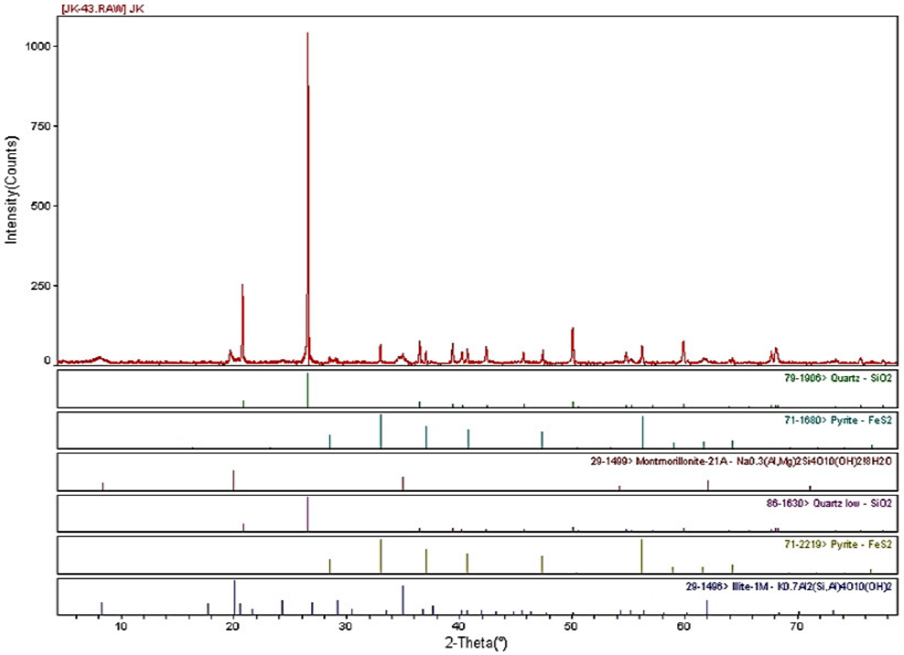
[JK-43.RAW] JK
Intensity(Counts)
1000
750
500
250
0
79-1906> Quartz - SiO2
71-1680> Pyrite - FeS2
29-1499> Montmorillonite-21A - Na0.3(Al,Mg)2Si4O10(OH)2!8H2O
86-1630> Quartz low - SiO2
71-2219> Pyrite - FeS2
29-1496> Illite-1M - K0.7Al2(Si,Al)4O10(OH)2
10
20
30
40
50
60
70
2-Theta(°)

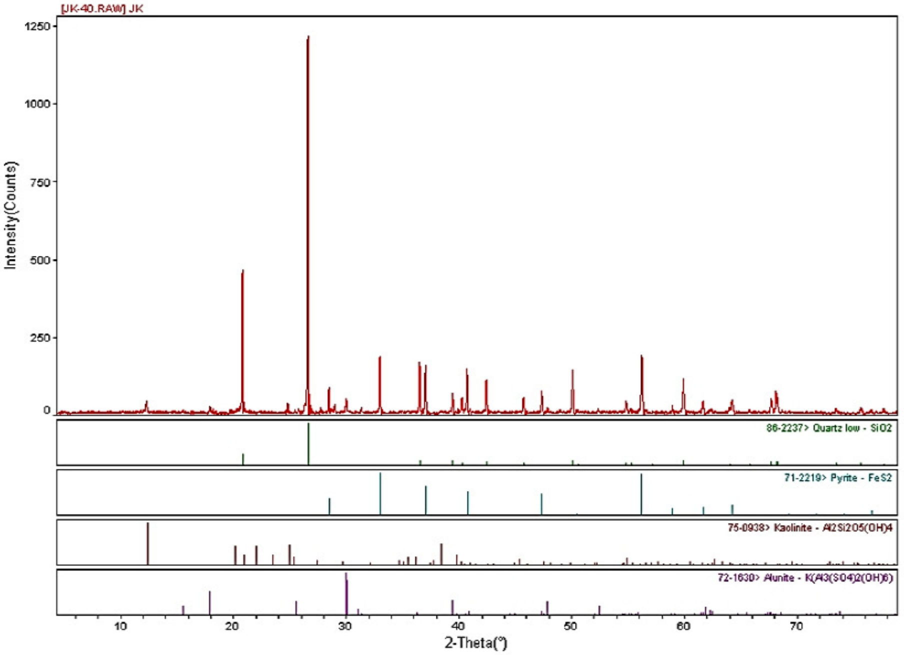
[JK-40.RAW] JK
Intensity(Counts)
1250
1000
750
500
250
0
86-2237> Quartz low - SiO2
71-2219> Pyrite - FeS2
75-0938> Kaolinite - Al2Si2O5(OH)4
72-1630> Alunite - K(Al3(SO4)2(OH)6)
10
20
30
40
50
60
70
2-Theta(°)

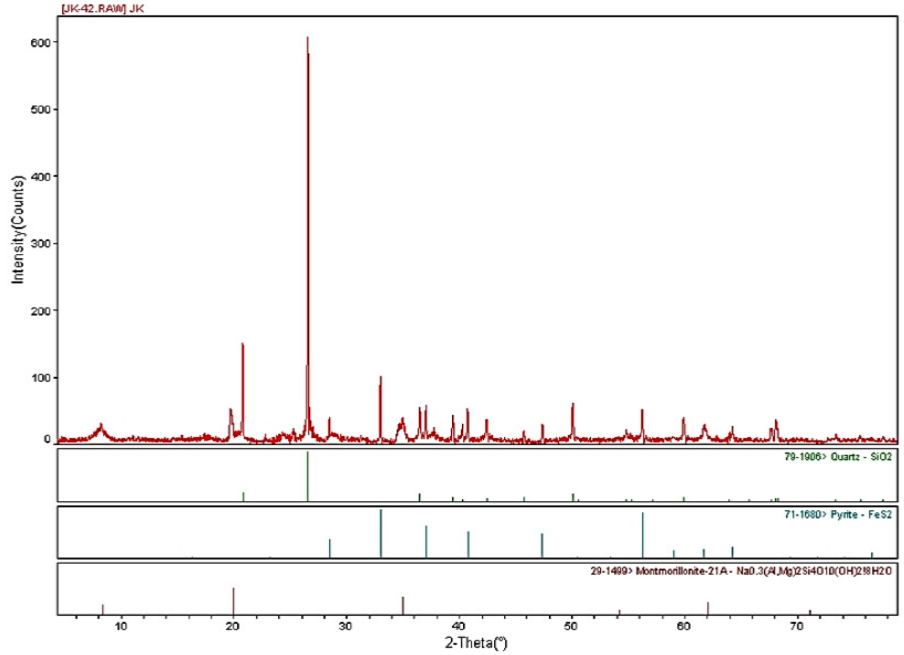
[JK-42.RAW] JK
Intensity(Counts)
600
500
400
300
200
100
0
79-1906> Quartz - SiO2
71-1680> Pyrite - FeS2
29-1499> Montmorillonite-21A - Na0.3(Al,Mg)2Si4O10(OH)2!8H2O
10
20
30
40
50
60
70
2-Theta(°)

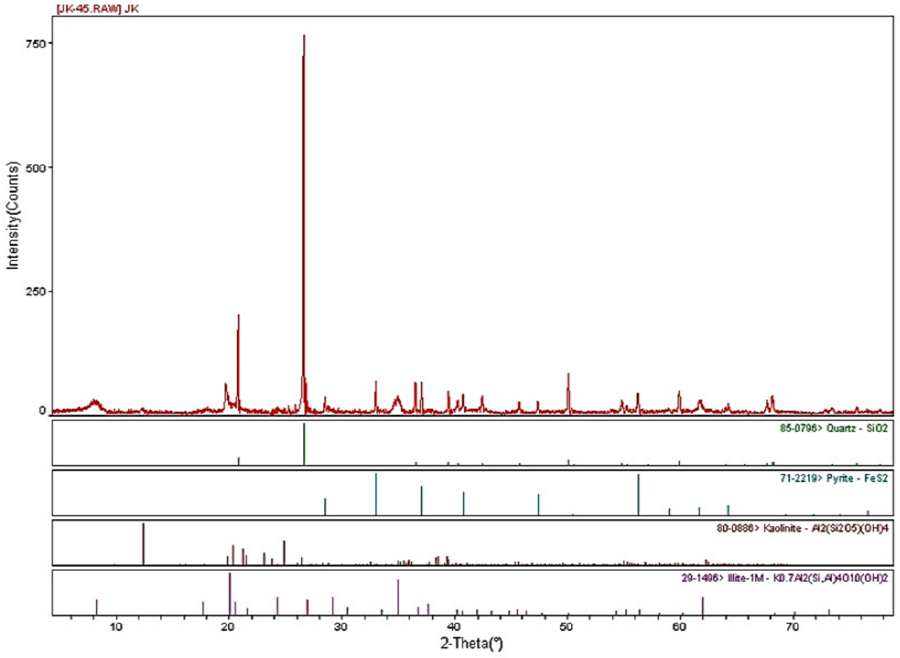
[JK-45.RAW] JK
Intensity(Counts)
750
500
250
0
85-0796> Quartz - SiO2
71-2219> Pyrite - FeS2
80-0886> Kaolinite - Al2(Si2O5)(OH)4
29-1496> Illite-1M - K0.7Al2(Si,Al)4O10(OH)2
10
20
30
40
50
60
70
2-Theta(°)

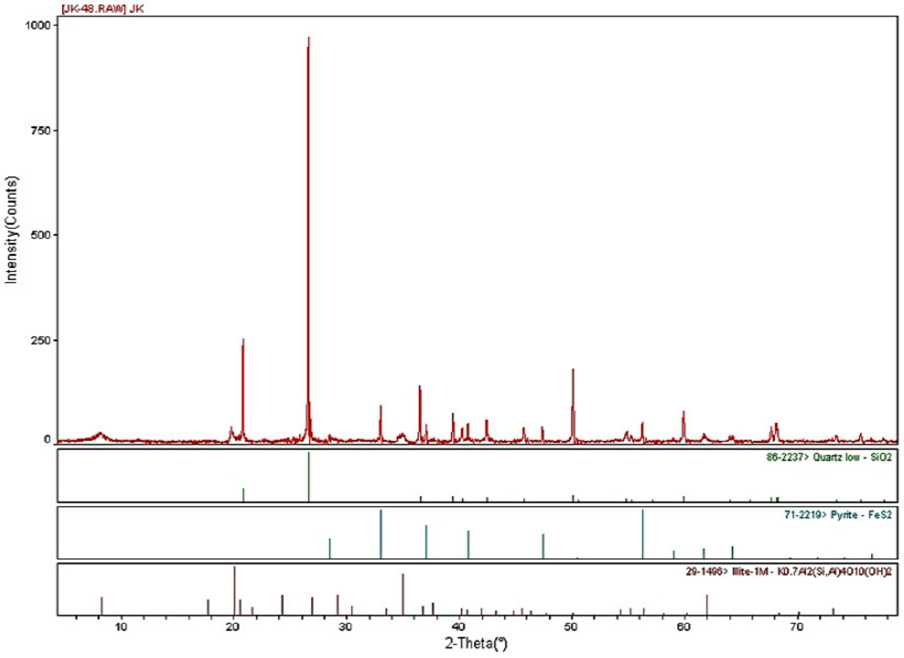
[JK-48.RAW] JK
Intensity(Counts)
1000
750
500
250
0
86-2237> Quartz low - SiO2
71-2219> Pyrite - FeS2
29-1496> Illite-1M - K0.7Al2(Si,Al)4O10(OH)2
10
20
30
40
50
60
70
2-Theta(°)

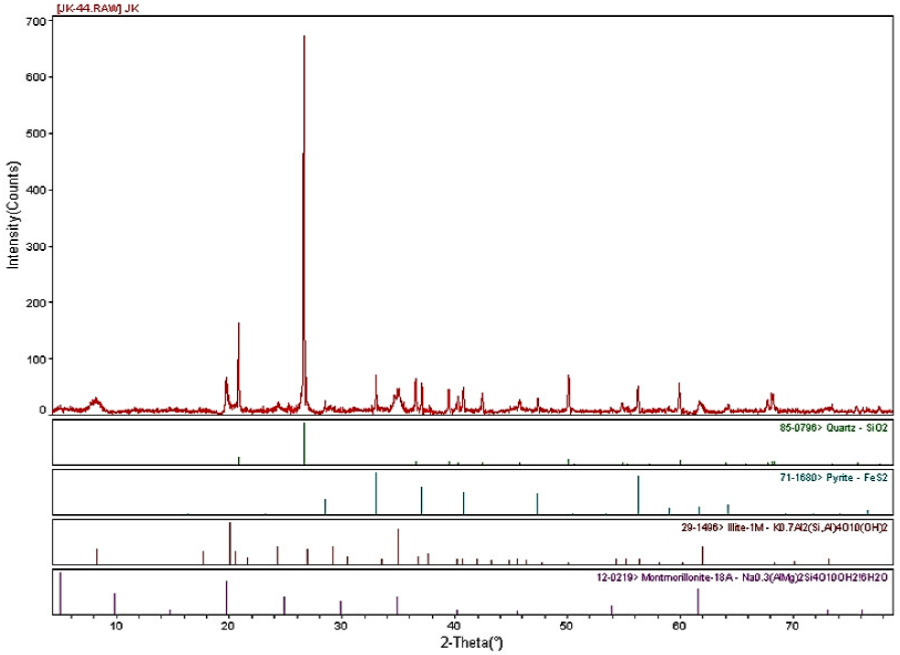
[JK-44.RAW] JK
Intensity(Counts)
700
600
500
400
300
200
100
0
85-0796> Quartz - SiO2
71-1680> Pyrite - FeS2
29-1496> Illite-1M - K0.7Al2(Si,Al)4O10(OH)2
12-0219> Montmorillonite-18A - Na0.3(AlMg)2Si4O10OH2!6H2O
10
20
30
40
50
60
70
2-Theta(°)

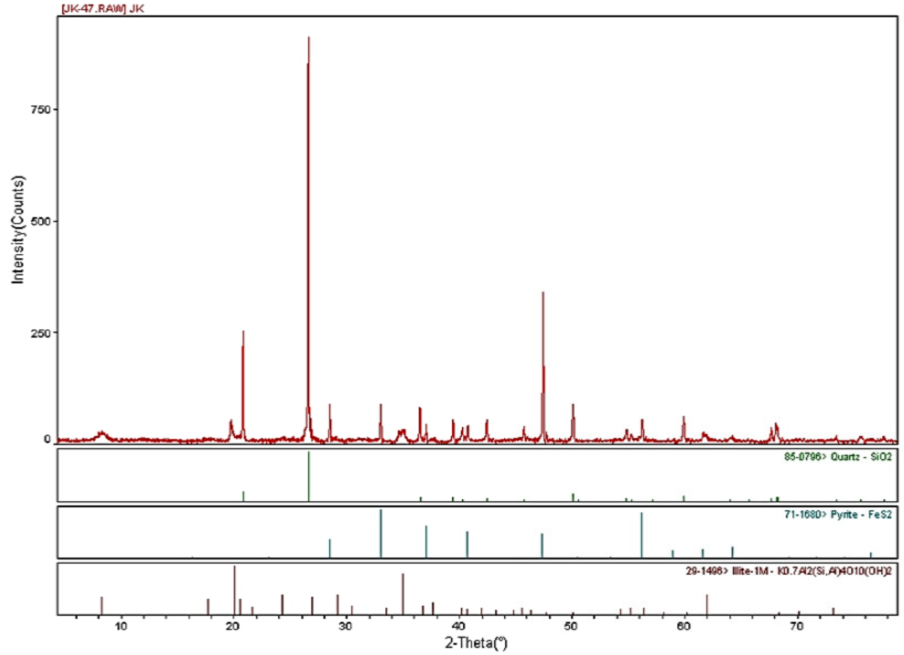
[JK-47.RAW] JK
Intensity(Counts)
750
500
250
0
85-0796> Quartz - SiO2
71-1680> Pyrite - FeS2
29-1496> Illite-1M - K0.7Al2(Si,Al)4O10(OH)2
10
20
30
40
50
60
70
2-Theta(°)

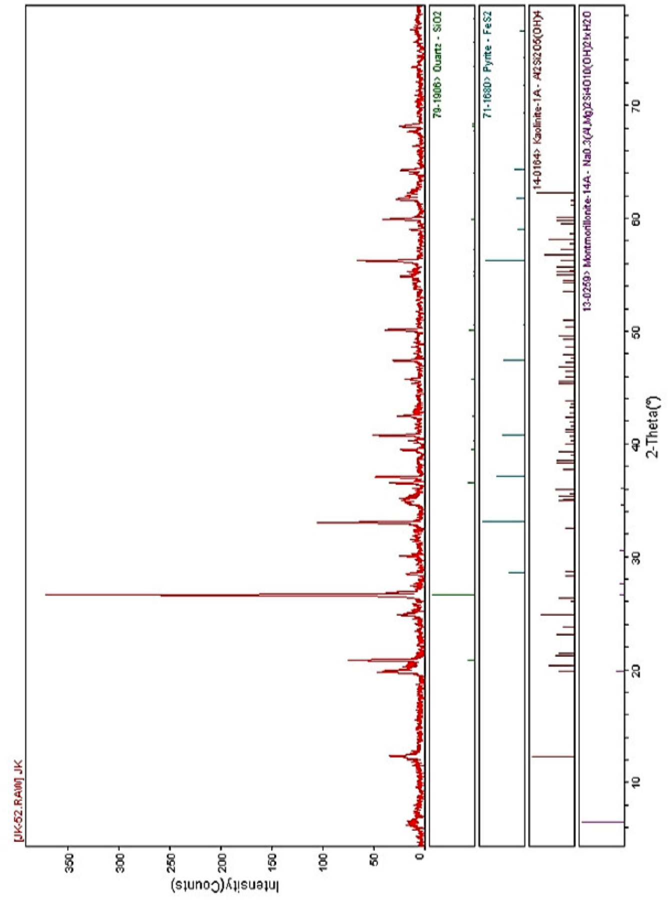
[JK-52.RAW] JK
Intensity(Counts)
0
50
100
150
200
250
300
350
2-Theta(°)
10
20
30
40
50
60
70
79-1906> Quartz - SiO2
71-1680> Pyrite - FeS2
14-0164> Kaolinite-1A - Al2Si2O5(OH)4
13-0259> Montmorillonite-14A - Na0.3(Al,Mg)2Si4O10(OH)2!xH2O

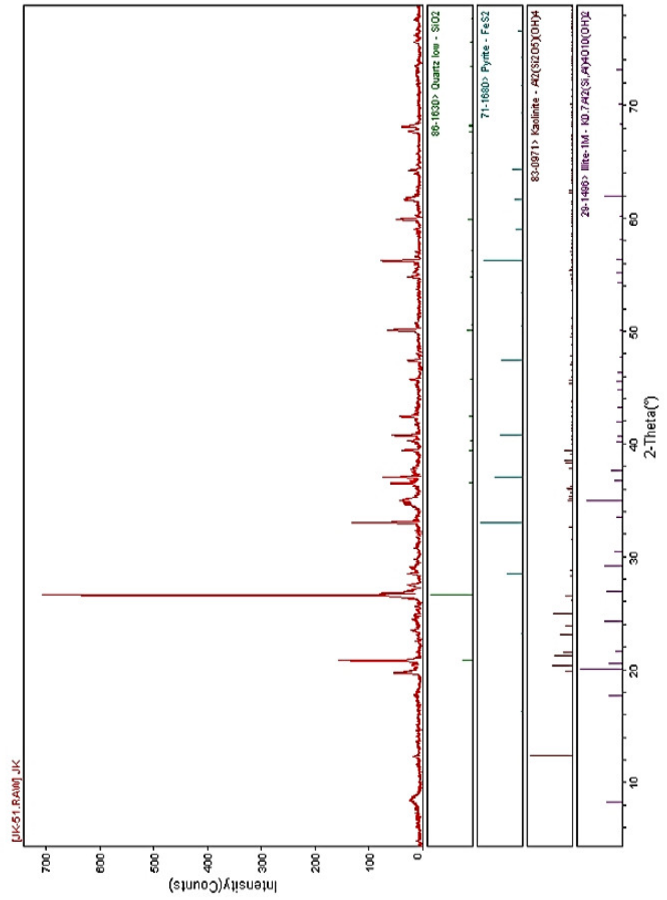
[JK-51.RAW] JK
Intensity(Counts)
0
100
200
300
400
500
600
700
2-Theta(°)
10
20
30
40
50
60
70
86-1630> Quartz low - SiO2
71-1680> Pyrite - FeS2
83-0971> Kaolinite - Al2(Si2O5)(OH)4
29-1496> Illite-1M - K0.7Al2(Si,Al)4O10(OH)2

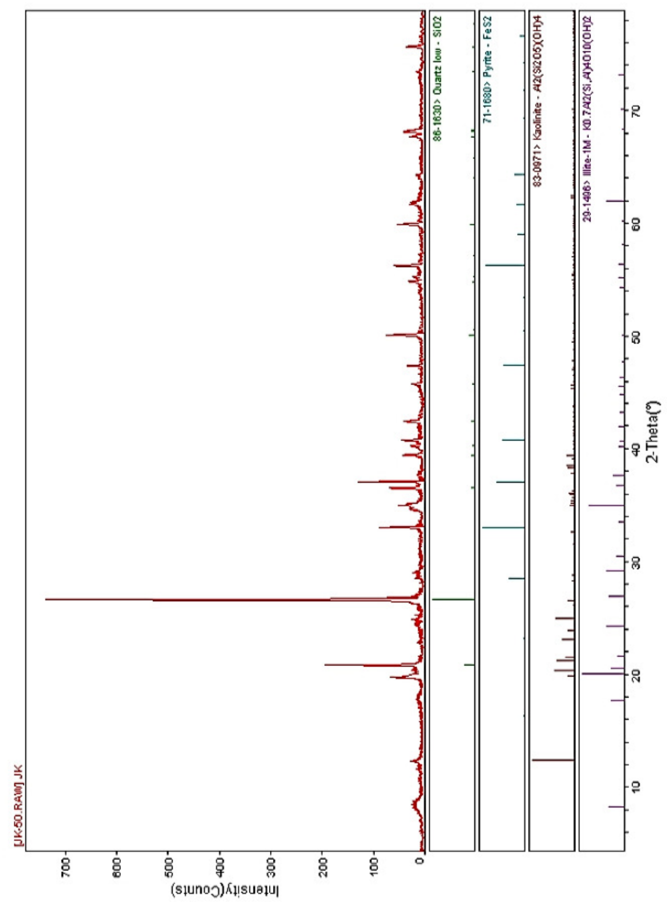
[JK-50.RAW] JK
Intensity(Counts)
0
100
200
300
400
500
600
700
2-Theta(°)
10
20
30
40
50
60
70
86-1630> Quartz low - SiO2
71-1680> Pyrite - FeS2
83-0971> Kaolinite - Al2(Si2O5)(OH)4
29-1496> Illite-1M - K0.7Al2(Si,Al)4O10(OH)2

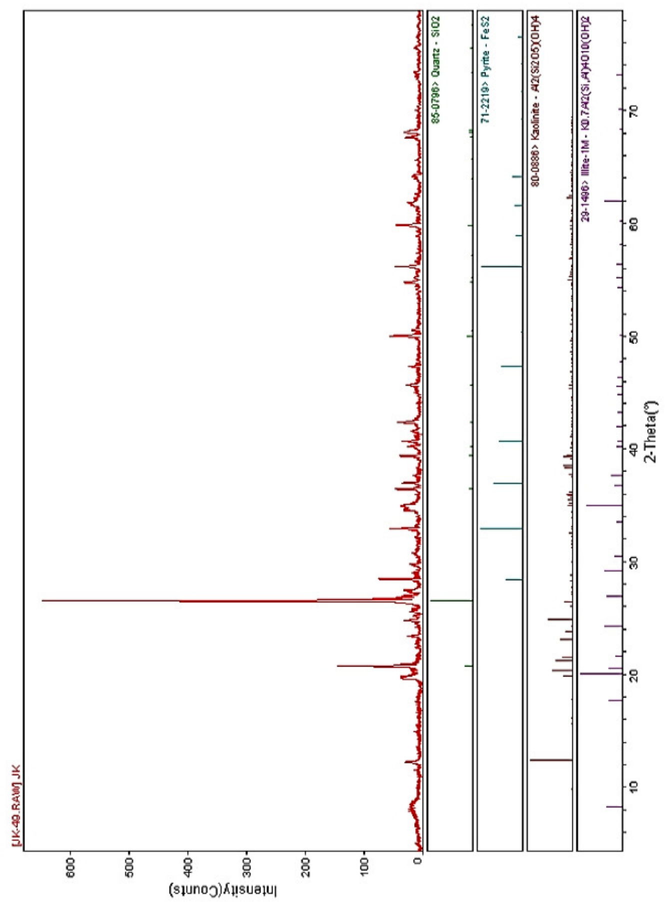
[JK-49.RAW] JK
Intensity(Counts)
0
100
200
300
400
500
600
2-Theta(°)
10
20
30
40
50
60
70
85-0796> Quartz - SiO2
71-2219> Pyrite - FeS2
80-0886> Kaolinite - Al2(Si2O5)(OH)4
29-1496> Illite-1M - K0.7Al2(Si,Al)4O10(OH)2

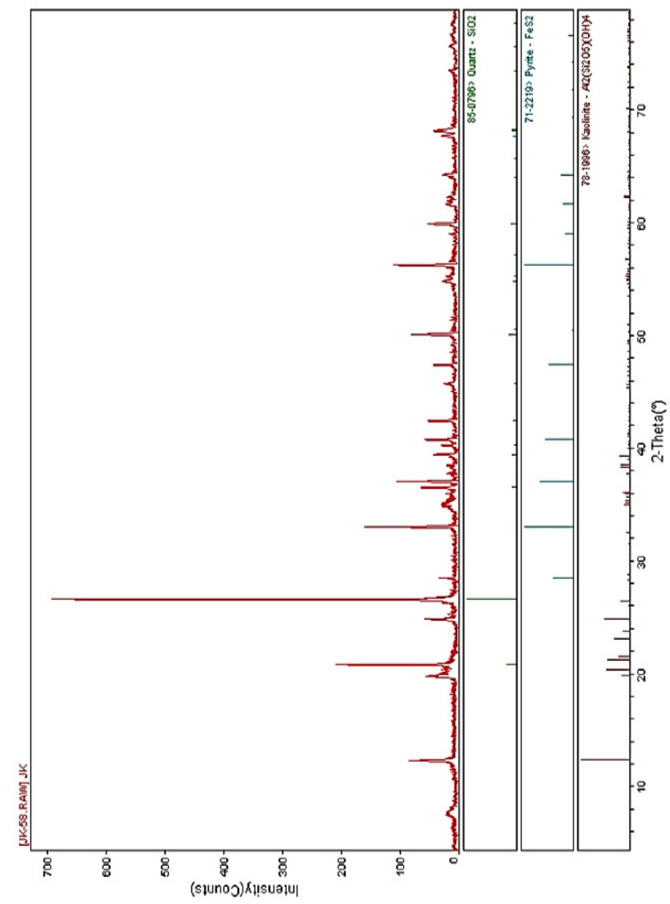
[UK-58.RAW] JK
Intensity(Counts)
0
100
200
300
400
500
600
700
2-Theta(°)
10
20
30
40
50
60
70
85-0796> Quartz - SiO2
71-2219> Pyrite - FeS2
78-1996> Kaolinite - Al2(Si2O5)(OH)4

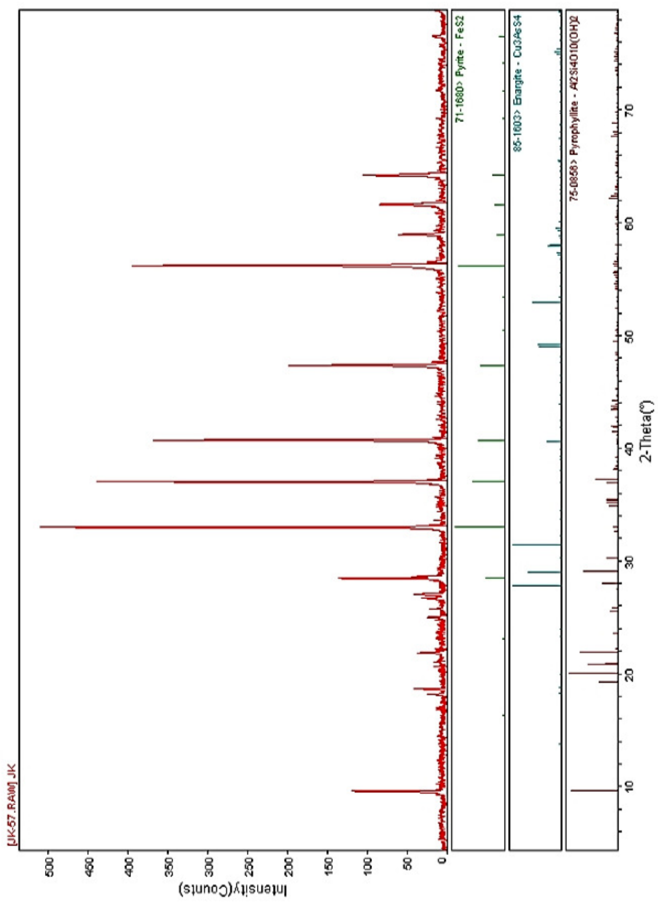
[UK-57.RAW] JK
Intensity(Counts)
0
50
100
150
200
250
300
350
400
450
500
2-Theta(°)
10
20
30
40
50
60
70
71-1680> Pyrite - FeS2
85-1603> Enargite - Cu3AsS4
75-0856> Pyrophyllite - Al2Si4O10(OH)2

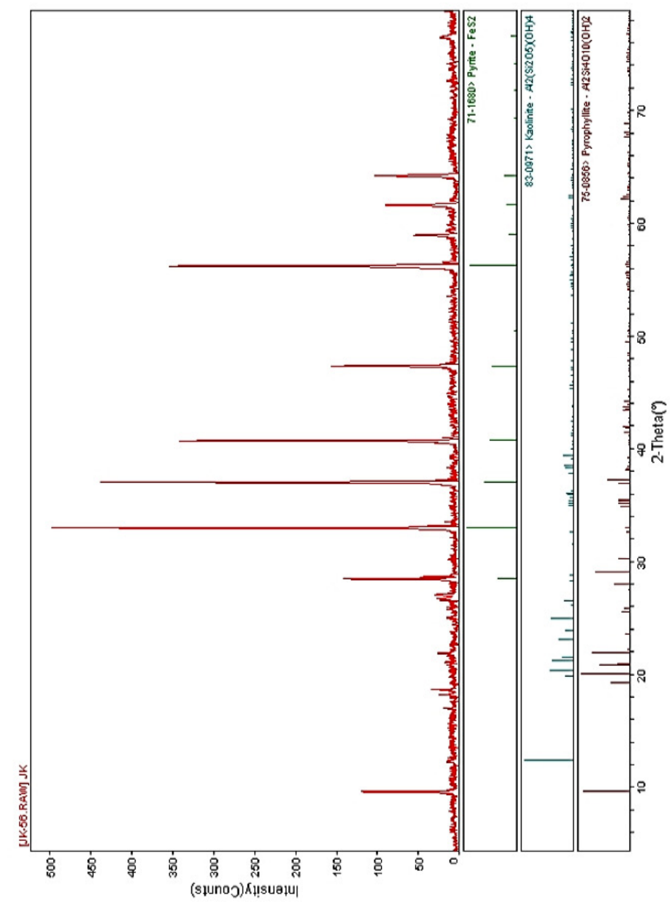
[UK-56.RAW] JK
Intensity(Counts)
0
50
100
150
200
250
300
350
400
450
500
2-Theta(°)
10
20
30
40
50
60
70
71-1680> Pyrite - FeS2
83-0971> Kaolinite - Al2(Si2O5)(OH)4
75-0856> Pyrophyllite - Al2Si4O10(OH)2

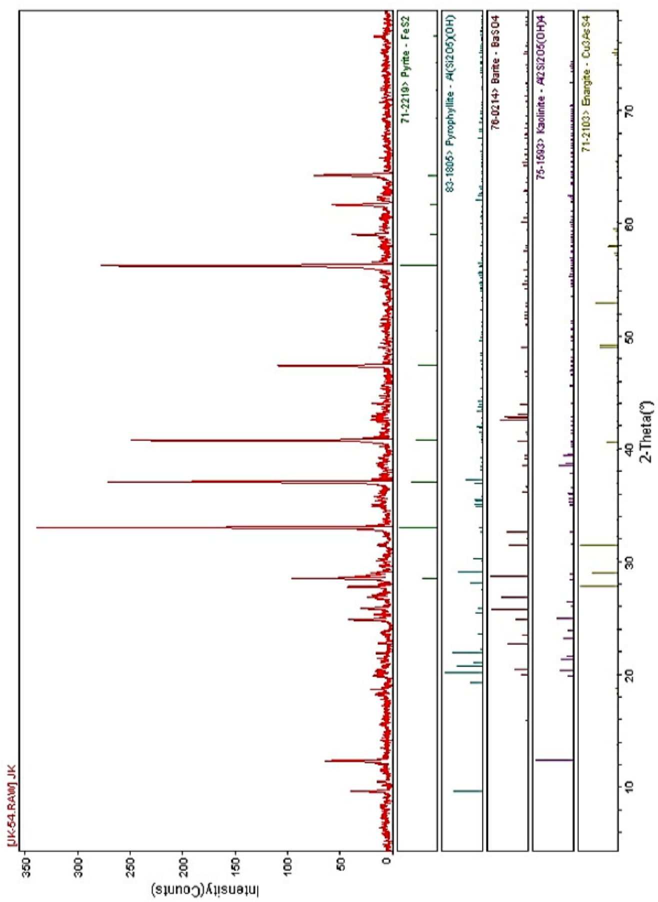
[UK-54.RAW] JK
Intensity(Counts)
0
50
100
150
200
250
300
350
2-Theta(°)
10
20
30
40
50
60
70
71-2219> Pyrite - FeS2
83-1805> Pyrophyllite - Al(Si2O5)(OH)
76-0214> Barite - BaSO4
75-1593> Kaolinite - Al2Si2O5(OH)4
71-2103> Enargite - Cu3AsS4

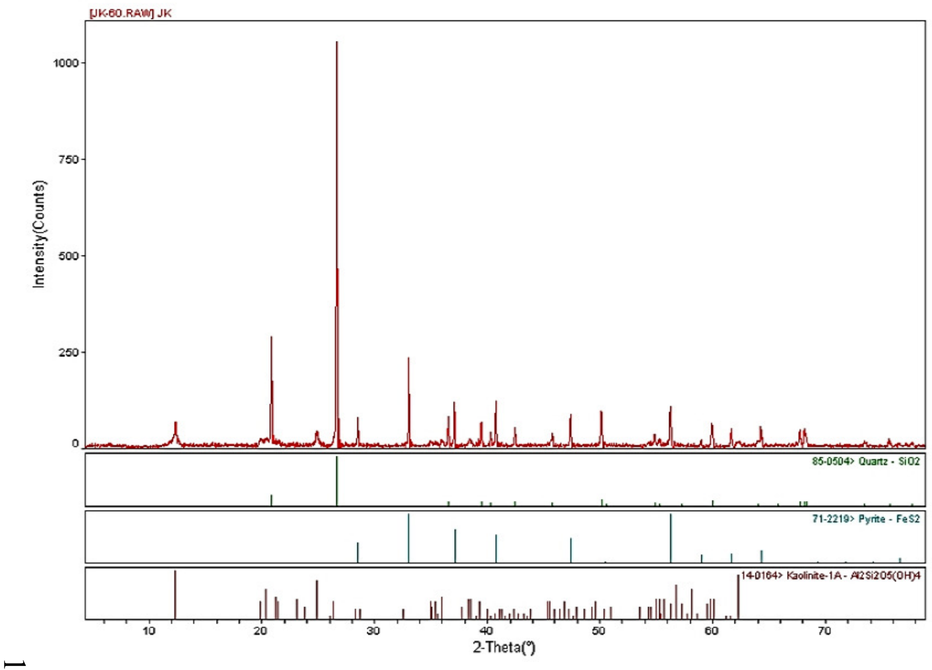
[JK-60.RAW] JK
Intensity(Counts)
0
250
500
750
1000
85-0504> Quartz - SiO2
71-2219> Pyrite - FeS2
14-0164> Kaolinite-1A - Al2Si2O5(OH)4
10
20
30
40
50
60
70
2-Theta(°)

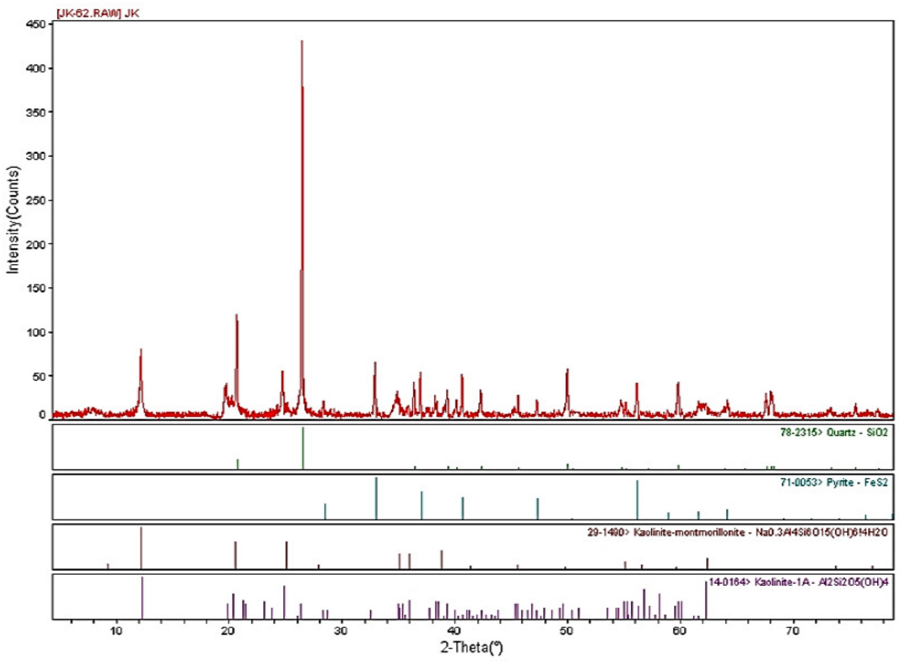
[JK-62.RAW] JK
Intensity(Counts)
0
50
100
150
200
250
300
350
400
450
78-2315> Quartz - SiO2
71-0053> Pyrite - FeS2
29-1490> Kaolinite-montmorillonite - Na0.3Al4Si6O15(OH)6!4H2O
14-0164> Kaolinite-1A - Al2Si2O5(OH)4
10
20
30
40
50
60
70
2-Theta(°)

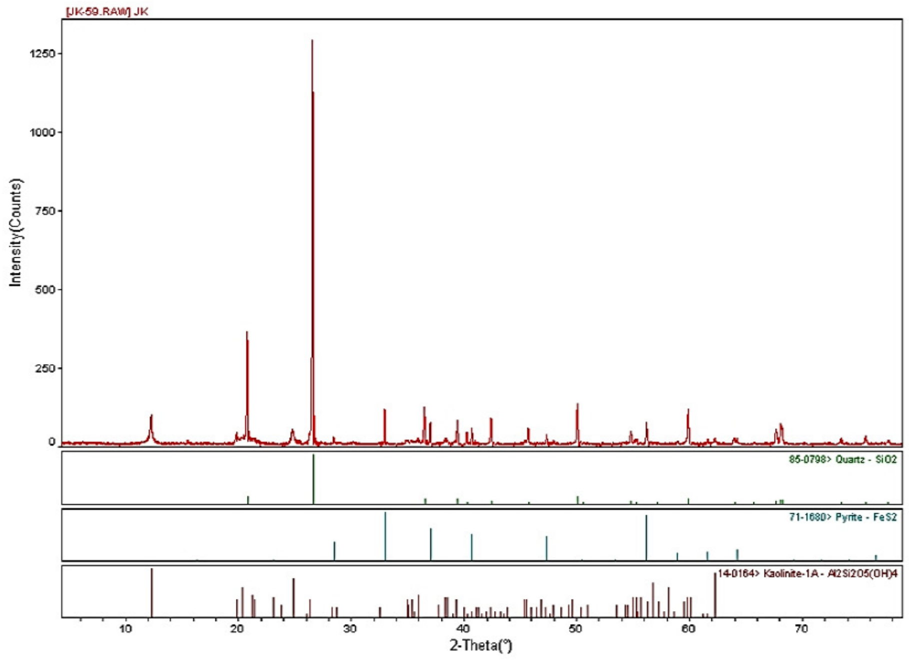
[JK-59.RAW] JK
Intensity(Counts)
0
250
500
750
1000
1250
85-0798> Quartz - SiO2
71-1680> Pyrite - FeS2
14-0164> Kaolinite-1A - Al2Si2O5(OH)4
10
20
30
40
50
60
70
2-Theta(°)

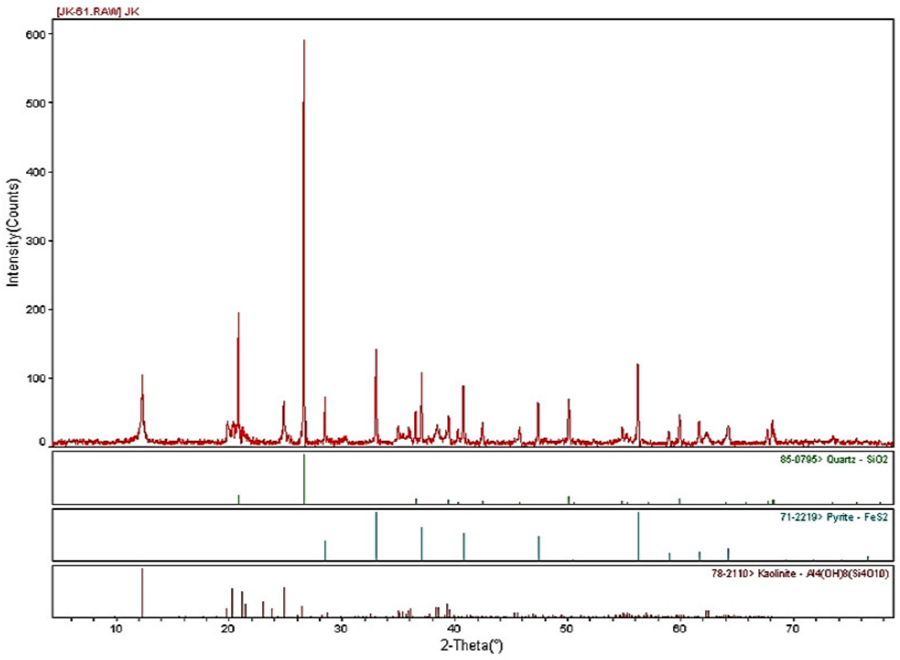
[JK-61.RAW] JK
Intensity(Counts)
0
100
200
300
400
500
600
85-0795> Quartz - SiO2
71-2219> Pyrite - FeS2
78-2110> Kaolinite - Al4(OH)8(Si4O10)
10
20
30
40
50
60
70
2-Theta(°)

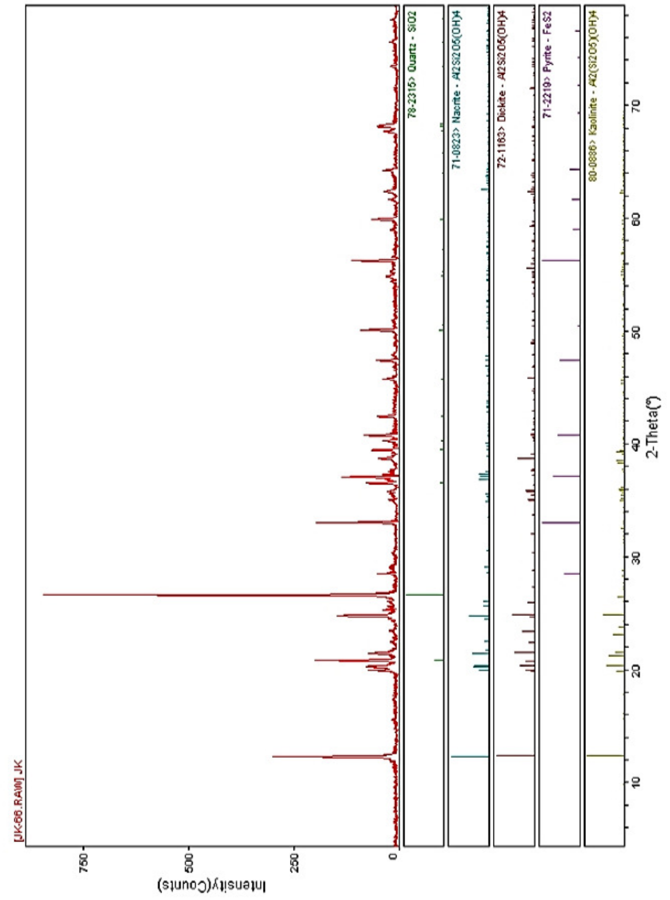
[JK-66.RAW] JK
Intensity(Counts)
750
500
250
0
78-2315> Quartz - SiO2
71-0823> Nacrite - Al2Si2O5(OH)4
72-1163> Dickite - Al2Si2O5(OH)4
71-2219> Pyrite - FeS2
80-0886> Kaolinite - Al2(Si2O5)(OH)4
10
20
30
40
50
60
70
2-Theta(°)

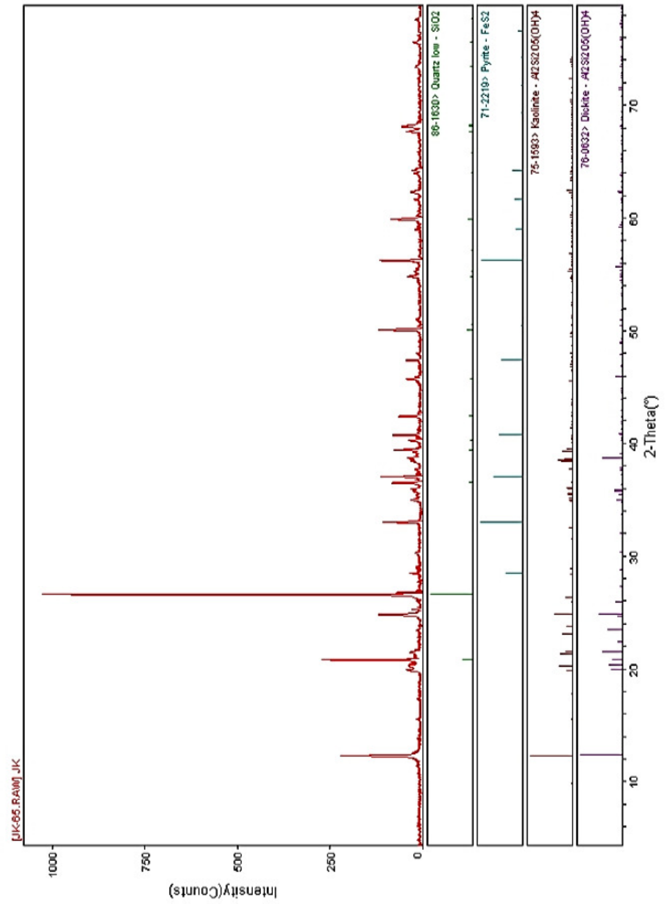
[JK-65.RAW] JK
Intensity(Counts)
1000
750
500
250
0
86-1630> Quartz low - SiO2
71-2219> Pyrite - FeS2
75-1593> Kaolinite - Al2Si2O5(OH)4
76-0832> Dickite - Al2Si2O5(OH)4
10
20
30
40
50
60
70
2-Theta(°)

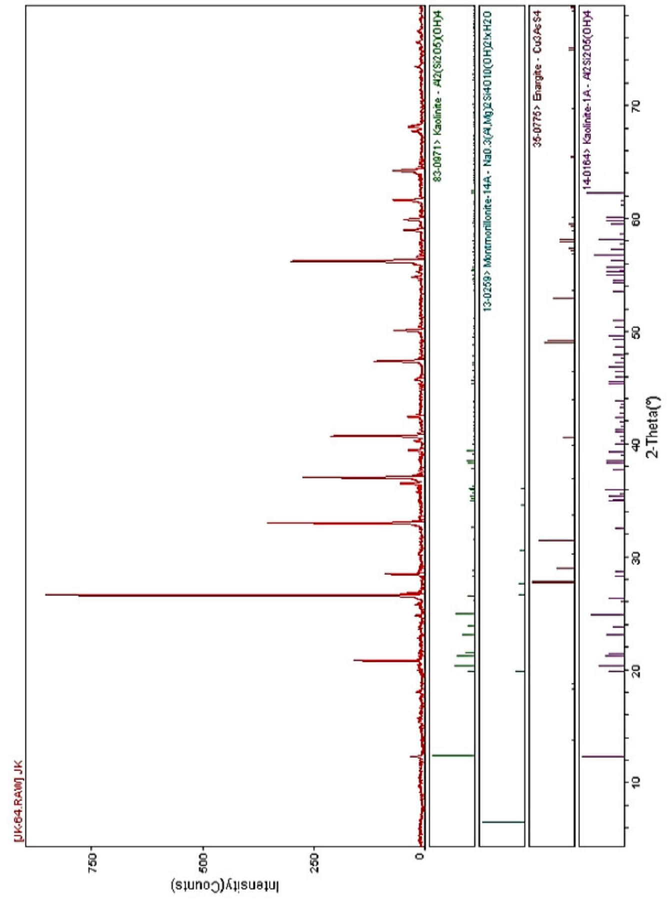
[JK-64.RAW] JK
Intensity(Counts)
750
500
250
0
83-0971> Kaolinite - Al2(Si2O5)(OH)4
13-0259> Montmorillonite-14A - Na0.3(Al,Mg)2Si4O10(OH)2!xH2O
35-0775> Enargite - Cu3AsS4
14-0164> Kaolinite-1A - Al2Si2O5(OH)4
10
20
30
40
50
60
70
2-Theta(°)

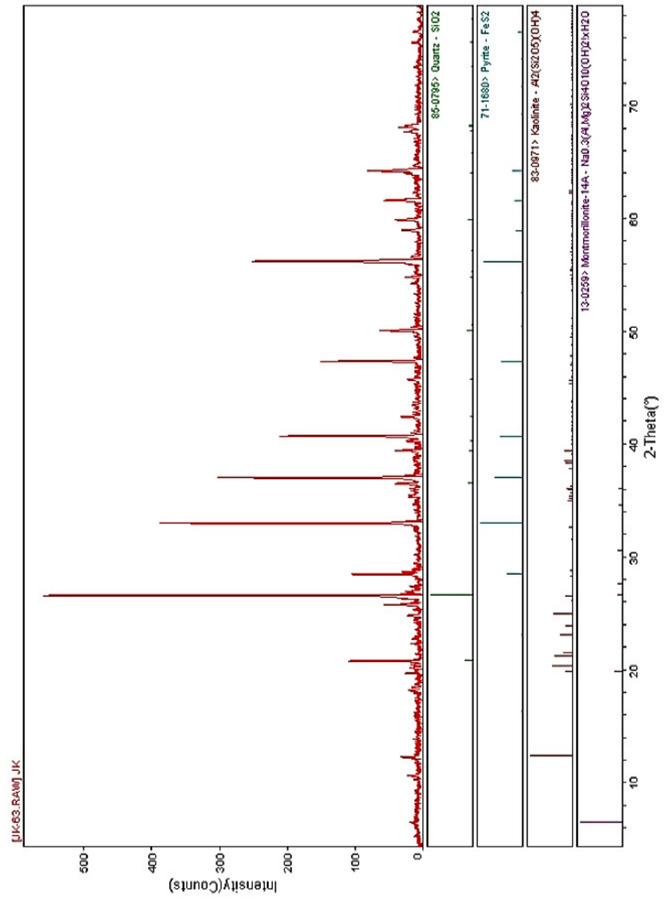
[JK-63.RAW] JK
Intensity(Counts)
500
400
300
200
100
0
85-0795> Quartz - SiO2
71-1680> Pyrite - FeS2
83-0971> Kaolinite - Al2(Si2O5)(OH)4
13-0259> Montmorillonite-14A - Na0.3(Al,Mg)2Si4O10(OH)2!xH2O
10
20
30
40
50
60
70
2-Theta(°)

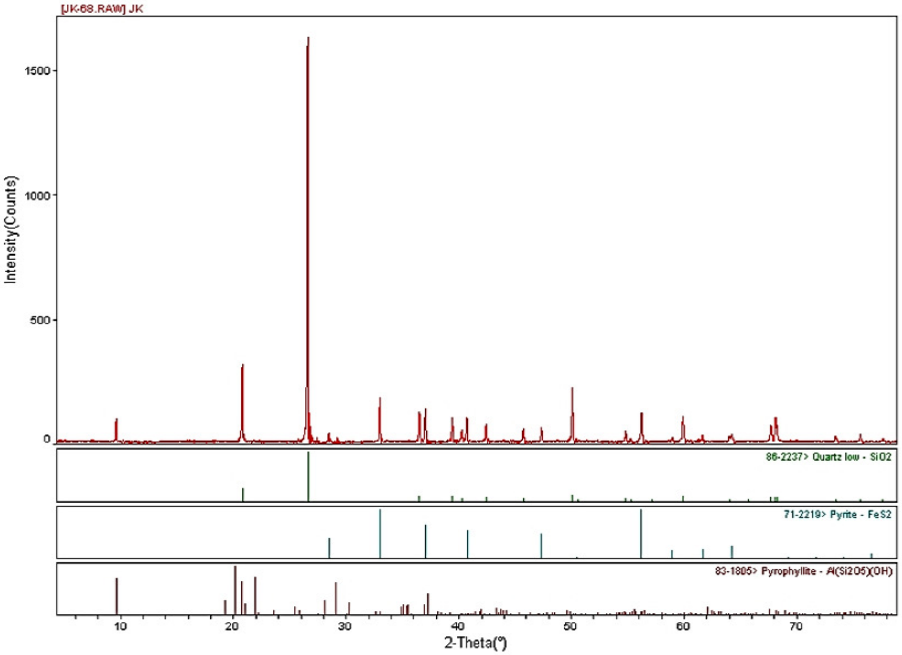
[JK-68.RAW] JK
Intensity(Counts)
1500
1000
500
0
86-2237> Quartz low - SiO2
71-2219> Pyrite - FeS2
83-1805> Pyrophyllite - Al(Si2O5)(OH)
10
20
30
40
50
60
70
2-Theta(°)

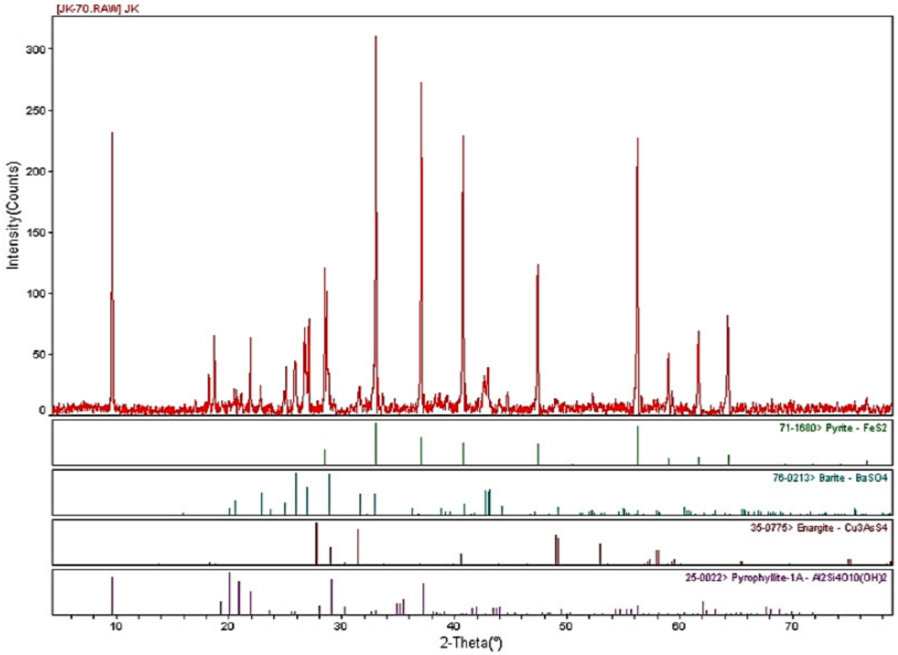
[JK-70.RAW] JK
Intensity(Counts)
300
250
200
150
100
50
0
71-1680> Pyrite - FeS2
76-0213> Barite - BaSO4
35-0775> Enargite - Cu3AsS4
25-0022> Pyrophyllite-1A - Al2Si4O10(OH)2
10
20
30
40
50
60
70
2-Theta(°)

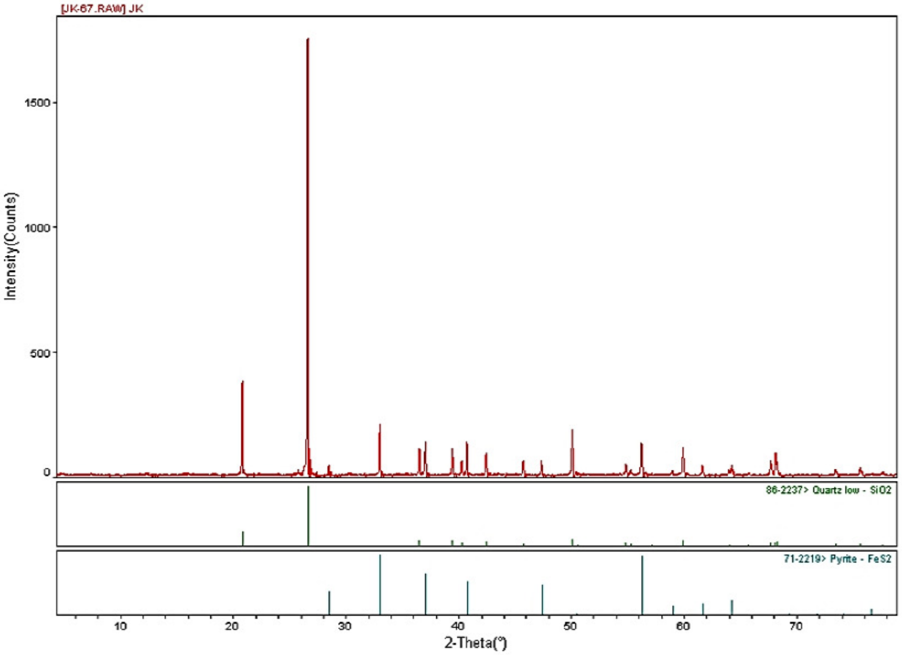
[JK-67.RAW] JK
Intensity(Counts)
1500
1000
500
0
86-2237> Quartz low - SiO2
71-2219> Pyrite - FeS2
10
20
30
40
50
60
70
2-Theta(°)

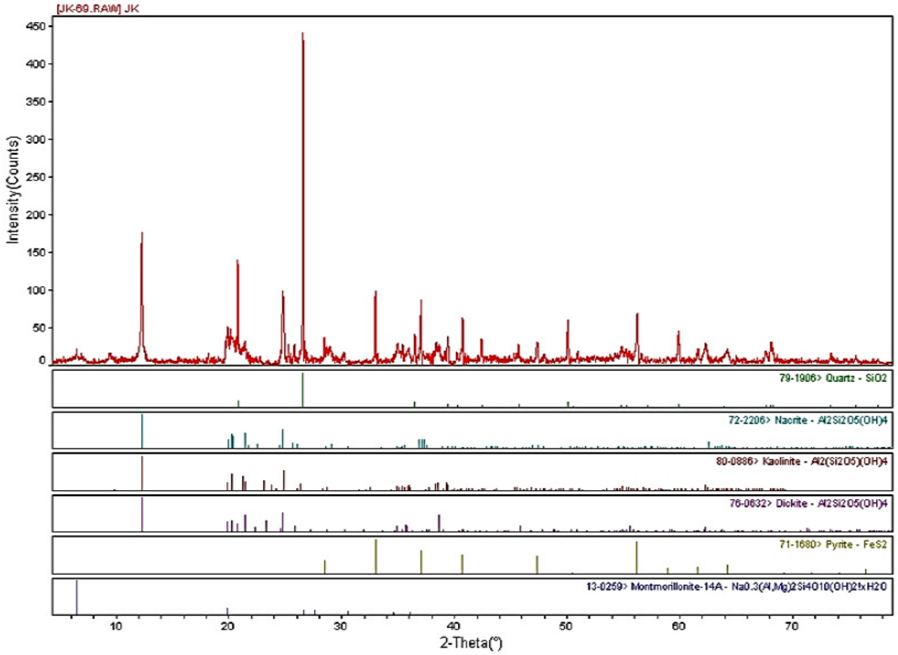
[JK-69.RAW] JK
Intensity(Counts)
450
400
350
300
250
200
150
100
50
0
79-1906> Quartz - SiO2
72-2206> Nacrite - Al2Si2O5(OH)4
80-0886> Kaolinite - Al2(Si2O5)(OH)4
76-0632> Dickite - Al2Si2O5(OH)4
71-1680> Pyrite - FeS2
13-0259> Montmorillonite-14A - Na0.3(Al,Mg)2Si4O10(OH)2·xH2O
10
20
30
40
50
60
70
2-Theta(°)

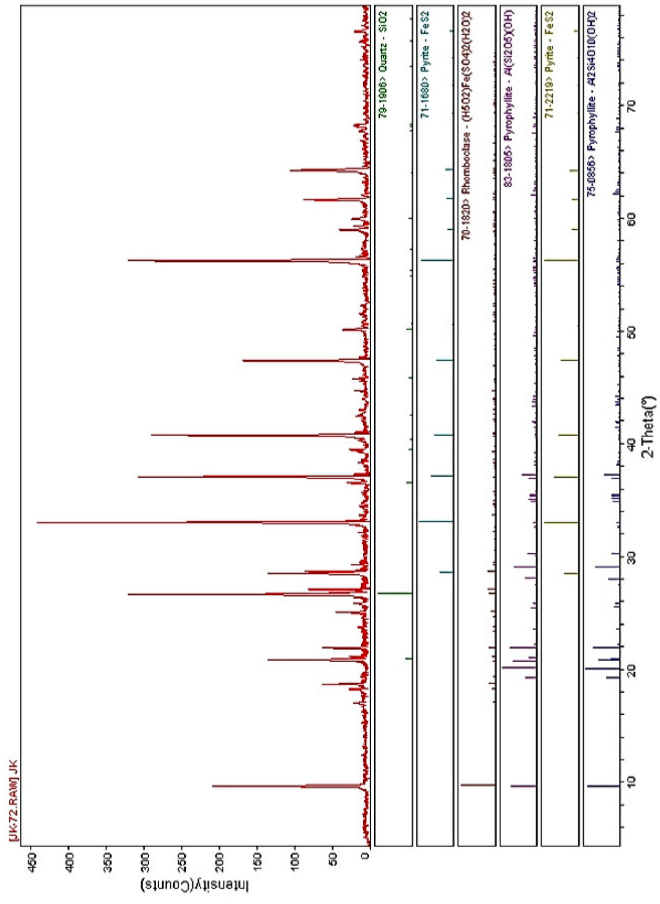
[JK-72.RAW] JK
Intensity(Counts)
0
50
100
150
200
250
300
350
400
450
10
20
30
40
50
60
70
2-Theta(°)
79-1906> Quartz - SiO2
71-1680> Pyrite - FeS2
70-1820> Rhomboclase - (H5O2)Fe(SO4)2(H2O)2
83-1805> Pyrophyllite - Al(Si2O5)(OH)
71-2219> Pyrite - FeS2
75-0856> Pyrophyllite - Al2Si4O10(OH)2

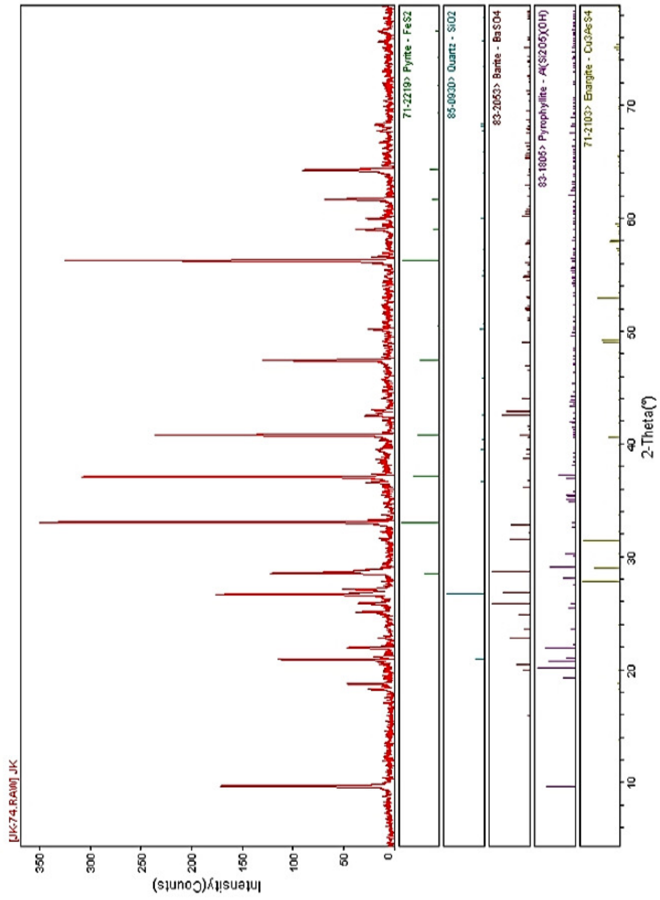
[JK-74.RAW] JK
Intensity(Counts)
0
50
100
150
200
250
300
350
10
20
30
40
50
60
70
2-Theta(°)
71-2219> Pyrite - FeS2
85-0930> Quartz - SiO2
83-2053> Barite - BaSO4
83-1805> Pyrophyllite - Al(Si2O5)(OH)
71-2103> Enargite - Cu3AsS4

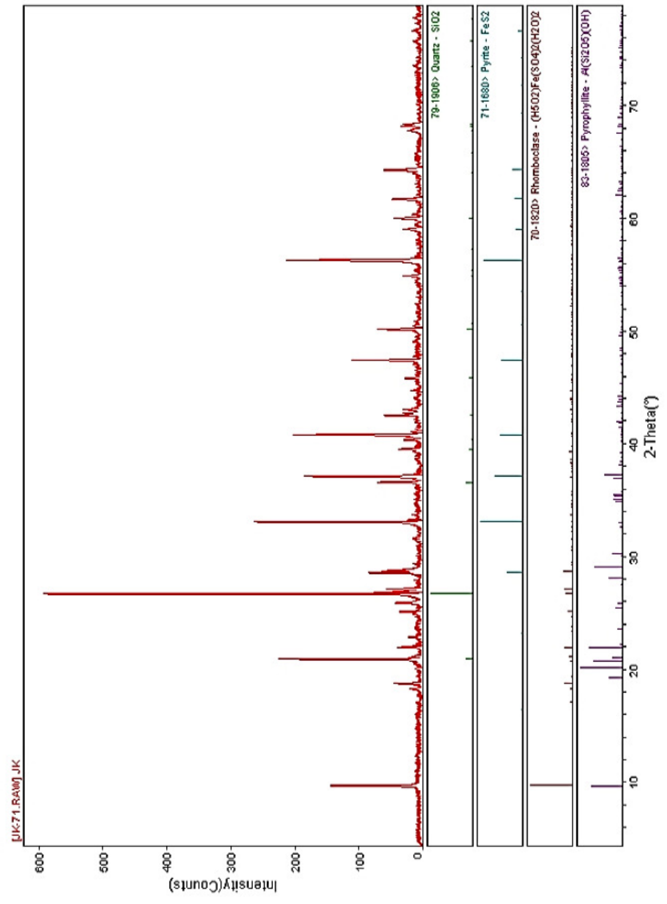
[JK-71.RAW] JK
Intensity(Counts)
0
100
200
300
400
500
600
10
20
30
40
50
60
70
2-Theta(°)
79-1906> Quartz - SiO2
71-1680> Pyrite - FeS2
70-1820> Rhomboclase - (H5O2)Fe(SO4)2(H2O)2
83-1805> Pyrophyllite - Al(Si2O5)(OH)

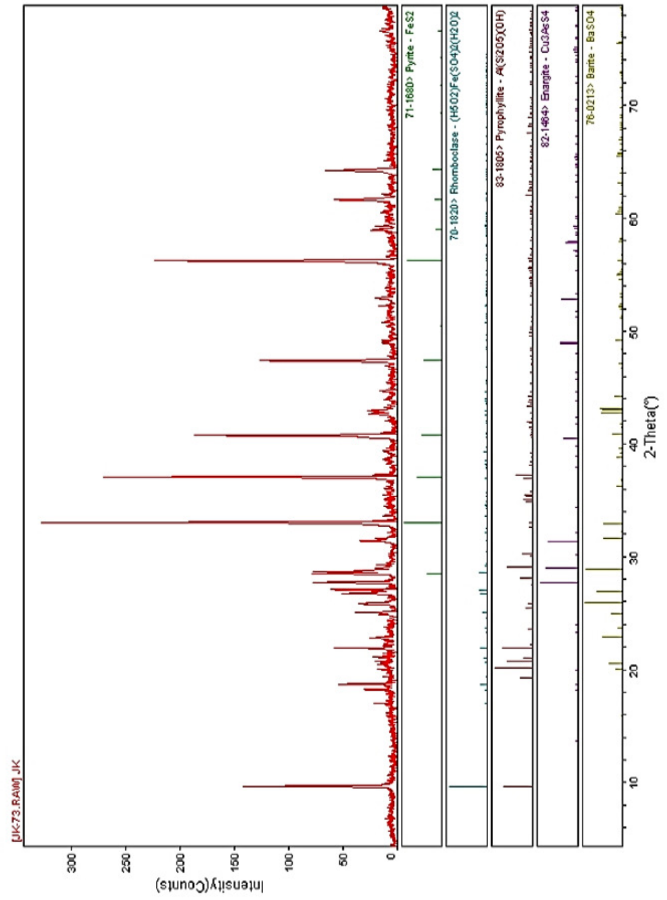
[JK-73.RAW] JK
Intensity(Counts)
0
50
100
150
200
250
300
10
20
30
40
50
60
70
2-Theta(°)
71-1680> Pyrite - FeS2
70-1820> Rhomboclase - (H5O2)Fe(SO4)2(H2O)2
83-1805> Pyrophyllite - Al(Si2O5)(OH)
82-1464> Enargite - Cu3AsS4
76-0213> Barite - BaSO4

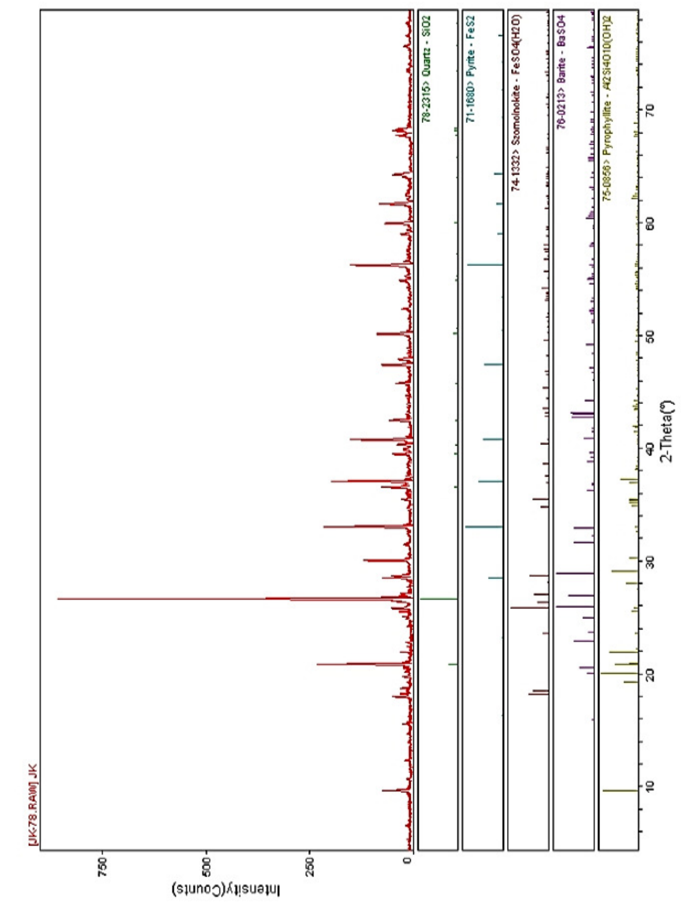
[JK-78.RAW] JK
Intensity(Counts)
750
500
250
0
78-2315> Quartz - SiO2
71-1680> Pyrite - FeS2
74-1332> Szomolnokite - FeSO4(H2O)
76-0213> Barite - BaSO4
75-0856> Pyrophyllite - Al2Si4O10(OH)2
10
20
30
40
50
60
70
2-Theta(°)

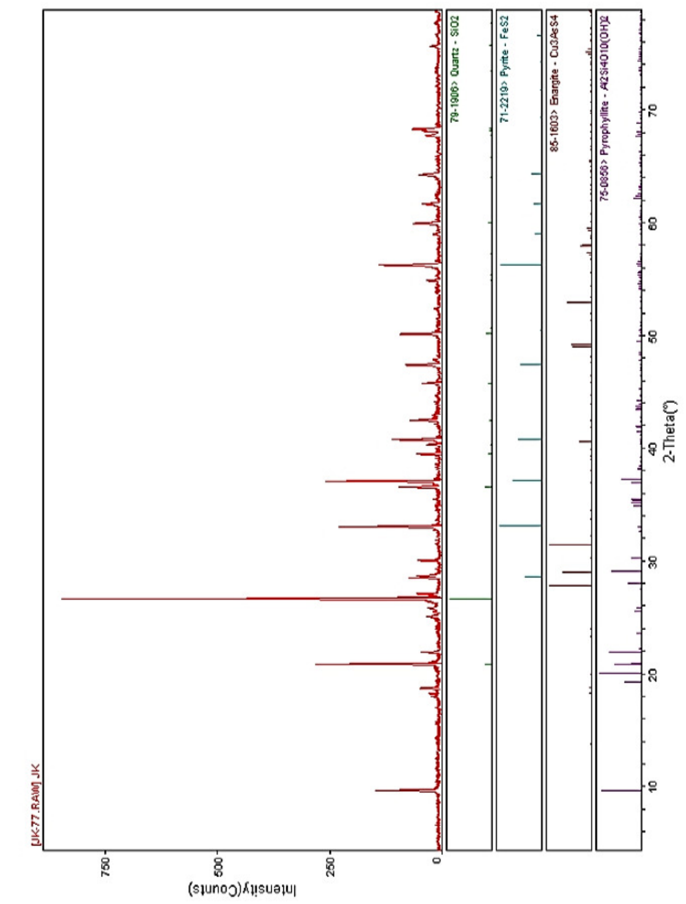
[JK-77.RAW] JK
Intensity(Counts)
750
500
250
0
79-1906> Quartz - SiO2
71-2219> Pyrite - FeS2
85-1603> Enargite - Cu3AsS4
75-0856> Pyrophyllite - Al2Si4O10(OH)2
10
20
30
40
50
60
70
2-Theta(°)

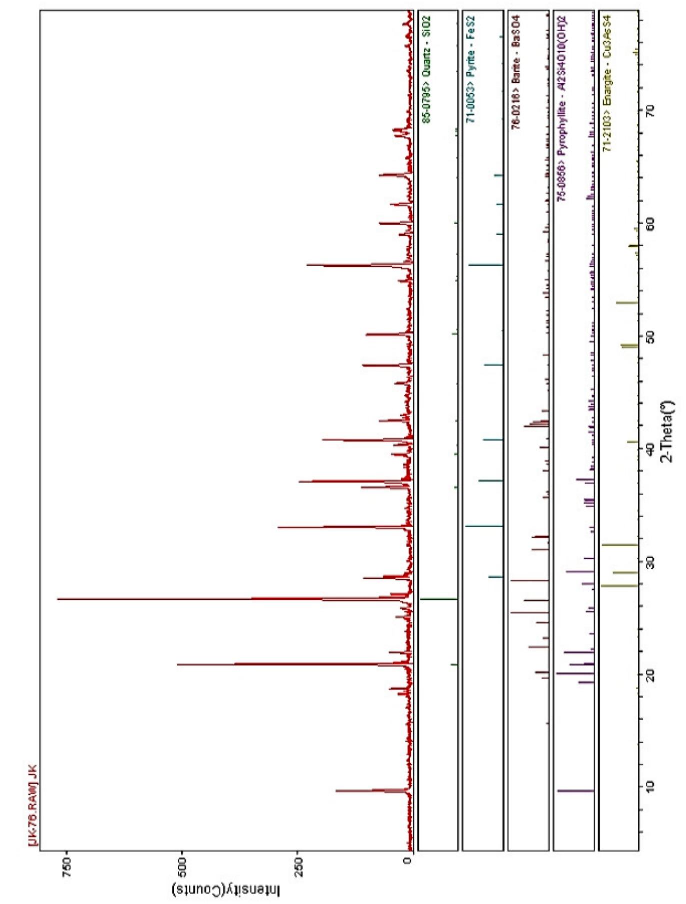
[JK-76.RAW] JK
Intensity(Counts)
750
500
250
0
85-0795> Quartz - SiO2
71-0053> Pyrite - FeS2
76-0216> Barite - BaSO4
75-0856> Pyrophyllite - Al2Si4O10(OH)2
71-2103> Enargite - Cu3AsS4
10
20
30
40
50
60
70
2-Theta(°)

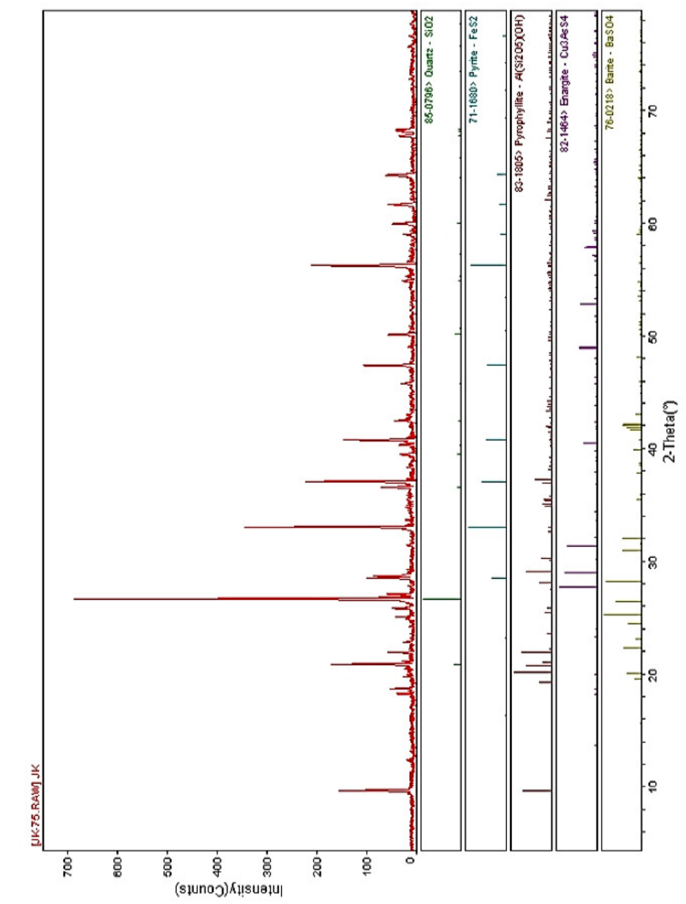
[JK-75.RAW] JK
Intensity(Counts)
700
600
500
400
300
200
100
0
85-0796> Quartz - SiO2
71-1680> Pyrite - FeS2
83-1805> Pyrophyllite - Al(Si2O5)(OH)
82-1464> Enargite - Cu3AsS4
76-0218> Barite - BaSO4
10
20
30
40
50
60
70
2-Theta(°)

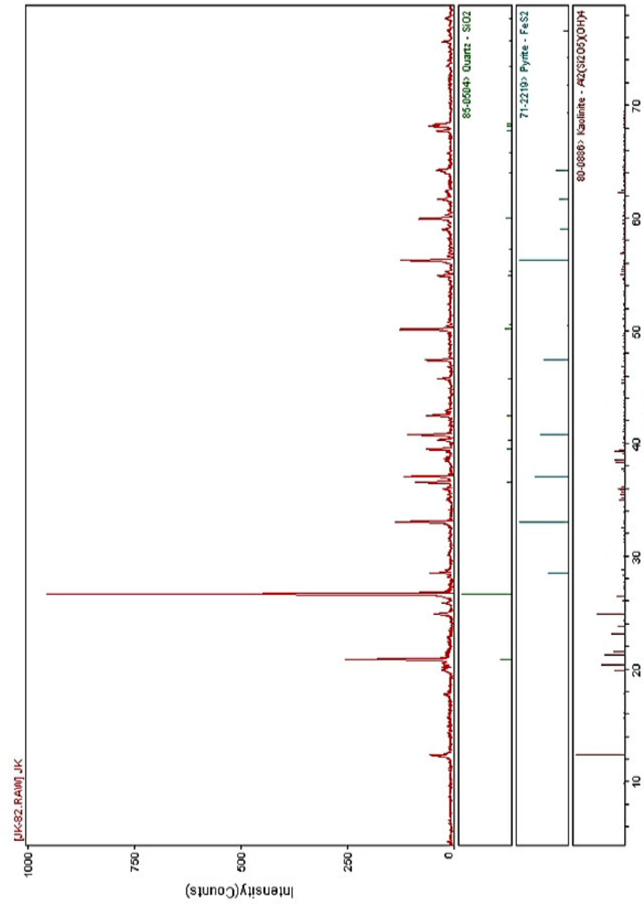
[JK-82.RAW] JK
Intensity(Counts)
1000
750
500
250
0
10
20
30
40
50
60
70
2-Theta(°)
85-0504> Quartz - SiO2
71-2219> Pyrite - FeS2
80-0886> Kaolinite - Al2(Si2O5)(OH)4

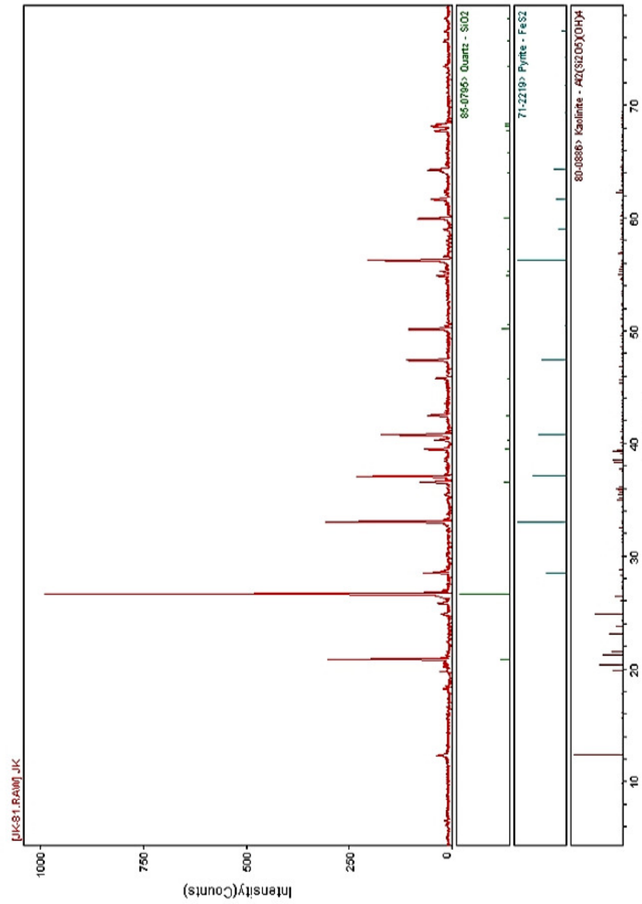
[JK-81.RAW] JK
Intensity(Counts)
1000
750
500
250
0
10
20
30
40
50
60
70
2-Theta(°)
85-0795> Quartz - SiO2
71-2219> Pyrite - FeS2
80-0886> Kaolinite - Al2(Si2O5)(OH)4

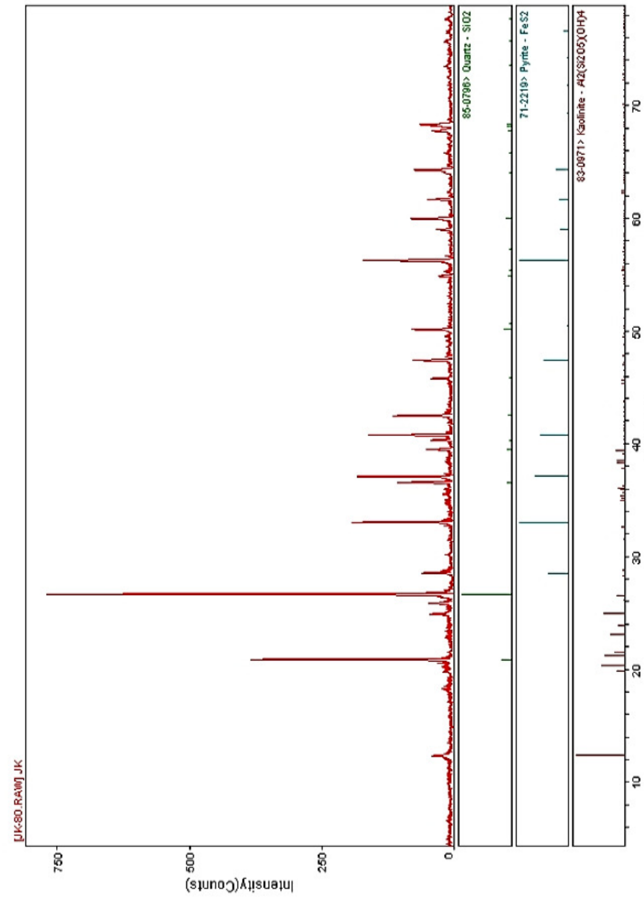
[JK-80.RAW] JK
Intensity(Counts)
750
500
250
0
10
20
30
40
50
60
70
2-Theta(°)
85-0796> Quartz - SiO2
71-2219> Pyrite - FeS2
83-0971> Kaolinite - Al2(Si2O5)(OH)4

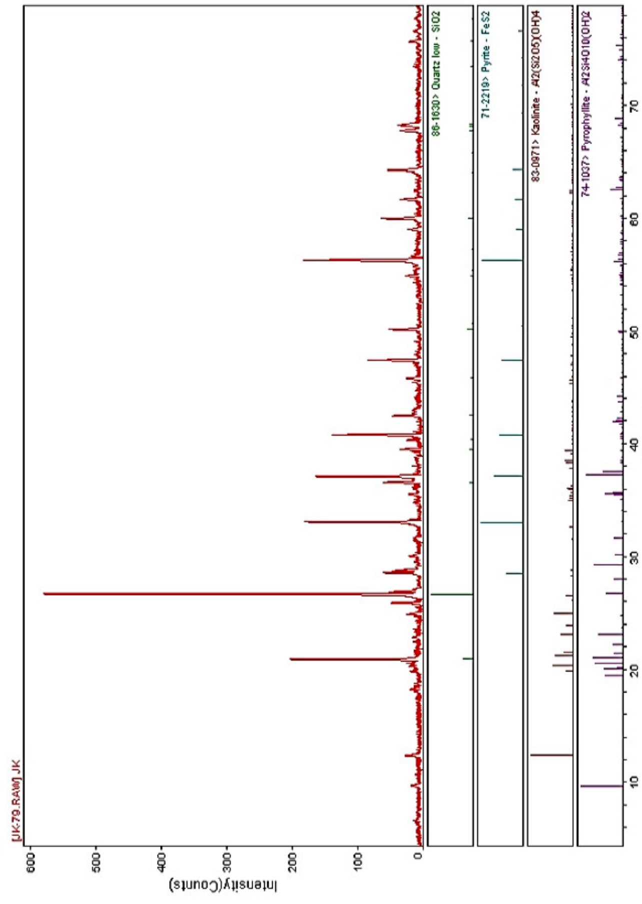
[JK-79.RAW] JK
Intensity(Counts)
600
500
400
300
200
100
0
10
20
30
40
50
60
70
2-Theta(°)
86-1630> Quartz low - SiO2
71-2219> Pyrite - FeS2
83-0971> Kaolinite - Al2(Si2O5)(OH)4
74-1037> Pyrophyllite - Al2Si4O10(OH)2

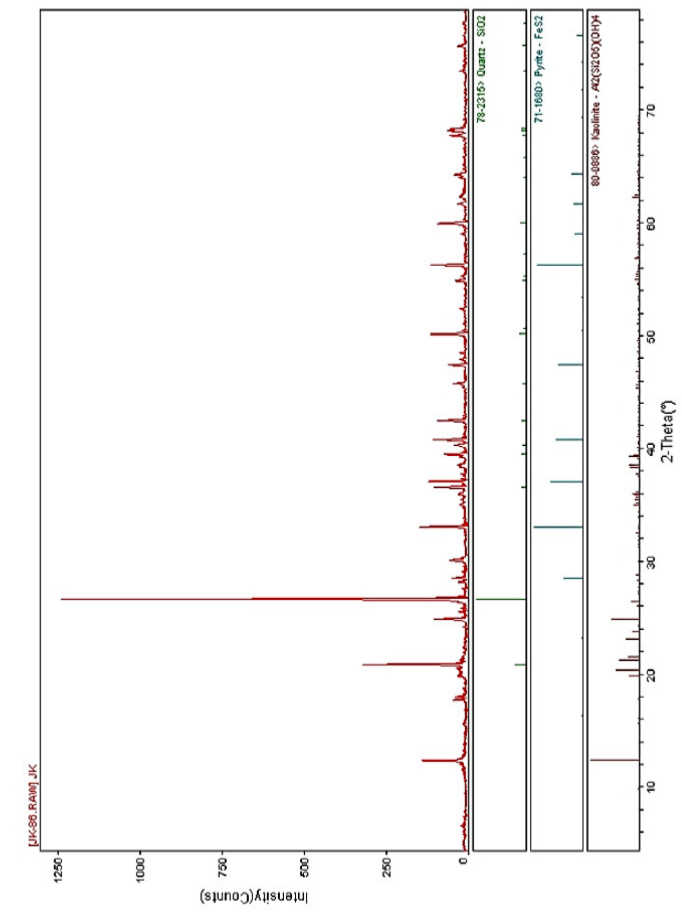
[JK-86.RAW] JK
Intensity(Counts)
0
250
500
750
1000
1250
78-2315> Quartz - SiO2
71-1680> Pyrite - FeS2
80-0886> Kaolinite - Al2(Si2O5)(OH)4
10
20
30
40
50
60
70
2-Theta(°)

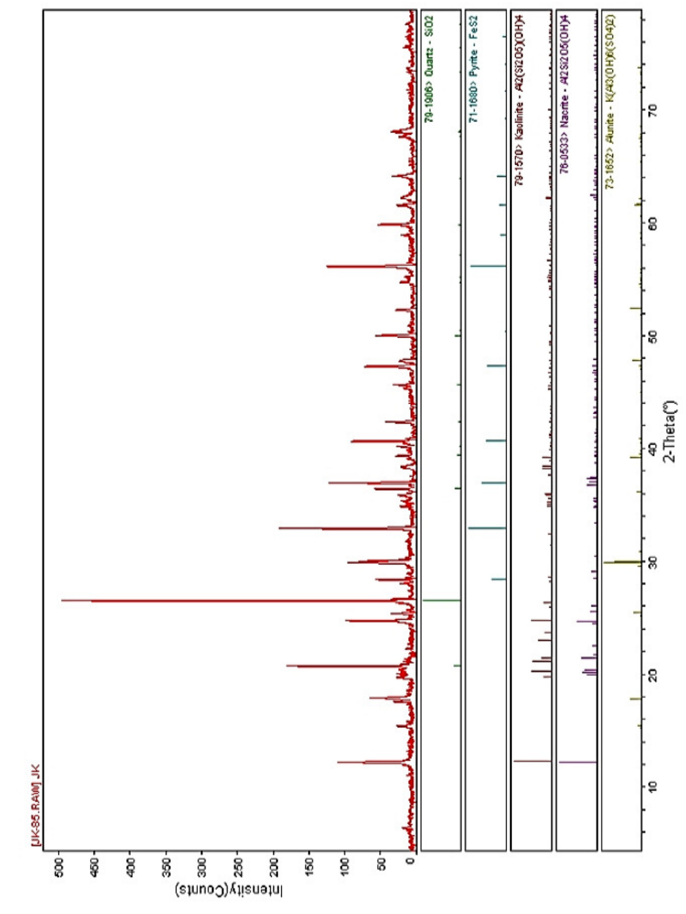
[JK-85.RAW] JK
Intensity(Counts)
0
50
100
150
200
250
300
350
400
450
500
79-1906> Quartz - SiO2
71-1680> Pyrite - FeS2
79-1570> Kaolinite - Al2(Si2O5)(OH)4
76-0533> Nacrite - Al2Si2O5(OH)4
73-1652> Alunite - K(Al3(OH)6(SO4)2)
10
20
30
40
50
60
70
2-Theta(°)

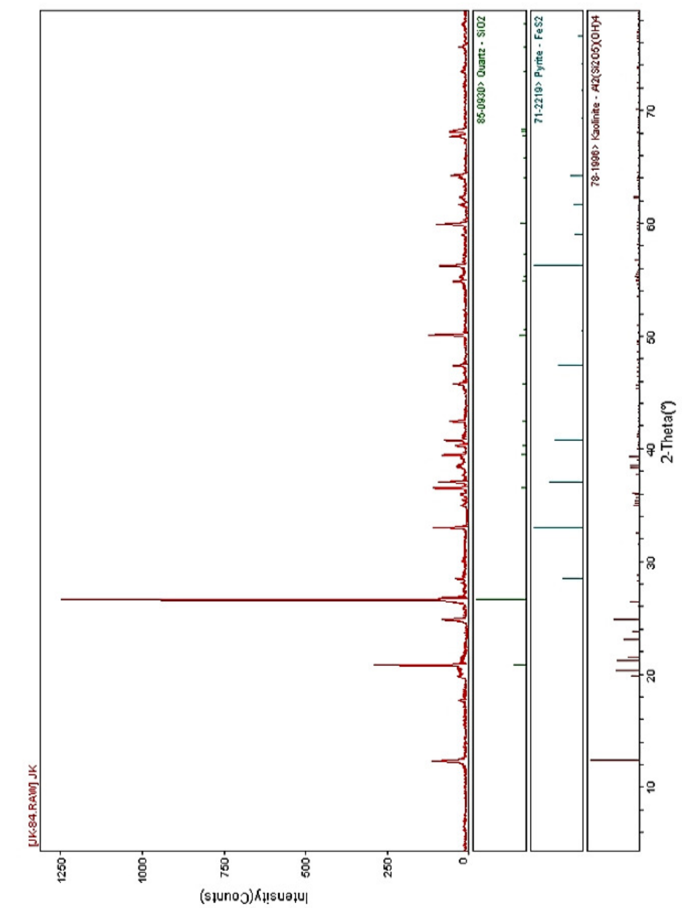
[JK-84.RAW] JK
Intensity(Counts)
0
250
500
750
1000
1250
85-0930> Quartz - SiO2
71-2219> Pyrite - FeS2
78-1996> Kaolinite - Al2(Si2O5)(OH)4
10
20
30
40
50
60
70
2-Theta(°)

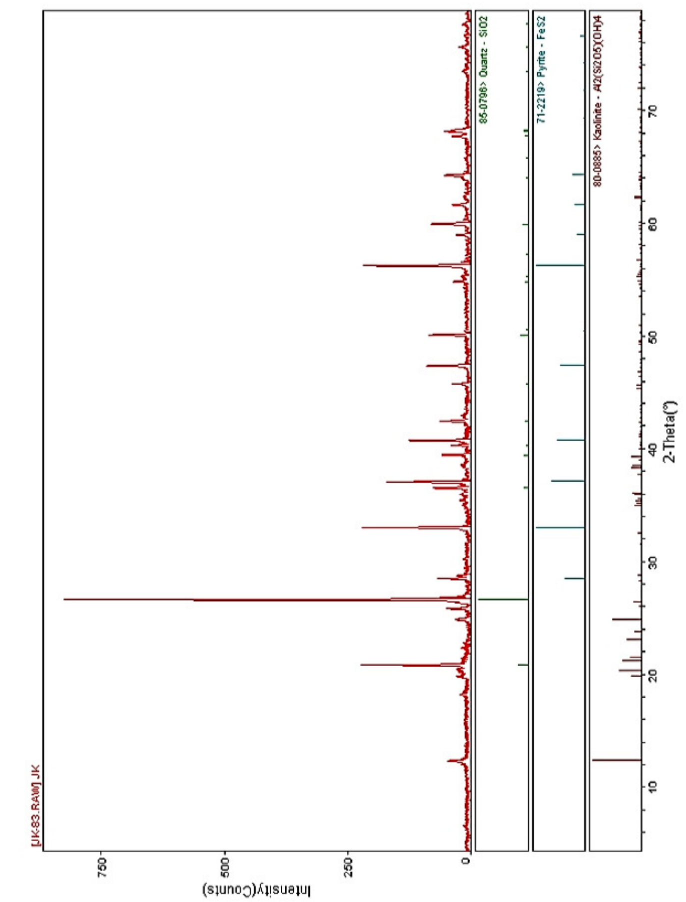
[JK-83.RAW] JK
Intensity(Counts)
0
250
500
750
85-0796> Quartz - SiO2
71-2219> Pyrite - FeS2
80-0885> Kaolinite - Al2(Si2O5)(OH)4
10
20
30
40
50
60
70
2-Theta(°)

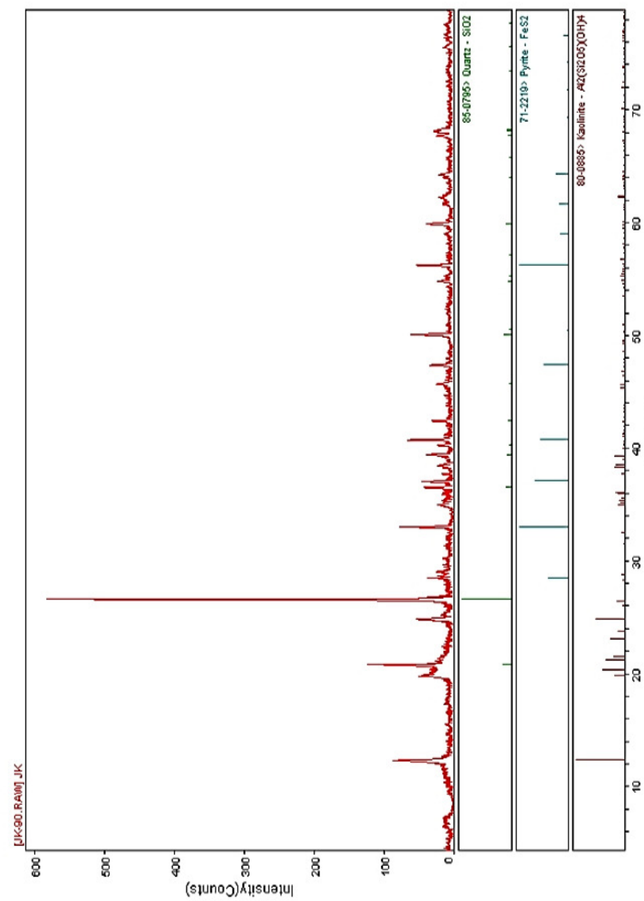
[JK-90.RAW] JK
Intensity(Counts)
0
100
200
300
400
500
600
85-0795> Quartz - SiO2
71-2219> Pyrite - FeS2
80-0885> Kaolinite - Al2(Si2O5)(OH)4
10
20
30
40
50
60
70
2-Theta(°)

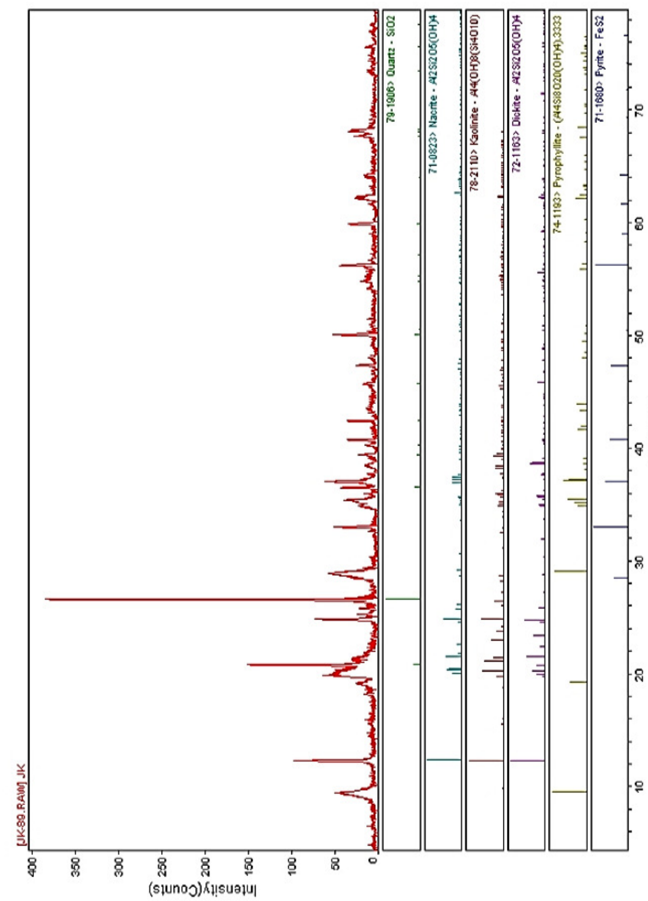
[JK-89.RAW] JK
Intensity(Counts)
0
50
100
150
200
250
300
350
400
79-1906> Quartz - SiO2
71-0823> Nacrite - Al2Si2O5(OH)4
78-2110> Kaolinite - Al4(OH)8(Si4O10)
72-1163> Dickite - Al2Si2O5(OH)4
74-1193> Pyrophyllite - (Al4Si8O20(OH)4).3333
71-1680> Pyrite - FeS2
10
20
30
40
50
60
70
2-Theta(°)

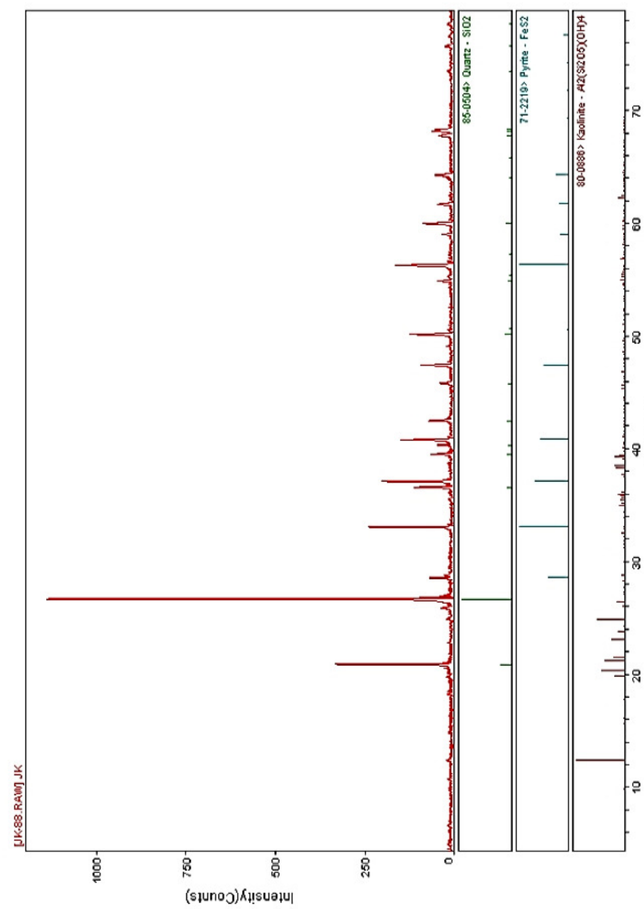
[JK-88.RAW] JK
Intensity(Counts)
0
250
500
750
1000
85-0504> Quartz - SiO2
71-2219> Pyrite - FeS2
80-0886> Kaolinite - Al2(Si2O5)(OH)4
10
20
30
40
50
60
70
2-Theta(°)

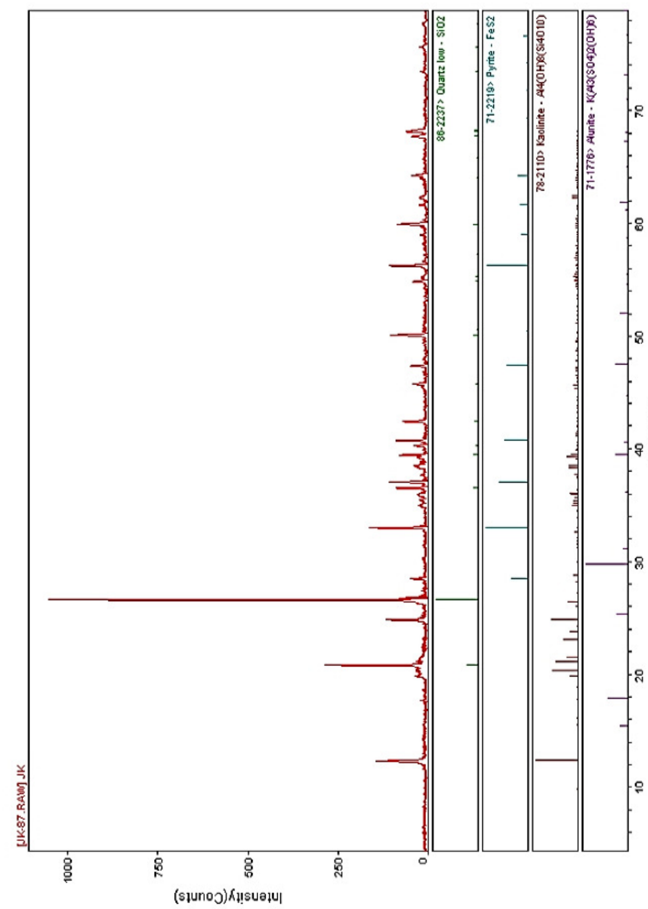
[JK-87.RAW] JK
Intensity(Counts)
0
250
500
750
1000
86-2237> Quartz low - SiO2
71-2219> Pyrite - FeS2
78-2110> Kaolinite - Al4(OH)8(Si4O10)
71-1776> Alunite - K(Al3(SO4)2(OH)6)
10
20
30
40
50
60
70
2-Theta(°)

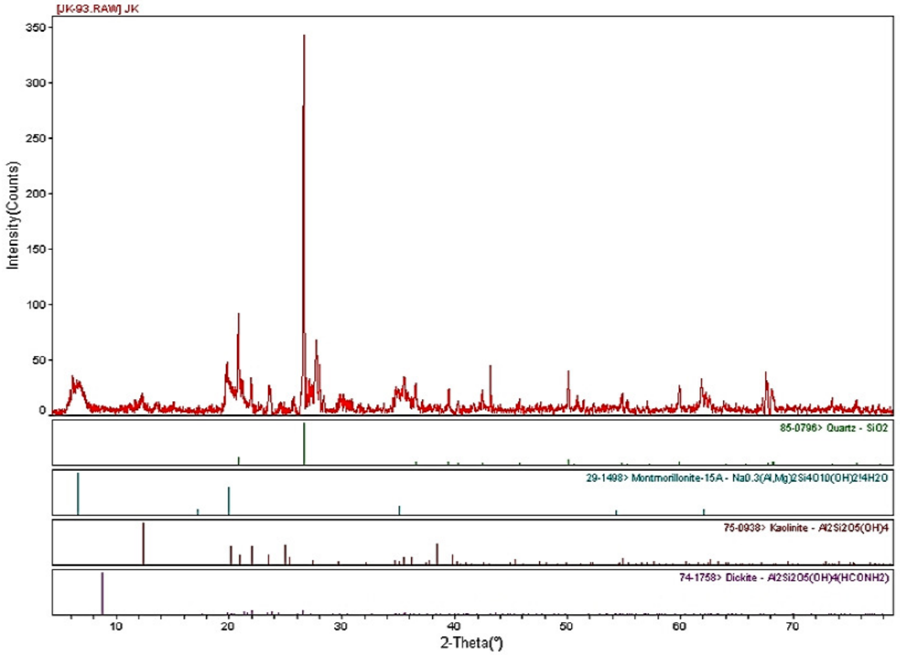
[JK-93.RAW] JK
Intensity(Counts)
0
50
100
150
200
250
300
350
85-0796> Quartz - SiO2
29-1498> Montmorillonite-15A - Na0.3(Al,Mg)2Si4O10(OH)2!4H2O
75-0938> Kaolinite - Al2Si2O5(OH)4
74-1758> Dickite - Al2Si2O5(OH)4(HCONH2)
10
20
30
40
50
60
70
2-Theta(°)

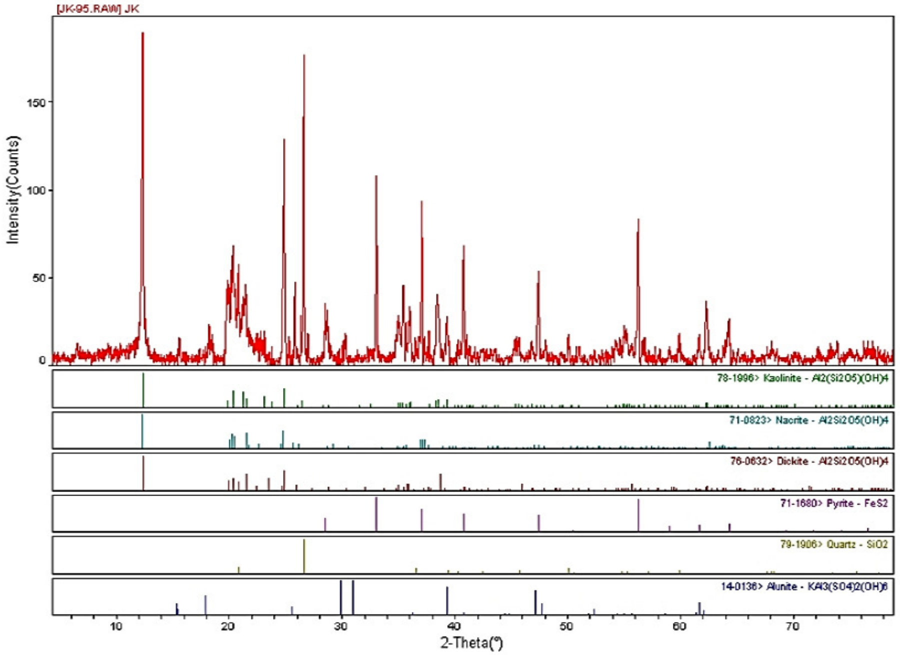
[JK-95.RAW] JK
Intensity(Counts)
0
50
100
150
78-1996> Kaolinite - Al2(Si2O5)(OH)4
71-0823> Nacrite - Al2Si2O5(OH)4
76-0632> Dickite - Al2Si2O5(OH)4
71-1680> Pyrite - FeS2
79-1906> Quartz - SiO2
14-0136> Alunite - KAl3(SO4)2(OH)6
10
20
30
40
50
60
70
2-Theta(°)

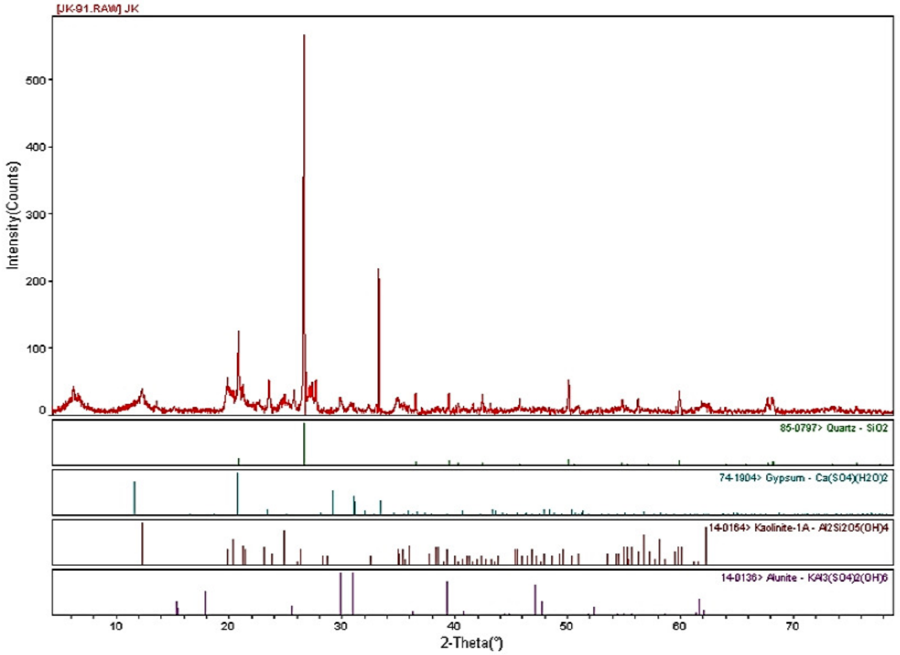
[JK-91.RAW] JK
Intensity(Counts)
0
100
200
300
400
500
85-0797> Quartz - SiO2
74-1904> Gypsum - Ca(SO4)(H2O)2
14-0164> Kaolinite-1A - Al2Si2O5(OH)4
14-0136> Alunite - KAl3(SO4)2(OH)6
10
20
30
40
50
60
70
2-Theta(°)

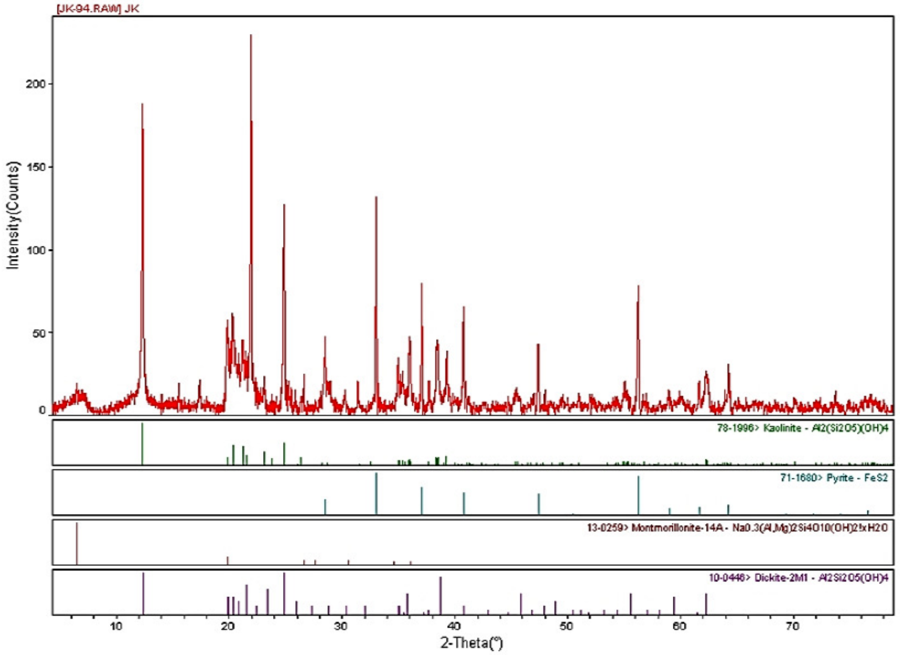
[JK-94.RAW] JK
Intensity(Counts)
0
50
100
150
200
78-1996> Kaolinite - Al2(Si2O5)(OH)4
71-1680> Pyrite - FeS2
13-0259> Montmorillonite-14A - Na0.3(Al,Mg)2Si4O10(OH)2!xH2O
10-0446> Dickite-2M1 - Al2Si2O5(OH)4
10
20
30
40
50
60
70
2-Theta(°)

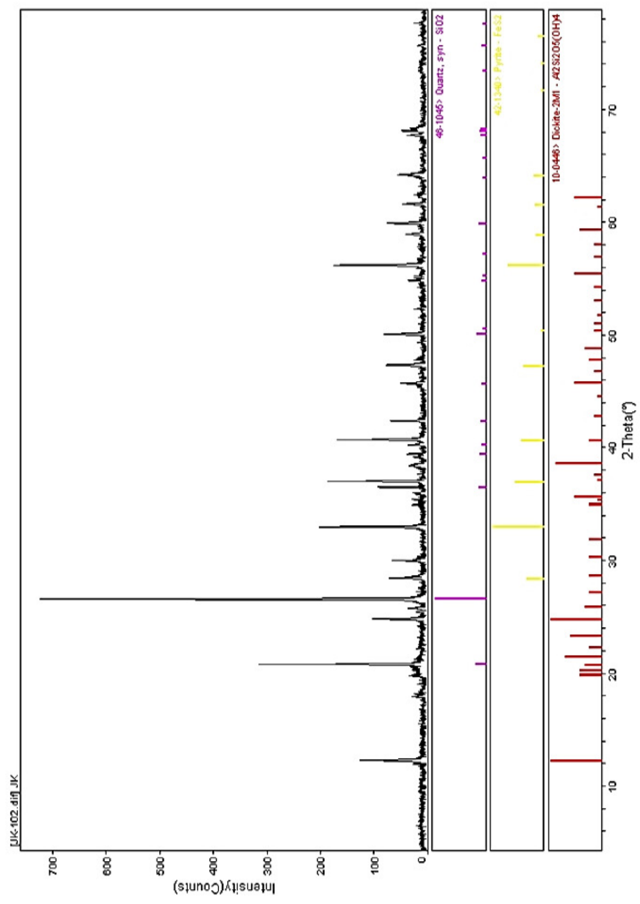
[UK-102.dif] JK
Intensity(Counts)
0
100
200
300
400
500
600
700
2-Theta(°)
10
20
30
40
50
60
70
46-1045> Quartz, syn - SiO2
42-1340> Pyrite - FeS2
10-0446> Dickite-2M1 - Al2Si2O5(OH)4

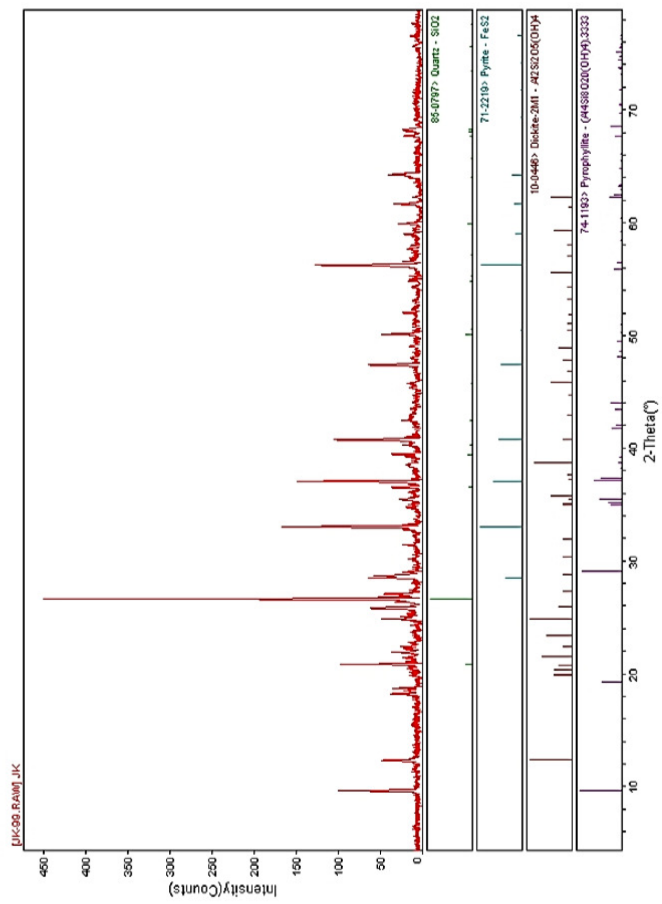
[UK-99.RAW] JK
Intensity(Counts)
0
50
100
150
200
250
300
350
400
450
2-Theta(°)
10
20
30
40
50
60
70
85-0797> Quartz - SiO2
71-2219> Pyrite - FeS2
10-0446> Dickite-2M1 - Al2Si2O5(OH)4
74-1193> Pyrophyllite - (Al4Si8O20(OH)4).3333

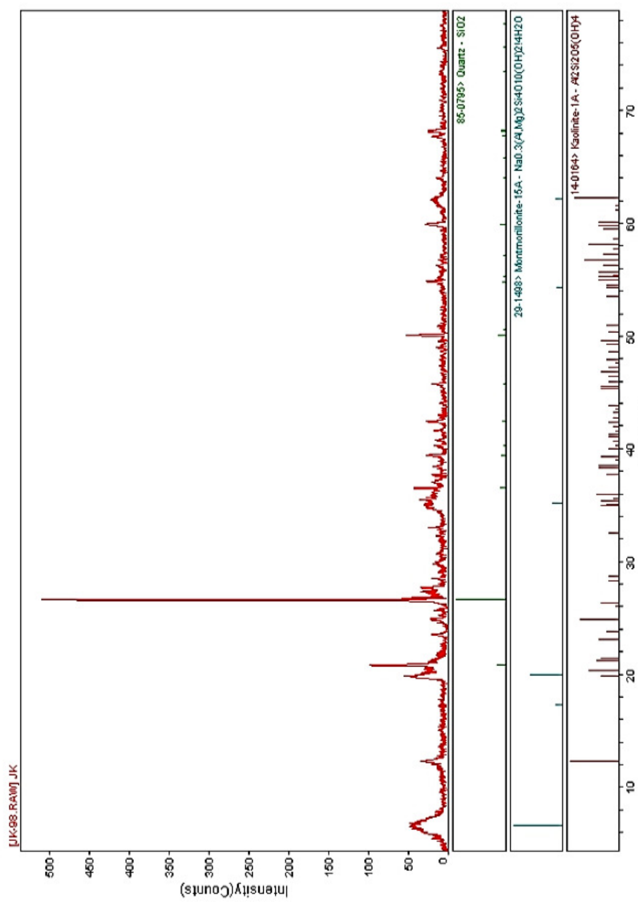
[UK-98.RAW] JK
Intensity(Counts)
0
50
100
150
200
250
300
350
400
450
500
2-Theta(°)
10
20
30
40
50
60
70
85-0795> Quartz - SiO2
29-1498> Montmorillonite-15A - Na0.3(Al,Mg)2Si4O10(OH)2!4H2O
14-0164> Kaolinite-1A - Al2Si2O5(OH)4

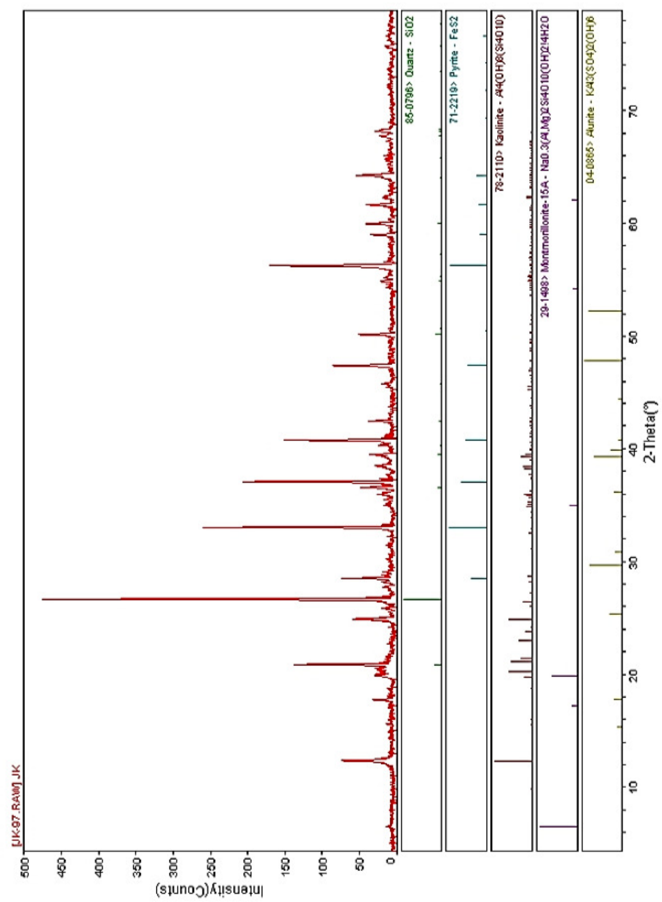
[UK-97.RAW] JK
Intensity(Counts)
0
50
100
150
200
250
300
350
400
450
500
2-Theta(°)
10
20
30
40
50
60
70
85-0796> Quartz - SiO2
71-2219> Pyrite - FeS2
78-2110> Kaolinite - Al4(OH)8(Si4O10)
29-1498> Montmorillonite-15A - Na0.3(Al,Mg)2Si4O10(OH)2!4H2O
04-0865> Alunite - K(Al3(SO4)2(OH)6

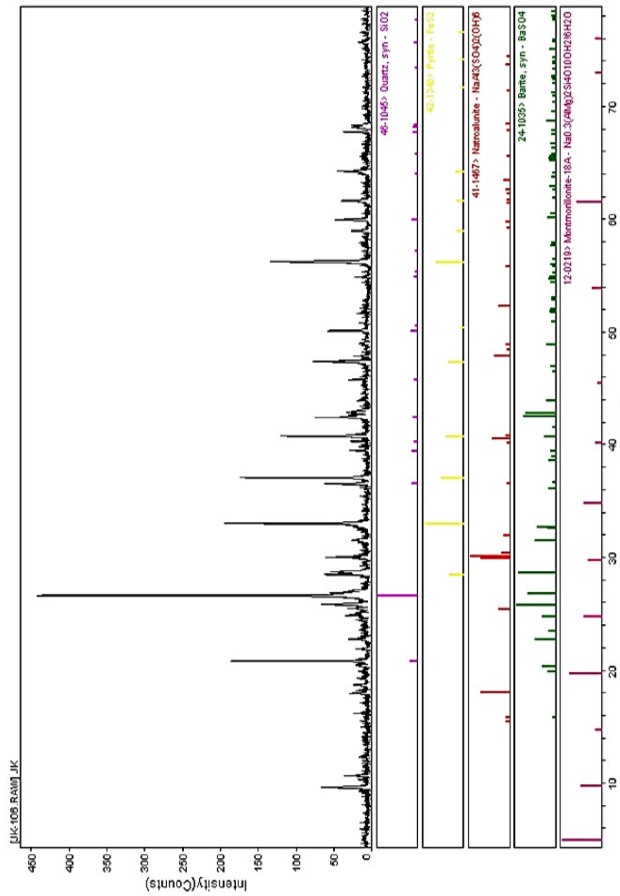
[UK-106.RAW] JK
Intensity(Counts)
450
400
350
300
250
200
150
100
50
0
46-1045> Quartz, syn - SiO2
42-1340> Pyrite - FeS2
41-1467> Natroalunite - NaAl3(SO4)2(OH)6
24-1035> Barite, syn - BaSO4
12-0219> Montmorillonite-18A - Na0.3(Al,Mg)2Si4O10OH2!6H2O
10
20
30
40
50
60
70
2-Theta(°)

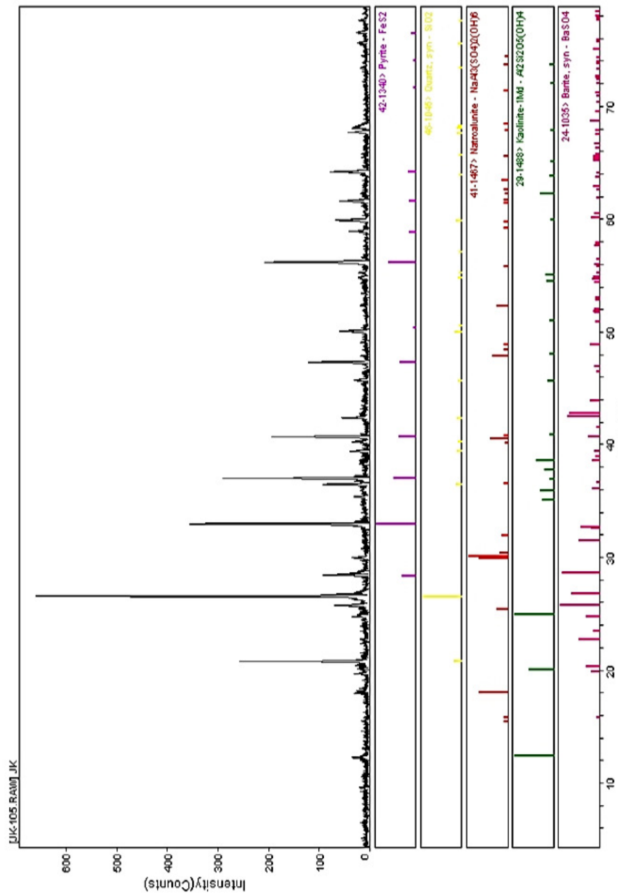
[UK-105.RAW] JK
Intensity(Counts)
600
500
400
300
200
100
0
42-1340> Pyrite - FeS2
46-1045> Quartz, syn - SiO2
41-1467> Natroalunite - NaAl3(SO4)2(OH)6
29-1488> Kaolinite-1Md - Al2Si2O5(OH)4
24-1035> Barite, syn - BaSO4
10
20
30
40
50
60
70
2-Theta(°)

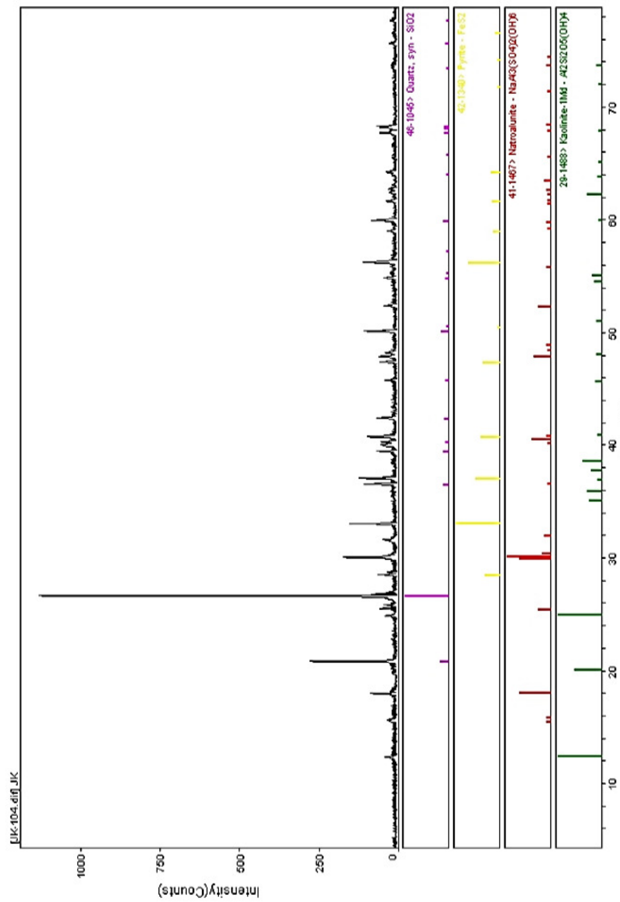
[UK-104.dif] JK
Intensity(Counts)
1000
750
500
250
0
46-1045> Quartz, syn - SiO2
42-1340> Pyrite - FeS2
41-1467> Natroalunite - NaAl3(SO4)2(OH)6
29-1488> Kaolinite-1Md - Al2Si2O5(OH)4
10
20
30
40
50
60
70
2-Theta(°)

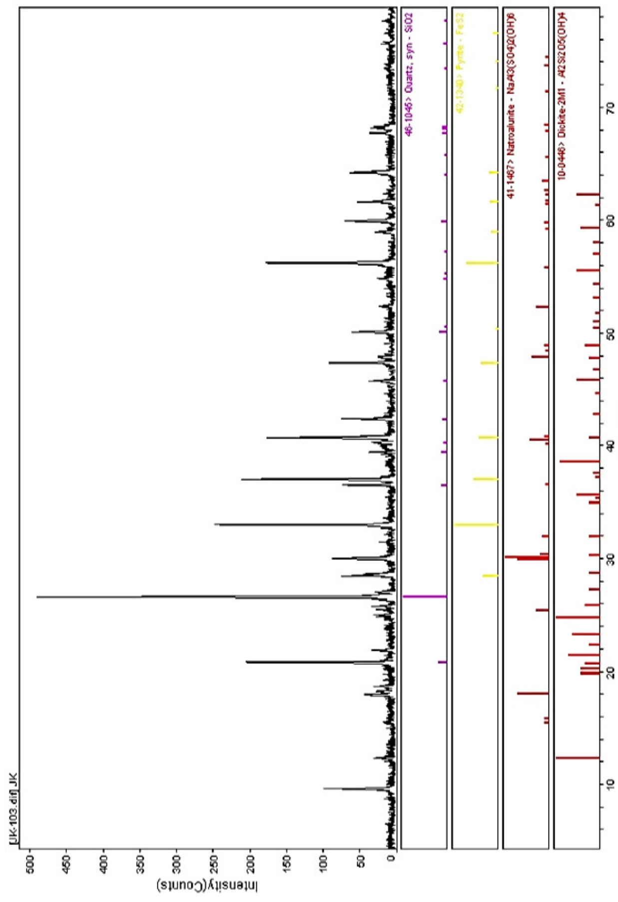
[UK-103.dif] JK
Intensity(Counts)
500
450
400
350
300
250
200
150
100
50
0
46-1045> Quartz, syn - SiO2
42-1340> Pyrite - FeS2
41-1467> Natroalunite - NaAl3(SO4)2(OH)6
10-0446> Dickite-2M1 - Al2Si2O5(OH)4
24-1035> Barite, syn - BaSO4
10
20
30
40
50
60
70
2-Theta(°)

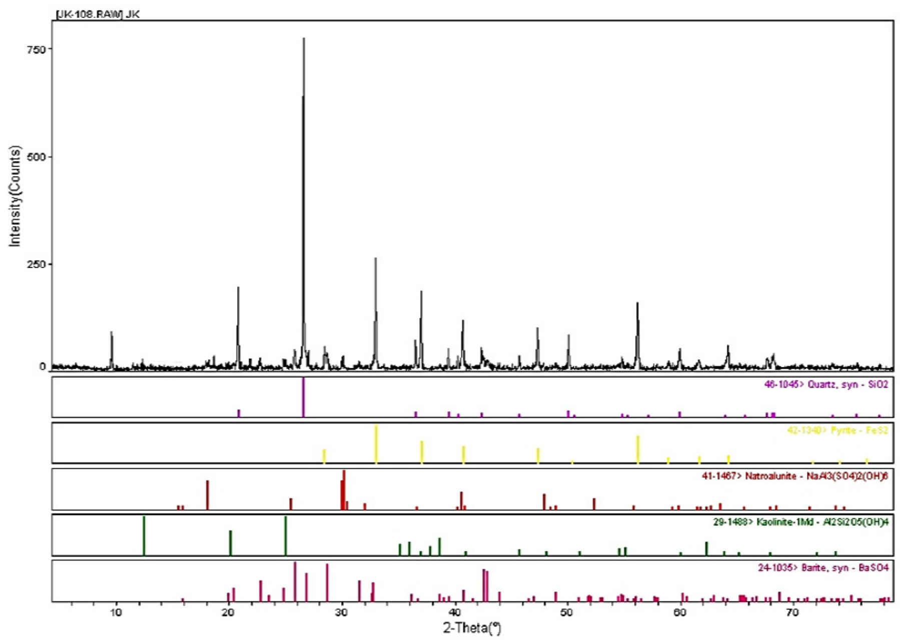
[JK-108.RAW] JK
Intensity(Counts)
750
500
250
0
46-1045> Quartz, syn - SiO2
42-1340> Pyrite - FeS2
41-1467> Natroalunite - NaAl3(SO4)2(OH)6
29-1488> Kaolinite-1Md - Al2Si2O5(OH)4
24-1035> Barite, syn - BaSO4
10
20
30
40
50
60
70
2-Theta(°)

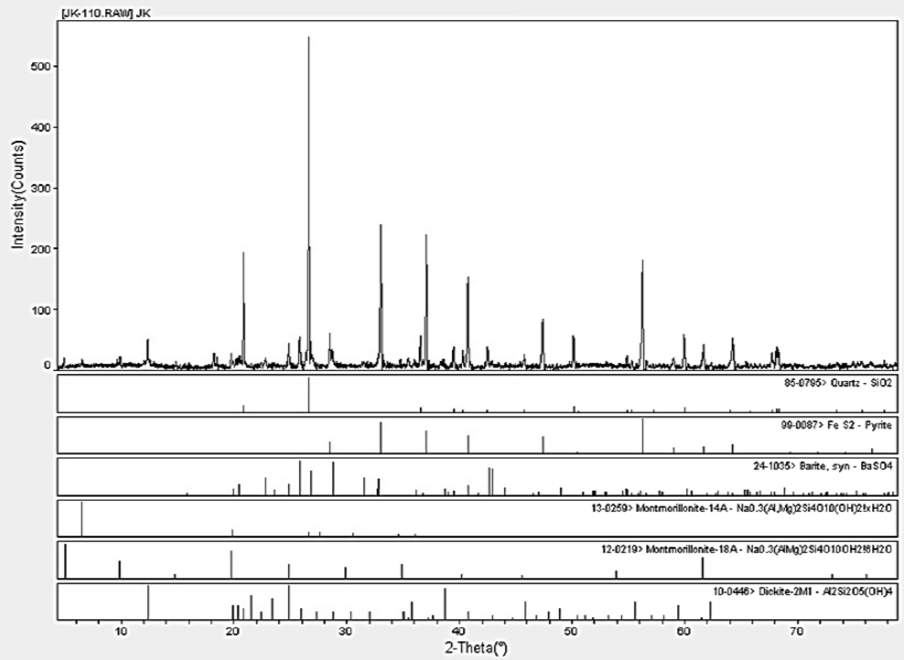
[JK-110.RAW] JK
Intensity(Counts)
500
400
300
200
100
0
85-0795> Quartz - SiO2
99-0087> Fe S2 - Pyrite
24-1035> Barite, syn - BaSO4
13-0259> Montmorillonite-14A - Na0.3(Al,Mg)2Si4O10(OH)2!xH2O
12-0219> Montmorillonite-18A - Na0.3(AlMg)2Si4O10OH2!6H2O
10-0446> Dickite-2M1 - Al2Si2O5(OH)4
10
20
30
40
50
60
70
2-Theta(°)

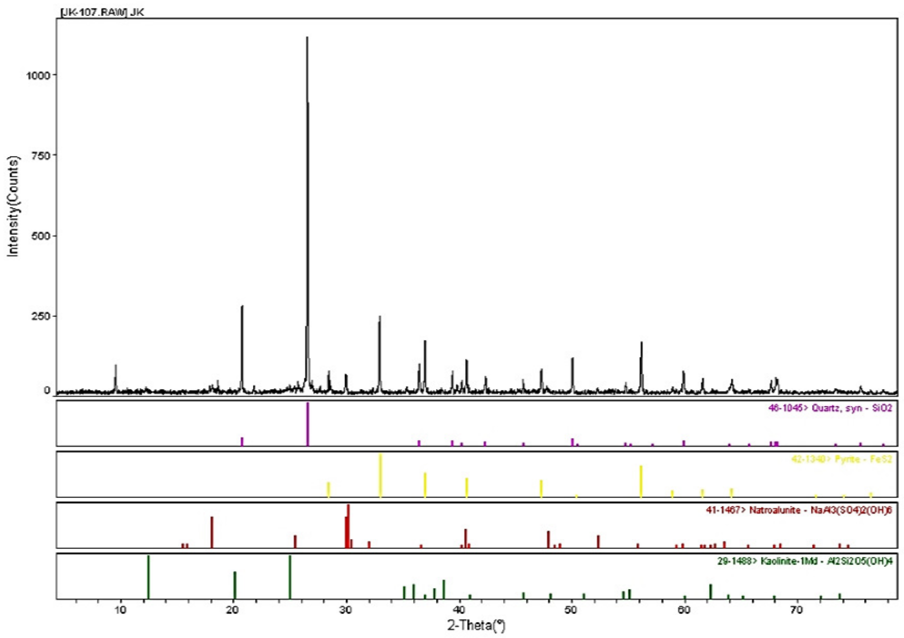
[JK-107.RAW] JK
Intensity(Counts)
1000
750
500
250
0
46-1045> Quartz, syn - SiO2
42-1340> Pyrite - FeS2
41-1467> Natroalunite - NaAl3(SO4)2(OH)6
29-1488> Kaolinite-1Md - Al2Si2O5(OH)4
10
20
30
40
50
60
70
2-Theta(°)

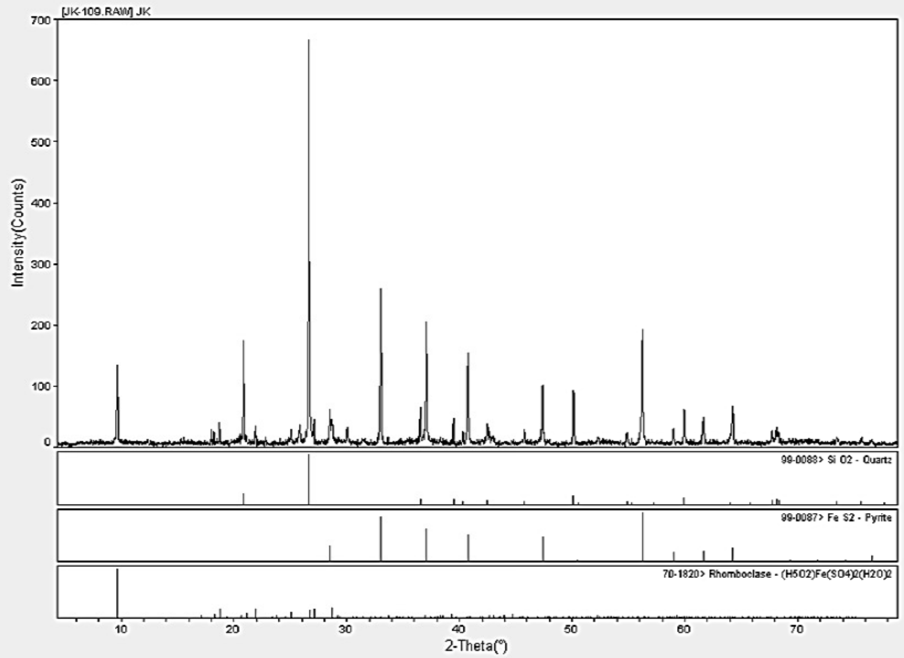
[JK-109.RAW] JK
Intensity(Counts)
700
600
500
400
300
200
100
0
99-0088> Si O2 - Quartz
99-0087> Fe S2 - Pyrite
70-1820> Rhomboclase - (H5O2)Fe(SO4)2(H2O)2
10
20
30
40
50
60
70
2-Theta(°)

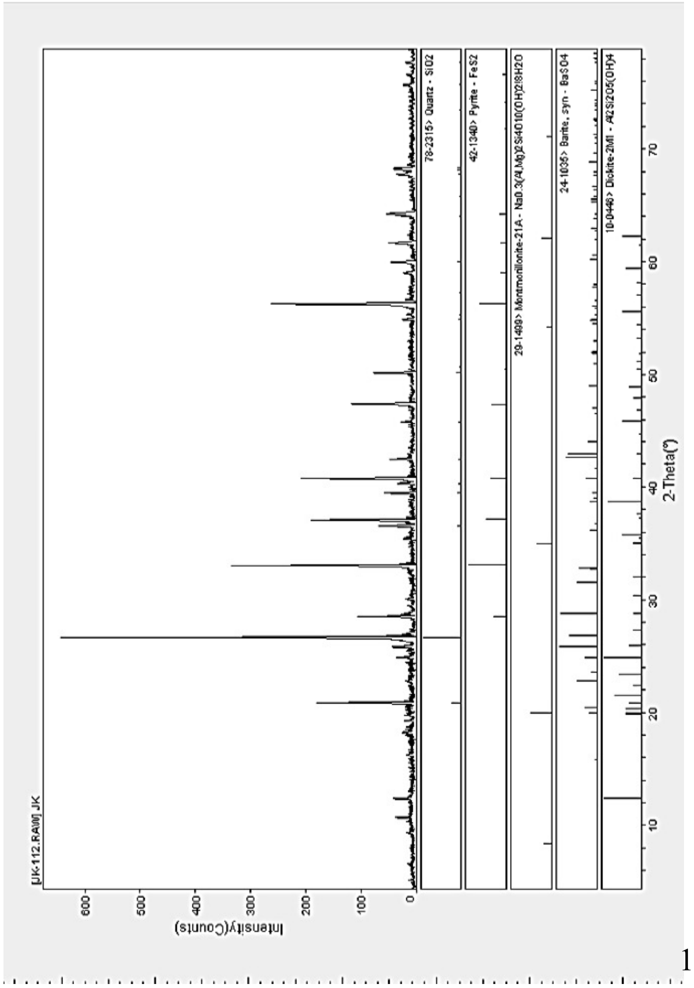
[UK-112.RAW] JK
Intensity(Counts)
0
100
200
300
400
500
600
2-Theta(°)
10
20
30
40
50
60
70
78-2315> Quartz - SiO2
42-1340> Pyrite - FeS2
29-1499> Montmorillonite-21A - Na0.3(Al,Mg)2Si4O10(OH)2!8H2O
24-1035> Barite, syn - BaSO4
10-0446> Dickite-2MI - Al2Si2O5(OH)4

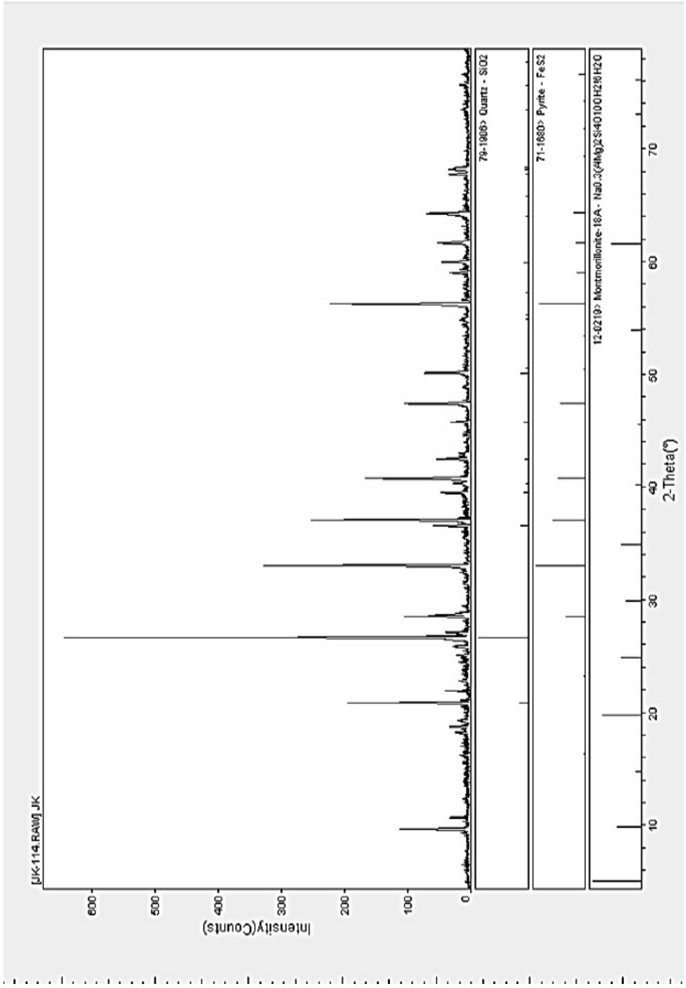
[UK-114.RAW] JK
Intensity(Counts)
0
100
200
300
400
500
600
2-Theta(°)
10
20
30
40
50
60
70
79-1906> Quartz - SiO2
71-1680> Pyrite - FeS2
12-0219> Montmorillonite-18A - Na0.3(Al,Mg)2Si4O10O H2!6H2O

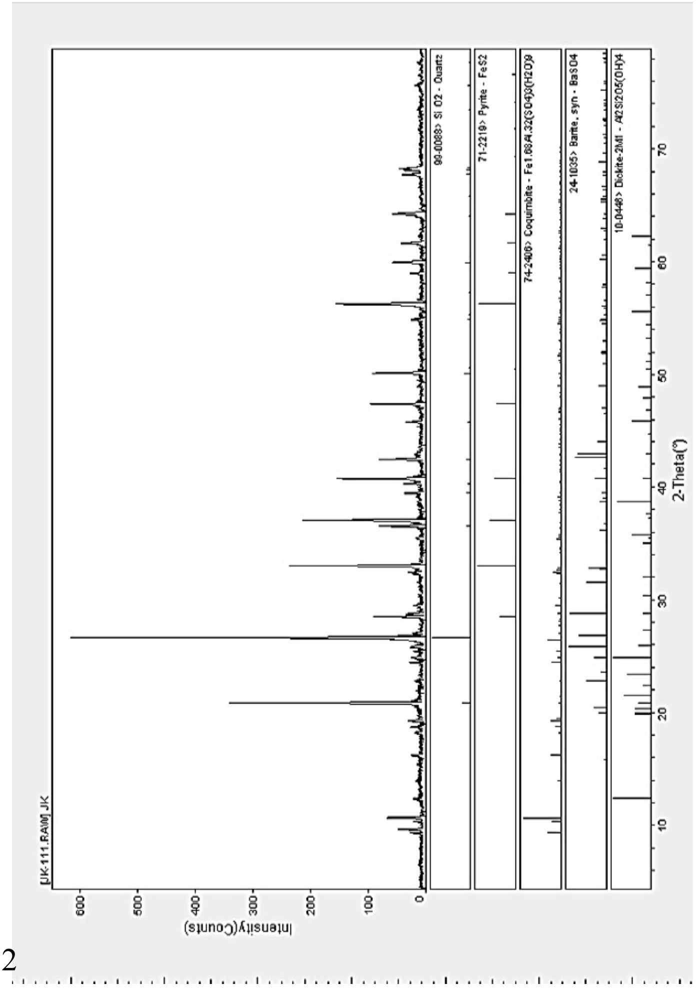
[UK-111.RAW] JK
Intensity(Counts)
0
100
200
300
400
500
600
2-Theta(°)
10
20
30
40
50
60
70
99-0088> SI O2 - Quartz
71-2219> Pyrite - FeS2
74-2406> Coquimbite - Fe1.68Al.32(SO4)3(H2O)9
24-1035> Barite, syn - BaSO4
10-0446> Dickite-2MI - Al2Si2O5(OH)4

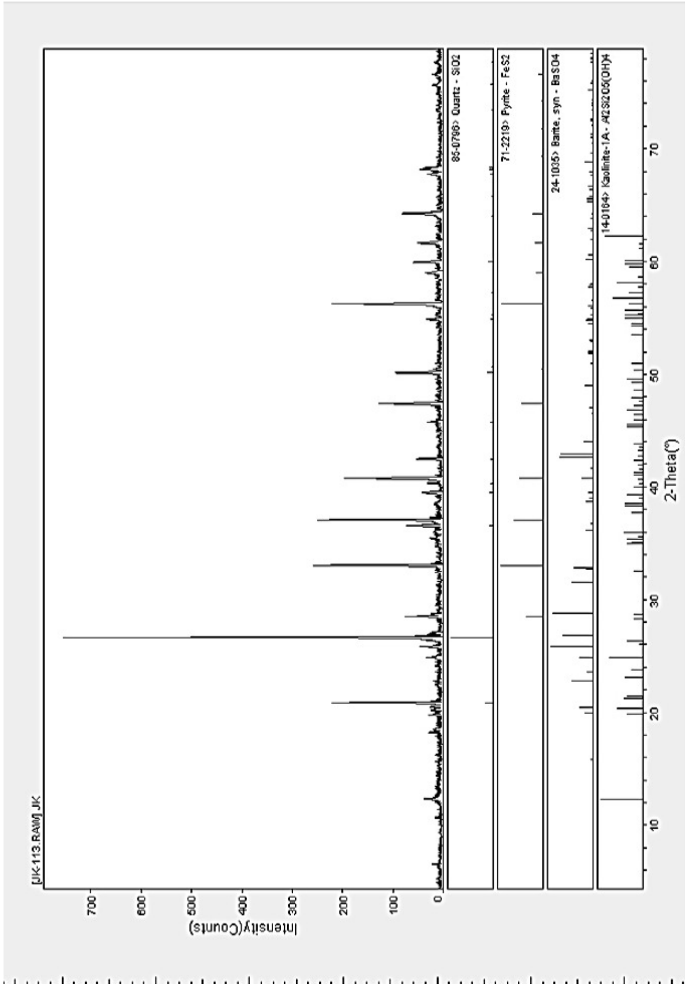
[UK-113.RAW] JK
Intensity(Counts)
0
100
200
300
400
500
600
700
2-Theta(°)
10
20
30
40
50
60
70
85-0796> Quartz - SiO2
71-2219> Pyrite - FeS2
24-1035> Barite, syn - BaSO4
14-0164> Kaolinite-1A - Al2Si2O5(OH)4

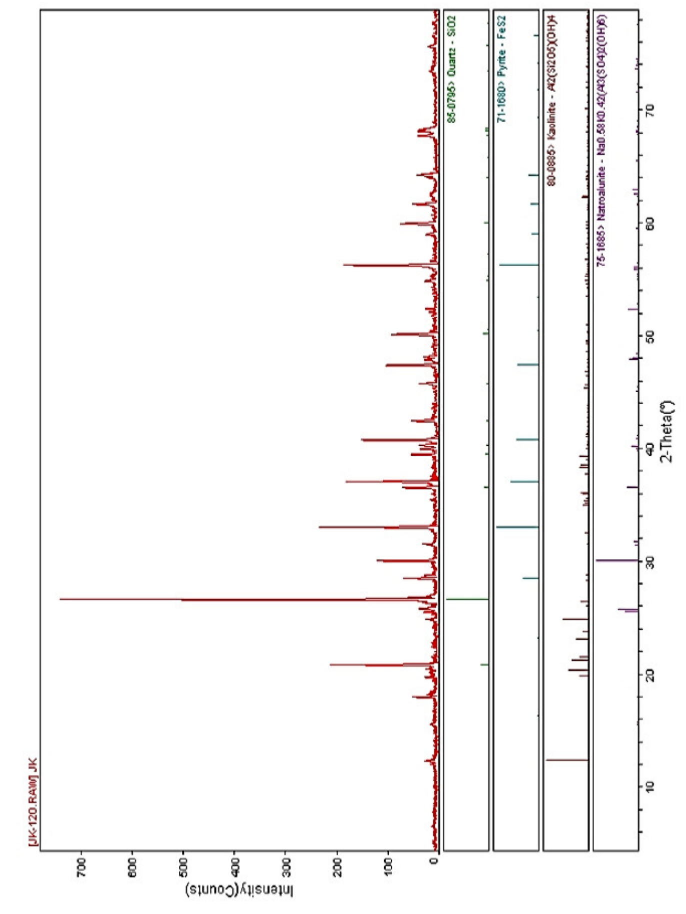
[JK-120.RAW] JK
Intensity(Counts)
0
100
200
300
400
500
600
700
2-Theta(°)
10
20
30
40
50
60
70
85-0795> Quartz - SiO2
71-1680> Pyrite - FeS2
80-0885> Kaolinite - Al2(Si2O5)(OH)4
75-1685> Natroalunite - Na0.58K0.42(Al3(SO4)2(OH)6)

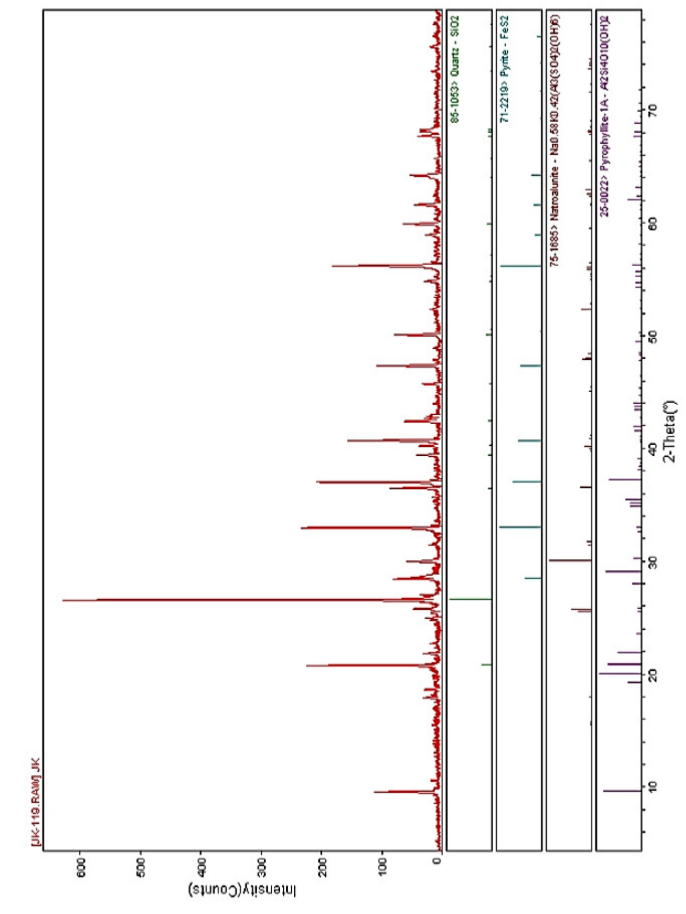
[JK-119.RAW] JK
Intensity(Counts)
0
100
200
300
400
500
600
2-Theta(°)
10
20
30
40
50
60
70
85-1053> Quartz - SiO2
71-2219> Pyrite - FeS2
75-1685> Natroalunite - Na0.58K0.42(Al3(SO4)2(OH)6)
25-0022> Pyrophyllite-1A - Al2Si4O10(OH)2

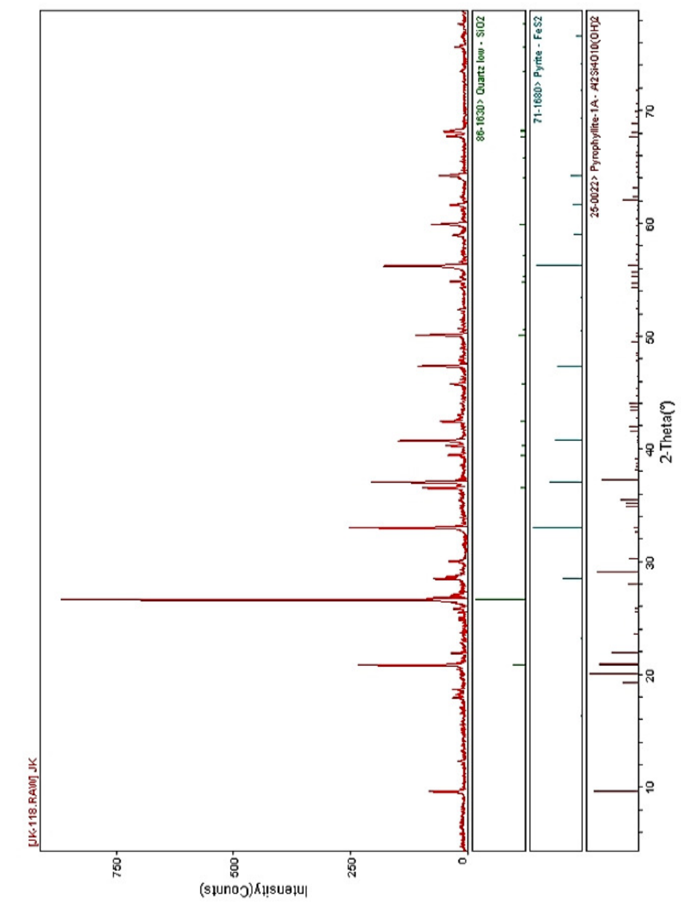
[JK-118.RAW] JK
Intensity(Counts)
0
250
500
750
2-Theta(°)
10
20
30
40
50
60
70
86-1630> Quartz low - SiO2
71-1680> Pyrite - FeS2
25-0022> Pyrophyllite-1A - Al2Si4O10(OH)2

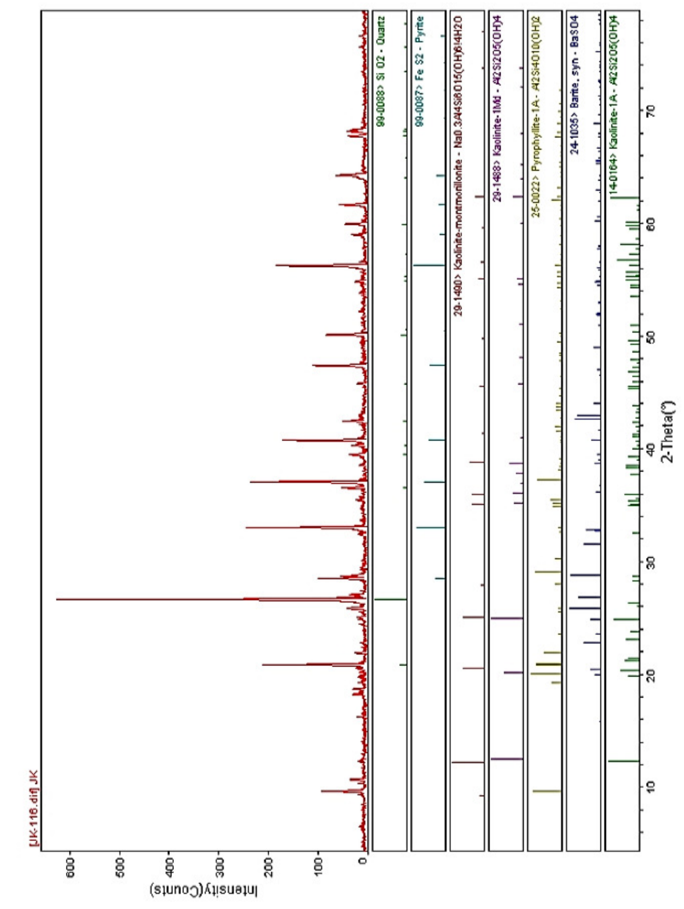
[JK-116.dif] JK
Intensity(Counts)
0
100
200
300
400
500
600
2-Theta(°)
10
20
30
40
50
60
70
99-0088> Si O2 - Quartz
99-0087> Fe S2 - Pyrite
29-1490> Kaolinite-montmorillonite - Na0.3Al4Si6O15(OH)6!4H2O
29-1488> Kaolinite-1Md - Al2Si2O5(OH)4
25-0022> Pyrophyllite-1A - Al2Si4O10(OH)2
24-1035> Barite, syn - BaSO4
14-0164> Kaolinite-1A - Al2Si2O5(OH)4

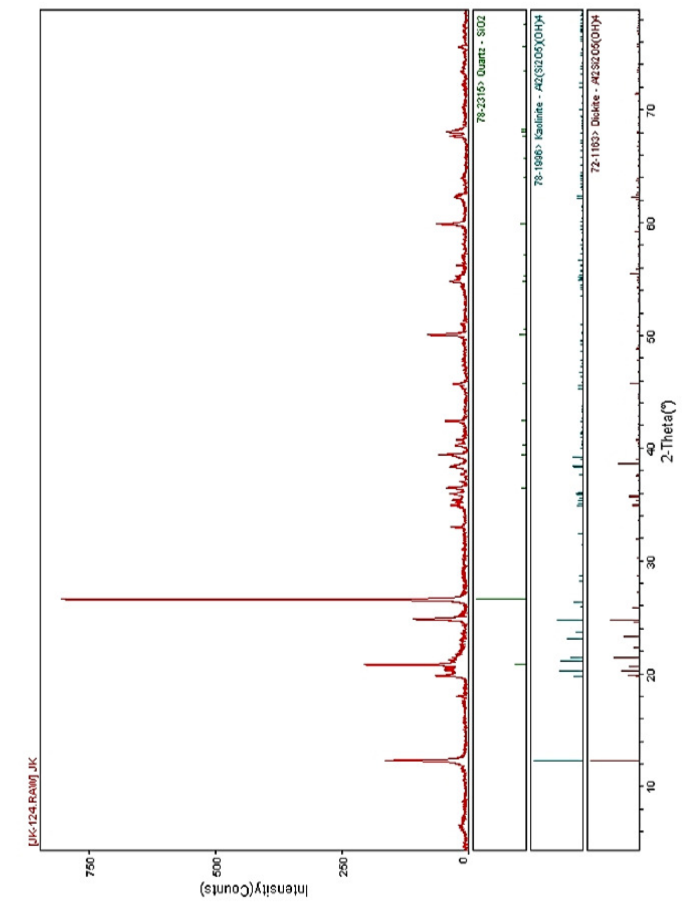
[JK-124.RAW] JK
Intensity(Counts)
0
250
500
750
10
20
30
40
50
60
70
2-Theta(°)
78-2315> Quartz - SiO2
78-1996> Kaolinite - Al2(Si2O5)(OH)4
72-1163> Dickite - Al2Si2O5(OH)4

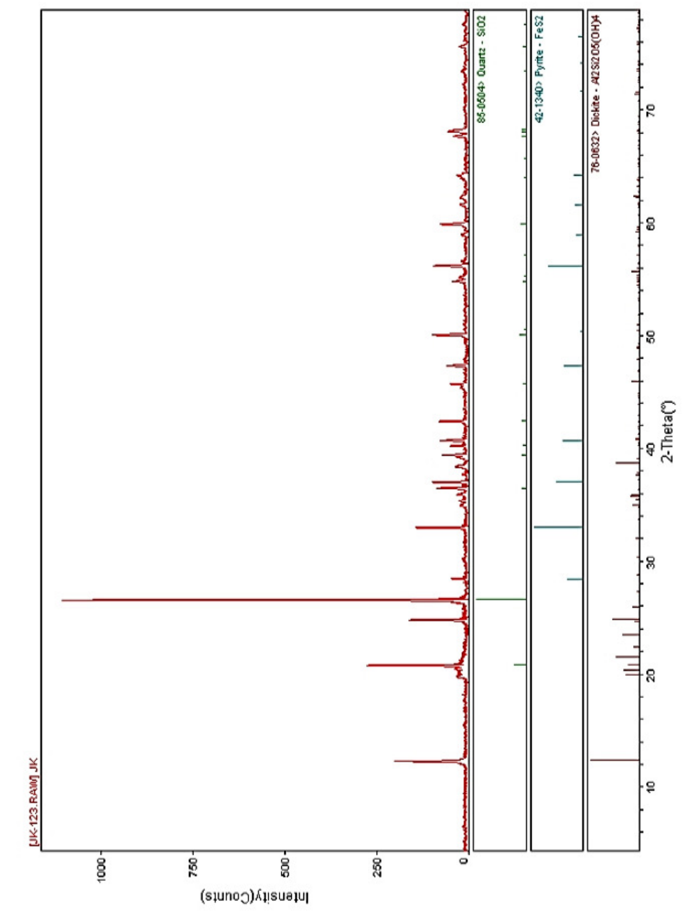
[JK-123.RAW] JK
Intensity(Counts)
0
250
500
750
1000
10
20
30
40
50
60
70
2-Theta(°)
85-0504> Quartz - SiO2
42-1340> Pyrite - FeS2
76-0632> Dickite - Al2Si2O5(OH)4

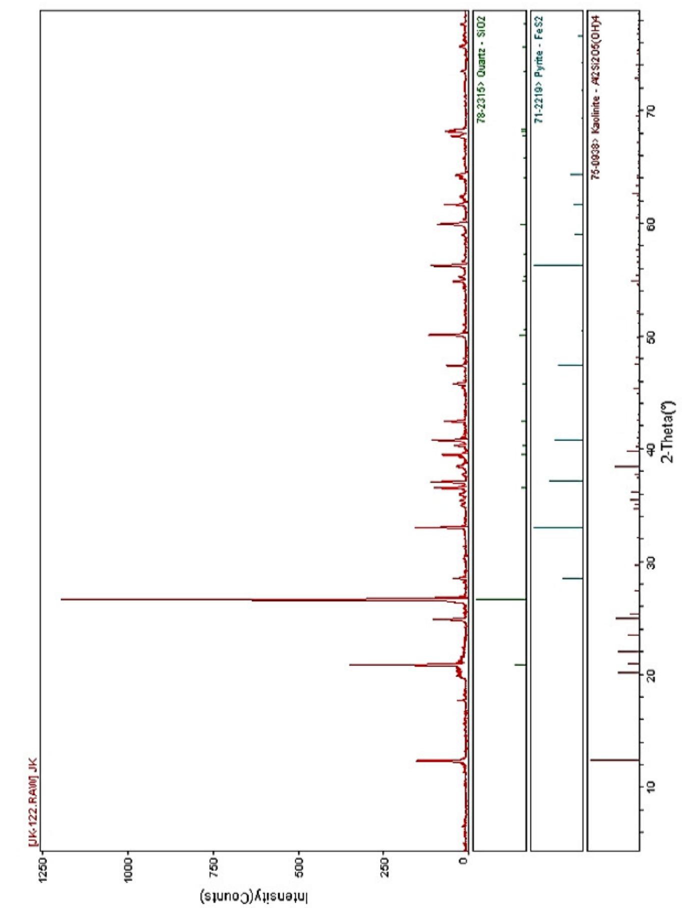
[JK-122.RAW] JK
Intensity(Counts)
0
250
500
750
1000
1250
10
20
30
40
50
60
70
2-Theta(°)
78-2315> Quartz - SiO2
71-2219> Pyrite - FeS2
75-0938> Kaolinite - Al2Si2O5(OH)4

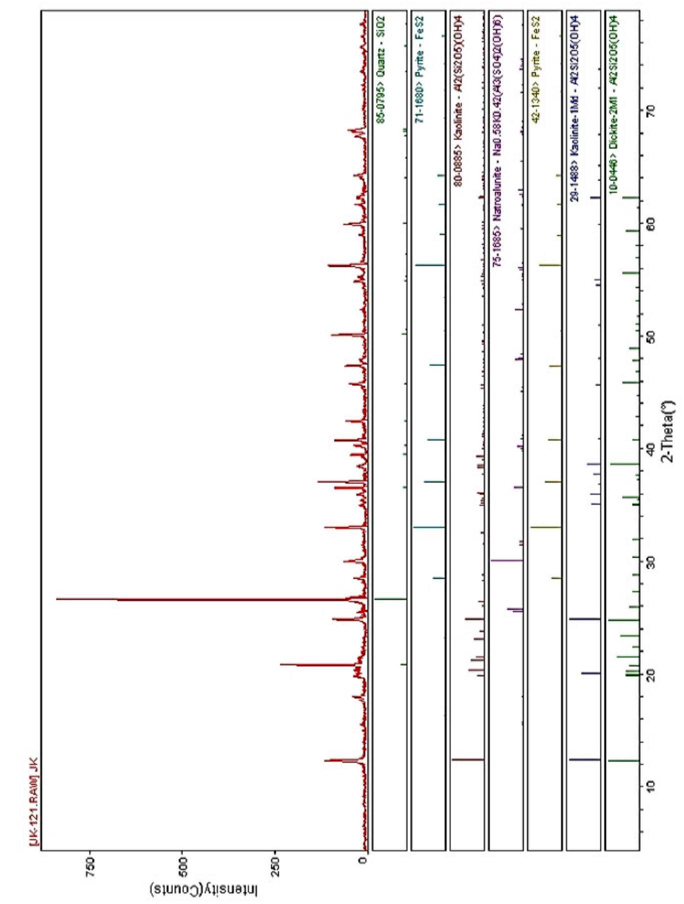
[JK-121.RAW] JK
Intensity(Counts)
0
250
500
750
10
20
30
40
50
60
70
2-Theta(°)
85-0795> Quartz - SiO2
71-1680> Pyrite - FeS2
80-0885> Kaolinite - Al2(Si2O5)(OH)4
75-1685> Natroalunite - Na0.58K0.42(Al3(SO4)2(OH)6)
42-1340> Pyrite - FeS2
29-1488> Kaolinite-1Md - Al2Si2O5(OH)4
10-0446> Dickite-2M1 - Al2Si2O5(OH)4

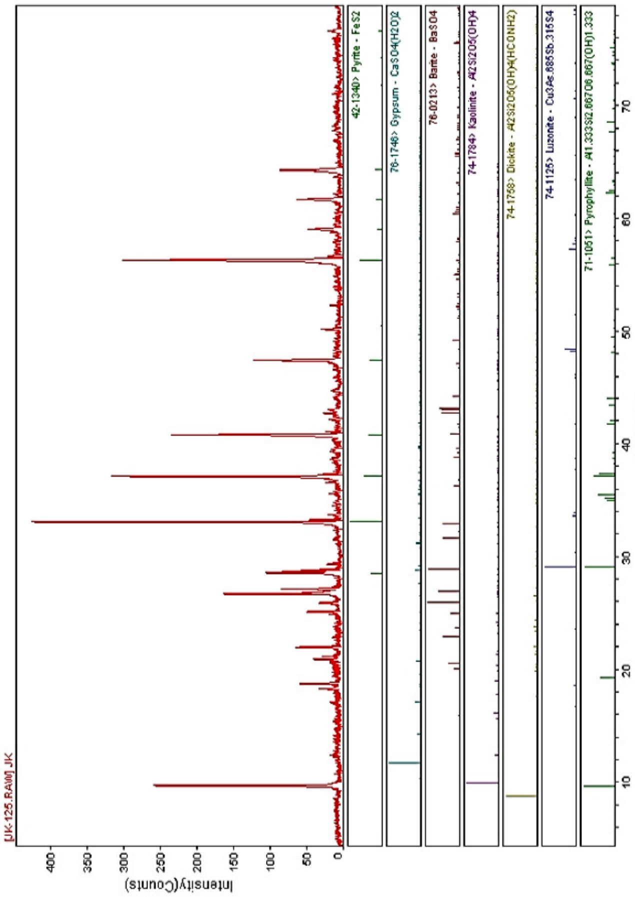
[JK-125.RAW] JK
Intensity(Counts)
400
350
300
250
200
150
100
50
0
42-1340> Pyrite - FeS2
76-1746> Gypsum - CaSO4(H2O)2
76-0213> Barite - BaSO4
74-1784> Kaolinite - Al2Si2O5(OH)4
74-1758> Dickite - Al2Si2O5(OH)4(HCONH2)
74-1125> Luzonite - Cu3As.685Sb.315S4
71-1051> Pyrophyllite - Al1.333Si2.667O6.667(OH)1.333
10
20
30
40
50
60
70
2-Theta(°)

Appendix C Electron Microprobe Analyses

Appendix C Composition of pyrite (A) and enargite (B) from Bowone (BOD) and Binebase (BID) based on EMPA analysis, reported in weight %

A. Pyrite

Sample	Type	Ag	As	Au	Cd	Co	Cu	Fe	Hg	Ni	Pb	S	Sb	Se	Te	Ti	Zn	Total
d.l.		0.016	0.022	0.007	0.034	0.02	0.007	0.036	0.034	0.01	0.023	0.012	0.01	0.012	0.015	0.01	0.013	
BOD3-97A	II	n.a.	b.d.	n.a.	n.a.	b.d.	2.769	43.89	n.a.	b.d.	n.a.	53.50	b.d.	b.d.	b.d.	n.a.	b.d.	100.16
BOD3-97A	II	n.a.	b.d.	n.a.	n.a.	b.d.	1.979	44.39	n.a.	b.d.	n.a.	53.11	b.d.	b.d.	b.d.	n.a.	b.d.	99.50
BOD3-97A	II	n.a.	b.d.	n.a.	n.a.	b.d.	1.322	45.31	n.a.	b.d.	n.a.	53.43	b.d.	0.012	b.d.	n.a.	b.d.	100.09
BOD3-113.2	II	n.a.	b.d.	n.a.	n.a.	b.d.	0.675	45.74	n.a.	b.d.	n.a.	53.16	b.d.	b.d.	b.d.	n.a.	b.d.	99.58
BOD3-100.4	II	n.a.	0.035	n.a.	n.a.	b.d.	0.319	46.74	n.a.	b.d.	n.a.	53.71	b.d.	b.d.	b.d.	n.a.	b.d.	100.81
BOD3-89.4	II	n.a.	b.d.	n.a.	n.a.	0.099	0.239	46.03	n.a.	0.048	n.a.	53.32	b.d.	b.d.	b.d.	n.a.	b.d.	99.75
BOD3-113.2	II	n.a.	b.d.	n.a.	n.a.	0.036	0.224	45.87	n.a.	b.d.	n.a.	53.29	b.d.	b.d.	b.d.	n.a.	b.d.	99.44
BOD3-113.2	II	n.a.	b.d.	n.a.	n.a.	0.036	0.207	46.27	n.a.	b.d.	n.a.	53.08	b.d.	b.d.	b.d.	n.a.	b.d.	99.60
BOD3-103.7	II	n.a.	b.d.	n.a.	n.a.	b.d.	0.043	46.22	n.a.	b.d.	n.a.	53.02	b.d.	b.d.	b.d.	n.a.	b.d.	99.28
BOD3-113.2	II	n.a.	b.d.	n.a.	n.a.	b.d.	b.d.	46.39	n.a.	b.d.	n.a.	53.02	b.d.	b.d.	b.d.	n.a.	b.d.	99.42
BOD3-96	I	n.a.	b.d.	n.a.	n.a.	b.d.	1.431	44.91	n.a.	b.d.	n.a.	53.17	b.d.	b.d.	b.d.	n.a.	b.d.	99.54
BID34-84	I	b.d.	b.d.	n.a.	b.d.	n.a.	0.868	45.87	n.a.	b.d.	b.d.	53.00	b.d.	0.050	0.040	n.a.	0.034	99.87
BOD3-96	I	n.a.	b.d.	n.a.	n.a.	0.059	0.690	45.43	n.a.	b.d.	n.a.	53.28	b.d.	0.014	b.d.	n.a.	b.d.	99.48
BID34-84	I	b.d.	0.035	n.a.	b.d.	b.d.	0.583	45.88	n.a.	b.d.	b.d.	53.77	b.d.	b.d.	b.d.	n.a.	0.018	100.29
BOD3-97A	I	0.039	b.d.	b.d.	b.d.	n.a.	0.540	46.38	b.d.	b.d.	b.d.	53.66	b.d.	b.d.	b.d.	b.d.	b.d.	100.63
BOD3-96	I	n.a.	b.d.	n.a.	n.a.	b.d.	0.431	45.82	n.a.	b.d.	n.a.	53.00	b.d.	b.d.	b.d.	n.a.	b.d.	99.27
BOD3-96	I	n.a.	b.d.	n.a.	n.a.	b.d.	0.411	45.88	n.a.	0.011	n.a.	53.14	b.d.	0.024	b.d.	n.a.	b.d.	99.47
BOD3-96	I	n.a.	b.d.	n.a.	n.a.	b.d.	0.392	45.46	n.a.	b.d.	n.a.	53.21	b.d.	b.d.	b.d.	n.a.	b.d.	99.07
BID34-84	I	b.d.	b.d.	b.d.	b.d.	b.d.	0.229	46.65	b.d.	b.d.	b.d.	53.77	b.d.	b.d.	b.d.	b.d.	b.d.	100.68
BOD3-96	I	b.d.	b.d.	n.a.	n.a.	b.d.	0.216	45.93	n.a.	b.d.	n.a.	53.26	b.d.	b.d.	b.d.	n.a.	b.d.	99.42
BID34-84	I	n.a.	b.d.	n.a.	b.d.	n.a.	b.d.	46.65	n.a.	b.d.	b.d.	53.42	b.d.	b.d.	b.d.	n.a.	0.074	100.16
BOD3-96	II	b.d.	b.d.	b.d.	b.d.	b.d.	5.252	41.95	b.d.	b.d.	b.d.	53.51	b.d.	b.d.	b.d.	b.d.	b.d.	100.73
BOD3-96	II	b.d.	b.d.	b.d.	b.d.	b.d.	3.173	43.92	b.d.	b.d.	b.d.	53.60	b.d.	0.082	b.d.	b.d.	b.d.	100.79
BOD3-97A	II	b.d.	b.d.	b.d.	b.d.	b.d.	3.086	43.94	b.d.	b.d.	b.d.	53.83	b.d.	b.d.	b.d.	b.d.	0.013	100.90
BID32-16	II	b.d.	b.d.	b.d.	b.d.	b.d.	1.322	45.69	b.d.	b.d.	b.d.	53.60	b.d.	b.d.	b.d.	b.d.	b.d.	100.62
BOD3-100.4	II	n.a.	b.d.	n.a.	n.a.	b.d.	0.925	45.73	n.a.	b.d.	n.a.	53.42	b.d.	0.122	b.d.	n.a.	b.d.	100.20
BID34-84	II	b.d.	b.d.	n.a.	b.d.	n.a.	0.788	45.62	n.a.	b.d.	b.d.	53.24	b.d.	0.015	0.037	n.a.	b.d.	99.69
BOD3-100.4	II	n.a.	b.d.	n.a.	n.a.	b.d.	0.680	45.95	n.a.	b.d.	n.a.	53.37	b.d.	0.105	b.d.	n.a.	b.d.	100.11
BOD3-100.4	II	n.a.	b.d.	n.a.	n.a.	b.d.	0.571	46.01	n.a.	b.d.	n.a.	53.51	b.d.	0.160	b.d.	n.a.	b.d.	100.25
BOD3-96	II	b.d.	b.d.	b.d.	b.d.	b.d.	0.562	46.22	b.d.	b.d.	b.d.	53.71	b.d.	b.d.	b.d.	b.d.	b.d.	100.50
BID24-4.3b	I	n.a.	b.d.	n.a.	n.a.	b.d.	0.665	45.62	n.a.	b.d.	n.a.	53.08	b.d.	0.014	0.092	n.a.	b.d.	99.49
BOD3-113.2	I	n.a.	b.d.	n.a.	n.a.	b.d.	0.365	46.22	n.a.	b.d.	n.a.	52.56	b.d.	b.d.	b.d.	n.a.	b.d.	99.15
BOD3-97A	I	n.a.	b.d.	n.a.	n.a.	b.d.	0.281	46.43	n.a.	b.d.	n.a.	53.54	b.d.	b.d.	b.d.	n.a.	b.d.	100.27
BOD3-113.2	I	n.a.	b.d.	n.a.	n.a.	b.d.	0.244	45.85	n.a.	b.d.	n.a.	52.99	b.d.	b.d.	b.d.	n.a.	b.d.	99.09
BOD3-97A	I	n.a.	b.d.	n.a.	n.a.	b.d.	b.d.	45.56	n.a.	b.d.	n.a.	53.40	b.d.	b.d.	b.d.	n.a.	0.017	99.01
BOD3-97A	II	n.a.	b.d.	n.a.	n.a.	b.d.	3.168	43.70	n.a.	b.d.	n.a.	52.89	b.d.	b.d.	b.d.	n.a.	b.d.	99.79
BOD3-97A	II	n.a.	0.022	n.a.	n.a.	b.d.	3.143	43.54	n.a.	b.d.	n.a.	53.19	b.d.	b.d.	b.d.	n.a.	b.d.	99.90
BID34-34.7a	II	n.a.	b.d.	n.a.	n.a.	b.d.	2.623	43.75	n.a.	b.d.	n.a.	53.08	b.d.	b.d.	b.d.	n.a.	b.d.	99.46
BOD3-97A	II	n.a.	b.d.	n.a.	n.a.	b.d.	1.995	44.91	n.a.	b.d.	n.a.	53.59	b.d.	b.d.	b.d.	n.a.	b.d.	100.50
BOD3-96	II	n.a.	0.165	n.a.	n.a.	b.d.	1.942	45.43	n.a.	b.d.	n.a.	53.23	b.d.	0.011	b.d.	n.a.	b.d.	100.78
BOD3-96	II	n.a.	b.d.	n.a.	n.a.	b.d.	1.870	45.59	n.a.	b.d.	n.a.	53.38	b.d.	b.d.	b.d.	n.a.	b.d.	100.84
BID34-34.7a	II	n.a.	b.d.	n.a.	n.a.	b.d.	1.817	45.04	n.a.	b.d.	n.a.	53.62	b.d.	b.d.	b.d.	n.a.	b.d.	100.48
BID34-34.7a	II	n.a.	b.d.	n.a.	n.a.	0.157	1.686	44.68	n.a.	b.d.	n.a.	53.50	b.d.	b.d.	b.d.	n.a.	b.d.	100.03
BID34-34.7a	II	n.a.	0.021	n.a.	n.a.	0.152	1.673	44.79	n.a.	b.d.	n.a.	53.61	b.d.	b.d.	b.d.	n.a.	b.d.	100.26
BID34-34.7a	II	n.a.	b.d.	n.a.	n.a.	b.d.	1.658	45.26	n.a.	b.d.	n.a.	53.40	b.d.	b.d.	0.032	n.a.	b.d.	100.37
BID34-34.7a	II	n.a.	b.d.	n.a.	n.a.	0.024	1.614	45.24	n.a.	b.d.	n.a.	53.50	b.d.	0.014	b.d.	n.a.	b.d.	100.41
BOD3-96	II	n.a.	0.022	n.a.	n.a.	b.d.	1.452	46.02	n.a.	b.d.	n.a.	53.43	b.d.	b.d.	b.d.	n.a.	b.d.	100.94
BID34-77.9	II	n.a.	b.d.	n.a.	n.a.	b.d.	1.421	45.33	n.a.	b.d.	n.a.	53.21	b.d.	b.d.	b.d.	n.a.	b.d.	99.96
BID34-34.7a	II	n.a.	0.060	n.a.	n.a.	b.d.	1.209	45.59	n.a.	b.d.	n.a.	53.55	b.d.	b.d.	b.d.	n.a.	b.d.	100.44
BID34-77.9	II	n.a.	b.d.	n.a.	n.a.	0.428	1.168	45.12	n.a.	0.017	n.a.	53.32	b.d.	0.145	b.d.	n.a.	b.d.	100.20
BID34-77.9	II	n.a.	b.d.	n.a.	n.a.	b.d.	1.058	45.73	n.a.	b.d.	n.a.	53.06	b.d.	b.d.	b.d.	n.a.	b.d.	99.86
BID34-84	II	n.a.	b.d.	n.a.	n.a.	b.d.	1.039	45.50	n.a.	b.d.	n.a.	53.47	b.d.	b.d.	b.d.	n.a.	b.d.	100.01
BID34-84	II	n.a.	b.d.	n.a.	n.a.	b.d.	0.967	45.86	n.a.	b.d.	n.a.	53.63	b.d.	b.d.	b.d.	n.a.	b.d.	100.47
BID34-34.7a	II	n.a.	b.d.	n.a.	n.a.	0.037	0.944	44.97	n.a.	b.d.	n.a.	53.43	b.d.	b.d.	b.d.	n.a.	b.d.	99.41
BOD3-100.4	II	n.a.	b.d.	n.a.	n.a.	b.d.	0.940	45.82	n.a.	b.d.	n.a.	53.60	b.d.	b.d.	b.d.	n.a.	b.d.	100.37
BID34-34.7a	II	n.a.	b.d.	n.a.	n.a.	0.089	0.906	45.61	n.a.	b.d.	n.a.	53.39	b.d.	b.d.	b.d.	n.a.	b.d.	100.01
BID34-84	II	n.a.	b.d.	n.a.	n.a.	b.d.	0.836	45.74	n.a.	b.d.	n.a.	53.65	b.d.	b.d.	b.d.	n.a.	b.d.	100.24
BOD3-100.4	II	n.a.	b.d.	n.a.	n.a.	b.d.	0.814	45.97	n.a.	b.d.	n.a.	53.59	b.d.	b.d.	b.d.	n.a.	b.d.	100.38
BOD3-89.4	II	n.a.	b.d.	n.a.	n.a.	0.022	0.762	45.66	n.a.	0.024	n.a.	53.37	b.d.	b.d.	b.d.	n.a.	b.d.	99.84
BID34-84	II	b.d.	b.d.	b.d.	b.d.	b.d.	0.716	45.94	b.d.	b.d.	b.d.	53.93	b.d.	0.057	b.d.	b.d.	b.d.	100.68
BOD3-96	II	n.a.	b.d.	n.a.	n.a.	b.d.	0.683	46.42	n.a.	b.d.	n.a.	53.00	b.d.	0.025	0.115	n.a.	b.d.	100.25
BID34-77.9	II	n.a.	b.d.	n.a.	n.a.	b.d.	0.549	46.24	n.a.	b.d.	n.a.	53.25	b.d.	0.138	b.d.	n.a.	b.d.	100.19
BOD3-100.4	II	n.a.	b.d.	n.a.	n.a.	b.d.	0.441	46.77	n.a.	b.d.	n.a.	53.39	b.d.	b.d.	0.120	n.a.	b.d.	100.73
BID34-84	II	b.d.	b.d.	b.d.	b.d.	b.d.	0.385	46.05	b.d.	b.d.	b.d.	53.84	b.d.	0.034	b.d.	b.d.	b.d.	100.33
BOD3-89.4	II	n.a.	b.d.	n.a.	n.a.	b.d.	0.365	46.19	n.a.	b.d.	n.a.	52.58	b.d.	0.011	b.d.	n.a.	b.d.	99.17
BOD3-100.4	II	n.a.	b.d.	n.a.	n.a.	b.d.	0.313	46.60	n.a.	b.d.	n.a.	53.54	b.d.	b.d.	b.d.	n.a.	b.d.	100.47
BID34-84	II	b.d.	b.d.	b.d.	b.d.	b.d.	0.298	46.49	b.d.	b.d.	b.d.	53.64	b.d.	0.048	b.d.	b.d.	b.d.	100.52
BOD3-100.4	II	n.a.	b.d.	n.a.	n.a.	0.025	0.277	46.89	n.a.	b.d.	n.a.	53.48	b.d.	b.d.	b.d.	n.a.	b.d.	100.69
BOD3-100.4	II	n.a.	b.d.	n.a.	n.a.	b.d.	0.254	46.43	n.a.	b.d.	n.a.	53.75	b.d.	b.d.	b.d.	n.a.	b.d.	100.44
BOD3-89.4	II	n.a.	b.d.	n.a.	n.a.	0.069	0.205	46.21	n.a.	0.031	n.a.	53.20	b.d.	0.013	b.d.	n.a.	b.d.	99.73
BOD3-100.4	II	n.a.	b.d.	n.a.	n.a.	b.d.	0.203	46.10	n.a.	b.d.	n.a.	52.93	b.d.	b.d.	b.d.	n.a.	0.015	99.27
BOD3-100.4	II	n.a.	b.d.	n.a.	n.a.	0.034	0.202	46.51	n.a.	b.d.	n.a.	53.85	b.d.	b.d.	b.d.	n.a.	b.d.	100.60
BID14-4.3b	II	n.a.	b.d.	n.a.	n.a.	b.d.	0.199	46.16	n.a.	b.d.	n.a.	53.32	b.d.	b.d.	b.d.	n.a.	b.d.	99.70
BOD3-89.4	II	n.a.	b.d.	n.a.	n.a.	b.d.	0.191	46.52	n.a.	b.d.	n.a.	53.20	b.d.	b.d.	b.d.	n.a.	b.d.	99.92
BOD3-89.4	II	n.a.	b.d.	n.a.	n.a.	b.d.	0.190	46.30	n.a.	b.d.	n.a.	53.24	b.d.	b.d.	b.d.	n.a.	b.d.	99.73
BOD3-100.4	II	n.a.	b.d.	n.a.	n.a.	b.d.	0.170	46.28	n.a.	b.d.	n.a.	53.63	b.d.	0.091	b.d.	n.a.	b.d.	100.17
BID34-77.9	II	n.a.	0.027	n.a.	n.a.	b.d.	0.135	46.29	n.a.	b.d.	n.a.	53.45	b.d.	b.d.	b.d.	n.a.	0.184	100.11
BOD3-107	II	n.a.	b.d.	n.a.	n.a.	b.d.	0.130	46.48	n.a.	b.d.	n.a.	53.61	b.d.	b.d.	b.d.	n.a.	b.d.	100.24
BOD3-89.4	II	n.a.	b.d.	n.a.	n.a.	b.d.	0.114	46.20	n.a.	b.d.	n.a.	53.06	b.d.	b.d.	b.d.	n.a.	b.d.	99.39
BOD3-100.4	II	n.a.	0.111	n.a.	n.a.	b.d.	0.112	46.44	n.a.	b.d.	n.a.	53.87	b.d.	b.d.	b.d.	n.a.	b.d.	100.54
BID14-4.3b	II	n.a.	0.099	n.a.	n.a.	b.d.	0.110	46.14	n.a.	b.d.	n.a.	53.47	b.d.	b.d.	b.d.	n.a.	b.d.	99.84
BID34-84	II	n.a.	b.d.	n.a.	n.a.	b.d.	0.101	46.54	n.a.	b.d.	n.a.	53.69	b.d.	b.d.	b.d.	n.a.	b.d.	100.34
BID34-34.7a	II	n.a.	b.d.	n.a.	n.a.	b.d.	0.084	46.67	n.a.	b.d.	n.a.	53.77	b.d.	b.d.	b.d.	n.a.	b.d.	100.52
BID34-77.9	II	n.a.	b.d.	n.a.	n.a.	b.d.	0.071	46.68	n.a.	b.d.	n.a.	53.29	b.d.	0.019	b.d.	n.a.	b.d.	100.07
BOD3-100.4	II	n.a.	b.d.	n.a.	n.a.	b.d.	0.069	46.44	n.a.	b.d.	n.a.	53.45	b.d.	b.d.	b.d.	n.a.	0.022	99.99
BOD3-96	II	n.a.	b.d.	n.a.	n.a.	b.d.	0.065	46.97	n.a.	b.d.	n.a.	53.68	b.d.	0.020	b.d.	n.a.	b.d.	100.75
BOD3-97A	II	n.a.	b.d.	n.a.	n.a.	b.d.	0.052	46.51	n.a.	b.d.	n.a.	53.00	b.d.	0.038	b.d.	n.a.	b.d.	99.61
BOD3-107	II	n.a.	b.d.	n.a.	n.a.	b.d.	0.045	46.74	n.a.	0.014	n.a.	53.84	b.d.	0.027	b.d.	n.a.	b.d.	100.67
BOD3-96	II	n.a.	b.d.	n.a.	n.a.	b.d.	0.036	47.07	n.a.	b.d.	n.a.	53.76	b.d.	0.024	0.068	n.a.	b.d.	100.98

Sample	Type	Ag	As	Au	Cd	Co	Cu	Fe	Hg	Ni	Pb	S	Sb	Se	Te	Ti	Zn	Total
d.l.		0.016	0.022	0.007	0.034	0.02	0.007	0.036	0.034	0.01	0.023	0.012	0.01	0.012	0.015	0.01	0.013	
BOD3-97A	II	n.a.	b.d.	n.a.	n.a.	b.d.	b.d.	46.52	n.a.	b.d.	n.a.	53.37	b.d.	0.011	b.d.	n.a.	b.d.	99.94
BOD3-100.4	II	n.a.	b.d.	n.a.	n.a.	b.d.	b.d.	46.65	n.a.	b.d.	n.a.	53.75	b.d.	b.d.	b.d.	n.a.	b.d.	100.43
BOD1-99.3	II	n.a.	b.d.	n.a.	n.a.	b.d.	b.d.	46.35	n.a.	0.011	n.a.	53.71	b.d.	b.d.	b.d.	n.a.	b.d.	100.09
BOD3-89.4	II	n.a.	b.d.	n.a.	n.a.	b.d.	b.d.	46.56	n.a.	b.d.	n.a.	53.24	b.d.	b.d.	b.d.	n.a.	b.d.	99.83
BOD3-89.4	II	n.a.	0.158	n.a.	n.a.	b.d.	b.d.	45.96	n.a.	b.d.	n.a.	53.35	b.d.	b.d.	b.d.	n.a.	b.d.	99.48
BOD1-99.3	II	n.a.	b.d.	n.a.	n.a.	b.d.	b.d.	46.72	n.a.	b.d.	n.a.	53.81	b.d.	b.d.	b.d.	n.a.	b.d.	100.54
BID34-77.9	II	n.a.	b.d.	n.a.	n.a.	b.d.	b.d.	46.67	n.a.	b.d.	n.a.	53.60	b.d.	0.012	b.d.	n.a.	b.d.	100.29
BOD1-99.3	II	n.a.	b.d.	n.a.	n.a.	b.d.	b.d.	46.53	n.a.	b.d.	n.a.	53.68	b.d.	b.d.	b.d.	n.a.	b.d.	100.23
BOD1-99.3	II	n.a.	b.d.	n.a.	n.a.	b.d.	b.d.	46.55	n.a.	b.d.	n.a.	53.76	b.d.	b.d.	b.d.	n.a.	b.d.	100.31
BOD3-100.4	II	n.a.	b.d.	n.a.	n.a.	b.d.	b.d.	46.47	n.a.	b.d.	n.a.	53.74	b.d.	b.d.	b.d.	n.a.	b.d.	100.22
BOD1-99.3	II	n.a.	b.d.	n.a.	n.a.	b.d.	b.d.	46.46	n.a.	b.d.	n.a.	53.64	b.d.	b.d.	b.d.	n.a.	b.d.	100.11
BOD3-97a	II	n.a.	0.021	n.a.	n.a.	b.d.	2.694	43.95	n.a.	b.d.	n.a.	53.38	b.d.	b.d.	b.d.	n.a.	b.d.	100.05
BOD3-97A	II	b.d.	b.d.	b.d.	0.000	b.d.	2.540	44.37	b.d.	b.d.	b.d.	53.69	b.d.	0.021	b.d.	b.d.	b.d.	100.64
BOD3-107	II	n.a.	b.d.	n.a.	n.a.	b.d.	1.695	45.19	n.a.	b.d.	n.a.	53.67	b.d.	b.d.	b.d.	n.a.	b.d.	100.57
BOD3-107	II	n.a.	b.d.	n.a.	n.a.	b.d.	1.692	45.00	n.a.	b.d.	n.a.	53.70	b.d.	0.014	b.d.	n.a.	b.d.	100.40
BOD3-107	II	n.a.	b.d.	n.a.	n.a.	b.d.	1.307	45.28	n.a.	b.d.	n.a.	53.45	b.d.	b.d.	b.d.	n.a.	b.d.	100.06
BOD3-97a	II	n.a.	b.d.	n.a.	n.a.	b.d.	1.136	45.63	n.a.	b.d.	n.a.	53.62	b.d.	0.024	b.d.	n.a.	b.d.	100.41
BOD3-96	II	b.d.	b.d.	b.d.	b.d.	b.d.	0.671	46.67	b.d.	b.d.	b.d.	53.34	b.d.	b.d.	b.d.	b.d.	b.d.	100.69
BOD3-107	II	n.a.	b.d.	n.a.	n.a.	b.d.	0.601	46.08	n.a.	b.d.	n.a.	53.93	b.d.	b.d.	b.d.	n.a.	b.d.	100.62
BID34-84	II	b.d.	b.d.	n.a.	b.d.	n.a.	0.571	46.38	n.a.	b.d.	b.d.	53.72	b.d.	b.d.	b.d.	n.a.	0.015	100.69
BOD3-107	II	n.a.	b.d.	n.a.	n.a.	0.021	0.540	46.30	n.a.	b.d.	n.a.	53.81	b.d.	b.d.	b.d.	n.a.	b.d.	100.71
BOD3-107	II	n.a.	b.d.	n.a.	n.a.	b.d.	0.408	46.23	n.a.	b.d.	n.a.	53.54	b.d.	b.d.	b.d.	n.a.	0.013	100.19
BOD3-97A	II	b.d.	b.d.	b.d.	b.d.	b.d.	0.363	46.36	b.d.	b.d.	b.d.	53.97	b.d.	b.d.	b.d.	b.d.	b.d.	100.72
BOD3-96	II	b.d.	b.d.	b.d.	b.d.	b.d.	0.246	46.75	b.d.	b.d.	b.d.	53.50	b.d.	0.140	b.d.	b.d.	b.d.	100.67
BOD3-97a	II	n.a.	b.d.	n.a.	n.a.	b.d.	0.161	46.47	n.a.	b.d.	n.a.	53.61	b.d.	b.d.	b.d.	n.a.	b.d.	100.26
BOD3-107	II	n.a.	b.d.	n.a.	n.a.	b.d.	0.090	46.55	n.a.	b.d.	n.a.	53.71	b.d.	b.d.	b.d.	n.a.	b.d.	100.37
BOD3-107	II	n.a.	0.092	n.a.	n.a.	b.d.	0.031	46.40	n.a.	b.d.	n.a.	53.92	b.d.	b.d.	b.d.	n.a.	b.d.	100.45
BOD3-107	II	n.a.	0.058	n.a.	n.a.	b.d.	b.d.	46.10	n.a.	b.d.	n.a.	54.09	b.d.	b.d.	b.d.	n.a.	b.d.	100.28
BOD3-107	II	n.a.	b.d.	n.a.	n.a.	b.d.	b.d.	46.64	n.a.	b.d.	n.a.	53.46	b.d.	0.027	b.d.	n.a.	b.d.	100.15
BOD3-97A	II	n.a.	b.d.	b.d.	b.d.	b.d.	5.089	41.91	b.d.	b.d.	b.d.	53.59	b.d.	b.d.	b.d.	b.d.	b.d.	100.62
BID32-16	II	b.d.	b.d.	b.d.	b.d.	b.d.	3.286	43.44	b.d.	b.d.	b.d.	53.45	b.d.	0.015	b.d.	b.d.	b.d.	100.22
BOD3-97A	II	0.050	b.d.	b.d.	b.d.	b.d.	1.458	45.40	b.d.	b.d.	b.d.	53.35	b.d.	0.055	b.d.	b.d.	b.d.	100.33
BOD3-96	II	b.d.	b.d.	b.d.	b.d.	b.d.	0.651	46.54	b.d.	b.d.	b.d.	53.36	b.d.	0.024	b.d.	b.d.	b.d.	100.61
BOD3-96	II	b.d.	b.d.	b.d.	b.d.	b.d.	0.200	46.87	b.d.	b.d.	b.d.	53.72	b.d.	b.d.	b.d.	b.d.	b.d.	100.81
BOD3-97A	II	b.d.	b.d.	b.d.	b.d.	b.d.	0.166	46.68	b.d.	b.d.	b.d.	53.93	b.d.	0.080	b.d.	b.d.	b.d.	100.86
BID34-84	II	b.d.	b.d.	b.d.	b.d.	b.d.	b.d.	46.89	b.d.	b.d.	b.d.	53.82	b.d.	0.029	b.d.	b.d.	b.d.	100.77
BOD3-97A	II	0.023	b.d.	b.d.	b.d.	b.d.	2.531	44.83	b.d.	b.d.	b.d.	53.55	b.d.	0.018	b.d.	b.d.	0.019	100.97
BOD3-107	II	n.a.	b.d.	n.a.	n.a.	b.d.	0.495	46.07	n.a.	b.d.	n.a.	53.69	b.d.	b.d.	b.d.	n.a.	b.d.	100.26
BOD3-100.4	II	n.a.	b.d.	n.a.	n.a.	b.d.	0.259	46.49	n.a.	b.d.	n.a.	53.76	b.d.	b.d.	b.d.	n.a.	b.d.	100.51
BOD3-107	II	n.a.	b.d.	n.a.	n.a.	0.055	0.257	46.27	n.a.	0.011	n.a.	53.72	b.d.	b.d.	b.d.	n.a.	b.d.	100.32
BOD3-103.7	II	n.a.	b.d.	n.a.	n.a.	b.d.	0.246	46.55	n.a.	b.d.	n.a.	53.21	b.d.	b.d.	0.182	n.a.	b.d.	100.19
BOD3-107	II	n.a.	b.d.	n.a.	n.a.	b.d.	0.236	46.26	n.a.	b.d.	n.a.	53.53	b.d.	b.d.	b.d.	n.a.	b.d.	100.04
BID16-112	II	b.d.	0.031	b.d.	b.d.	b.d.	0.184	46.80	b.d.	b.d.	b.d.	53.57	b.d.	b.d.	b.d.	b.d.	0.016	100.63
BID16-112	II	0.040	0.034	b.d.	b.d.	b.d.	0.152	46.53	b.d.	b.d.	b.d.	53.44	b.d.	b.d.	b.d.	b.d.	0.018	100.22
BOD3-97A	II	b.d.	b.d.	b.d.	b.d.	b.d.	0.137	46.64	b.d.	b.d.	b.d.	54.01	b.d.	b.d.	b.d.	b.d.	b.d.	100.81
BID16-112	II	b.d.	b.d.	b.d.	b.d.	b.d.	0.066	46.46	b.d.	b.d.	b.d.	53.75	b.d.	b.d.	b.d.	b.d.	b.d.	100.31
BOD3-100.4	II	n.a.	b.d.	n.a.	n.a.	b.d.	0.038	46.43	n.a.	b.d.	n.a.	53.34	b.d.	b.d.	b.d.	n.a.	b.d.	99.83
BOD3-107	II	n.a.	b.d.	n.a.	n.a.	b.d.	b.d.	46.32	n.a.	b.d.	n.a.	53.30	b.d.	b.d.	b.d.	n.a.	b.d.	99.65
BOD3-100.4	II	n.a.	b.d.	n.a.	n.a.	b.d.	b.d.	46.68	n.a.	b.d.	n.a.	53.70	b.d.	b.d.	b.d.	n.a.	b.d.	100.38
BOD3-96	II	n.a.	b.d.	n.a.	n.a.	b.d.	1.423	45.12	n.a.	b.d.	n.a.	53.36	b.d.	0.011	b.d.	n.a.	b.d.	99.93
BOD3-96	II	n.a.	b.d.	n.a.	n.a.	b.d.	1.205	45.34	n.a.	b.d.	n.a.	53.09	b.d.	b.d.	b.d.	n.a.	b.d.	99.66
BOD3-96	II	n.a.	b.d.	n.a.	n.a.	b.d.	1.158	45.37	n.a.	b.d.	n.a.	53.32	b.d.	0.014	b.d.	n.a.	b.d.	99.86
BOD3-96	II	n.a.	b.d.	n.a.	n.a.	b.d.	0.696	45.91	n.a.	b.d.	n.a.	53.46	b.d.	b.d.	b.d.	n.a.	b.d.	100.08
BOD3-96	II	n.a.	b.d.	n.a.	n.a.	b.d.	0.339	46.35	n.a.	b.d.	n.a.	53.34	b.d.	0.018	b.d.	n.a.	b.d.	100.05
BID34-84	I	b.d.	b.d.	n.a.	b.d.	n.a.	2.328	44.18	n.a.	b.d.	b.d.	53.11	b.d.	b.d.	b.d.	n.a.	0.092	99.72
BOD1-32	I	0.051	0.086	b.d.	b.d.	b.d.	1.709	44.29	b.d.	b.d.	b.d.	53.72	b.d.	b.d.	b.d.	b.d.	0.014	99.88
BID34-84	I	b.d.	b.d.	n.a.	b.d.	n.a.	1.196	45.33	n.a.	b.d.	b.d.	53.94	b.d.	b.d.	b.d.	n.a.	0.029	100.52
BID34-84	I	0.028	b.d.	n.a.	b.d.	n.a.	1.096	45.56	n.a.	b.d.	b.d.	53.84	b.d.	b.d.	b.d.	n.a.	b.d.	100.54
BOD1-32	I	n.a.	0.047	n.a.	n.a.	b.d.	1.047	45.11	n.a.	b.d.	b.d.	53.03	b.d.	b.d.	b.d.	n.a.	b.d.	99.25
BOD1-32	I	n.a.	b.d.	n.a.	n.a.	b.d.	0.798	45.69	n.a.	b.d.	n.a.	53.29	b.d.	0.038	b.d.	n.a.	0.011	99.83
BOD1-32	I	n.a.	0.081	n.a.	n.a.	b.d.	0.753	45.36	n.a.	b.d.	n.a.	53.21	b.d.	b.d.	b.d.	n.a.	b.d.	99.41
BOD1-32	I	n.a.	0.375	n.a.	n.a.	b.d.	0.724	44.95	n.a.	b.d.	n.a.	52.99	b.d.	b.d.	b.d.	n.a.	0.018	99.07
BID34-84	I	0.050	b.d.	n.a.	b.d.	n.a.	0.709	45.30	n.a.	b.d.	n.a.	53.83	b.d.	b.d.	b.d.	n.a.	0.034	99.93
BID34-84	I	0.041	0.022	n.a.	b.d.	n.a.	0.604	45.70	n.a.	b.d.	b.d.	53.97	b.d.	b.d.	0.038	n.a.	b.d.	100.38
BOD3-100.4	I	n.a.	b.d.	n.a.	n.a.	b.d.	0.553	46.24	n.a.	b.d.	b.d.	53.57	b.d.	b.d.	b.d.	n.a.	b.d.	100.38
BID34-84	I	b.d.	0.031	n.a.	b.d.	n.a.	0.446	46.18	n.a.	b.d.	n.a.	54.12	b.d.	0.046	0.023	n.a.	b.d.	100.85
BID34-84	I	0.030	0.030	n.a.	b.d.	n.a.	0.375	46.45	n.a.	b.d.	b.d.	53.67	b.d.	b.d.	b.d.	n.a.	0.012	100.58
BID34-76	I	b.d.	b.d.	b.d.	b.d.	b.d.	0.357	46.55	b.d.	b.d.	b.d.	53.87	b.d.	0.012	b.d.	b.d.	b.d.	100.80
BID34-84	I	b.d.	0.041	b.d.	b.d.	b.d.	0.250	46.56	b.d.	b.d.	b.d.	53.70	b.d.	0.039	b.d.	b.d.	b.d.	100.60
BID34-84	I	b.d.	b.d.	b.d.	b.d.	b.d.	0.217	46.56	b.d.	b.d.	b.d.	53.70	b.d.	b.d.	b.d.	b.d.	b.d.	100.50
BID34-76	I	b.d.	b.d.	b.d.	b.d.	b.d.	0.178	46.38	b.d.	b.d.	b.d.	53.92	b.d.	0.052	b.d.	b.d.	b.d.	100.54
BOD3-100.4	I	n.a.	b.d.	n.a.	n.a.	b.d.	0.109	46.29	n.a.	b.d.	n.a.	53.58	b.d.	b.d.	b.d.	n.a.	b.d.	100.00
BID34-84	I	b.d.	0.062	n.a.	b.d.	n.a.	0.080	46.09	n.a.	b.d.	b.d.	53.17	b.d.	b.d.	0.029	n.a.	b.d.	99.42
BID34-84	I	b.d.	b.d.	b.d.	b.d.	b.d.	0.067	46.26	b.d.	b.d.	b.d.	53.85	b.d.	b.d.	b.d.	b.d.	b.d.	100.19
BID34-76	I	b.d.	b.d.	b.d.	b.d.	b.d.	0.035	46.71	b.d.	b.d.	b.d.	53.75	b.d.	b.d.	b.d.	b.d.	b.d.	100.54
BOD3-97A	I	b.d.	b.d.	b.d.	b.d.	b.d.	0.035	46.68	b.d.	b.d.	b.d.	53.86	b.d.	0.023	b.d.	b.d.	b.d.	100.60
BID34-76	I	b.d.	b.d.	b.d.	b.d.	b.d.	b.d.	46.85	b.d.	b.d.	b.d.	53.87	b.d.	0.050	b.d.	b.d.	b.d.	100.79
BID34-84	I	b.d.	0.024	n.a.	b.d.	n.a.	b.d.	46.36	n.a.	b.d.	b.d.	53.87	b.d.	b.d.	b.d.	n.a.	b.d.	100.26
BID34-84	I	b.d.	0.217	b.d.	b.d.	b.d.	1.667	44.81	b.d.	b.d.	b.d.	53.71	b.d.	0.018	b.d.	b.d.	b.d.	100.43
BID32-16	I	b.d.	b.d.	b.d.	b.d.	0.040	0.256	46.60	b.d.	b.d.	b.d.	53.90	b.d.	b.d.	b.d.	b.d.	b.d.	100.80
BID34-84	II	0.036	b.d.	n.a.	b.d.	n.a.	5.196	41.78	n.a.	b.d.	b.d.	53.72	b.d.	b.d.	b.d.	n.a.	b.d.	100.73
BID34-84-15	II	b.d.	b.d.	b.d.	b.d.	0.234	5.041	42.02	b.d.	b.d.	b.d.	53.25	b.d.	0.120	b.d.	b.d.	0.018	100.70
BID34-84-16	II	b.d.	b.d.	b.d.	b.d.	0.560	4.034	42.37	b.d.	b.d.	b.d.	53.68	b.d.	0.134	b.d.	b.d.	b.d.	100.80
BID34-84-14	II	b.d.	b.d.	b.d.	b.d.	b.d.	1.206	45.73	b.d.	b.d.	b.d.	53.80	b.d.	b.d.	b.d.	b.d.	b.d.	100.74
BID34-84-19	II	b.d.	b.d.	b.d.	b.d.	b.d.	0.814	46.03	b.d.	b.d.	b.d.	53.97	b.d.	b.d.	b.d.	b.d.	0.019	100.85
BID34-84	II	b.d.	0.035	n.a.	b.d.	n.a.	0.421	45.55	n.a.	b.d.	b.d.	54.22	0.011	b.d.	0.054	n.a.	0.021	100.31
BOD3-100.4	II	n.a.	b.d.	n.a.	n.a.	b.d.	0.127	46.31	n.a.	b.d.	n.a.	53.56	b.d.	b.d.	b.d.	n.a.	b.d.	100.01
BOD3-100.4	II	n.a.	0.050	n.a.	n.a.	b.d.	0.050	46.39	n.a.	b.d.	n.a.	53.77	b.d.	b.d.	b.d.	n.a.	b.d.	100.26
BOD3-100.4	II	n.a.	0.396	n.a.	n.a.	b.d.	b.d.	45.29	n.a.	b.d.	n.a.	54.39	b.d.	b.d.	b.d.	n.a.	0.020	100.12
BID34-84	II	b.d.	0.130	n.a.	b.d.	n.a.	0.492	44.88	n.a.	b.d.	b.d.	54.50	0.019	b.d.	b.d.	n.a.	0.044	100.06
BID34-84	II	0.023	b.d.	n.a.	b.d.	n.a.	0.312	46.04	n.a.	b.d.	b.d.	54.18	b.d.	b.d.	b.d.	n.a.	0.087	100.65

Sample	Type	Ag	As	Au	Cd	Co	Cu	Fe	Hg	Ni	Pb	S	Sb	Se	Te	Ti	Zn	Total
d.l.		0.016	0.022	0.007	0.034	0.02	0.007	0.036	0.034	0.01	0.023	0.012	0.01	0.012	0.015	0.01	0.013	
BOD3-96	II	b.d.	b.d.	b.d.	b.d.	b.d.	0.252	46.32	b.d.	b.d.	b.d.	53.50	b.d.	b.d.	b.d.	b.d.	b.d.	100.11
BID34-84	II	b.d.	0.047	n.a.	b.d.	n.a.	0.191	45.63	n.a.	b.d.	b.d.	54.51	b.d.	b.d.	b.d.	n.a.	0.106	100.52
BID34-84	II	b.d.	b.d.	n.a.	b.d.	n.a.	0.167	44.23	n.a.	b.d.	b.d.	54.96	b.d.	b.d.	b.d.	n.a.	0.111	99.47
BID34-84	II	b.d.	b.d.	n.a.	b.d.	n.a.	b.d.	46.36	n.a.	b.d.	b.d.	53.76	b.d.	b.d.	0.039	n.a.	0.040	100.20
BID34-84	II	b.d.	b.d.	b.d.	b.d.	b.d.	0.304	45.80	b.d.	b.d.	b.d.	54.48	b.d.	b.d.	b.d.	0.021	b.d.	100.62
BOD3-107	II	n.a.	b.d.	n.a.	n.a.	b.d.	0.246	46.57	n.a.	b.d.	n.a.	53.49	b.d.	b.d.	b.d.	n.a.	b.d.	100.31
BOD3-107	II	n.a.	b.d.	n.a.	n.a.	b.d.	0.225	46.42	n.a.	b.d.	n.a.	53.40	b.d.	0.024	b.d.	n.a.	b.d.	100.07
BOD3-107	II	n.a.	b.d.	n.a.	n.a.	b.d.	0.144	46.46	n.a.	b.d.	n.a.	53.55	b.d.	0.026	b.d.	n.a.	b.d.	100.19
BID34-84	II	b.d.	0.038	n.a.	b.d.	n.a.	0.118	45.13	n.a.	b.d.	b.d.	54.51	b.d.	b.d.	0.021	n.a.	0.069	99.91
BID34-84	II	b.d.	b.d.	b.d.	b.d.	b.d.	0.077	46.32	b.d.	b.d.	b.d.	54.05	b.d.	b.d.	b.d.	b.d.	b.d.	100.49
BOD3-107	II	n.a.	0.064	n.a.	n.a.	b.d.	b.d.	46.30	n.a.	b.d.	n.a.	53.33	b.d.	b.d.	b.d.	n.a.	b.d.	99.71
BID34-84	II	n.a.	0.171	n.a.	n.a.	n.a.	2.478	41.67	n.a.	0.086	n.a.	52.74	n.a.	0.160	0.109	n.a.	n.a.	97.41
BID34-84	II	n.a.	0.156	n.a.	n.a.	n.a.	2.373	41.47	n.a.	0.082	n.a.	52.32	n.a.	0.150	0.105	n.a.	n.a.	96.65
BID34-84	II	n.a.	0.045	n.a.	n.a.	n.a.	1.107	45.14	n.a.	b.d.	n.a.	53.20	n.a.	0.034	0.032	n.a.	n.a.	99.57
BID34-84	II	n.a.	0.197	n.a.	n.a.	n.a.	3.467	40.42	n.a.	0.097	n.a.	52.60	n.a.	0.160	0.154	n.a.	n.a.	97.10
BID34-84	II	n.a.	0.194	n.a.	n.a.	n.a.	3.715	40.34	n.a.	0.092	n.a.	52.63	n.a.	0.132	0.136	n.a.	n.a.	97.24
BID34-84	II	n.a.	0.169	n.a.	n.a.	n.a.	3.528	40.02	n.a.	0.085	n.a.	52.08	n.a.	0.164	0.142	n.a.	n.a.	96.18
BID34-84	II	n.a.	0.183	n.a.	n.a.	n.a.	3.378	40.76	n.a.	0.089	n.a.	52.74	n.a.	0.159	0.123	n.a.	n.a.	97.43
BID34-84	II	n.a.	0.171	n.a.	n.a.	n.a.	3.366	40.86	n.a.	0.078	n.a.	52.68	n.a.	0.152	0.112	n.a.	n.a.	97.42
BID34-84	II	n.a.	0.161	n.a.	n.a.	n.a.	3.365	41.05	n.a.	0.086	n.a.	52.89	n.a.	0.148	0.114	n.a.	n.a.	97.81
BID34-84	II	n.a.	0.136	n.a.	n.a.	n.a.	3.356	40.98	n.a.	0.081	n.a.	52.50	n.a.	0.158	0.116	n.a.	n.a.	97.33
BID34-84	II	n.a.	0.156	n.a.	n.a.	n.a.	3.219	40.33	n.a.	0.083	n.a.	52.04	n.a.	0.154	0.117	n.a.	n.a.	96.10
BID34-84	II	n.a.	0.170	n.a.	n.a.	n.a.	3.228	41.05	n.a.	0.079	n.a.	52.61	n.a.	0.171	0.122	n.a.	n.a.	97.43
BID34-84	II	n.a.	0.155	n.a.	n.a.	n.a.	3.338	41.13	n.a.	0.071	n.a.	52.53	n.a.	0.175	0.115	n.a.	n.a.	97.51
BID34-84	II	n.a.	0.158	n.a.	n.a.	n.a.	3.411	41.01	n.a.	0.078	n.a.	52.65	n.a.	0.168	0.137	n.a.	n.a.	97.62
BID34-84	II	n.a.	0.173	n.a.	n.a.	n.a.	3.447	40.89	n.a.	0.072	n.a.	52.64	n.a.	0.168	0.119	n.a.	n.a.	97.52
BID34-84	II	n.a.	0.137	n.a.	n.a.	n.a.	3.560	41.02	n.a.	0.074	n.a.	52.62	n.a.	0.172	0.118	n.a.	n.a.	97.70
BID34-84	II	n.a.	0.159	n.a.	n.a.	n.a.	3.626	41.01	n.a.	0.068	n.a.	52.82	n.a.	0.172	0.109	n.a.	n.a.	97.96
BID34-84	II	n.a.	0.134	n.a.	n.a.	n.a.	3.667	41.02	n.a.	0.066	n.a.	52.75	n.a.	0.174	0.088	n.a.	n.a.	97.89
BID34-84	II	n.a.	0.139	n.a.	n.a.	n.a.	3.664	41.14	n.a.	0.072	n.a.	52.81	n.a.	0.167	0.111	n.a.	n.a.	98.10
BID34-84	II	n.a.	0.115	n.a.	n.a.	n.a.	3.697	41.11	n.a.	0.054	n.a.	52.58	n.a.	0.172	0.106	n.a.	n.a.	97.83
BID34-84	II	n.a.	0.124	n.a.	n.a.	n.a.	3.666	41.20	n.a.	0.061	n.a.	52.68	n.a.	0.174	0.105	n.a.	n.a.	98.02
BID34-84	II	n.a.	0.127	n.a.	n.a.	n.a.	3.391	41.35	n.a.	0.062	n.a.	52.61	n.a.	0.171	0.105	n.a.	n.a.	97.82
BID34-84	II	n.a.	0.142	n.a.	n.a.	n.a.	3.193	41.64	n.a.	0.058	n.a.	52.67	n.a.	0.197	0.129	n.a.	n.a.	98.02
BID34-84	II	n.a.	0.140	n.a.	n.a.	n.a.	3.419	41.74	n.a.	0.048	n.a.	52.77	n.a.	0.215	0.135	n.a.	n.a.	98.46
BID34-84	II	n.a.	0.075	n.a.	n.a.	n.a.	2.909	43.02	n.a.	0.024	n.a.	52.97	n.a.	0.171	0.079	n.a.	n.a.	99.24
BID34-84	II	n.a.	b.d.	n.a.	n.a.	n.a.	3.297	42.23	n.a.	0.052	n.a.	52.86	n.a.	0.168	b.d.	n.a.	n.a.	98.60
BID34-84	II	n.a.	b.d.	n.a.	n.a.	n.a.	3.108	42.52	n.a.	0.048	n.a.	52.89	n.a.	0.158	b.d.	n.a.	n.a.	98.73
BID34-84	II	n.a.	b.d.	n.a.	n.a.	n.a.	2.214	44.07	n.a.	0.022	n.a.	53.06	n.a.	0.087	b.d.	n.a.	n.a.	99.47
BID34-84	II	n.a.	b.d.	n.a.	n.a.	n.a.	4.250	41.14	n.a.	0.056	n.a.	52.88	n.a.	0.164	b.d.	n.a.	n.a.	98.52
BID34-84	II	n.a.	b.d.	n.a.	n.a.	n.a.	4.544	41.14	n.a.	0.052	n.a.	52.83	n.a.	0.171	b.d.	n.a.	n.a.	98.74
BID34-84	II	n.a.	b.d.	n.a.	n.a.	n.a.	4.504	41.17	n.a.	0.047	n.a.	52.72	n.a.	0.160	b.d.	n.a.	n.a.	98.62
BID34-84	II	n.a.	b.d.	n.a.	n.a.	n.a.	4.340	41.17	n.a.	0.044	n.a.	52.82	n.a.	0.158	b.d.	n.a.	n.a.	98.53
BID34-84	II	n.a.	b.d.	n.a.	n.a.	n.a.	4.185	41.36	n.a.	0.047	n.a.	52.84	n.a.	0.163	b.d.	n.a.	n.a.	98.61
BID34-84	II	n.a.	b.d.	n.a.	n.a.	n.a.	4.177	41.51	n.a.	0.043	n.a.	52.78	n.a.	0.173	b.d.	n.a.	n.a.	98.70
BID34-84	II	n.a.	b.d.	n.a.	n.a.	n.a.	4.032	41.60	n.a.	0.045	n.a.	52.85	n.a.	0.161	b.d.	n.a.	n.a.	98.71
BID34-84	II	n.a.	b.d.	n.a.	n.a.	n.a.	3.958	41.51	n.a.	0.042	n.a.	52.90	n.a.	0.164	b.d.	n.a.	n.a.	98.59
BID34-84	II	n.a.	b.d.	n.a.	n.a.	n.a.	3.872	41.66	n.a.	0.036	n.a.	52.91	n.a.	0.164	b.d.	n.a.	n.a.	98.65
BID34-84	II	n.a.	b.d.	n.a.	n.a.	n.a.	3.935	41.69	n.a.	0.044	n.a.	52.99	n.a.	0.166	b.d.	n.a.	n.a.	98.84
BID34-84	II	n.a.	b.d.	n.a.	n.a.	n.a.	3.958	41.61	n.a.	0.049	n.a.	52.82	n.a.	0.171	b.d.	n.a.	n.a.	98.62
BID34-84	II	n.a.	b.d.	n.a.	n.a.	n.a.	3.987	41.66	n.a.	0.044	n.a.	52.85	n.a.	0.169	b.d.	n.a.	n.a.	98.72
BID34-84	II	n.a.	b.d.	n.a.	n.a.	n.a.	4.035	41.64	n.a.	0.040	n.a.	52.80	n.a.	0.149	b.d.	n.a.	n.a.	98.68
BID34-84	II	n.a.	b.d.	n.a.	n.a.	n.a.	4.044	41.63	n.a.	0.036	n.a.	52.91	n.a.	0.167	b.d.	n.a.	n.a.	98.80
BID34-84	II	n.a.	b.d.	n.a.	n.a.	n.a.	4.097	41.55	n.a.	0.033	n.a.	52.61	n.a.	0.171	b.d.	n.a.	n.a.	98.48
BID34-84	II	n.a.	b.d.	n.a.	n.a.	n.a.	4.083	41.64	n.a.	0.035	n.a.	52.61	n.a.	0.164	b.d.	n.a.	n.a.	98.54
BID34-84	II	n.a.	b.d.	n.a.	n.a.	n.a.	4.075	41.69	n.a.	0.033	n.a.	52.82	n.a.	0.163	b.d.	n.a.	n.a.	98.80
BID34-84	II	n.a.	b.d.	n.a.	n.a.	n.a.	4.181	41.58	n.a.	0.039	n.a.	52.83	n.a.	0.172	b.d.	n.a.	n.a.	98.82
BID34-84	II	n.a.	b.d.	n.a.	n.a.	n.a.	4.136	41.73	n.a.	0.037	n.a.	53.06	n.a.	0.165	b.d.	n.a.	n.a.	99.14
BID34-84	II	n.a.	b.d.	n.a.	n.a.	n.a.	4.060	41.80	n.a.	0.033	n.a.	52.69	n.a.	0.178	b.d.	n.a.	n.a.	98.77
BID34-84	II	n.a.	b.d.	n.a.	n.a.	n.a.	3.911	41.95	n.a.	0.036	n.a.	52.82	n.a.	0.169	b.d.	n.a.	n.a.	98.90
BID34-84	II	n.a.	b.d.	n.a.	n.a.	n.a.	3.853	41.98	n.a.	0.032	n.a.	52.60	n.a.	0.184	b.d.	n.a.	n.a.	98.67
BID34-84	II	n.a.	b.d.	n.a.	n.a.	n.a.	0.890	45.70	n.a.	b.d.	n.a.	53.34	n.a.	b.d.	b.d.	n.a.	n.a.	99.96
BID34-84	II	n.a.	b.d.	n.a.	n.a.	n.a.	0.885	45.61	n.a.	b.d.	n.a.	53.27	n.a.	b.d.	b.d.	n.a.	n.a.	99.78
BID34-84	II	n.a.	b.d.	n.a.	n.a.	n.a.	0.710	45.90	n.a.	b.d.	n.a.	53.42	n.a.	b.d.	b.d.	n.a.	n.a.	100.06
BID34-84	II	n.a.	b.d.	n.a.	n.a.	n.a.	1.356	45.31	n.a.	b.d.	n.a.	53.17	n.a.	b.d.	0.026	n.a.	n.a.	99.89
BID34-84	II	n.a.	b.d.	n.a.	n.a.	n.a.	1.186	44.89	n.a.	b.d.	n.a.	53.04	n.a.	b.d.	b.d.	n.a.	n.a.	99.13
BID34-84	II	n.a.	0.049	n.a.	n.a.	n.a.	0.860	44.05	n.a.	0.069	n.a.	53.12	n.a.	b.d.	b.d.	n.a.	n.a.	98.17
BID34-84	II	n.a.	0.045	n.a.	n.a.	n.a.	0.562	43.42	n.a.	0.114	n.a.	52.96	n.a.	b.d.	b.d.	n.a.	n.a.	97.12
BID34-84	II	n.a.	0.046	n.a.	n.a.	n.a.	0.632	43.38	n.a.	0.121	n.a.	52.90	n.a.	b.d.	b.d.	n.a.	n.a.	97.11
BID34-84	II	n.a.	0.041	n.a.	n.a.	n.a.	0.579	43.49	n.a.	0.118	n.a.	53.09	n.a.	b.d.	b.d.	n.a.	n.a.	97.34
BID34-84	II	n.a.	0.097	n.a.	n.a.	n.a.	1.473	42.14	n.a.	0.148	n.a.	52.68	n.a.	0.069	0.040	n.a.	n.a.	96.64
BID34-84	II	n.a.	b.d.	n.a.	n.a.	n.a.	0.854	45.65	n.a.	b.d.	n.a.	53.11	n.a.	b.d.	b.d.	n.a.	n.a.	99.62
BID34-84	II	n.a.	b.d.	n.a.	n.a.	n.a.	0.858	45.21	n.a.	0.017	n.a.	52.85	n.a.	b.d.	b.d.	n.a.	n.a.	98.94
BID34-84	II	n.a.	b.d.	n.a.	n.a.	n.a.	0.576	44.93	n.a.	0.042	n.a.	52.95	n.a.	b.d.	b.d.	n.a.	n.a.	98.50
BID34-84	II	n.a.	b.d.	n.a.	n.a.	n.a.	0.569	45.03	n.a.	0.046	n.a.	52.80	n.a.	b.d.	b.d.	n.a.	n.a.	98.45
BID34-84	II	n.a.	b.d.	n.a.	n.a.	n.a.	0.693	44.75	n.a.	0.066	n.a.	53.21	n.a.	b.d.	b.d.	n.a.	n.a.	98.73
BID34-84	II	n.a.	b.d.	n.a.	n.a.	n.a.	0.638	44.76	n.a.	0.069	n.a.	52.97	n.a.	b.d.	b.d.	n.a.	n.a.	98.45
BID34-84	II	n.a.	b.d.	n.a.	n.a.	n.a.	0.714	44.74	n.a.	0.071	n.a.	53.10	n.a.	b.d.	b.d.	n.a.	n.a.	98.64
BID34-84	II	n.a.	b.d.	n.a.	n.a.	n.a.	0.898	44.37	n.a.	0.074	n.a.	53.05	n.a.	b.d.	b.d.	n.a.	n.a.	98.41
BID34-84	II	n.a.	b.d.	n.a.	n.a.	n.a.	0.735	44.57	n.a.	0.080	n.a.	53.01	n.a.	b.d.	b.d.	n.a.	n.a.	98.43
BID34-84	II	n.a.	b.d.	n.a.	n.a.	n.a.	0.706	44.48	n.a.	0.073	n.a.	52.77	n.a.	b.d.	b.d.	n.a.	n.a.	98.06
BID34-84	II	n.a.	0.130	n.a.	n.a.	n.a.	3.618	41.80	n.a.	0.040	n.a.	52.33	n.a.	0.140	0.062	n.a.	n.a.	98.12
BID34-84	II	n.a.	0.196	n.a.	n.a.	n.a.	3.236	41.73	n.a.	0.061	n.a.	52.42	n.a.	0.128	0.074	n.a.	n.a.	97.84
BID34-84	II	n.a.	0.187	n.a.	n.a.	n.a.	3.243	41.78	n.a.	0.056	n.a.	52.61	n.a.	0.119	0.078	n.a.	n.a.	98.07
BID34-84	II	n.a.	0.223	n.a.	n.a.	n.a.	3.231	41.98	n.a.	0.038	n.a.	52.62	n.a.	0.129	0.070	n.a.	n.a.	98.29
BID34-84	II	n.a.	0.223	n.a.	n.a.	n.a.	3.111	42.05	n.a.	0.045	n.a.	52.79	n.a.	0.122	0.079	n.a.	n.a.	98.41
BID34-84	II	n.a.	0.188	n.a.	n.a.	n.a.	3.145	42.00	n.a.	0.039	n.a.	52.53	n.a.	0.122	0.077	n.a.	n.a.	98.09
BID34-84	II	n.a.	0.188	n.a.	n.a.	n.a.	3.172	42.09	n.a.	0.041	n.a.	52.45	n.a.	0.121	0.092	n.a.	n.a.	98.15
BID34-84	II	n.a.	0.133	n.a.	n.a.	n.a.	3.539	41.97	n.a.	0.039	n.a.	52.43	n.a.	0.122	0.063	n.a.	n.a.	98.29
BID34-84	II	n.a.	0.184	n.a.	n.a.	n.a.	3.392	42.07	n.a.	0.034	n.a.	52.49	n.a.	0.112	0.076	n.a.	n.a.	98.35
BID34-84	II	n.a.	0.160	n.a.	n.a.	n.a.	3.441	42.07	n.a.	0.035	n.a.	52.54	n.a.	0.113	0.061	n.a.	n.a.	98.43

Sample	Type	Ag	As	Au	Cd	Co	Cu	Fe	Hg	Ni	Pb	S	Sb	Se	Te	Ti	Zn	Total
d.l.		0.016	0.022	0.007	0.034	0.02	0.007	0.036	0.034	0.01	0.023	0.012	0.01	0.012	0.015	0.01	0.013	
BID34-84	II	n.a.	0.174	n.a.	n.a.	n.a.	3.299	42.12	n.a.	0.033	n.a.	52.73	n.a.	0.113	0.062	n.a.	n.a.	98.53
BID34-84	II	n.a.	0.209	n.a.	n.a.	n.a.	3.184	42.23	n.a.	0.043	n.a.	52.43	n.a.	0.111	0.079	n.a.	n.a.	98.29
BID34-84	II	n.a.	0.164	n.a.	n.a.	n.a.	3.409	42.10	n.a.	0.038	n.a.	52.38	n.a.	0.107	0.065	n.a.	n.a.	98.26
BID34-84	II	n.a.	0.166	n.a.	n.a.	n.a.	3.345	42.22	n.a.	0.028	n.a.	52.50	n.a.	0.110	0.057	n.a.	n.a.	98.43
BID34-84	II	n.a.	0.172	n.a.	n.a.	n.a.	3.285	42.26	n.a.	0.035	n.a.	52.69	n.a.	0.099	0.074	n.a.	n.a.	98.62
BID34-84	II	n.a.	0.189	n.a.	n.a.	n.a.	3.030	42.29	n.a.	0.037	n.a.	52.63	n.a.	0.111	0.083	n.a.	n.a.	98.37
BID34-84	II	n.a.	0.185	n.a.	n.a.	n.a.	2.774	42.33	n.a.	0.041	n.a.	52.57	n.a.	0.121	0.083	n.a.	n.a.	98.10
BID34-84	II	n.a.	0.130	n.a.	n.a.	n.a.	2.218	42.28	n.a.	0.064	n.a.	52.40	n.a.	0.152	0.089	n.a.	n.a.	97.33
BID34-84	II	n.a.	b.d.	n.a.	n.a.	n.a.	0.587	46.09	n.a.	b.d.	n.a.	53.55	n.a.	b.d.	b.d.	n.a.	n.a.	100.24
BID34-84	II	n.a.	b.d.	n.a.	n.a.	n.a.	0.698	45.91	n.a.	b.d.	n.a.	53.31	n.a.	b.d.	b.d.	n.a.	n.a.	99.93
BID34-84	II	n.a.	b.d.	n.a.	n.a.	n.a.	0.586	46.02	n.a.	b.d.	n.a.	53.32	n.a.	b.d.	b.d.	n.a.	n.a.	99.96
BID34-84	II	n.a.	b.d.	n.a.	n.a.	n.a.	0.445	46.00	n.a.	b.d.	n.a.	53.39	n.a.	b.d.	b.d.	n.a.	n.a.	99.87
BID34-84	II	n.a.	b.d.	n.a.	n.a.	n.a.	0.497	45.87	n.a.	0.015	n.a.	53.15	n.a.	b.d.	b.d.	n.a.	n.a.	99.58
BID34-84	II	n.a.	b.d.	n.a.	n.a.	n.a.	0.571	45.67	n.a.	0.024	n.a.	53.44	n.a.	b.d.	b.d.	n.a.	n.a.	99.74
BID34-84	II	n.a.	b.d.	n.a.	n.a.	n.a.	0.411	45.47	n.a.	0.051	n.a.	52.97	n.a.	0.034	b.d.	n.a.	n.a.	98.94
BID34-84	II	n.a.	b.d.	n.a.	n.a.	n.a.	0.456	46.35	n.a.	b.d.	n.a.	53.51	n.a.	0.116	b.d.	n.a.	n.a.	100.46
BID34-84	II	n.a.	b.d.	n.a.	n.a.	n.a.	0.775	45.97	n.a.	b.d.	n.a.	53.51	n.a.	b.d.	b.d.	n.a.	n.a.	100.28
BID34-84	II	n.a.	0.085	n.a.	n.a.	n.a.	0.991	45.73	n.a.	b.d.	n.a.	53.59	n.a.	b.d.	0.022	n.a.	n.a.	100.42
BID34-84	II	n.a.	b.d.	n.a.	n.a.	n.a.	1.085	45.83	n.a.	b.d.	n.a.	53.79	n.a.	0.040	b.d.	n.a.	n.a.	100.76
BID34-84	II	n.a.	b.d.	n.a.	n.a.	n.a.	0.829	46.00	n.a.	b.d.	n.a.	53.34	n.a.	0.058	b.d.	n.a.	n.a.	100.24
BID34-84	II	n.a.	0.089	n.a.	n.a.	n.a.	3.819	41.34	n.a.	0.056	n.a.	52.61	n.a.	0.106	0.058	n.a.	n.a.	98.07
BID34-84	II	n.a.	0.098	n.a.	n.a.	n.a.	3.703	41.20	n.a.	0.068	n.a.	52.95	n.a.	0.090	0.064	n.a.	n.a.	98.17
BID34-84	II	n.a.	0.099	n.a.	n.a.	n.a.	3.765	41.27	n.a.	0.059	n.a.	52.65	n.a.	0.097	0.057	n.a.	n.a.	98.00
BID34-84	II	n.a.	0.121	n.a.	n.a.	n.a.	3.735	41.33	n.a.	0.067	n.a.	52.79	n.a.	0.103	0.053	n.a.	n.a.	98.20
BID34-84	II	n.a.	0.109	n.a.	n.a.	n.a.	3.763	41.33	n.a.	0.055	n.a.	52.68	n.a.	0.086	0.062	n.a.	n.a.	98.09
BID34-84	II	n.a.	0.088	n.a.	n.a.	n.a.	3.844	41.32	n.a.	0.045	n.a.	52.52	n.a.	0.097	0.044	n.a.	n.a.	97.96
BID34-84	II	n.a.	0.066	n.a.	n.a.	n.a.	3.850	41.43	n.a.	0.054	n.a.	52.76	n.a.	0.075	0.047	n.a.	n.a.	98.28
BID34-84	II	n.a.	0.094	n.a.	n.a.	n.a.	3.968	41.57	n.a.	0.043	n.a.	52.88	n.a.	0.078	0.054	n.a.	n.a.	98.69
BID34-84	II	n.a.	0.092	n.a.	n.a.	n.a.	3.978	41.56	n.a.	0.051	n.a.	52.85	n.a.	0.073	0.046	n.a.	n.a.	98.64
BID34-84	II	n.a.	0.089	n.a.	n.a.	n.a.	3.983	41.62	n.a.	0.045	n.a.	52.87	n.a.	0.081	0.054	n.a.	n.a.	98.74
BID34-84	II	n.a.	0.069	n.a.	n.a.	n.a.	3.985	41.59	n.a.	0.039	n.a.	52.76	n.a.	0.087	0.059	n.a.	n.a.	98.59
BID34-84	II	n.a.	0.061	n.a.	n.a.	n.a.	4.038	41.64	n.a.	0.035	n.a.	52.90	n.a.	0.075	0.043	n.a.	n.a.	98.79
BID34-84	II	n.a.	0.062	n.a.	n.a.	n.a.	4.071	41.62	n.a.	0.036	n.a.	52.84	n.a.	0.080	0.050	n.a.	n.a.	98.76
BID34-84	II	n.a.	0.064	n.a.	n.a.	n.a.	4.052	41.55	n.a.	0.034	n.a.	52.80	n.a.	0.075	0.044	n.a.	n.a.	98.62
BID34-84	II	n.a.	0.069	n.a.	n.a.	n.a.	4.011	41.81	n.a.	0.032	n.a.	52.73	n.a.	0.084	0.045	n.a.	n.a.	98.78
BID34-84	II	n.a.	0.045	n.a.	n.a.	n.a.	4.022	41.75	n.a.	0.026	n.a.	52.80	n.a.	0.070	0.053	n.a.	n.a.	98.76
BID34-84	II	n.a.	0.042	n.a.	n.a.	n.a.	4.001	41.70	n.a.	0.030	n.a.	52.91	n.a.	0.066	0.044	n.a.	n.a.	98.79
BID34-84	II	n.a.	0.044	n.a.	n.a.	n.a.	3.917	41.80	n.a.	0.027	n.a.	53.01	n.a.	0.075	0.062	n.a.	n.a.	98.94
BID34-84	II	n.a.	0.048	n.a.	n.a.	n.a.	3.791	41.89	n.a.	0.035	n.a.	52.75	n.a.	0.079	0.054	n.a.	n.a.	98.64
BID34-84	II	n.a.	0.066	n.a.	n.a.	n.a.	3.470	41.79	n.a.	0.047	n.a.	52.81	n.a.	0.089	0.060	n.a.	n.a.	98.33
BID34-84	II	n.a.	0.204	n.a.	n.a.	n.a.	0.915	33.47	n.a.	0.046	n.a.	35.35	n.a.	0.121	0.043	n.a.	n.a.	70.15
BID34-84	II	n.a.	b.d.	n.a.	n.a.	n.a.	1.276	45.35	n.a.	b.d.	n.a.	53.27	n.a.	b.d.	b.d.	n.a.	n.a.	99.90
BID34-84	II	n.a.	b.d.	n.a.	n.a.	n.a.	1.127	45.37	n.a.	b.d.	n.a.	53.46	n.a.	b.d.	b.d.	n.a.	n.a.	99.96
BID34-84	II	n.a.	b.d.	n.a.	n.a.	n.a.	1.193	45.38	n.a.	b.d.	n.a.	53.23	n.a.	b.d.	b.d.	n.a.	n.a.	99.83
BID34-84	II	n.a.	b.d.	n.a.	n.a.	n.a.	1.085	45.33	n.a.	b.d.	n.a.	52.91	n.a.	b.d.	b.d.	n.a.	n.a.	99.35
BID34-84	II	n.a.	b.d.	n.a.	n.a.	n.a.	1.094	45.21	n.a.	0.016	n.a.	53.06	n.a.	b.d.	b.d.	n.a.	n.a.	99.38
BID34-84	II	n.a.	b.d.	n.a.	n.a.	n.a.	0.782	45.20	n.a.	0.025	n.a.	53.01	n.a.	b.d.	b.d.	n.a.	n.a.	99.03
BID34-84	II	n.a.	b.d.	n.a.	n.a.	n.a.	0.328	44.62	n.a.	0.078	n.a.	53.09	n.a.	b.d.	b.d.	n.a.	n.a.	98.15
BID34-84	II	n.a.	b.d.	n.a.	n.a.	n.a.	0.844	45.87	n.a.	b.d.	n.a.	53.30	n.a.	b.d.	b.d.	n.a.	n.a.	100.01
BID34-84	II	n.a.	0.092	n.a.	n.a.	n.a.	0.928	45.70	n.a.	b.d.	n.a.	53.06	n.a.	b.d.	b.d.	n.a.	n.a.	99.79
BID34-84	II	n.a.	0.226	n.a.	n.a.	n.a.	3.734	40.63	n.a.	0.080	n.a.	52.68	n.a.	0.124	0.103	n.a.	n.a.	97.57
BID34-84	II	n.a.	0.248	n.a.	n.a.	n.a.	3.497	40.63	n.a.	0.093	n.a.	52.27	n.a.	0.121	0.093	n.a.	n.a.	96.95
BID34-84	II	n.a.	0.206	n.a.	n.a.	n.a.	3.597	40.66	n.a.	0.082	n.a.	52.44	n.a.	0.142	0.101	n.a.	n.a.	97.23
BID34-84	II	n.a.	0.208	n.a.	n.a.	n.a.	3.497	40.72	n.a.	0.092	n.a.	52.44	n.a.	0.150	0.095	n.a.	n.a.	97.20
BID34-84	II	n.a.	0.201	n.a.	n.a.	n.a.	3.673	40.86	n.a.	0.084	n.a.	52.63	n.a.	0.140	0.082	n.a.	n.a.	97.67
BID34-84	II	n.a.	0.213	n.a.	n.a.	n.a.	3.566	40.88	n.a.	0.077	n.a.	52.42	n.a.	0.138	0.091	n.a.	n.a.	97.38
BID34-84	II	n.a.	0.210	n.a.	n.a.	n.a.	3.790	40.85	n.a.	0.074	n.a.	52.41	n.a.	0.138	0.089	n.a.	n.a.	97.56
BID34-84	II	n.a.	0.159	n.a.	n.a.	n.a.	3.830	40.83	n.a.	0.069	n.a.	52.51	n.a.	0.142	0.078	n.a.	n.a.	97.62
BID34-84	II	n.a.	0.159	n.a.	n.a.	n.a.	3.997	40.91	n.a.	0.067	n.a.	52.53	n.a.	0.148	0.075	n.a.	n.a.	97.89
BID34-84	II	n.a.	0.178	n.a.	n.a.	n.a.	3.830	41.01	n.a.	0.072	n.a.	52.57	n.a.	0.144	0.068	n.a.	n.a.	97.87
BID34-84	II	n.a.	0.184	n.a.	n.a.	n.a.	3.619	40.98	n.a.	0.068	n.a.	52.20	n.a.	0.152	0.073	n.a.	n.a.	97.28
BID34-84	II	n.a.	0.151	n.a.	n.a.	n.a.	3.588	41.21	n.a.	0.080	n.a.	52.56	n.a.	0.147	0.088	n.a.	n.a.	97.82
BID34-84	II	n.a.	0.168	n.a.	n.a.	n.a.	3.384	41.27	n.a.	0.071	n.a.	52.78	n.a.	0.170	0.078	n.a.	n.a.	97.93
BID34-84	II	n.a.	0.215	n.a.	n.a.	n.a.	3.080	41.27	n.a.	0.087	n.a.	52.34	n.a.	0.146	0.088	n.a.	n.a.	97.22
BID34-84	II	n.a.	0.169	n.a.	n.a.	n.a.	3.079	41.37	n.a.	0.083	n.a.	52.48	n.a.	0.165	0.095	n.a.	n.a.	97.44
BID34-84	II	n.a.	0.187	n.a.	n.a.	n.a.	2.967	41.36	n.a.	0.084	n.a.	52.40	n.a.	0.166	0.087	n.a.	n.a.	97.25
BID34-84	II	n.a.	0.188	n.a.	n.a.	n.a.	3.059	41.41	n.a.	0.065	n.a.	52.51	n.a.	0.151	0.093	n.a.	n.a.	97.48
BID34-84	II	n.a.	0.096	n.a.	n.a.	n.a.	3.750	41.18	n.a.	0.071	n.a.	52.81	n.a.	0.114	0.058	n.a.	n.a.	98.08
BID34-84	II	n.a.	0.096	n.a.	n.a.	n.a.	3.658	41.25	n.a.	0.059	n.a.	52.80	n.a.	0.118	0.076	n.a.	n.a.	98.05
BID34-84	II	n.a.	b.d.	n.a.	n.a.	n.a.	2.159	26.75	n.a.	0.022	n.a.	26.20	n.a.	0.040	b.d.	n.a.	n.a.	55.21
BID34-84	II	n.a.	b.d.	n.a.	n.a.	n.a.	4.377	41.75	n.a.	0.042	n.a.	52.77	n.a.	0.133	b.d.	n.a.	n.a.	99.08
BID34-84	II	n.a.	b.d.	n.a.	n.a.	n.a.	4.404	41.76	n.a.	0.032	n.a.	52.70	n.a.	0.137	b.d.	n.a.	n.a.	99.03
BID34-84	II	n.a.	b.d.	n.a.	n.a.	n.a.	4.573	41.53	n.a.	0.029	n.a.	52.45	n.a.	0.145	0.046	n.a.	n.a.	98.79
BID34-84	II	n.a.	0.067	n.a.	n.a.	n.a.	4.105	41.46	n.a.	0.043	n.a.	52.77	n.a.	0.145	0.038	n.a.	n.a.	98.63
BID34-84	II	n.a.	0.213	n.a.	n.a.	n.a.	3.709	41.07	n.a.	0.075	n.a.	52.52	n.a.	0.127	0.090	n.a.	n.a.	97.80
BID34-84	II	n.a.	0.213	n.a.	n.a.	n.a.	3.615	40.95	n.a.	0.066	n.a.	52.13	n.a.	0.131	0.091	n.a.	n.a.	97.19
BID34-84	II	n.a.	0.176	n.a.	n.a.	n.a.	3.797	41.10	n.a.	0.057	n.a.	52.35	n.a.	0.150	0.083	n.a.	n.a.	97.71
BID34-84	II	n.a.	0.190	n.a.	n.a.	n.a.	3.854	41.00	n.a.	0.074	n.a.	52.41	n.a.	0.132	0.080	n.a.	n.a.	97.74
BID34-84	II	n.a.	0.126	n.a.	n.a.	n.a.	4.061	40.96	n.a.	0.064	n.a.	52.59	n.a.	0.116	0.069	n.a.	n.a.	97.98
BID34-84	II	n.a.	0.191	n.a.	n.a.	n.a.	3.596	41.34	n.a.	0.064	n.a.	52.63	n.a.	0.144	0.076	n.a.	n.a.	98.05
BID34-84	II	n.a.	0.138	n.a.	n.a.	n.a.	3.780	41.42	n.a.	0.050	n.a.	52.39	n.a.	0.144	0.061	n.a.	n.a.	97.97
BID34-84	II	n.a.	0.160	n.a.	n.a.	n.a.	3.644	41.31	n.a.	0.048	n.a.	52.49	n.a.	0.151	0.077	n.a.	n.a.	97.89
BID34-84	II	n.a.	0.185	n.a.	n.a.	n.a.	3.499	41.48	n.a.	0.052	n.a.	52.56	n.a.	0.146	0.084	n.a.	n.a.	98.00
BID34-84	II	n.a.	0.162	n.a.	n.a.	n.a.	3.435	41.25	n.a.	0.071	n.a.	52.88	n.a.	0.154	0.096	n.a.	n.a.	98.05
BID34-84	II	n.a.	0.223	n.a.	n.a.	n.a.	2.977	41.54	n.a.	0.069	n.a.	52.62	n.a.	0.154	0.083	n.a.	n.a.	97.66
BID34-84	II	n.a.	0.146	n.a.	n.a.	n.a.	2.841	35.23	n.a.	0.041	n.a.	44.53	n.a.	0.083	0.034	n.a.	n.a.	82.90
BID34-84	II	n.a.	b.d.	n.a.	n.a.	n.a.	3.633	41.76	n.a.	0.029	n.a.	51.25	n.a.	0.149	b.d.	n.a.	n.a.	96.86
BID34-84	II	n.a.	0.153	n.a.	n.a.	n.a.	3.358	41.84	n.a.	0.035	n.a.	52.54	n.a.	0.148	0.071	n.a.	n.a.	98.14
BID34-84	II	n.a.	0.163	n.a.	n.a.	n.a.	3.136	41.90	n.a.	0.039	n.a.	52.40	n.a.	0.143	0.078	n.a.	n.a.	97.86
BID34-84	II	n.a.	0.163	n.a.	n.a.	n.a.	3.337	41.85	n.a.	0.033	n.a.	52.80	n.a.	0.141	0.062	n.a.	n.a.	98.39
BOD3-97	II	n.a.	b.d.	n.a.	n.a.	n.a.	0.569	45.99	n.a.	b.d.	n.a.	52.98	n.a.	b.d.	b.d.	n.a.	n.a.	99.54

Sample	Type	Ag	As	Au	Cd	Co	Cu	Fe	Hg	Ni	Pb	S	Sb	Se	Te	Ti	Zn	Total
d.l.		0.016	0.022	0.007	0.034	0.02	0.007	0.036	0.034	0.01	0.023	0.012	0.01	0.012	0.015	0.01	0.013	
BOD3-98	II	n.a.	b.d.	n.a.	n.a.	n.a.	0.527	46.04	n.a.	b.d.	n.a.	53.17	n.a.	b.d.	b.d.	n.a.	n.a.	99.74
BOD3-99	II	n.a.	b.d.	n.a.	n.a.	n.a.	0.441	46.25	n.a.	b.d.	n.a.	53.12	n.a.	b.d.	b.d.	n.a.	n.a.	99.83
BOD3-100	II	n.a.	b.d.	n.a.	n.a.	n.a.	1.868	44.66	n.a.	b.d.	n.a.	52.85	n.a.	b.d.	b.d.	n.a.	n.a.	99.38
BOD3-101	II	n.a.	b.d.	n.a.	n.a.	n.a.	0.090	46.21	n.a.	b.d.	n.a.	52.93	n.a.	b.d.	b.d.	n.a.	n.a.	99.25
BOD3-102	II	n.a.	0.033	n.a.	n.a.	n.a.	0.014	46.31	n.a.	b.d.	n.a.	53.29	n.a.	b.d.	b.d.	n.a.	n.a.	99.64
BOD3-103	II	n.a.	b.d.	n.a.	n.a.	n.a.	0.012	46.25	n.a.	b.d.	n.a.	53.17	n.a.	b.d.	b.d.	n.a.	n.a.	99.46
BOD3-104	II	n.a.	b.d.	n.a.	n.a.	n.a.	0.015	46.46	n.a.	b.d.	n.a.	53.10	n.a.	b.d.	b.d.	n.a.	n.a.	99.59
BOD3-105	II	n.a.	b.d.	n.a.	n.a.	n.a.	0.016	46.51	n.a.	b.d.	n.a.	53.35	n.a.	b.d.	b.d.	n.a.	n.a.	99.92
BOD3-106	II	n.a.	0.036	n.a.	n.a.	n.a.	0.012	46.29	n.a.	b.d.	n.a.	53.32	n.a.	b.d.	b.d.	n.a.	n.a.	99.67
BOD3-107	II	n.a.	b.d.	n.a.	n.a.	n.a.	0.024	46.55	n.a.	b.d.	n.a.	53.05	n.a.	b.d.	b.d.	n.a.	n.a.	99.64
BOD3-108	II	n.a.	b.d.	n.a.	n.a.	n.a.	0.044	46.50	n.a.	b.d.	n.a.	53.31	n.a.	b.d.	b.d.	n.a.	n.a.	99.85
BOD3-109	II	n.a.	b.d.	n.a.	n.a.	n.a.	0.643	45.89	n.a.	b.d.	n.a.	53.34	n.a.	b.d.	b.d.	n.a.	n.a.	99.89
BOD3-110	II	n.a.	b.d.	n.a.	n.a.	n.a.	6.001	40.62	n.a.	b.d.	n.a.	52.46	n.a.	b.d.	b.d.	n.a.	n.a.	99.10
BOD3-111	II	n.a.	b.d.	n.a.	n.a.	n.a.	0.168	46.09	n.a.	b.d.	n.a.	52.98	n.a.	b.d.	b.d.	n.a.	n.a.	99.28
BOD3-112	II	n.a.	b.d.	n.a.	n.a.	n.a.	0.061	46.36	n.a.	b.d.	n.a.	53.31	n.a.	b.d.	b.d.	n.a.	n.a.	99.74
BOD3-113	II	n.a.	b.d.	n.a.	n.a.	n.a.	4.769	41.88	n.a.	b.d.	n.a.	52.99	n.a.	b.d.	b.d.	n.a.	n.a.	99.66
BOD3-114	II	n.a.	0.035	n.a.	n.a.	n.a.	0.163	46.50	n.a.	b.d.	n.a.	53.03	n.a.	b.d.	b.d.	n.a.	n.a.	99.74
BOD3-115	II	n.a.	0.039	n.a.	n.a.	n.a.	0.123	45.80	n.a.	b.d.	n.a.	53.28	n.a.	b.d.	b.d.	n.a.	n.a.	99.25
BOD3-116	II	n.a.	b.d.	n.a.	n.a.	n.a.	1.374	45.36	n.a.	b.d.	n.a.	52.86	n.a.	b.d.	b.d.	n.a.	n.a.	99.61
BOD3-117	II	n.a.	b.d.	n.a.	n.a.	n.a.	0.494	45.93	n.a.	b.d.	n.a.	52.96	n.a.	b.d.	b.d.	n.a.	n.a.	99.39
BOD3-118	II	n.a.	0.123	n.a.	n.a.	n.a.	0.426	44.69	n.a.	b.d.	n.a.	52.96	n.a.	b.d.	b.d.	n.a.	n.a.	98.20
BOD3-119	II	n.a.	b.d.	n.a.	n.a.	n.a.	0.065	46.38	n.a.	b.d.	n.a.	52.90	n.a.	b.d.	b.d.	n.a.	n.a.	99.35
BOD3-120	II	n.a.	0.124	n.a.	n.a.	n.a.	0.288	45.47	n.a.	b.d.	n.a.	52.90	n.a.	b.d.	b.d.	n.a.	n.a.	98.78
BOD3-121	II	n.a.	b.d.	n.a.	n.a.	n.a.	0.543	46.10	n.a.	b.d.	n.a.	53.23	n.a.	b.d.	b.d.	n.a.	n.a.	99.91
BOD3-122	II	n.a.	b.d.	n.a.	n.a.	n.a.	0.481	45.68	n.a.	b.d.	n.a.	52.62	n.a.	b.d.	b.d.	n.a.	n.a.	98.79
BOD3-123	II	n.a.	b.d.	n.a.	n.a.	n.a.	0.560	45.82	n.a.	b.d.	n.a.	52.97	n.a.	b.d.	b.d.	n.a.	n.a.	99.35
BOD3-124	II	n.a.	b.d.	n.a.	n.a.	n.a.	1.266	45.16	n.a.	b.d.	n.a.	53.18	n.a.	b.d.	b.d.	n.a.	n.a.	99.61
BOD3-125	II	n.a.	b.d.	n.a.	n.a.	n.a.	0.026	46.67	n.a.	b.d.	n.a.	53.22	n.a.	b.d.	b.d.	n.a.	n.a.	99.94
BOD3-126	II	n.a.	b.d.	n.a.	n.a.	n.a.	0.015	46.44	n.a.	b.d.	n.a.	53.05	n.a.	b.d.	b.d.	n.a.	n.a.	99.50
BOD3-127	II	n.a.	b.d.	n.a.	n.a.	n.a.	0.021	46.57	n.a.	b.d.	n.a.	52.99	n.a.	b.d.	b.d.	n.a.	n.a.	99.59
BOD3-128	II	n.a.	b.d.	n.a.	n.a.	n.a.	b.d.	46.69	n.a.	b.d.	n.a.	53.19	n.a.	b.d.	b.d.	n.a.	n.a.	99.89
BOD3-129	II	n.a.	b.d.	n.a.	n.a.	n.a.	b.d.	46.63	n.a.	b.d.	n.a.	53.30	n.a.	b.d.	b.d.	n.a.	n.a.	99.94
BOD3-130	II	n.a.	b.d.	n.a.	n.a.	n.a.	b.d.	46.46	n.a.	b.d.	n.a.	53.09	n.a.	b.d.	b.d.	n.a.	n.a.	99.57
BOD3-131	II	n.a.	b.d.	n.a.	n.a.	n.a.	0.013	46.42	n.a.	b.d.	n.a.	53.31	n.a.	b.d.	b.d.	n.a.	n.a.	99.74
BOD3-132	II	n.a.	b.d.	n.a.	n.a.	n.a.	b.d.	46.38	n.a.	b.d.	n.a.	53.10	n.a.	b.d.	b.d.	n.a.	n.a.	99.50
BOD3-133	II	n.a.	b.d.	n.a.	n.a.	n.a.	0.014	46.60	n.a.	b.d.	n.a.	53.12	n.a.	b.d.	b.d.	n.a.	n.a.	99.73
BOD3-134	II	n.a.	b.d.	n.a.	n.a.	n.a.	0.448	46.05	n.a.	b.d.	n.a.	52.94	n.a.	b.d.	b.d.	n.a.	n.a.	99.43
BOD3-135	II	n.a.	b.d.	n.a.	n.a.	n.a.	0.033	46.53	n.a.	b.d.	n.a.	52.91	n.a.	b.d.	b.d.	n.a.	n.a.	99.48
BOD3-136	II	n.a.	b.d.	n.a.	n.a.	n.a.	0.034	46.47	n.a.	b.d.	n.a.	52.94	n.a.	b.d.	b.d.	n.a.	n.a.	99.45
BOD3-137	II	n.a.	b.d.	n.a.	n.a.	n.a.	0.610	45.86	n.a.	b.d.	n.a.	53.05	n.a.	b.d.	b.d.	n.a.	n.a.	99.53
BOD3-138	II	n.a.	b.d.	n.a.	n.a.	n.a.	0.055	46.47	n.a.	b.d.	n.a.	53.03	n.a.	b.d.	b.d.	n.a.	n.a.	99.56
BOD3-139	II	n.a.	b.d.	n.a.	n.a.	n.a.	0.064	46.26	n.a.	b.d.	n.a.	53.30	n.a.	b.d.	b.d.	n.a.	n.a.	99.62
BOD3-140	II	n.a.	b.d.	n.a.	n.a.	n.a.	0.873	45.59	n.a.	b.d.	n.a.	53.09	n.a.	b.d.	b.d.	n.a.	n.a.	99.55
BOD3-141	II	n.a.	b.d.	n.a.	n.a.	n.a.	2.021	44.60	n.a.	b.d.	n.a.	53.17	n.a.	b.d.	b.d.	n.a.	n.a.	99.79
BOD3-142	II	n.a.	0.127	n.a.	n.a.	n.a.	0.791	44.68	n.a.	b.d.	n.a.	53.01	n.a.	b.d.	b.d.	n.a.	n.a.	98.61
BOD3-143	II	n.a.	b.d.	n.a.	n.a.	n.a.	0.022	46.48	n.a.	b.d.	n.a.	53.27	n.a.	b.d.	b.d.	n.a.	n.a.	99.78
BOD3-144	II	n.a.	0.193	n.a.	n.a.	n.a.	0.108	45.66	n.a.	b.d.	n.a.	53.49	n.a.	b.d.	b.d.	n.a.	n.a.	99.45
BOD3-145	II	n.a.	b.d.	n.a.	n.a.	n.a.	1.181	45.36	n.a.	b.d.	n.a.	52.94	n.a.	b.d.	b.d.	n.a.	n.a.	99.48
BOD3-146	II	n.a.	0.111	n.a.	n.a.	n.a.	0.433	45.11	n.a.	b.d.	n.a.	53.42	n.a.	b.d.	b.d.	n.a.	n.a.	99.07
BID32-16	II	n.a.	b.d.	n.a.	n.a.	n.a.	0.507	46.22	n.a.	b.d.	n.a.	53.51	n.a.	b.d.	b.d.	n.a.	n.a.	100.26
BID32-16	II	n.a.	b.d.	n.a.	n.a.	n.a.	0.437	46.30	n.a.	b.d.	n.a.	52.94	n.a.	b.d.	b.d.	n.a.	n.a.	99.70
BID32-16	II	n.a.	b.d.	n.a.	n.a.	n.a.	0.404	46.38	n.a.	b.d.	n.a.	53.46	n.a.	b.d.	b.d.	n.a.	n.a.	100.26
BID32-16	II	n.a.	b.d.	n.a.	n.a.	n.a.	0.509	46.16	n.a.	b.d.	n.a.	53.31	n.a.	b.d.	b.d.	n.a.	n.a.	99.99
BID32-16	II	n.a.	b.d.	n.a.	n.a.	n.a.	0.705	46.03	n.a.	b.d.	n.a.	53.16	n.a.	b.d.	b.d.	n.a.	n.a.	99.90
BID32-16	II	n.a.	b.d.	n.a.	n.a.	n.a.	0.819	45.87	n.a.	b.d.	n.a.	52.93	n.a.	b.d.	b.d.	n.a.	n.a.	99.62
BID32-16	II	n.a.	b.d.	n.a.	n.a.	n.a.	0.267	46.44	n.a.	b.d.	n.a.	53.24	n.a.	b.d.	b.d.	n.a.	n.a.	99.95
BID32-16	II	n.a.	b.d.	n.a.	n.a.	n.a.	0.266	46.43	n.a.	b.d.	n.a.	53.11	n.a.	b.d.	b.d.	n.a.	n.a.	99.82
BID32-16	II	n.a.	b.d.	n.a.	n.a.	n.a.	0.727	45.96	n.a.	b.d.	n.a.	53.16	n.a.	b.d.	b.d.	n.a.	n.a.	99.84
BID32-16	II	n.a.	b.d.	n.a.	n.a.	n.a.	1.474	45.32	n.a.	b.d.	n.a.	53.19	n.a.	b.d.	b.d.	n.a.	n.a.	100.02
BID32-16	II	n.a.	b.d.	n.a.	n.a.	n.a.	1.849	44.90	n.a.	b.d.	n.a.	53.16	n.a.	b.d.	b.d.	n.a.	n.a.	99.91
BID32-16	II	n.a.	b.d.	n.a.	n.a.	n.a.	1.694	45.13	n.a.	b.d.	n.a.	53.06	n.a.	b.d.	b.d.	n.a.	n.a.	99.89
BID32-16	II	n.a.	b.d.	n.a.	n.a.	n.a.	1.638	45.13	n.a.	b.d.	n.a.	53.30	n.a.	b.d.	b.d.	n.a.	n.a.	100.07
BID32-16	II	n.a.	b.d.	n.a.	n.a.	n.a.	1.423	45.28	n.a.	b.d.	n.a.	53.07	n.a.	b.d.	b.d.	n.a.	n.a.	99.78
BID32-16	II	n.a.	b.d.	n.a.	n.a.	n.a.	1.150	45.63	n.a.	b.d.	n.a.	53.12	n.a.	b.d.	b.d.	n.a.	n.a.	99.92
BID32-16	II	n.a.	b.d.	n.a.	n.a.	n.a.	0.584	46.13	n.a.	b.d.	n.a.	53.05	n.a.	b.d.	b.d.	n.a.	n.a.	99.78
BID32-16	II	n.a.	b.d.	n.a.	n.a.	n.a.	0.080	46.55	n.a.	b.d.	n.a.	53.37	n.a.	0.049	b.d.	n.a.	n.a.	100.06
BID32-16	II	n.a.	0.184	n.a.	n.a.	n.a.	0.143	46.13	n.a.	b.d.	n.a.	53.26	n.a.	b.d.	b.d.	n.a.	n.a.	99.72
BID32-16	II	n.a.	0.323	n.a.	n.a.	n.a.	1.070	44.64	n.a.	b.d.	n.a.	52.57	n.a.	b.d.	b.d.	n.a.	n.a.	98.64
BID32-16	II	n.a.	0.531	n.a.	n.a.	n.a.	0.556	44.20	n.a.	b.d.	n.a.	53.16	n.a.	0.039	0.050	n.a.	n.a.	98.54
BID32-16	II	n.a.	b.d.	n.a.	n.a.	n.a.	0.610	45.78	n.a.	b.d.	n.a.	52.87	n.a.	b.d.	b.d.	n.a.	n.a.	99.27
BID32-16	II	n.a.	b.d.	n.a.	n.a.	n.a.	1.105	45.58	n.a.	b.d.	n.a.	52.75	n.a.	b.d.	b.d.	n.a.	n.a.	99.45
BID32-16	II	n.a.	b.d.	n.a.	n.a.	n.a.	0.518	46.17	n.a.	b.d.	n.a.	52.98	n.a.	b.d.	b.d.	n.a.	n.a.	99.68
BID32-16	II	n.a.	b.d.	n.a.	n.a.	n.a.	0.612	46.13	n.a.	b.d.	n.a.	53.06	n.a.	b.d.	b.d.	n.a.	n.a.	99.81
BID32-16	II	n.a.	b.d.	n.a.	n.a.	n.a.	0.579	46.15	n.a.	b.d.	n.a.	53.29	n.a.	b.d.	b.d.	n.a.	n.a.	100.02
BID32-16	II	n.a.	b.d.	n.a.	n.a.	n.a.	0.565	46.13	n.a.	b.d.	n.a.	53.14	n.a.	b.d.	b.d.	n.a.	n.a.	99.84
BID32-16	II	n.a.	b.d.	n.a.	n.a.	n.a.	0.583	46.16	n.a.	b.d.	n.a.	53.24	n.a.	b.d.	b.d.	n.a.	n.a.	100.03
BID32-16	II	n.a.	b.d.	n.a.	n.a.	n.a.	0.431	46.23	n.a.	b.d.	n.a.	52.90	n.a.	b.d.	b.d.	n.a.	n.a.	99.57
BID32-16	II	n.a.	b.d.	n.a.	n.a.	n.a.	0.585	46.14	n.a.	b.d.	n.a.	52.88	n.a.	b.d.	b.d.	n.a.	n.a.	99.60
BID32-16	II	n.a.	b.d.	n.a.	n.a.	n.a.	0.450	46.31	n.a.	b.d.	n.a.	53.02	n.a.	b.d.	b.d.	n.a.	n.a.	99.79
BID32-16	II	n.a.	b.d.	n.a.	n.a.	n.a.	0.773	45.98	n.a.	b.d.	n.a.	53.17	n.a.	b.d.	b.d.	n.a.	n.a.	99.93
BID32-16	II	n.a.	b.d.	n.a.	n.a.	n.a.	1.161	45.58	n.a.	b.d.	n.a.	53.09	n.a.	b.d.	b.d.	n.a.	n.a.	99.84
BID32-16	II	n.a.	b.d.	n.a.	n.a.	n.a.	1.742	44.93	n.a.	b.d.	n.a.	52.88	n.a.	b.d.	b.d.	n.a.	n.a.	99.57
BID32-16	II	n.a.	b.d.	n.a.	n.a.	n.a.	1.599	45.17	n.a.	b.d.	n.a.	53.05	n.a.	b.d.	b.d.	n.a.	n.a.	99.83
BID32-16	II	n.a.	b.d.	n.a.	n.a.	n.a.	1.401	45.33	n.a.	b.d.	n.a.	52.48	n.a.	b.d.	b.d.	n.a.	n.a.	99.24
BID32-16	II	n.a.	b.d.	n.a.	n.a.	n.a.	1.082	45.73	n.a.	b.d.	n.a.	52.92	n.a.	b.d.	b.d.	n.a.	n.a.	99.76
BID32-16	II	n.a.	b.d.	n.a.	n.a.	n.a.	0.899	45.85	n.a.	b.d.	n.a.	53.25	n.a.	b.d.	b.d.	n.a.	n.a.	100.00
BID32-16	II	n.a.	b.d.	n.a.	n.a.	n.a.	0.130	46.64	n.a.	b.d.	n.a.	52.87	n.a.	0.039	b.d.	n.a.	n.a.	99.68
BID32-16	II	n.a.	0.192	n.a.	n.a.	n.a.	0.396	45.81	n.a.	b.d.	n.a.	53.06	n.a.	b.d.	b.d.	n.a.	n.a.	99.46
BID32-16	II	n.a.	0.603	n.a.	n.a.	n.a.	0.138	44.86	n.a.	b.d.	n.a.	52.94	n.a.	b.d.	b.d.	n.a.	n.a.	98.58

B. Enargite

Sample d.l.	Spot	As 0.230	Co 0.021	Cu 0.009	Fe 0.043	Ni 0.010	S 0.028	Sb 0.016	Se 0.014	Te 0.020	Zn 0.015	Total
BOD1-32	1	17.854	b.d.	47.278	0.651	b.d.	33.122	1.387	0.033	b.d.	b.d.	100.3
BOD1-32	2	18.096	b.d.	47.567	0.748	b.d.	32.858	1.390	0.029	b.d.	b.d.	100.7
BOD1-32	3	18.094	b.d.	48.603	0.666	b.d.	32.963	0.287	0.020	0.021	0.046	100.7
BOD1-32	4	18.518	b.d.	48.589	0.547	b.d.	32.894	0.375	0.036	0.031	b.d.	101.0
BOD1-32	5	18.959	b.d.	48.263	0.421	b.d.	32.832	0.053	0.022	0.287	b.d.	100.8
BOD1-32	6	15.264	b.d.	46.798	0.316	0.005	32.130	5.177	0.033	b.d.	0.018	99.7
BOD1-32	7	18.970	b.d.	49.033	0.150	b.d.	32.987	0.283	0.025	b.d.	b.d.	101.5
BOD1-32	8	18.671	b.d.	48.785	0.278	b.d.	33.050	0.495	0.034	b.d.	b.d.	101.3
BOD1-32	9	18.496	b.d.	48.329	0.493	b.d.	33.040	0.635	0.038	0.200	b.d.	101.2
BOD1-32	10	18.828	b.d.	48.663	0.264	b.d.	32.867	0.268	0.025	b.d.	b.d.	100.9
BOD1-32	11	19.151	b.d.	48.848	0.130	b.d.	33.040	0.288	0.021	0.159	b.d.	101.6
BOD3-97A	3	17.695	b.d.	47.496	0.034	n.a.	31.602	0.278	0.046	n.a.	0.089	100.5
BOD3-97A	4	18.137	b.d.	48.823	0.034	n.a.	32.229	1.329	0.026	n.a.	0.046	100.7
BOD1-32	1	18.764	b.d.	48.734	0.037	n.a.	32.955	0.157	0.030	n.a.	b.d.	100.7
BOD3-96	7	18.303	b.d.	48.422	0.680	n.a.	32.543	0.445	0.032	n.a.	b.d.	100.5
BOD1-32	5	18.779	b.d.	48.911	0.126	n.a.	32.836	0.108	0.049	n.a.	b.d.	100.8

Appendix D Laser-Ablation Inductively Coupled Mass Spectrometry

Tables of pyrite and enargite

Appendix D Composition of pyrite (A) and enargite (B) from Bowone (BOD) and Binebase (BID) based on LA-ICPMS analyses, reported in ppm.

A. Pyrite

Analysis No.	Pyrite Type	Ag (ppm)	As (ppm)	Au (ppm)	Bi (ppm)	Co (ppm)	Cu (wt%)	Fe (wt%)	Ni (ppm)	Pb (ppm)	Sb (ppm)	S (wt%)	Se (ppm)	Te (ppm)	Zn (ppm)
1	I	0.611	61.87	0.04	0.57	15.60	0.027	52.79	2.76	3.20	0.30	53.37	1.7	0.66	< 2.17
2	I	11.558	33.31	2.53	4.64	123.31	1.509	61.26	14.25	79.73	4.17	53.37	118.6	33.35	4.7
3	I	9.139	75.94	1.14	13.34	226.07	0.751	53.11	18.17	87.58	4.28	51.73	111.9	35.47	22.9
4	I	0.512	467.31	< 0.01	0.10	4.64	0.037	52.59	0.68	9.49	1.08	53.63	23.5	2.19	< 2.12
5	I	2223.039	245.33	5.54	200.52	33.91	0.481	51.94	64.85	223.36	23.24	53.45	11.4	5.93	55.9
6	I	396.131	42.34	2.08	96.94	2.34	0.350	61.92	4.95	94.76	5.83	53.45	3.3	1.26	8.6
7	I	145.847	34.08	1.73	18.30	15.85	0.218	62.21	92.28	30.05	3.71	53.45	8.2	< 0.25	2.8
8	I	88.178	264.31	1.43	47.86	6.03	0.298	71.74	20.43	72.31	8.38	53.45	< 1.19	0.78	< 1.12
9	I	28.865	43.94	2.05	2.75	0.06	0.196	69.17	0.45	95.94	1.98	53.45	3.2	< 0.29	< 1.11
10	I	29.619	83.01	0.88	29.38	62.55	0.225	54.71	33.74	62.03	6.86	53.45	1.2	3.69	12.2
11	I	0.296	2.29	0.15	0.98	404.31	0.747	56.66	182.90	0.47	0.36	52.44	10.2	3.82	0.8
12	I	1.146	15.65	0.85	5.81	54.82	0.462	62.48	40.13	10.72	11.04	52.71	38.5	11.41	0.6
13	I	4.575	146.14	1.26	2.93	231.09	0.494	58.36	68.43	199.77	4.05	53.40	9.0	8.54	6.1
14	I	5.837	6.96	0.17	0.97	206.10	0.636	52.31	49.93	59.57	0.58	54.62	49.0	2.15	1.1
15	I	102.597	5.08	0.77	3.90	171.40	0.232	68.99	35.90	8.47	0.78	53.68	7.1	8.68	1.0
16	II	71.051	636.75	1.55	16.15	28.80	0.124	44.53	39.43	7205.35	10.31	52.82	5.6	8.97	1936.3
17	II	166.584	785.05	2.57	16.09	24.05	0.229	55.87	67.42	1588.32	23.66	52.71	10.5	11.05	82.9
18	II	19.048	86.70	3.05	28.38	473.84	0.471	58.03	112.84	185.31	11.20	53.40	55.8	53.29	6.8
19	II	24.033	476.29	6.31	23.14	101.14	0.694	54.62	10.36	639.60	10.26	53.28	102.1	115.55	128.6
20	II	1.354	4.84	0.78	1.41	< 0.001	0.158	59.63	< 0.01	2.97	1.48	52.14	137.0	147.39	0.8
21	II	8.249	325.04	3.45	10.30	196.92	0.370	55.47	21.67	168.09	3.86	52.59	39.8	43.83	374.1
22	II	7.982	1335.60	3.39	10.73	87.48	0.498	54.63	5.73	482.99	3.32	53.75	82.1	39.52	65.0
23	II	3.660	39.89	1.27	8.94	2.31	1.074	46.95	0.36	581.95	3.60	52.71	14.4	32.01	< 0.45
24	II	0.532	0.87	0.18	1.28	1.31	0.119	45.10	0.14	0.71	0.09	53.84	1.2	13.22	0.6
25	II	0.162	15.45	0.19	0.74	6391.15	0.996	30.95	388.40	0.05	0.43	52.25	83.0	51.13	< 0.99
26	II	0.894	1636.61	11.88	4.04	14875.36	2.655	40.14	455.35	1.82	2.43	48.28	505.8	916.80	0.8
27	II	0.924	1594.40	9.41	5.73	21417.67	3.211	39.55	800.22	0.13	3.31	48.41	640.1	1062.10	0.8
28	II	1.594	338.44	2.38	5.08	1245.61	0.965	48.97	93.88	3.47	1.99	54.04	105.5	197.17	1.2
29	II	5.462	250.67	2.71	14.66	165.86	0.559	59.56	20.39	1242.96	5.27	54.81	65.1	104.22	2.3
30	II	0.915	4.76	0.44	2.12	30.45	0.134	51.72	0.89	41.95	0.19	54.81	25.9	22.11	0.5
31	II	6.451	10.79	2.44	14.67	62.57	1.562	52.01	13.97	6.31	1.40	53.63	18.8	29.34	< 0.70
32	II	5.885	9.70	3.15	14.47	73.30	1.997	52.02	13.56	7.53	2.29	53.63	14.1	26.68	3.9
33	II	1.123	143.72	1.08	5.70	520.41	1.236	37.53	11.21	0.54	2.20	53.84	6.4	96.55	0.6
34	II	3.759	252.88	1.72	9.51	130.05	0.689	49.04	16.88	38.36	3.83	54.19	24.2	81.65	1.3
35	II	2.151	188.72	2.88	7.17	9127.39	3.291	35.30	315.16	2.30	2.14	48.44	563.2	287.87	< 0.43
36	II	3.705	1075.55	10.18	10.30	21068.76	3.156	40.69	733.54	3.21	3.73	48.57	592.0	1226.20	0.6
37	II	1.512	1120.14	13.58	4.98	13372.47	3.220	37.03	372.86	0.74	2.83	48.57	604.8	1277.68	<0.43
38	II	1.783	759.75	7.81	5.47	15031.91	4.404	35.66	491.57	1.10	3.47	48.57	585.4	935.36	<1.25
39	II	0.922	18.14	1.12	4.48	10226.26	3.818	40.22	414.26	0.35	3.29	49.13	618.9	137.93	<0.97
40	II	0.334	913.23	4.53	3.33	14634.74	1.309	41.36	599.53	0.55	1.91	52.80	261.5	548.56	<0.97
41	II	0.058	7.59	<0.009	0.06	113.19	0.002	76.08	41.12	129.63	4.69	52.59	2.2	<0.22	87.1
42	II	<0.007	23.57	0.01	0.01	3.33	0.021	54.29	4.59	0.18	0.05	52.14	2.3	<0.11	1.2
43	II	0.107	79.11	0.01	0.00	1.47	0.056	53.16	1.45	3.38	0.12	52.37	0.7	0.15	0.7
44	II	6.732	423.62	2.70	10.02	68.99	0.540	41.66	47.79	242.98	42.10	52.37	16.8	5.33	9.0
45	II	0.034	0.83	0.01	0.01	28.82	0.000	49.54	16.75	9.21	0.27	52.37	<0.40	<0.18	1.8
46	II	2.577	46.84	2.48	4.14	218.30	0.413	47.20	42.10	101.31	6.08	52.26	13.2	6.28	19.5
47	II	2.070	91.57	0.71	2.83	54.38	0.307	47.16	20.26	104.78	4.86	52.14	10.8	3.42	10.2
48	II	3.094	386.86	0.91	1.95	58.91	0.172	41.43	22.10	87.02	3.06	52.06	3.5	2.26	76.8
49	II	275.685	397.88	2.85	23.94	0.01	0.612	69.37	0.08	1020.37	169.60	52.44	2.3	11.47	13.3
50	II	11.852	181.58	5.69	12.11	249.06	0.350	37.22	64.63	623.38	24.66	51.98	12.0	8.85	28.1
51	II	0.059	2.79	0.27	0.19	13.70	0.425	44.81	15.56	0.47	0.12	52.31	15.5	1.52	0.9
52	II	13.313	155.78	3.21	14.60	292.42	0.255	59.36	85.68	802.18	23.80	52.69	33.7	18.23	25.2
53	II	1.484	238.57	0.15	4.15	573.04	0.564	55.26	255.52	237.52	2.46	52.59	3.2	3.67	2.7
54	II	10.873	200.27	2.02	6.04	332.77	0.595	40.91	126.15	189.73	8.49	53.28	15.7	14.05	52.8
55	II	3.609	40.39	0.91	2.34	302.60	0.291	46.16	118.19	52.71	4.42	52.59	22.6	9.64	13.7
56	II	22.749	1522.73	6.16	18.59	493.62	0.155	53.64	116.13	2866.54	37.63	53.75	12.8	30.69	86.4
57	II	2.214	57.85	0.70	0.82	81.10	0.324	37.97	26.46	32.13	2.01	52.59	72.4	53.51	7.6
58	II	204.588	38.75	3.02	12.33	120.74	2.192	49.57	69.79	1292.49	8.80	51.21	17.9	19.16	2.8
59	II	141.008	13.71	1.35	6.76	389.76	1.548	53.17	286.34	2490.22	3.94	51.44	40.2	11.02	12.4
60	II	13.287	8.59	3.06	4.72	<0.003	1.236	52.95	<0.025	2.66	5.98	54.74	41.9	3.56	0.8
61	II	72.343	50.79	1.89	20.82	<0.008	0.799	65.71	<0.057	94.11	26.49	54.74	39.1	31.30	3.8
62	II	1273.184	12.30	1.63	5.34	<0.008	2.094	40.06	0.31	117.51	2.77	55.16	94.8	424.11	<0.47
63	II	523.393	438.67	2.78	37.75	0.59	2.788	55.33	0.15	1932.19	26.17	52.46	23.7	13.59	510.8
64	II	844.087	35.17	4.34	43.19	<0.029	2.039	51.22	<0.21	939.98	13.68	51.84	122.2	688.99	<1.44
65	II	180.178	6.70	1.82	5.98	<0.035	1.328	39.45	0.13	9.02	4.13	51.73	144.2	1430.90	<2.03

B. Enargite

Sample	Ag (ppm)	As (wt%)	Au (ppm)	Cu (wt%)	Fe (ppm)	S (wt%)	Sb (ppm)	Se (ppm)	Te (ppm)
En-1	114.9	15.5	0.5	24.9	277.7	32.7	4987.7	2.6	189.2
En-2	214.5	11.8	0.7	38.5	548.6	32.7	4876.6	3.3	177.8
En-3	59.1	15	0.4	45.8	26.7	32.7	6525.8	1.8	188.9
En-4	108.5	13.4	0.6	37.2	82	32.7	9543.1	2.3	95.1
En-5	113	14.2	0.8	32.1	316.8	32.7	4574.5	3.2	211.3
En-6	48.9	13.9	0.1	33.2	117.8	32.7	8167.5	2.7	135.9
En-7	31.1	12.9	0.7	28.4	649.6	32.7	9220.2	3.4	108.5
En-8	171.7	12.5	0.7	28.8	1304.1	32.7	4273.7	5.5	82.6
En-9	52.7	12.3	0.3	34.9	786.5	32.7	5527.7	3.4	79.5

Appendix E Translated transect values for paired-transects of sector zoned pyrite crystals

Appendix E Translated and normalized Electron Microprobe values for 3 pairs of transects from samples BOD3-97, BID32-16, BID34-84. Each raw value from the 6 transects of sector zoned crystals has been translated and normalized to % of the total distance. Corresponding trace element concentrations are interpolated from the bracketing values enabling accurate matching of trace element concentrations between sectors (see van Hinsberg and Schumacher, 2007). Zeros indicate values were below the dection limit, blanks occur when there is no corresponding point in a transect.

BID32-16

	Dark (wt %)							Light (wt %)						
Distance	Cu	As	Ni	Se	Te	Fe	S	Cu	As	Ni	Se	Te	Fe	S
0	0.61	0	0	0.008	0	45.78	52.87	0.51	0.01	0	0	0	46.22	53.51
5	0.88	0.003	0	0.007	0.002	45.81	52.84	0.44	0.01	0	0.01	0	46.29	52.97
10	0.59	0	0	0.004	0.003	46.14	53.04	0.41	0.01	0	0	0	46.38	53.41
15	0.58	0.006	0	0.006	0	46.14	53.27	0.49	0	0	0	0	46.19	53.33
20	0.57	0.01	0.003	0.01	0.002	46.15	53.2	0.67	0	0	0	0	46.06	53.19
25	0.48	0.009	0.002	0.004	0.005	46.21	53	0.79	0	0	0	0	45.91	52.99
30	0.51	0.003	0.001	0.001	0.003	46.18	52.89	0.43	0	0	0	0	46.27	53.15
35	0.55	0.004	0.002	0.001	0	46.18	52.91	0.27	0	0	0.01	0	46.43	53.15
40	0.51	0.011	0	0	0	46.25	53.05	0.54	0	0	0	0	46.15	53.14
45	0.82	0	0	0.002	0	45.93	53.16	1.14	0.01	0	0.01	0	45.61	53.18
50	1.18	0	0	0.009	0	45.56	53.08	1.66	0.01	0	0.01	0	45.11	53.18
55	1.7	0.011	0	0.015	0	44.97	52.89	1.78	0	0	0.01	0	45	53.11
60	1.62	0.002	0	0.008	0.007	45.13	53.02	1.67	0	0	0.01	0	45.13	53.15
65	1.46	0.009	0.004	0.008	0.002	45.28	52.64	1.56	0	0	0	0	45.18	53.22
70	1.2	0.005	0.006	0.009	0.003	45.58	52.76	1.34	0.01	0	0	0	45.39	53.09
75	0.99	0	0.003	0.011	0.002	45.79	53.09	1.01	0.01	0	0.01	0	45.75	53.1
80	0.58	0	0	0.023	0	46.18	53.09	0.48	0	0	0.02	0	46.21	53.12
85	0.21	0.06	0.002	0.027	0	46.38	52.93	0.09	0.03	0	0.04	0.01	46.48	53.36
90	0.37	0.235	0.005	0.003	0.001	45.71	53.04	0.24	0.2	0	0	0.01	45.98	53.19
95	0.25	0.419	0.004	0.017	0.004	45.29	52.99	1.04	0.33	0	0.03	0	44.62	52.6

BOD3-97

	Dark (wt %)							Light (wt %)						
Distance	Cu	As	Ni	Se	Te	Fe	S	Cu	As	Ni	Se	Te	Fe	S
0	0.48	0	0.002	0.002	0.001	45.68	52.62	0.57	0	0	0	0	45.99	52.98
5	0.64	0	0.003	0.001	0.006	45.74	52.99							
10	0.98	0.004	0.001	0.005	0.003	45.52	53.19	1.01	0	0	0	0	45.61	53.02
15	0.02	0.01	0.003	0	0.003	46.59	53.16	0.8	0.01	0	0	0	45.59	52.9
20	0.02	0.002	0	0	0	46.5	53.02	0.03	0.03	0	0	0	46.29	53.21
25	0.01	0.002	0	0	0	46.64	53.11	0.01	0.02	0	0	0	46.25	53.17
30	0.01	0	0.002	0	0	46.64	53.27	0.02	0.01	0	0	0	46.47	53.15
35	0.01	0.004	0.001	0	0.007	46.48	53.12	0.01	0.03	0	0.01	0.01	46.42	53.34
40	0.01	0	0	0	0	46.42	53.3	0.02	0.02	0	0	0	46.44	53.16
45	0.01	0.01	0.002	0	0	46.41	53.1	0.04	0	0	0	0	46.51	53.26
50	0.12	0.002	0.003	0	0	46.46	53.07	0.64	0.01	0	0	0	45.89	53.34
55	0.29	0	0	0.001	0	46.23	52.93	4.83	0.02	0	0	0	41.71	52.57
60	0.03	0.001	0	0.001	0	46.5	52.93							
65	0.47	0.007	0.001	0	0	46.01	53.02	2.89	0.01	0	0	0.01	43.67	53.12
70	0.09	0.014	0	0	0	46.43	53.03	1.08	0.03	0	0.01	0	45.58	53.02
75	0.19	0.003	0	0	0	46.16	53.26	0.12	0.04	0	0	0	45.8	53.28
80	1.36	0	0	0.003	0	45.17	53.12	1.2	0	0	0	0.01	45.47	52.88
85	1.18	0.087	0	0.002	0	44.65	53.06	0.47	0.05	0	0	0	45.43	52.96
90	0.03	0.009	0	0	0	46.44	53.28	0.21	0.05	0	0	0	45.7	52.93
95	0.67	0.092	0.001	0.002	0	45.5	53.2	0.24	0.1	0	0	0	45.65	52.9
100	0.43	0.111	0	0	0	45.11	53.42	0.54	0.02	0	0.01	0	46.1	53.23

BID34-84

	Dark (wt %)							Light (wt %)						
Distance	Cu	As	Ni	Se	Te	Fe	S	Cu	As	Ni	Se	Te	Fe	S
0	2.48	0.171	0.086	0.16	0.109	41.67	52.74	3.3	0	0.05	0.17	0	42.23	52.86
1	2.12	0.134	0.068	0.127	0.09	42.2	52.49	3.12	0	0.05	0.16	0.01	42.51	52.89
2	2.05	0.106	0.045	0.084	0.081	43.26	52.96	2.27	0.01	0.02	0.09	0.01	43.97	53.04
3	3.62	0.195	0.094	0.143	0.143	40.38	52.61	4.29	0.01	0.06	0.17	0.01	41.14	52.87
5	3.57	0.174	0.086	0.158	0.141	40.08	52.19	4.53	0	0.05	0.17	0.01	41.15	52.79
6	3.38	0.183	0.089	0.159	0.123	40.76	52.74	4.41	0	0.05	0.16	0.01	41.17	52.78
7	3.37	0.169	0.08	0.151	0.112	40.89	52.72	4.21	0	0.05	0.16	0.01	41.33	52.83
8	3.36	0.151	0.084	0.152	0.115	41.02	52.74	4.17	0	0.04	0.17	0.02	41.51	52.79
9	3.27	0.148	0.082	0.156	0.117	40.59	52.23	4.01	0.01	0.04	0.16	0.01	41.58	52.86
10	3.23	0.167	0.08	0.168	0.121	40.9	52.5	3.91	0	0.04	0.16	0.01	41.59	52.9
12	3.34	0.155	0.071	0.175	0.115	41.13	52.53	3.92	0	0.04	0.17	0.01	41.68	52.97
13	3.42	0.161	0.077	0.168	0.133	40.99	52.65	3.96	0	0.05	0.17	0.01	41.62	52.83
14	3.49	0.159	0.073	0.17	0.119	40.94	52.64	4	0	0.04	0.17	0.01	41.66	52.84
15	3.6	0.15	0.07	0.172	0.113	41.01	52.74	4.04	0	0.04	0.16	0.02	41.63	52.84
16	3.66	0.139	0.066	0.174	0.092	41.01	52.76	4.08	0	0.03	0.17	0.02	41.58	52.72
17	3.66	0.139	0.072	0.167	0.111	41.14	52.81	4.08	0	0.03	0.16	0.01	41.63	52.61
18	3.69	0.117	0.055	0.172	0.106	41.13	52.6	4.08	0.01	0.03	0.16	0.01	41.68	52.82
20	3.56	0.125	0.061	0.173	0.105	41.26	52.65	4.17	0	0.04	0.17	0.01	41.63	52.91
21	3.27	0.136	0.06	0.187	0.119	41.52	52.64	4.09	0	0.03	0.17	0.01	41.77	52.86
22	3.37	0.14	0.05	0.211	0.134	41.72	52.75	3.94	0.02	0.04	0.17	0	41.91	52.79
23	2.91	0.075	0.024	0.171	0.079	43.02	52.97	3.85	0	0.03	0.18	0.01	41.98	52.6
25	0.63	0.004	0.038	0	0.001	44.98	52.93	0.89	0.02	0	0	0.01	45.7	53.34
25	0.57	0.002	0.044	0.002	0	44.98	52.88	0.89	0.01	0	0	0.01	45.62	53.28
26	0.58	0	0.047	0.004	0.001	45.01	52.83	0.75	0.02	0	0	0	45.84	53.39
26	0.66	0	0.06	0.003	0.006	44.84	53.08	1.16	0.03	0	0	0.02	45.49	53.25
27	0.68	0	0.067	0.007	0.006	44.75	53.13	1.25	0.01	0.01	0	0.02	45.05	53.09
27	0.64	0	0.069	0.015	0	44.76	52.98	1.02	0.03	0.04	0	0.02	44.47	53.08
28	0.68	0	0.07	0.014	0	44.75	53.05	0.74	0.05	0.09	0.01	0.02	43.8	53.06
28	0.75	0	0.072	0.014	0.002	44.66	53.09	0.58	0.05	0.12	0	0.01	43.41	52.95
29	0.87	0	0.074	0.015	0.006	44.43	53.06	0.62	0.05	0.12	0.01	0.02	43.4	52.94
29	0.82	0.007	0.077	0.016	0.004	44.47	53.03	0.67	0.05	0.12	0.02	0.01	43.35	53.05
30	3.73	0.226	0.08	0.124	0.103	40.63	52.68	4.38	0.01	0.04	0.13	0	41.75	52.77
31	3.51	0.247	0.092	0.121	0.094	40.63	52.29	4.5	0.01	0.03	0.14	0.03	41.63	52.56
32	3.59	0.21	0.083	0.14	0.1	40.65	52.43	4.07	0.08	0.05	0.14	0.04	41.43	52.75
33	3.51	0.208	0.091	0.149	0.096	40.71	52.44	3.68	0.21	0.07	0.13	0.09	41.04	52.41
33	3.64	0.202	0.086	0.142	0.085	40.83	52.59	3.66	0.2	0.06	0.14	0.09	40.99	52.19
34	3.59	0.21	0.079	0.139	0.089	40.87	52.47	3.81	0.18	0.06	0.15	0.08	41.07	52.36
35	3.72	0.211	0.075	0.138	0.09	40.86	52.41	3.91	0.17	0.07	0.13	0.08	40.99	52.45
36	3.82	0.177	0.071	0.141	0.082	40.84	52.48	3.95	0.14	0.06	0.12	0.07	41.05	52.6
37	3.93	0.159	0.068	0.146	0.076	40.88	52.52	3.64	0.18	0.06	0.14	0.07	41.36	52.58
38	3.91	0.169	0.07	0.146	0.071	40.97	52.55	3.75	0.14	0.05	0.15	0.06	41.39	52.41
38	3.72	0.181	0.07	0.148	0.071	41	52.38	3.61	0.17	0.05	0.15	0.08	41.35	52.51
39	3.61	0.169	0.073	0.15	0.08	41.08	52.36	3.49	0.18	0.06	0.15	0.09	41.43	52.62
40	3.51	0.158	0.076	0.156	0.084	41.23	52.65	3.38	0.17	0.07	0.15	0.09	41.29	52.85
41	3.28	0.185	0.077	0.162	0.082	41.27	52.63	3.06	0.21	0.07	0.15	0.09	41.48	52.67
42	3.08	0.201	0.086	0.152	0.09	41.3	52.38	2.91	0.18	0.06	0.12	0.06	38.4	48.59
43	3.05	0.174	0.083	0.165	0.093	41.36	52.46	2.98	0.12	0.04	0.09	0.03	36.41	45.74
44	2.99	0.187	0.08	0.163	0.088	41.37	52.42	3.52	0.04	0.03	0.14	0.01	40.86	50.33
44	3.16	0.174	0.066	0.145	0.088	41.38	52.55	3.46	0.11	0.03	0.15	0.05	41.81	52.05
45	3.74	0.096	0.07	0.114	0.06	41.19	52.81	3.27	0.16	0.04	0.15	0.07	41.86	52.48
50	3.43	0.163	0.051	0.134	0.068	41.76	52.37	3.82	0.09	0.06	0.11	0.06	41.34	52.61
52	3.24	0.193	0.059	0.125	0.076	41.75	52.49	3.72	0.1	0.07	0.09	0.06	41.22	52.9
53	3.24	0.195	0.052	0.121	0.076	41.82	52.61	3.75	0.1	0.06	0.1	0.06	41.25	52.73
55	3.23	0.223	0.038	0.129	0.07	41.98	52.63	3.75	0.11	0.06	0.1	0.05	41.31	52.73
56	3.13	0.223	0.044	0.123	0.077	42.03	52.76	3.75	0.12	0.06	0.09	0.06	41.33	52.74
58	3.13	0.201	0.041	0.122	0.078	42.02	52.62	3.79	0.1	0.05	0.09	0.06	41.33	52.62
59	3.16	0.188	0.04	0.122	0.083	42.03	52.49	3.85	0.08	0.05	0.09	0.04	41.35	52.57
61	3.24	0.178	0.041	0.121	0.087	42.06	52.44	3.86	0.07	0.05	0.08	0.05	41.44	52.77
62	3.5	0.138	0.039	0.122	0.066	41.98	52.43	3.96	0.09	0.04	0.08	0.05	41.57	52.87
64	3.45	0.163	0.036	0.116	0.071	42.03	52.46	3.98	0.09	0.05	0.07	0.05	41.56	52.85
65	3.41	0.177	0.034	0.112	0.072	42.07	52.51	3.98	0.09	0.05	0.08	0.05	41.6	52.86
67	3.44	0.161	0.035	0.113	0.062	42.07	52.54	3.98	0.08	0.04	0.08	0.06	41.6	52.81
68	3.35	0.169	0.034	0.113	0.062	42.1	52.66	4.01	0.07	0.04	0.08	0.05	41.61	52.82
70	3.26	0.186	0.036	0.112	0.068	42.16	52.63	4.05	0.06	0.04	0.08	0.05	41.63	52.88
71	3.19	0.208	0.043	0.111	0.079	42.23	52.43	4.07	0.06	0.04	0.08	0.05	41.61	52.83
73	3.34	0.177	0.04	0.108	0.069	42.14	52.4	4.05	0.06	0.03	0.08	0.04	41.56	52.8
74	3.38	0.165	0.034	0.108	0.062	42.15	52.43	4.01	0.07	0.03	0.08	0.04	41.79	52.74
76	3.34	0.167	0.029	0.109	0.058	42.23	52.51	4.02	0.05	0.03	0.07	0.05	41.76	52.78
77	3.3	0.171	0.033	0.102	0.07	42.25	52.64	4.01	0.04	0.03	0.07	0.05	41.71	52.87
79	3.17	0.18	0.036	0.104	0.078	42.27	52.66	3.96	0.04	0.03	0.07	0.05	41.75	52.97
80	3	0.189	0.038	0.112	0.083	42.29	52.62	3.87	0.05	0.03	0.08	0.06	41.83	52.91
82	2.82	0.186	0.04	0.119	0.083	42.32	52.58	3.7	0.05	0.04	0.08	0.06	41.86	52.76
83	2.49	0.157	0.053	0.137	0.086	42.3	52.48	3.32	0.06	0.04	0.08	0.06	42.04	52.84
85	1.76	0.094	0.047	0.109	0.067	43.36	52.72	2.36	0.03	0.02	0.04	0.03	43.59	53.04
86	0.62	0.003	0.003	0.001	0.009	46.04	53.48	1.41	0.01	0	0.01	0	45.14	53.24
88	0.66	0.009	0.003	0.003	0.002	45.94	53.31	1.16	0	0.01	0	0	45.36	53.41
89	0.54	0.023	0.008	0.001	0.004	46.01	53.34	1.17	0.01	0.01	0	0	45.37	53.32
91	0.46	0.029	0.01	0.003	0.005	45.96	53.31	1.14	0.01	0.01	0	0	45.36	53.07
92	0.52	0.027	0.018	0.004	0.01	45.8	53.24	1.09	0.01	0.01	0	0	45.29	52.96
94	0.52	0.017	0.033	0.015	0.001	45.6	53.28	1.02	0	0.02	0	0	45.21	53.05
95	0.43	0.009	0.033	0.062	0.004	45.77	53.16	0.74	0	0.03	0.01	0	45.15	53.02
97	0.57	0.024	0	0.075	0.004	46.21	53.51	0.34	0.01	0.08	0.02	0	44.63	53.09
98	0.85	0.046	0	0	0.01	45.88	53.54	0.76	0	0.01	0	0	45.67	53.27
100	1.03	0.06	0.002	0.015	0.014	45.77	53.67	0.9	0.07	0	0	0.01	45.75	53.13